Quantification of actin nanoarchitecture at the T cell immunological synapse using single molecule localisation microscopy

Peters, Ruby

Awarding institution:
King's College London

Quantification of actin nanoarchitecture at the T cell immunological synapse using single molecule localisation microscopy

A Thesis presented for the degree of Doctor of Philosophy by

Ruby Peters

Department of Physics and Randall Centre for Cell and Molecular Biophysics,

King's College London, 2019.

To my mother…

Originality Statement

I hereby declare that this submission is my own work and to the best of my knowledge it contains no materials previously published or written by another person, or substantial proportions of material which have been accepted for the award of any other degree or diploma at KCL or any other educational institution, except where due acknowledgement is made in the Thesis. Any contribution made to the research by others, with whom I have worked at KCL or elsewhere, is explicitly acknowledged in the Thesis. I also declare that the intellectual content of this Thesis is the product of my own work, except to the extent that assistance from others in the project's design and conception or in style, presentation and linguistic expression is acknowledged.

Acknowledgements

First and foremost, I would like to express my gratitude to Dr. (soon to be Prof!) Dylan Myers Owen for providing me his continued support, interest and guidance. In Dylan's words, "*I won't encourage you unless I think that you will fail*" and I am relieved to say that I have not had much encouragement. On a more serious note, if I become even half the scientist that you are, I will be immensely proud. On a personal level, I thank you for the innumerable gin and tonics you have bought me, the laughter we have shared (typically at your misfortune) and making it so easy to beat you at fantasy football.

I would also like to thank my second supervisor Dr. Christian Lorenz, a friendly face whom I admire greatly. I must also thank Prof. Mark Green, my masters project supervisor. On a professional note, it was through your encouragement and immense knowledge that I published my first paper and commenced my journey into an academic career. On a personal note, thank you for your honesty and emotional support over the last four years. Watching a "*big lad from Burnley*" drinking espresso martinis has also been a highlight for me.

To the members, past and present, of Dylan's lab: Thank you. Our many tea breaks, often heated lunchtime debates and pub sessions have been a source of great happiness for me. George, you showed me the ropes of the lab and welcomed me into this strange and exciting world of biology. Mike, thank you for your interest in my project and your passion for scientific debate. Garth, you were an inspiration to me and I can't thank you enough for your patience in the first few months. Dave, you are so talented and excel at everything that you do. Thank you for the many coffee breaks, insightful discussions and your desire to help others. Adam, I will not miss your constant foot tapping or murmuring to yourself, but, I will greatly miss your humorous one liners and our shared love

of all things drag. Iveta – believe in yourself, you are great! Thank you for your interest in my work; it has been a pleasure getting to know you over the last year. Sabrina, you are one of the most hardworking women I know. You deserve all the success in the world, and I can't wait to watch you achieve it.

Juliette: whilst our first impressions were controversial, we grew to become great friends and I cannot imagine what this journey would have been like without you. You are the smartest person I know, and I greatly admire you as a scientist, so much so that I can look past your horribly messy desk (just). After all, they say that a messy desk is a sign of genius!

Outside of the lab, I must thank Georgina, another strong feminine figure I look up to. You have always been my cheerleader and provided me with encouragement and support. To the recent additions to our office life, James, Hugo and Dylan thank you for providing interesting conversations and lightness to our days. To the staff at the Janelia Research Campus, in particular Jesse and Satya, I thank you for your great assistance in performing 3D iPALM experiments. I would also like to thank Prof. Helge Ewers, who provided me with the IRIS probe used in this Thesis. Finally, I would like to thank the staff of the Nikon Imaging Centre at King's, especially Isma, for their guidance and support.

Without the unconditional love and support I have received from my family, throughout my life and especially during the last three years, none of this would have been possible. My mother, my number one fan, I am eternally grateful to you for nurturing my passion for knowledge and imparting your kindness and morals onto me. My father, thank you for being so proud of me and sharing this journey with me from the very beginning. My step-father, thank you for loving

me as one of your own, and for shaping me into the person I am today. I love you all greatly.

My darling sister, my confident, my best friend I thank you for your unquavering love and support. You are giving me the greatest title I could wish for: Aunty Ruby. My grandparents, Beryl and Eric, Bez and Ez: the dynamic duo. Without you, none of this would be possible. I love you with all my heart.

To the girls, Sophie, Sarah, Emma and Jess. Although we have been apart for over seven years, our friendship has remained as strong as ever. I thank you all for believing in me, especially at times when I did not believe in myself.

Last but certainty not least, Jamie. You have been with me from day one to day one thousand and ninety-five. I will be eternally grateful to you for your unconditional emotional support, love and kindness during this phase of our lives. You are my rock, my soulmate and my future. On to our next adventure!

Table of Contents

Terms & Abbreviations

ABD	Actin binding domain
ABP	Actin binding protein
ADA	Actin disrupting agent
ADP	Adenosine diphosphate
AFM	Atomic force microscopy
AIS	Axon initial segment
APC	Antigen presenting cells
ARP	Actin related proteins
ARP 2/3	Actin related protein subunits 2/3
ATP	Adenosine tri-phosphate
BSA	Bovine serum albumin
CAPU	Cappuccino
CAS9	CRISPR associated protein 9
CD2	Cluster of differentiation 2
CD28	Cluster of differentiation 28
CD3	Cluster of differentiation 3
CD4	Cluster of differentiation 4
CD43	Cluster of differentiation 43
CD45	Cluster of differentiation 45
CD8	Cluster of differentiation 8
CD80	Cluster of differentiation 80
CDC42	Cell division control protein 42 homolog
CK666	2-Fluoro-N-[2-(2-methyl-1H-indol-3-yl)ethyl]benzamide
COBL	Cordon-bleu
COT	Cyclooctatetraene
CP	Capping protein
CPU	Central processing unit
CRISPR	Clustered regularly interspaced short palindromic repeats
CSMAC	Central supramolecular activation cluster
CSR	Completely spatially random
DAPI	4',6-diamidino-2-phenylindole
DBSCAN	Density-based spatial clustering of applications with noise
DHPSF	Double helix point spread function
DIA1	Diaphanous-related formin-1
DNA	Deoxyribonucleic acid
DNA-PAINT	Deoxyribonucleic acid-Point accumulation for imaging in nanoscale topography
DSMAC	Distal supramolecular activation cluster

DSTORM	Direct Stochastic optical reconstruction microscopy
ECM	Extracellular matrix
EGPF	Enhanced green fluorescent protein
EGTA	Egtazic acid
EM	Electron microscopy
EMCCD	Electron multiplying charged coupled device
ERK	Extracellular signal–regulated kinases
ERM	Ezrin-radixin-moesin
EWI-2	Glu-Trp-Ile EWI motif-containing protein 2
F(AB)	Antigen-binding fragment
F-ACTIN	Filamentous actin
FIRE	Fourier image resolution
FRC	Fourier ring correlation
FBS	Fetal bovine serum
FH2	Formin-homology 2
FLIM	Fluorescence lifetime imaging microscopy
FOV	Field of view
FSPP	Fibrous spatial point pattern
FWHM	Full width at half maximum
G-ACTIN	Globular actin
GAPDH	Glyceraldehyde 3-phosphate dehydrogenase
GEF	Guanine nucleotide exchange factor
GFP	Green fluorescent protein
GPI	Glycosylphosphatidylinositol
GRAP	Grb2-related adapter protein
GFP	Green fluorescent protein
HAWK	Haar wavelet kernel
HCS	High content screening
HIV-1	Human immunodeficiency virus-1
ICAM	Intercellular adhesion molecule
IL-2	Interleukin-2
IPALM	Interferometric photoactivated localization microscopy
IRIS	Image reconstruction by integrating exchangeable single-molecule localisation
ITAM	Immunoreceptor tyrosine activation motif
KD	Knock down
KIR	killer immunoglobulin-like receptor
KO	Knock out
LAT	Linker for activation of T cells
LBPA	Lysobisphosphatidic acid

LCK	Leukocyte specific protein tyrosine kinase
LFA-1	Lymphocyte function associated antigen-1
LPC	L-α-Lysophosphatidylcholine
MEA	Mercaptoethylamine
MES	2-(N-morpholino)ethanesulfonic acid
MGCL	Magnesium chloride
MHC	Major histocompatibility complex
MPR	Minimum point requirement
MTOC	Microtubule organisation centre
N_A	Numerical aperture
NACL	Sodium chloride
NK	Natural killer
NPF	Nucleation promoting factor
PC	Pair correlation
PA-FP	Photoactivatable fluorescent protein
PAINT	Point accumulation for imaging in nanoscale topography
PALM	Photoactivated localisation microscopy
PBS	Phosphate buffered saline
PFA	Paraformaldehyde
PFS	Perfect focus system
PLL	Poly-L-lysine
pMHC	Peptide-bound major histocompatibility complex
PSF	Point spread function
PSMAC	Peripheral supramolecular activation cluster
QD	Quantum dot
QY	Quantum yield
RESOLFT	Reversible switchable optically linear fluorescence transitions
RIP	Radial intensity profile
RNA	Ribonucleic acid
ROI	Region of interest
ROSE	Robust statistical estimation algorithm
SCMOS	Scientific complementary metal-oxide-semiconductor
SIM	Structured illumination microscopy
SLP-76	SH2-domain-containing leukocyte protein of 76 kDa
SMAC	Supramolecular activation cluster
SMIFH2	Small-molecule inhibitor of formin homology 2 domain
SMLM	Single molecule localisation microscopy
SPIM	Selective plane illumination microscopy
SPP	Spatial point pattern

SQUIRREL	Super-resolution quantitative image rating and reporting of error locations
SRC	Proto-oncogene tyrosine-protein kinase
SRRF	Super-resolution radial fluctuations
STED	Stimulated emission depletion
STICS	Spatiotemporal image correlation spectroscopy
STORM	Stochastic optical reconstruction microscopy
SYK	Spleen tyrosine kinase
TCR	T cell receptor
TIRFM	Total internal reflection microscopy
TRIS	Trisaminomethane
UPAINT	Universal point accumulation for imaging in nanoscale topography
UV	Ultra-violet
VOI	Volume of interest
WASP	Wiskott-Aldirch syndrome protein
WAVE	WASP-family verprolin-homologous
WH2	WASP homology 2
ZAP-70	ζ chain-associated tyrosine phosphoprotein of 70 kDa

Abstract

Much of our knowledge regarding cellular structure and function has derived from our ability to visualise distinct processes through fluorescence microscopy. The unparalleled combination of specificity and compatibility with live samples renders the fluorescent microscope an invaluable imaging modality across the life sciences. Owing to the diffraction of light, the resolution of an optical system is inherently limited. For centuries, a fundamental, immutable resolution was thus imposed on the fluorescence microscope and the study of cellular features existing beyond this limit was unfathomable. Circumvention of the diffraction barrier however was achieved experimentally in 2006, and the advent of super resolution microscopy, for whose discovery was awarded the 2014 Nobel Prize in Chemistry, represented a paradigm shift in our apperception of the resolution issue in microscopy. A repertoire of super resolution microscopy methods have since emerged, allowing unprecedented access to the cellular architecture on the nanoscale. The focus of this Thesis is the implementation of single molecule localisation microscopy (SMLM) for the study of sub-cellular fibrous organisation, which routinely achieves ~ 30 nm spatial resolution.

Concurrent with the remarkable technological advances in the field of SMLM is the need for complimentary data analysis methods, to help tune SMLM into a quantitative imaging tool. Despite variations in the working principles employed to achieve SMLM images, all modalities share a common data output: a spatial point pattern (SPP). One must therefore embrace new strategies for the study of SMLM images, compared to conventional fluorescence microscopy methods; a technical challenge. This challenge is exacerbated when studying filamentous structures, whose topologies and cytoarchitectures are typically complex. This Thesis aims to deliver analysis methods for the study of fibrous SPPs generated by SMLM, to compliment the varied tools currently available for clustered SPPs.

The presented analysis methods will be validated by use of simulated data and applied to the study of the actin cytoskeleton at the T cell synapse. The actin cytoskeleton is responsible for maintaining a wide range of cellular behaviours, and its malfunction has been implicated in various human diseases. Filamentous actin is subject to extensive remodelling to execute diverse cellular tasks, mediated by a catalogue of accessory proteins. Besides its structural role in maintaining cell morphology, the functional role of actin in regulating cell signals is a current topic of great interest. This Thesis primarily investigates the nanoarchitecture of the actin cytoskeleton at the T cell immunological synapse via SMLM. The effect of the actin crosslinking protein α-actinin on the nanoscale organisation of actin at the mature immunological synapse, and its role in the clustering of the linker for activation of T cells (LAT), a prominent signalling molecule involved in T cell activation, will be investigated.

Chapter 1 Actin and the T cell immunological synapse

1.1 Introduction

Actin is a highly abundant protein expressed in all eukaryotic cells. Actin is recognised as a central player in multifarious cellular functions such as cell morphogenesis, cell division and cell migration (Pollard and Cooper, 2009, Heng and Koh, 2010, Lanzetti, 2007). Actin, along with microtubules and intermediate filaments form the dynamic cytoskeleton, providing the cell and its cytoplasmic constituents mechanical support. A fundamental characteristic of the actin cytoskeleton is its ability to rapidly and precisely re-arrange over a matter of seconds, producing diverse structures in response to external stimuli that vary across cell types. Such processes are highly regulated across multiple levels mediated by various actin binding proteins (ABPs), and the cumulative re-arrangement of the actin cytoskeleton relies upon the interplay between regulatory, capping, severing and nucleating proteins.

T cells form a crucial part of the adaptive immune system, performing specialised functions required for a healthy immune response. For this, T cells must engage with antigen presenting cells (APCs), forming a junctional

structure termed the immunological synapse (Bromley et al., 2001, Dustin, 2014). It is through this interface that external cues are translated into downstream T cell effector functions, via specific intracellular signalling pathways. The actin cytoskeleton participates in each stage of the immunological synapse formation, from remodelling at initial contact with the APC, to maturation and eventually disassembly of the interface (Dustin and Cooper, 2000, Piragyte and Jun, 2012). Indeed, the role of actin at the T cell immunological synapse is manifold. Upon synapse formation, the T cell must transition from a migratory cell to a highly adherent cell, achieved through rapid cytoskeletal remodelling. Further, the actin cytoskeleton generates force through polymerisation, thus allowing an expansive scan of the APC membrane (Burkhardt et al., 2008). Upon T cell activation, numerous signalling cascades that induce further actin re-arrangements, polymerisation and dynamics are activated (Kumari et al., 2014). Various molecules, proteins and co-factors orchestrate this process, which ultimately governs signalling outcomes. Owing to its scaffolding ability, the cytoskeletal framework further acts as a platform to which other signalling molecules can bind, enhancing T cell activation (Campi et al., 2005). Conversely, the actin cytoskeleton is also thought to downregulate T cell activation, through its spatio-temporal re-organisation (Fooksman et al., 2010), perhaps facilitating T cell receptor (TCR) internalisation (Alarcón et al., 2011). As such, the role of actin at the immunological synapse is complex.

The execution of many cellular functions attributed in part to the actin cytoskeleton are manifestations of its macro- and nano scale architecture (Blanchoin et al., 2014, Skau and Waterman, 2015) particularly at the T cell immunological synapse. With recent advances in super resolution microscopy methods, it has now become possible to visualise this nanoarchitecture.

However, the quantitative analysis of these fibrous super-resolved data sets is comparatively understudied. As such, this Thesis aims to provide precise characterisation of the actin cytoskeleton at the T cell immunological synapse, by adopting the fields of spatial descriptive statistics and single molecule localisation microscopy (SMLM).

1.2 Actin and the eukaryotic cytoskeleton

Actin was first isolated from muscle cells in the early 1940s. As a partner of myosin, actin was found to play a crucial role in muscle contraction, through Adenosine Tri-Phosphate (ATP) hydrolysis mediated superprecipitation (Hatano and Oosawa, 1966). Although actin function was primarily understood to be uniquely confined to muscle contraction, it is now well established that actin is implicated in various cellular processes such as cell migration, polarisation and division across all eukaryotes (Pollard and Cooper, 2009, van den Ent et al., 2001, Gunning et al., 2015), and more recently in certain prokaryotes (Jones et al., 2001, van den Ent et al., 2001). Recent work suggests that diversity in cellular function can be understood through the presence, or lack of, of the actin gene family. Yeast for example presents only one actin gene (Gallwitz and Sures, 1980) whilst humans possess six genes, each encoding a different isoform. These isoforms, $\alpha_{Skeletal}$, $\alpha_{Cardiac}$, α_{Smooth}, γ_{Smooth}, β_{Cyto} and γ_{Cyto}, are responsible for differing functions and located in a cell specific manner (Herman, 1993). Despite minor differences between isoforms, eukaryotic actins are highly conserved between diverse species with varying gene numbers.

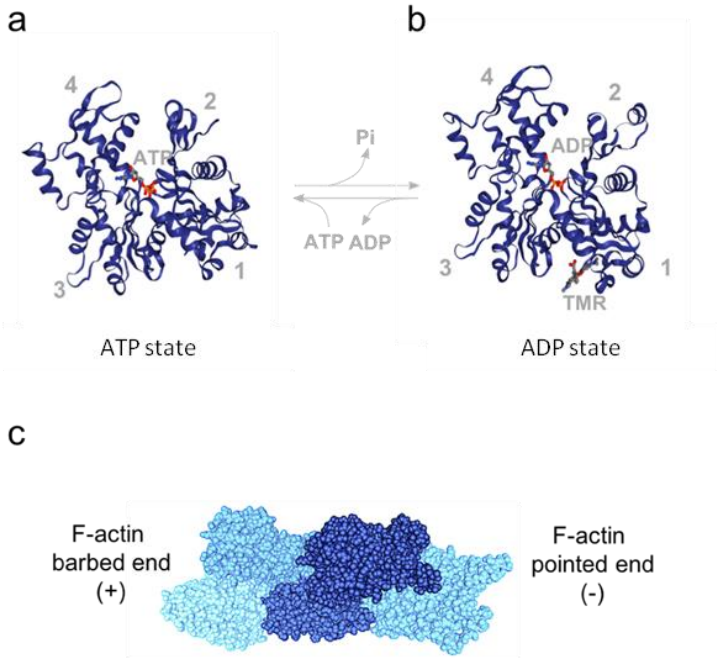

Figure 1: Structure of the G-actin monomer and F-actin. Ribbon models of and ATP bound actin (a, PDB: 2HF4) and ADP bound actin (b, PDB: 1J6Z). Labelling actin with tetramethylrhodamine (TMR) renders actin non-polymerisable and enabled the crystal structure of uncomplexed actin to be resolved. Numbers 1-4 represent the domain numbers. Space fill model of F-actin (c, PDB:4A7N).

1.2.1 Actin polymerisation

Actin is a moderately sized (43 kDa) protein and may exist as either a free monomer in its globular form, termed G-actin (Figure 1a, b), or as a constituent of a liner protofilament termed filamentous (F-) actin (Figure 1c) (Holmes et al., 1990). G-actin can assemble into F-actin filaments in a reversible process termed polymerisation. The first stage of actin polymerisation is spontaneous nucleation, in which G-actin monomers coalesce into unstable oligomers which subsequently serve as the stable seed of filament growth upon incorporation of multiple subunits (Figure 2a) (Sept and McCammon, 2001). During this elongation stage, actin monomers reversibly bind to both ends of

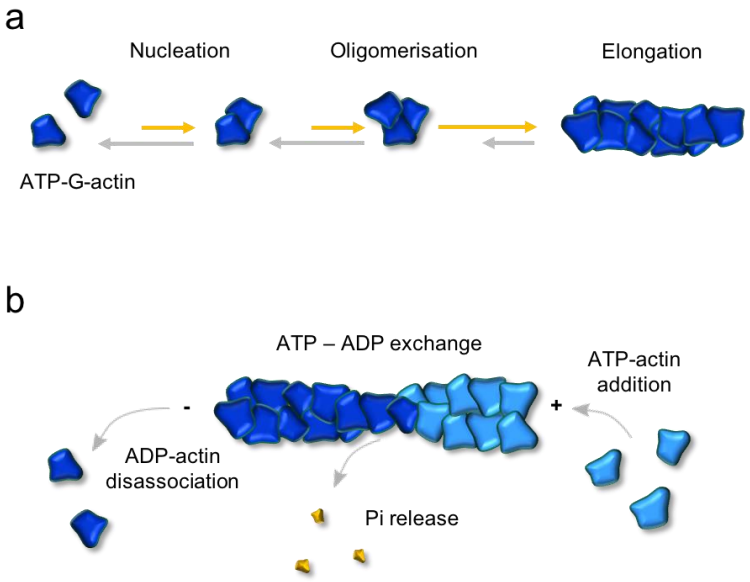

Figure 2: Schematic depicting actin polymerisation. The first stage of actin polymerisation is spontaneous nucleation (a), in which ATP primed G-actin monomers coalesce into unstable oligomers. During the elongation phase (a), ATP-G-actin subunits reversibly bind to the actin oligomer, contributing to the filament growth. At the steady state, actin treadmilling can occur (b), in which monomer addition at the barbed (+) terminus is balanced by monomer loss at the pointed (–) terminus.

the pre-existing filament until the steady state is reached, in which G-actin monomeric exchange at the filament ends does not result in a net growth (Figure 2b). This equilibrium stage indicates the ability of G-actin to polymerise, as the concentration of free subunits (termed the critical concentration) determines either further polymerisation or depolymerisation of F-actin (Wegner and Engel, 1975).

Whilst G-actin presents a globular structure, each globule is decomposed into two lobes divided by an upper cleft at subdomains 2 and 4 (Kabsch et al., 1990). This cleft serves as an ATP binding site (Figure 1a), interchangeably

termed the ATPase fold, at which ATP undergoes hydrolysis to adenosine diphosphate (ADP) (Figure 1b). A lower cleft subdivides domains 1 and 3 and is termed the target binding cleft, as numerous actin binding ABPs interact with the monomer at this site (Dominguez, 2004). The communication between the two large clefts influences the nucleotide-dependent conformational state of the G-actin monomer (Pfaendtner et al., 2009).

ATP bound G-actin can readily polymerise into F-actin, consisting of two protofilaments forming a helix structure of ~7 nm diameter. Despite the intrinsic ATPase activity of G-actin being relatively low, upon incorporation to a growing filament, its activity is enhanced significantly (Wegner and Engel, 1975). As the F-actin filament is an ATPase, it is subject to an array of interesting dynamic behaviours. Owing to its structurally polarised nature, the filament must maintain differing critical concentrations at both termini, as ATP-actin and ADP-actin exhibit unique disassociation "off" rates (Fujiwara et al., 2007). As such, elongation occurs at a faster rate at the barbed (+) end of the filament (Drenckhahn and Pollard, 1986). This nonequilibrium feature of F-actin enables the treadmilling effect, which occurs at the steady state (Wegner, 1976). For this, the critical concentration of free G-actin monomers must be interposed between those required for polymerisation of the filament termini. If this condition is met, a balanced exchange between monomer addition at the barbed end (ATP-actin binding) and subunit loss at the pointed end (ADP-actin disassociation) occurs such that the filament length remains constant. This treadmilling effect has also been observed in microtubule filaments, despite their dynamic instability and structural dissimilarities (Rodionov and Borisy, 1997). This turnover process has remarkable implications in cell motility and function, directing cell migration and force generation to mention but a few (Lai et al., 2008, Small, 1995).

1.2.2 Regulators of actin

The actin cytoskeleton undergoes continuous remodelling and regulation across multiple levels; elongation by monomer addition, shrinkage via depolymerisation, controlled filament growth via capping or sequestering agents to prevent new monomer addition, severing to encourage new filament formation and branched filamentous arrays via actin related proteins (ARPs) (Pollard and Borisy, 2003). Working in concert, this array of proteins serve to regulate the highly dynamic turnover of actin assemblies (Lee and Dominguez, 2010). In the post genomic epoch, a multitude of ABPs have been discovered, and their structure-function relationships in the assembly and disassembly of both individual filaments and higher ordered networks have been widely studied in diverse biological systems (Qu et al., 2015, Borovac et al., 2018, Johnson et al., 2014). Defects in cytoskeletal proteins or indeed uncontrolled actin dynamics have been implicated in numerous human diseases (Huang et al., 2008, Yamaguchi and Condeelis, 2007, Doctor and Fouassier, 2002) and as such, actin remodelling and cellular coordination of these differing hierarchical structures is a highly regulated process.

1.2.2.1 G-actin binding proteins

Proteins that bind the G-actin monomer are important for the maintenance of the unpolymerized actin pool at concentrations higher than the critical concentration (Figure 3a). A notable example is profilin, whose function has been extensively studied (Metzler et al., 1994, Goldschmidt-Clermont et al., 1990, Dong et al., 2000). The actin-sequestering activity of profilin promotes depolymerisation, however, profilin also serves as the catalysis for ADP-ATP exchange to increase local concentrations of ATP-actin which can be readily incorporated into filaments and thus can be considered as a F-actin promoter

(Korenbaum et al., 1998, Pantaloni and Carlier, 1993). Moreover, profilin bound G-actin monomers are preferentially recruited to the barbed termini of pre-existing filaments which at high concentrations can antagonise the binding ability of capping proteins (Kang et al., 1999). Profilin however cannot regulate the monomeric pool of free monomers alone; its activity is complex and is influenced by the assembly and or disassembly of filaments, the balance of which is further mediated by capping, severing and nucleating agents.

1.2.2.2 Rho family Guanosine-5'-triphosphate (GTP)ases

Cell-cell interactions, contacts with the extracellular matrix (ECM), and communication of chemical messengers via cell surface receptors all generate signals that prompt the actin cytoskeleton to undergo remodelling at a specific time and location. Whilst the exact molecular mechanisms underpinning this remodelling process remain to be fully characterised, it is largely accepted that Rho family GTPases, members of the Ras superfamily, play a critical role (Hall, 1994, Sit and Manser, 2011). Rho, Rac and Cdc42 remain the most studied classes of the GTPases, each binding numerous target proteins or kinases in eukaryotes (Bustelo et al., 2007). In the active state (GTP-bound) upon recognition of their cytoskeletal effectors, whether this be the actin nucleators or nucleation promoting factors (NPFs), specifically integrated signalling pathways which can directly or indirectly alter actin assembly are activated, dictating the direction of cell migration (Nobes and Hall, 1999), filopodia and lamellipodia formation (Kozma et al., 1995, Ridley et al., 1992) and inducing acto-myosin movement (Ridley and Hall, 1992). Indeed, several studies report defects in actin driven cellular processes such as migration and cytokinesis upon expression of Rho-family GTPase mutants (Nobes and Hall, 1999, Mabuchi et al., 1993).

1.2.2.3 Nucleators

Nucleators of actin are critical for surmounting the rate-limiting stage of actin polymerisation and influence the architecture of actin networks in cells. Actin nucleators can be split into three main families: the Arp 2/3 complex and its associated NPFs (Mullins et al., 1998), formins (Pring et al., 2003) and tandem monomer binding nucleators (Qualmann and Kessels, 2009).

The Arp 2/3 complex is composed of seven subunits, with actin related proteins 2 and 3 possessing structural similarities to the G-actin monomer (Figure 3b) (Goley and Welch, 2006). As such, the complex is proposed to serve as a nucleation site by mimicking the role of the actin dimer. Unique to this nucleator is its ability to promote daughter filaments, extending from pre-existing mother filaments at a characteristic 70° angle, thus enabling the formation of a branched actin network (Mullins et al., 1998). For potent Arp 2/3 activation, NPFs are required. Examples include the Wiskott-Aldirch syndrome protein (WASP) family, and WASP-family verprolin-homologous (WAVE) proteins, which cumulatively act to regulate Arp 2/3 mediated actin polymerisation (Machesky and Insall, 1998, Machesky et al., 1999, Yarar et al., 1999).

Formins are Rho targets and participate in actin polymerisation independently of Arp 2/3 activation, through their conserved formin-homology 2 (FH2) domains (Pruyne et al., 2002). In contrast to the Arp 2/3 nucleator, the family of formins are multi-domain proteins which regulate un-branched actin filaments (Pring et al., 2003). Formins associate with the barbed ends of elongating filaments enabling further elongation, thus serving as a barrier to capping proteins, that otherwise localise to the growing filament terminus (Figure 3e) (Otomo et al., 2005). The family of formins is broad and

diverse, examples include Dia1 and formin-like protein 1 (FMNL-1), each offering differing nucleation activities (Goode and Eck, 2007).

More recently, the family of tandem monomer binding nucleators including but not limited to Spire (Qualmann and Kessels, 2009) and cordon-bleu (Cobl) (Ahuja et al., 2007) have emerged as interesting regulators of actin. These nucleators are thought to gather actin monomers into a nucleation complex, although the mechanism driving the formation of this polymerisation nucleus remains to be elucidated. The commonality among these proteins is their WH2 domains, despite differences in additional actin binding elements for each nucleator (Qualmann and Kessels, 2009). Indeed, owing to their structural heterogeneity, it is likely that more tandem monomer binding nucleators have yet to be discovered. To date, branched tandem monomer binding nucleator mediated actin networks have yet to be observed.

Communication between the three major families of actin nucleators is complex. For example, whilst Arp 2/3 activation is not a pre-requisite for formin driven actin nucleation, the formin Capu has been demonstrated to interact with both Spire and the NPF WASH (Liu et al., 2009), a fundamental regulator of the Arp 2/3 complex. As such, the delicate interplay between the nucleators controls actin assembly and governs the architecture of filamentous networks observed in cells.

1.2.2.4 Severing proteins

Actin severing proteins regulate the assembly of actin networks by shortening pre-existing filaments. Cofilin (a member of the actin depolymerising factor family of proteins) is unusual, for it binds both G- and

F-actin. Cofilin severs actin filaments, and upon binding the disassociation rate constant of actin subunits at the pointed end is increased, thereby encouraging their disassociation from the filaments pointed terminus (Lappalainen and Drubin, 1997). Cofilin binding inhibits the exchange of ADP to ATP, thus precluding further polymerisation at this site (Figure 3c). The severing activity of Cofilin however can promote formation of new actin structures, for example by facilitating the re-organisation of the new shorter filaments into a bundled network (Ghosh et al., 2004, Wu et al., 2016).

1.2.2.5 Capping proteins

Actin filament growth is further mediated by the binding of capping proteins to either of the filament termini. Dependent upon the binding location, the incorporation of capping proteins can either promote or inhibit filament elongation. For example, capping protein (CP) or CAPZ in muscle cells, acts to prevent elongation by binding to the barbed terminus (Yamashita et al., 2003), leading to a shorter filament provided that ADP-G-actin disassociation at the pointed terminus persists (Figure 3c). Tropomoldulin on the other hand, binds to the pointed end of pre-existing filaments, thus inhibiting disassociation of ADP-G-actin resulting in filament elongation and stabilisation (Weber et al., 1994).

1.2.2.6 Crosslinking proteins

Actin crosslinking proteins gather pre-existing filaments to form bundled and crosslinked networks and are typically localised to the cytoskeleton. Many actin crosslinking proteins also serve as molecular scaffolds, providing a physical linkage between actin networks and ECM related proteins (Figure 3d) (Bennett and Baines, 2001, Bachir et al., 2017). A notable actin crosslinking

protein, α-actinin, belongs to the spectrin superfamily of proteins, and acts to organise actin filaments into networks. In its native form, α-actinin is a homodimer formed of 2 polypeptide subunits arranged in an antiparallel manner (Sjöblom et al., 2008). To date, 4 human α-actinin genes have been described (α-actinin1-4) (Murphy and Young, 2015). Nonsarcomeric α-actinin (of α-actinin1 and α-actinin4) is associated with crosslinking activity of the actin cytoskeleton (Sjöblom et al., 2008), whereas the muscle isoforms (of α-actinin2 and α-actinin3) play critical roles in anchoring actin filaments to the muscle Z-disk (Squire, 1997). Nonsarcomeric α-actinin is typically located at focal adhesion sites (at which actin filaments attach to the cytoplasmic face of the plasma membrane), at which it interacts with the cytoplasmic tail of several adhesion related receptors such as integrins and Intercellular adhesion molecules (ICAMs) (Otey et al., 1990, Carpén et al., 1992). Further, α-actinin has been proposed to anchor actin filaments to the plasma membrane through ECM related protein paxillin and focal adhesion molecule zyxin (reviewed by (Otey and Carpen, 2004)). Nonsarcomeric α-actinin has also been shown to interact with various signalling molecules, such as those belonging to the ERK family (Trulsson et al., 2011, Otey and Carpen, 2004), thus acting as a scaffold to promote protein-protein interactions.

A summation of the numerous ABPs that influence actin assembly is presented in Figure 3.

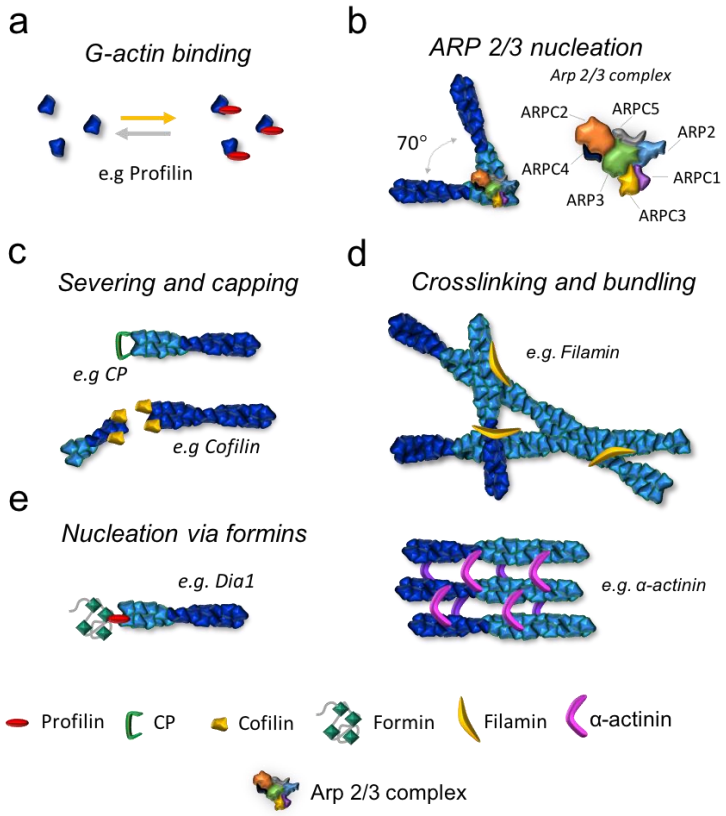

Figure 3: Schematic depicting processes that regulate actin polymerisation and architectures. G-actin binding proteins such as profilin (a) are important for maintenance of the monomer pool. Arp 2/3 mediated actin nucleation via NPFs are responsible for the formation of branched filament arrays (b), whereas capping and severing agents (c) disrupt pre-existing filaments. Crosslinking and bundling proteins (d), organise filaments into a 3D network, and are proposed to anchor actin to the ECM. Actin can also be nucleated via formins, which associate with the barbed ends of filaments and whose activity can be enhanced via profilin interaction (e).

1.3 The architecture of F-actin and its implications in cellular processes

Macroscale cellular dynamics arise from the activity of actin monomers and filaments with numerous other proteins that not only govern cell shape and movement, but also drive biological processes such as cytokinesis and endocytosis (Blanchoin et al., 2014, Weinberg and Drubin, 2012, Collins et al., 2011). In eukaryotic cells, various higher order structures of actin exist such as stress fibres, dendritic arrays, cortical networks, parallel and anti-parallel bundles and contractile ring like structures (Chhabra and Higgs, 2007). Whilst the macro and nanoscale architecture of cellular actin is diverse, it remains spatio-temporally site specific in order to drive distinct cellular processes. Indeed, the structure-function relationship of actin and its interaction with the plasma membrane remains a current subject of interest.

1.3.1 F-actin organisation in mammalian cells

In mammalian cells, actin filaments are organised into various structures (Figure 4). In actin bundles filaments are organised into arrays, mediated by a repertoire of ABPs. Actin bundles can be further separated into those formed through parallel or anti-parallel filaments, which are structurally and functionally distinct (Blanchoin et al., 2014). For example, parallel actin bundles possess the same polarity and since their barbed termini are juxtaposed with the plasma membrane, these structures support microvilli and filopodia based projections (Chhabra and Higgs, 2007). In migratory cells, these actin rich protrusions are responsible for sensing the extracellular environment thus prompting cellular response upon encountering a stimulus. Anti-parallel actin bundles however consist of filaments with opposite

orientations, capable of driving contractile based functions (Blanchoin et al., 2014). In actin networks, filaments are crosslinked to form a 3D meshwork which is proposed to exhibit properties similar to those of a semisolid gel (Bray, 2001). Actin networks are highly abundant at the cell periphery, which together with numerous ABPs and motor proteins forms the cell cortex. The cortex is bound to the plasma membrane and provides the cell its shape and structure. Arp 2/3 mediated branched networks of actin in lamellipodia for example, are responsible for macroscale advancement of the cell edge, through co-ordinated polymerisation.

Actin stress fibres, composed of bundled fibres of various orientations, are also present in mammalian cells although the mechanism of formation varies per stress fibre and as such, their contractile properties also varies (Hotulainen and Lappalainen, 2006). Actin stress fibres are held together primarily through α-actinin and connect the cytoskeleton to the ECM, through focal adhesions. Consistent amongst these stress fibres is their ability to produce a cellular response to imposed mechanical forces. The motor protein myosin assembles into filaments that incorporate into the cortex, thus providing a global cellular contractility (Chugh and Paluch, 2018). The cortex is composed of both bundled, crosslinked and branched filaments, typically providing a mesh size of 50 – 200 nm (Eghiaian et al., 2015, Kronlage et al., 2015), dependent on the cell type. Interestingly, actin and proteins that promote its nucleation (Arp 2/3, WASP) have also been found in the nucleus (Weston et al., 2012). Evidence suggests that nuclear actin plays an important role in RNA transcription (Percipalle and Visa, 2006) and chromatin remodelling (Olave et al., 2002), and whilst it is generally accepted that monomeric nuclear actin exists, the

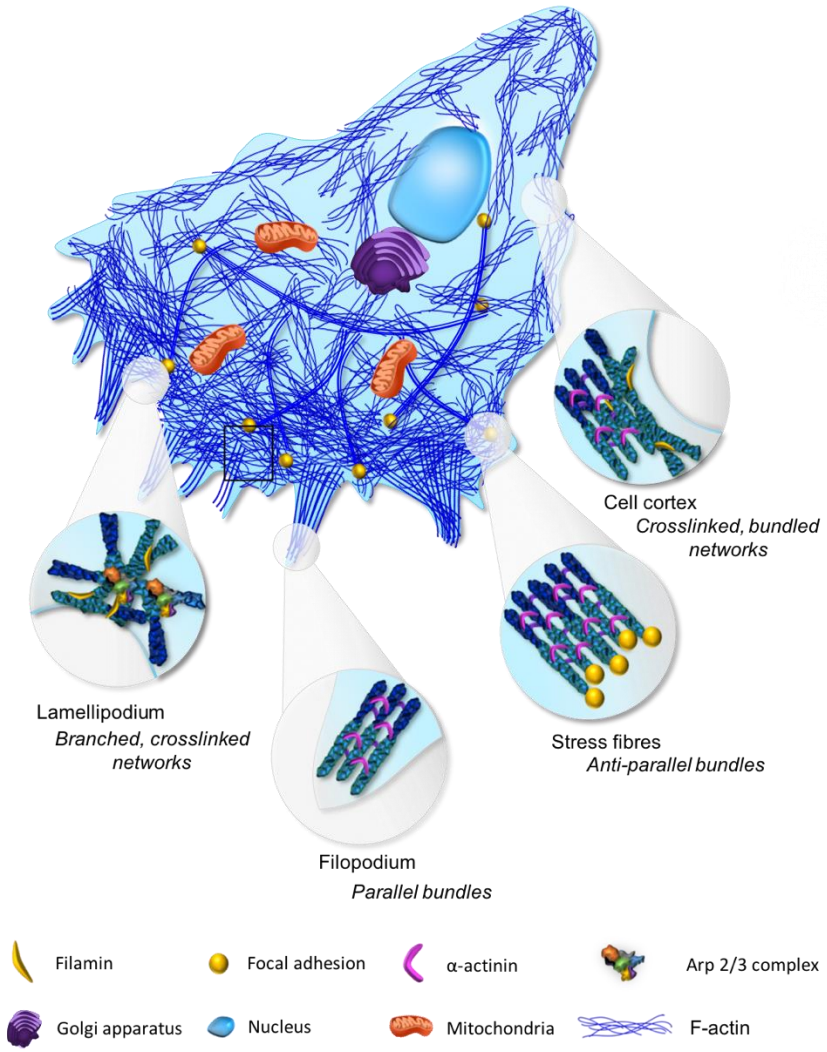

Figure 4: Schematic depicting F-actin organisation in a cross section of a hypothetical mammalian cell. The lamellipodium, filopodium and cell cortex present differing actin architectures, mediated by a repertoire of accessory proteins. Actin stress fibres are also present, and act to connect the cytoskeleton to the ECM, providing the cell structural integrity.

existence of polymeric nuclear actin is controversial. A schematic of the varied actin networks in a typical mammalian cell is presented in Figure 4.

The physical size and density of actin networks is important to their functions, with various cell types responding differently to perturbations in actin networks. The presence of ABPs directly influences the size and density of the actin meshwork (Bovellan et al., 2014), as previously discussed. Formins primarily act to promote filament elongation and protect the barbed ends of pre-existing filaments from capping agents. As such, formin inhibition could result in a differing actin network topology. Arp 2/3 inhibition in fibroblasts for example, results in lamellipodial disruption and thus defects in cell migration (Suraneni et al., 2012). Further, disruption of contractile actomyosin arcs at the T cell immunological synapse via formin inhibition results in diminished T cell signalling (Murugesan et al., 2016). These actomyosin arcs contribute to internetwork competition for the G-actin monomer pool, and recently, their interaction with Arp 2/3 networks in has been implicated in transitions from immobile to migratory systems (Ponti et al., 2004, Burke et al., 2014).

Owing to its importance in numerous cellular functions, unsurprisingly, defects in actin polymerisation and architectures are linked to various human diseases. WAS is a severe immunodeficiency disorder, characterised by immune dysregulation, lymphoid malignancies and eczema (Burkhardt et al., 2008). Mutations of the WAS gene prevents normal WASP expression, resulting in compromised typical cellular activities such as proliferation and immunological synapse formation. The role of actin mechanics in the invasion stage of cancer metastasis has also garnered increasing attention over the last decade. At the invasion stage, the cancerous tumour can penetrate the ECM

via invadopodia and begins to enter the surrounding tissue (Paz et al., 2014). This translocation is further facilitated by lamellipodia and filopodia. Actin has also been implicated in Alzheimer's disease, the most common cause of dementia. Cofilin-actin rod structures have been found in the neurons of Alzheimer's disease, and synapse loss leading to cognitive impairment, has been linked to abnormalities in the actin cytoskeleton (Bamburg and Bernstein, 2016). The actin cortex can also serve as a platform for viral infections. The human immunodeficiency virus-1 (HIV-1) coerces the cortex into facilitating viral entry, reverse transcription and migration by taking command of a vast range of actin regulators and pathways (Stolp and Fackler, 2011).

1.3.2 The association of actin with the plasma membrane

The cytoskeleton is anchored to the plasma membrane through linkers such as ezrin-radixin-moesin (ERM) family proteins (Neisch and Fehon, 2011) and myosin-1 motor proteins (Cooper, 2009). In mammalian cells, ERM activation occurs during mitosis, and is a pre-requisite for correct spindle orientation (Machicoane et al., 2014). ERM proteins typically localise to regions of cytoskeleton-membrane proximity, such as the filopodia, membrane protrusions and ruffles. Thus, ERM locality can influence membrane topology, providing more linkages at specific cellular regions. Cytoskeleton-membrane interactions are also important for bleb mediated cell migration, in which blebs are located at regions of looser attachment (Paluch and Raz, 2013). Proteins related to spectrin such as filamin and ankyrin also act as a physical linkage between the cortex and the plasma membrane (Cooper, 2009). Filamin-A (expressed in mammalian cells) possesses an α-actinin like actin binding domain (ABD), and crosslinks actin filaments whilst

anchoring a wide variety of transmembrane proteins to the cortex (reviewed by (Feng and Walsh, 2004)). Actin stress fibres, crosslinked by α-actinin, also provide a linkage between the cytoskeleton and the membrane. They are anchored to the membrane through their interactions with integrins at focal adhesion sites, as previously discussed. It is thought that many proteins influence this interplay, including talin and vinculin (Zamir and Geiger, 2001). Both talin and α-actinin bind the cytoplasmic tail of integrins, with talin also influencing Arp 2/3 activity through its binding to vinculin. At these focal adhesion sites, α–actinin bound actin filaments are also thought to be linked to the plasma membrane via paxillin and zyxin (Otey and Carpen, 2004).

1.3.3 Plasma membrane compartmentalisation and actin driven protein clustering

Plasma membrane organisation through compartmentalisation is a general property of mammalian cells. In addition to the ECM and the actin cortex, the plasma membrane is also arranged to orchestrate the spatio-temporal execution of cellular tasks.

Originally considered as a sea of lipids and proteins, one of the first theories of plasma membrane organisation was described by Singer and Nicholson, termed the fluid mosaic model (Singer and Nicolson, 1972). In this model, lipids and proteins were proposed to freely diffuse in an unstructured fluid environment. Two major problems of the fluid mosaic model exist. Firstly, the diffusion coefficients of lipids/proteins within artificial reconstituted membranes are significantly larger than those measured for plasma membranes (Peters and Cherry, 1982, Kusumi et al., 2005b). Secondly, from single particle tracking experiments the motion of transmembrane

proteins within the plasma membrane have displayed complex behaviours. Consistent with the fluid mosaic model of homogeneous organisation, one would expect a Brownian motion of transmembrane lipids/proteins. However, experimental studies demonstrate deviations in the linear dependence of the mean squared displacement against time, suggesting the presence of membrane domains and a more complex organisation than a randomised sea of lipids (reviewed by (Destainville et al., 2008)).

The lipid raft hypothesis of membrane compartmentalisation has been considered controversial since its inception more than 20 years ago (Simons and Van Meer, 1988, Brown and Rose, 1992). In this model, lipids partition into specific small plasma membrane compartments enriched in cholesterol and sphingolipids thus compartmentalising the membrane. Lipid rafts can further modulate their size and composition in response to a stimulus, thus encouraging specific protein-protein interactions which is thought to aid signal transduction at the cell surface. These so called 'raft' specialised domains are proposed to be highly dynamic and physically small and are thus elusive to detection. Expansions of the lipid raft model have been proposed, such as the lipid shell model (Jacobson et al., 2007) in which a portion of the raft associated molecules at the plasma membrane surface are surrounded with lipid shells. Jacobson et al. propose that 30% of the membrane lipids are attributed to lipid shells, which can be considered as conceptually similar to hydration shells of proteins.

Kusumi proposed the picket fence theory in 2005, introducing the role of cortical actin in the compartmentalisation of the plasma membrane. In this model, transmembrane proteins anchored to the actin cytoskeleton ('fence') are considered as obstacles ('pickets') to other diffusing molecules (Kusumi et

al., 2005b). The cytoskeleton acts to delimit the membrane, providing boundaries for membrane compartments. The cytoplasmic domains of transmembrane proteins interact with the actin 'fence', inducing a transient confinement of proteins within the meshwork. The cortical actin fence is thought to organise its associated transmembrane proteins to corral membrane compartments, thus forming a steric hinderance to the lateral diffusion of other membrane constituents (Johannes et al., 2018). These transmembrane proteins can however traverse to another membrane compartment via hop diffusion, mediated by perturbations in the actin mesh (Kusumi et al., 2005b). Specifically, for hop diffusion to occur a physical space, interposed between the actin cytoskeleton and the plasma membrane must be made available (Kusumi et al., 2005a). This condition is achieved through thermal fluctuations of the 'picket-fence' structure. If the actin 'fence' delimiting the membrane transiently disassociates and the transmembrane protein possess sufficient kinetic energy to escape confinement by the actin barrier, a hop to a neighbouring compartment can be made. This model has been has tested via simulations (Koldsø et al., 2016) and has found increasing support in experimental studies of mammalian cells (Kusumi et al., 2010, Albrecht et al., 2016). A schematic depicting membrane compartmentalisation per the aforementioned theories is presented in Figure 5, and the effect of modulating the actin mesh on the organisation of transmembrane proteins is presented in Figure 6.

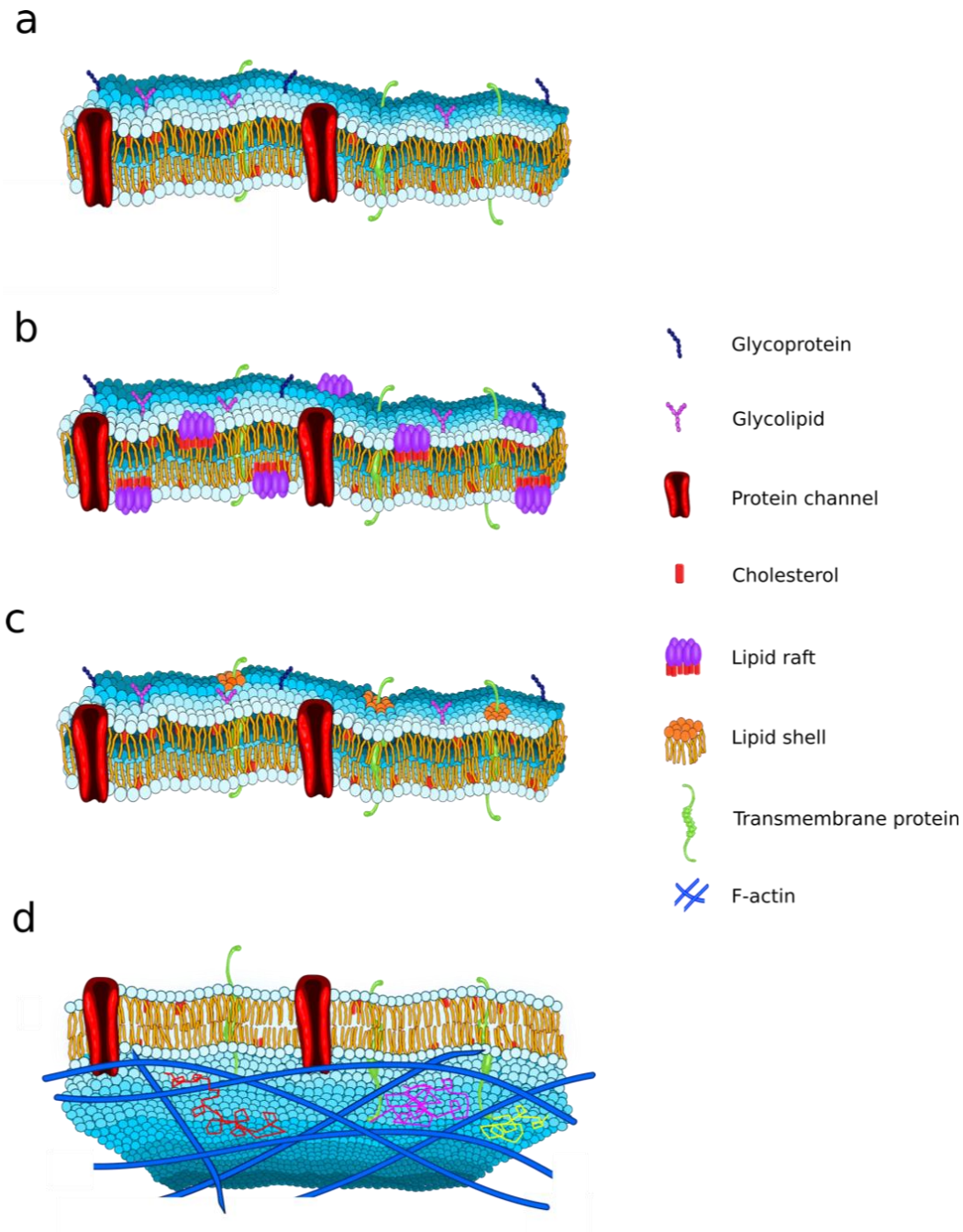

Figure 5: Models of plasma membrane compartmentalisation. The fluid mosaic model (a) considers the plasma as a 2D fluid, in which proteins (depicted green) are homogenously distributed within the bilayer. The lipid raft model (b) hypothesises that specialised domains enriched in cholesterol and sphingolipids (depicted red and purple respectively) exist. In the lipid shell model (c), proteins are proposed to be surrounded by lipid rings or shells (depicted orange). The picket fence model (d) introduces the role of the actin cytoskeleton (depicted dark blue) in compartmentalising the plasma membrane. Molecules can become trapped in membrane compartments (tracks depicted green, magenta and red), yet given sufficient energy, can hop to an adjacent compartment (red case).

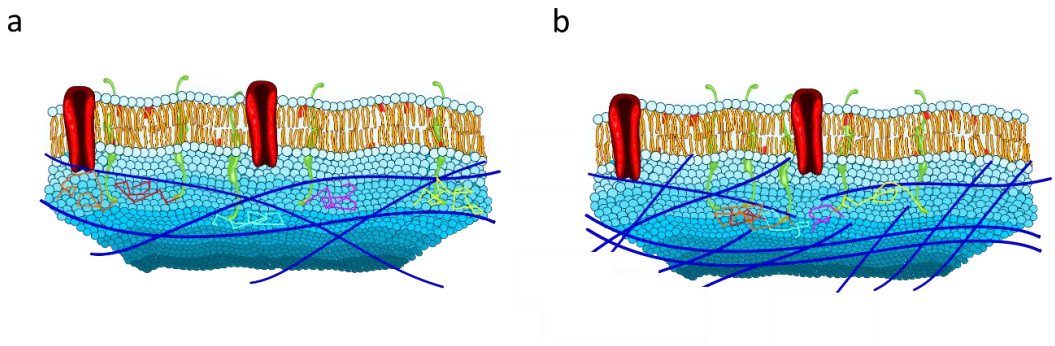

Figure 6: The effect of the density of the actin meshwork on modulating protein organisation and dynamics. Depending on actin re-organisation, plasma membrane associated proteins can be confined. For example, from case (a) to (b), the meshwork becomes denser, comprising of more filaments of shorter lengths. This enables protein diffusion and interactions in the same membrane compartment, thus increasing the local protein density.

Several other methods have been proposed concerning the compartmentalisation of the plasma membrane, including the protein island theory (Lillemeier et al., 2006) and the active composite model (Köster et al., 2016, Gowrishankar et al., 2012). The protein island theory proposes that most plasma membrane associated proteins exist in clusters within cholesterol abundant microdomains ('islands'), interspersed with protein-free cholesterol poor membrane domains. Within these islands, actin is highly abundant, and is typically excluded from non-island regions. The role of actin in island formation and sustentation is unknown, however the authors suggest that the cytoskeleton stabilises protein islands.

Gowrishanker et al. further propose the active composite model, in which there exist three types of proteins classified according to their ability to interact with the actin cytoskeleton: inert, active and passive. The inert refers to molecules which are considered to not interact with the actin cortex,

membrane dyes for example. The active corresponds to molecules that are directly influenced by dynamic actin filaments, for example the TCR. The passive element refers to molecules that can bind the dynamic cytoskeleton, but whose dynamics does not regulate actin, such as Glycosylphosphatidylinositol (GPI)-anchored proteins. Transient nanoscale clustering of transmembrane proteins is proposed to occur through their linkage with dynamic actin filaments localised to the inner leaflet, which remodel into asters; spontaneously occurring asterisk like structures of short individual actin filaments. As passive molecules bind actin for example, they are proposed to be advected with the filament as it stochastically patterns into asters. As a result, the passive molecules are driven to the aster cores, and clustering is induced.

Plasma membrane organisation remains a current subject of debate, with no clear consensus. Interestingly, not all models are mutually exclusive, and it is possible that certain features of the proposed models act in concert to orchestrate compartmentalisation.

1.4 The role of Actin at the T cell immunological synapse

The following section is dedicated to the role of actin at the T cell immunological synapse, which in unison with the microtubule system, provides the dynamic framework required to orchestrate crucial aspects of T cell activation.

1.4.1 The immune system

The human immune system relies upon physical barriers and the interdependent innate and adaptive networks of immune cells to produce an effective immune response. The unison of these three levels of the human defence system dictates the susceptibility of infection, with failure on any level producing an atypical immune response.

Physiological barriers to infection such as intact skin, muscociliary clearance and other secretion mechanisms serve as the first line of defence against pathogenic threats. Acting as a continuous barricade, intact skin prevents pathogen invasion though desiccation and acidic reactions. Permeable barriers such as the eyes or mucus membranes however, are more susceptible to invasion and must adopt different protection strategies. For example, cilia in the nasal passage acts to collect pathogens which are expelled via mucus (Houtmeyers et al., 1999).

If the pathogen bypasses the first line of defence, the innate system responds with local inflammation, pathogen engulfment and secretion of immune factors. Whilst the repertoire of receptors associated with the innate immune system is limited, these invariant receptors can respond to a broad range of pathogens generating a rapid protective response (Janeway et al., 2005). Both hematopoietic and non-hematopoietic cells contribute to the innate immunity including macrophages, dendritic cells, neutrophils, eosinophils and natural killer (NK) cells. Many cells of the innate immune system are APCs, thus enabling a cross-talk and communication between the innate and adaptive response. Dendritic cells for example are APCs, and mediate

adaptive immune responses by presenting peptide on their cell surface via their synthesised major histocompatibility complex (MHC) for recognition.

The adaptive immune system overcomes the constraints faced by the innate immune system, enabling a versatile means of defence through recognition of diverse, numerous antigens (Jain and Pasare, 2017). In this way, adaptive immunity is highly pathogen specific and importantly, can confer long lasting immunological memory to protect against re-infection. Adaptive immune responses are executed by antibodies and lymphocytes. Lymphocytes bear surface receptors with a high affinity for a specific peptide sequence, generated by stochastic recombination of variable receptor genes and parings of differing variable chains. As such, the catalogue of lymphocytes of the adaptive immune response can respond to numerous antigens (Janeway et al., 2005).

The two major types of adaptive immune response, antibody (humoral) and cell-mediated, are functionalised by B cells and T cells respectively. For antibody responses, B cells become activated to release specific immunoglobulins that bind the pathogen, thereby hindering the pathogens ability to bind host receptors. Subsequently, phagocytosis via cells of the innate immune system (macrophages, neutrophils for example) occurs (Janeway et al., 2005). For cell-mediated adaptive immune responses, different subsets of T cells interact with cells that have engulfed pathogen, or indeed cells producing pathogen such as virus infected cells and matured into an APC. Specialised APCs express antigen in the form of pMHC on their surface, and upon recognition by the unique TCR expressed on the T cell surface, an immunological synapse is formed (Grakoui et al., 1999). The successful formation of this specialised interface has multiple implications for

cell signalling, to be discussed. Interestingly, B cells that have engulfed the specific pathogen may also act as an APC by bearing surface pMHC, thus serving as a target for the T cell. This antigen specific binding induces cell proliferation, generating a clonal expansion, the offspring of which ultimately differentiates into effector T cells and memory T cells (Janeway et al., 2005).

1.4.2 T cell origins

Lymphoid progenitors, derived from hematopoietic stem cells in the bone marrow, migrate to the thymus to mature and develop into T cells (reviewed by (Kumar et al., 2018)). The thymus coordinates both T cell selection and differentiation, producing functional T cells expressing markers such as TCRs and cluster of differentiation 3 (CD3). During the selection process, T cells are exposed to MHCs expressed on epithelial cells and their TCR recognition to either class I or II MHC determines their lineage and subsequent development into either cytotoxic (CD8+, MHC class I reactive) or helper (CD4+, MHC class II reactive) T cells. Positive selection is the process by which an immature lymphoid progenitor expressing both CD4 and CD8 (++) and TCR with intermediate affinity for self MHC produce a survival signal and differentiate into either CD4+ or CD8+ mature T cells, dependent upon the MHC class specificity. Negative selection is the process by which T cells with high affinity for self MHC or self MHC and self-peptide are eliminated by apoptosis. Thus, positive selection ensures that the T cells can participate in the immune response and negative selection safeguards against autoimmunity. Owing to the demands required by both positive selection and negative selection, most cells that enter the thymic education system die of apoptosis (Hernandez et al., 2010). Figure 7 depicts the origins of differing T cell cohorts and their

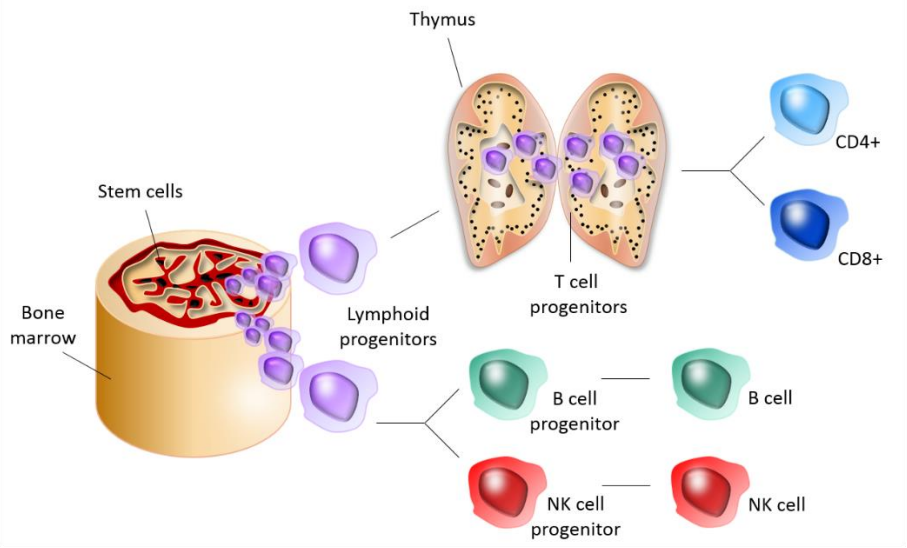

Figure 7: Simplified schematic depicting the origins of T cells. T cells undergo differentiation in the thymus and eventually mature to either CD4+ or CD8+ cells dependent upon their specificity and affinity for cells expressing Class I (CD8+) or Class II (CD4+) MHC peptide.

thymic maturation. In the context of this Thesis, CD4+ T cells will be discussed.

1.4.3 Actin organisation in circulating T cells

Naïve resting T cells, those that have not yet encountered antigen in the peripheral tissue, receive tonic signals from self pMHC in the periphery, whose functional role in cell survival remains to be studied (Myers et al., 2017). Circulatory T cells are encompassed by short microvilli consisting of numerous parallel bundles of actin filaments, stabilised by ERM family proteins (Majstoravich et al., 2004). Scanning electron microscopy (EM) studies have demonstrated the abundance of microvilli on the surface of T cells (Figure 8), with low affinity adhesion molecules typically located at the

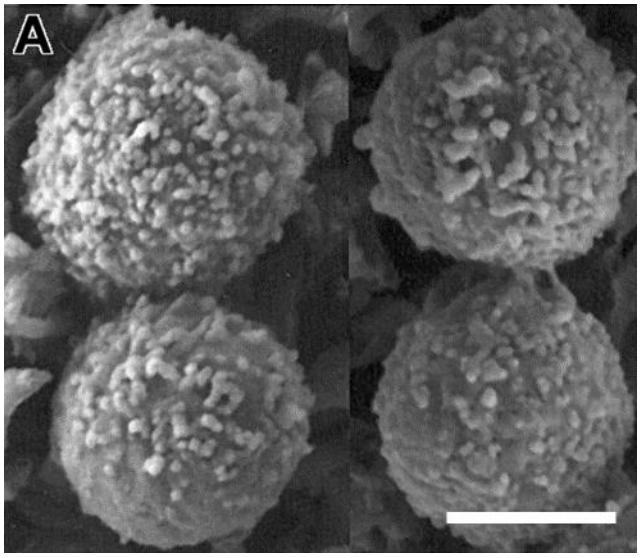

Figure 8: SEM imaging of T cells in the peripheral tissue. Figure adapted from Brown et al. 2003. Scale = 5μm.

microvilli termini and their higher affinity counterparts are thought to be excluded from microvilli termini, as to prevent non-specific attachment (Bruehl et al., 1996, Brown et al., 2003). The integrin lymphocyte function associated antigen 1 (LFA-1) is maintained in a low- affinity mode in resting T cells via a negatively regulating interaction with actin, which is thought to be influenced by talin (Comrie et al., 2015). This inhibitory interaction constrains the lateral motion of the integrins, which could be important for its clustering behaviour.

In resting T cells, TCRs have been shown to be pre-clustered via both biochemical and microscopy techniques (Crites et al., 2014). These TCR clusters are proposed to form islands of 40 – 100 nm diameter containing up to 30 molecules (Lillemeier et al., 2010). Jung et al. demonstrate that pre-clustered TCR molecules are located at microvilli tips in resting T cells, suggesting that microvilli act as a scaffold for TCR clustering upon T cell

activation (Jung et al., 2016). Interestingly, the co-localisation of TCR clusters and actin at microvilli tips could provide a mechanism by which TCR clusters are corralled by actin flow upon activation, to be discussed. A recent study has rebuked this claim however, demonstrating that the TCR distribution at the membrane of resting cells is randomly distributed, thus facilitating rapid and expansive detection of antigen (Rossboth et al., 2018). The localisation of TCRs and their associated signalling proteins to rafts is also controversial, with numerous contradictory studies (Kabouridis, 2006). Many actin accessory molecules, for example cofilin, are inactivated in resting T cells (Seeland et al., 2018) and certain NPFs such as WASP, exist in their auto-inhibited forms, thus preventing Arp 2/3 nucleation (Kim et al., 2000). The microtubule organisation centre (MTOC) is radially organised in resting T cells and polarises upon activation.

Studying the cortical actin meshwork of resting cells in detail via fluorescence microscopy is intrinsically problematic, owing to its cellular abundance and the requirement of imaging such cells on a surface. To obtain enhanced resolution, compared to conventional microscopy, total internal reflection microscopy (TIRFM) is typically employed. This method is particularly suited to the study of cellular interfaces, owing to its excitation extending a few hundred nanometres into the sample (Section 2.4.2). To capture the resting state of T cells, either glass or poly-L-lysine (PLL) coated coverslips are thus used, to facilitate TIRFM. Recent studies however have questioned if this surface is truly inert, demonstrating that PLL directly perturbs TCR dynamics and induces calcium fluxes, despite the absence of a stimulator (Santos et al., 2018). Suspending T cells in a hydrogel could be a promising alternative for the study of resting T cells.

1.4.4 The T cell immunological synapse

The interface formed between the T cell and APC membranes upon TCR-pMHC engagement is a highly specialised juncture, dedicated to the transmission of signals promoting effector functions. This interface is commonly referred to as the T cell immunological synapse, and encompasses molecules involved in the activation of T cells. One of the most striking events to occur upon the formation of the immunological synapse is the drastic changes in cytoarchitecture from the resting to the activated state, which is heavily dependent on actin and its array of accessory proteins. Formation of an immunological synapse occurs in stages: initial contact with APC and TCR-pMHC binding, T cell spreading over the APC membrane, T cell contraction, the formation of a mature synapse with a distinct canonical organization and finally synapse disassembly.

Initial studies focusing on the role of actin in at the immunological synapse made use of actin disrupting agents (ADAs), for example the family of Cytochalasins (Henney and Bubbers, 1973, Valitutti et al., 1995a). Cytochalsin D acts to induce a net de-polymerisation of the cytoskeletal network by binding the barbed termini of pre-existing filaments thus precluding monomer addition. By monitoring interleukin-2 (IL-2) production for example, the effect of the actin meshwork on the signalling outcome of the T cell could be elucidated (Rivas et al., 2004). Many studies demonstrated that actin is a fundamental requirement of the T cell immunological synapse, enabling adherence to the target cell and its cytotoxic activities (Valitutti et al., 1995a, Ritter et al., 2015, Delon et al., 2006). The role of actin at the immunological synapse however is multifaceted. Actin is proposed to enhance activation through promoting the formation of signalling complexes and its role in the compartmentalisation of the plasma membrane however,

more recently, it has been proposed that actin dynamics at the immunological synapse downregulate activation by corralling signalling molecules to the site of signal termination, to be discussed. Nonetheless, actin dynamics play a critical role in the formation, sustentation and disassociation of the immunological synapse.

1.4.4.1 Early signalling via the TCR-CD3 complex

The initial stage of T cell activation is TCR triggering upon encountering specific pMHC on the surface of APCs, leading to an adaptive immune response, (reviewed extensively by (Huppa and Davis, 2003)). Indeed, inappropriate triggering has been implicated in numerous autoimmune and immunodeficient conditions (Zeissig et al., 2015, Fischer et al., 1994). TCR-pMHC binding initiates a cascade of intracellular signals, leading to secretion of IL-2 which recruits other cells of the immune system. Interestingly, the TCR heterodimer possesses no intrinsic signalling capabilities, owing to a lack of phosphorylation sites, and as such relies upon complexing with CD3 subunits to generate a downstream signal (Figure 9) (Samelson et al., 1985, Brenner et al., 1985). The TCR-CD3 complex in T cells comprises of four homologous subunits: ε, γ, δ, and ζ. Each subunit presents immunoreceptor tyrosine activation motifs (ITAMs) on their intracellular tails which serve as phosphorylation sites (Reth, 1989, Isakov, 1997), which are thought to be of a folded conformation prior to TCR engagement (Aivazian and Stern, 2000). Once phosphorylated, ITAMs function as a docking site for ζ chain-associated 70 kDa tyrosine phosphoprotein (ZAP-70) thus promoting signalling and eliciting downstream effector functions.

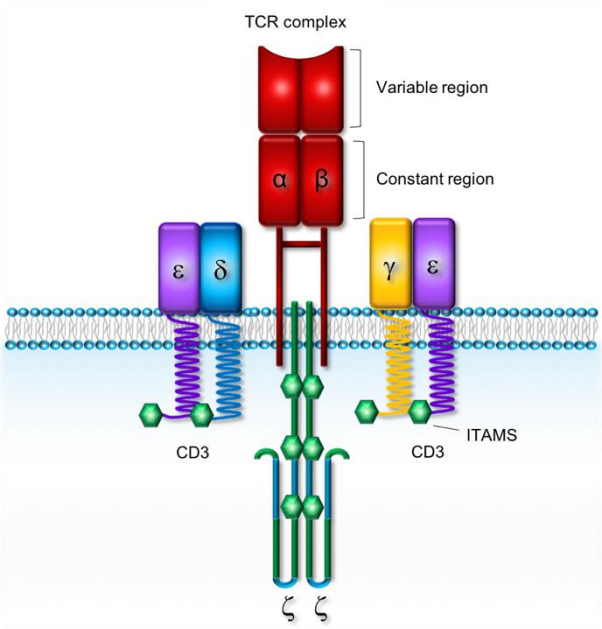

Figure 9: Composition of the TCR-CD3 complex in the context of the T cell membrane. The α and β subunits are held together through a disulphide bond, and the TCR itself possesses a small intracellular tail. Following TCR-pMHC engagement via the variable region of the TCR complex, phosphorylation of ITAMs present on the intracellular tails of the four CD3 subunits initiates downstream signalling and phosphorylated ITAMs serve as future protein docking sites.

Numerous models have been proposed to explain TCR triggering, including the conformational change model (Risueño et al., 2006) and the kinetic segregation model (Davis and van der Merwe, 2006) which place actin as an important player. The conformational change model suggests that the binding of TCR to pMHC alters the TCR conformational state, thus initiating signalling. The kinetic segregation model however suggests that TCR triggering is facilitated by the segregation of bulky phosphatases such as CD45 from the T cell – APC membrane that would otherwise downregulate TCR activity. Actin is further proposed to mediate this size and force dependent exclusion at the immunological synapse in part through its role in generating

membrane tension (Kumari et al., 2014). On the T cell membrane of the T cell – APC initial contact site, TCRs have been demonstrated to be clustered, which are proposed to be stabilised within and/or anchored to the actin meshwork (Beemiller and Krummel, 2010). As such, actin could be considered as a facilitator of early T cell signalling.

Following TCR triggering, ITAM phosphorylation at the intracellular domain of the CD3 subunits of the TCR-CD3 complex via Lck, of the Src family kinase, induces a signalling cascade downstream of the receptor complex (Veillette et al., 1988). Lck interacts with the intracellular domain of CD4, a pMHC class II reactive transmembrane protein expressed in CD4+ T cells, thus forming a signalling platform at the T cell APC interface (Davis and van der Merwe, 2011). Post Src family kinase phosphorylation, Syk family kinases such as ZAP-70, can dock to the ITAMs of the CD3 subunits (Chan et al., 1992). Lck activation precedes ZAP-70 recruitment, yet post Lck phosphorylation, ZAP-70 can phosphorylate itself thus promoting its catalytic activity (van Oers et al., 1996). Active ZAP-70 then phosphorylates a number of signalling molecules such as the linker for the activation of T cells (LAT) (Williams et al., 1998, Zhang et al., 1998) and the SH2-domain-containing leukocyte protein of 76 kDa (SLP-76) (Wardenburg et al., 1996, Raab et al., 1997), which act as signalosomes and scaffolds for further protein binding. Activation of various signalling pathways due to the interactions between transmembrane proteins and associated kinases regulates the actin cytoskeleton and many of its accessory proteins at the T cell – APC interface, to be discussed in detail.

LAT is a 36 kDa transmembrane protein that provides a docking site through its phosphorylation sites at its large intracellular domain for the Src homology 2 (SH2) domain of numerous proteins, including Vav, Gads, SOS,

SLP-76 and Itk (Shan and Wange, 1999, Wange, 2000). Owing to its interaction with multiple signalling molecules, LAT promotes signal diversification and amplification downstream of TCR engagement. In addition to its positive regulation of T cell signals, LAT also associates with negative regulatory molecules such as Grb2-related adapter protein (Grap) (Liu et al., 1999b). LAT has also been proposed to preferentially localise to lipid rafts, due to palmitoylation (Tanimura et al., 2006), although its functional role at these specialised domains remains controversial.

At the activated T cell membrane, LAT has been demonstrated to cluster (Balagopalan et al., 2015) and sub-synaptic vesicular pools of phosphorylated LAT are thought to be recruited to the site of TCR engagement (Williamson et al., 2011). This dual population of LAT and its role in the early activation of T cells is also controversial. Williamson et al. postulate that vesicular phosphorylated LAT is the major component of LAT based signalling upon TCR engagement by serving as a signalling hub, and that whilst plasma membrane associated LAT is pre-clustered it is not a pre-requisite for propagating downstream effector functions, nor is it phosphorylated. Conversely, others propose that clusters of plasma membrane LAT are the main contributors to T cell activation and question the role of vesicular LAT in early activation. For example, it was recently demonstrated that at the early stages of synapse formation, microclusters of plasma membrane associated LAT were highly abundant whereas vesicular LAT was absent (Balagopalan et al., 2018). Upon continued activation as the synapse matures however, the vesicular LAT population was recruited to interact with plasma membrane associated LAT microclusters. Nonetheless, a consensus regarding the essential nature of LAT complexes to TCR-CD3 signalling is reached. Upon LAT knock down (KD) in an immortalised line of T cells (Jurkat T cells),

defects in TCR mediated T cell signalling was observed (Finco et al., 1998). LAT has been implicated in both T cell development and the function of mature T cells, with thymocyte development impeded upon introduction of LAT phosphorylation mutations and LAT knock out (KO) resulting in hindered T cell signalling (Nuñez-Cruz et al., 2003, Sommers et al., 2001, Mingueneau et al., 2009). A schematic depicting the various signalling molecules associated with early T cell signalling through the TCR pathway is presented in Figure 10.

The cascade of early signals through the TCR-CD3 complex is accompanied by the spatio-temporal re-organisation of many of the signalling molecules associated with early signalling upon immunological synapse formation. This re-organisation typically involves protein clustering, or indeed changes in clustering behaviours of pre-clustered molecules (Campi et al., 2005, Sherman et al., 2011, Seminario and Bunnell, 2008). For example, Krummel et al. report clustering of CD3ζ at the initial contact site of a T cell and a B cell lymphoma, whose appearance was synchronised with the onset of a calcium flux (Krummel et al., 2000). For synapses formed by Jurkat T cells activated via anti-CD3 coated glass coverslips, the dynamic nature of TCR microclusters upon activation can be observed. The TCR microclusters, typically consisting of 30-300 TCRs, are first present at the T cell – APC contact site and translocate during spreading and contractile phases of the synapse formation (Hashimoto-Tane and Saito, 2016, Krummel and Davis, 2002), to be discussed. The lateral mobility of TCRs is perturbed upon antigen recognition, and within seconds various actin regulatory agents such as Vav1, WASP, cdc42 and Rac are recruited with triggered TCRs (Burkhardt et al., 2008, Dushek et al., 2008).

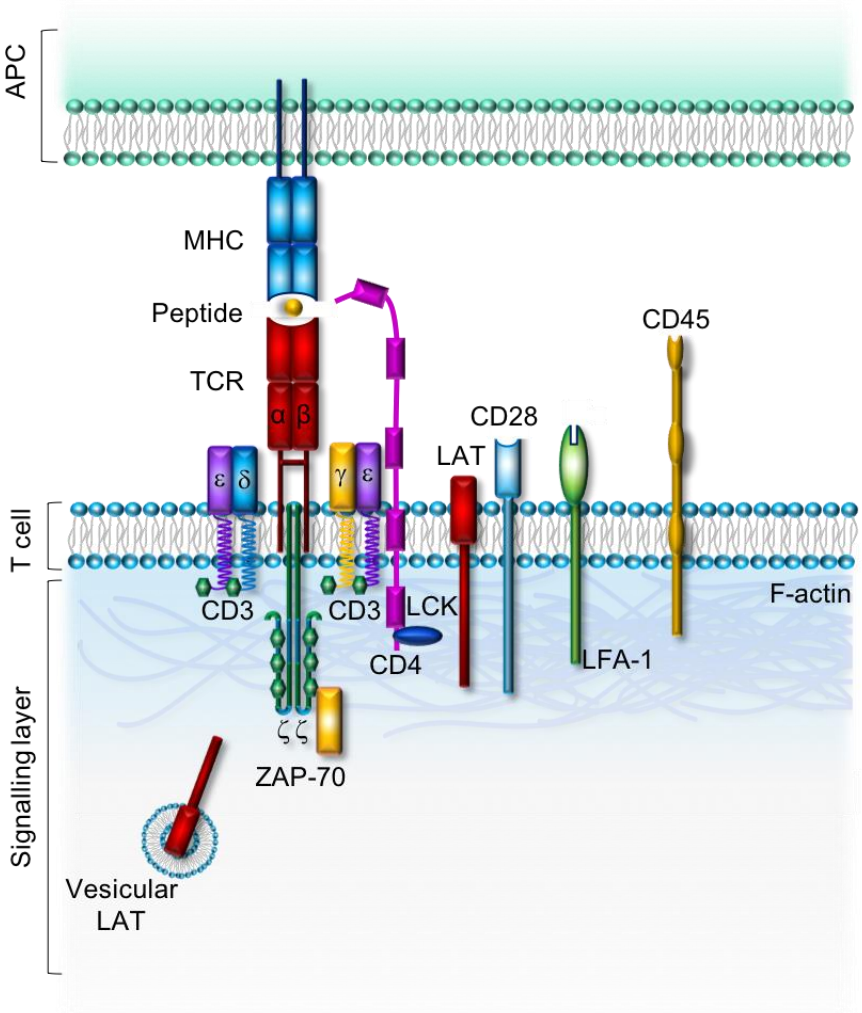

Figure 10: Schematic depicting the main components involved in the initiation of T cell signalling following TCR engagement with pMHC. CD4 associated Lck phosphorylates ITAMs on the intracellular chains of CD3 subunits, thus forming a docking site for ZAP-70. Active ZAP-70 phosphorylates numerous signalling molecules including LAT, enabling signal propagation downstream of the TCR. Co-stimulation via CD28 binding to its APC membrane residing ligand is also important for complete T cell activation. Concurrent with phosphorylation events is the translocation of negative regulators of T cell signalling such as CD45 away from the engagement site. Adhesion based molecules such as LFA-1 act to stabilise the cell-cell interface. The actin meshwork is situated directly beneath the T cell plasma membrane, and plays an important role in the clustering, segregation and dynamics of signalling molecules at the interface.

The cytoskeleton is proposed to transiently trap TCR complexes (Dushek et al., 2008) thus acting as a scaffold that can facilitate the amalgamation of signalling molecules to their receptors post triggering. Indeed, at the early stages of immunological synapse formation, WASP co-localises with numerous receptor molecules and kinases such as ZAP-70, LAT and SLP-76 (Bunnell et al., 2002, Ehrlich et al., 2002, Barda-Saad et al., 2004, Tskvitaria-Fuller et al., 2006). Through the linkage of the relatively stable cytoskeleton to these signalling molecules at the initial contact site, signalling clusters are more likely to endure and sustain activation, despite pMHC release, and actin is thus thought to facilitate the serial triggering of multiple TCR complexes (Valitutti et al., 1995b).

The engagement of the TCR prompts the activation of numerous actin regulatory proteins that work in unison to regulate actin re-organisation at the immunological synapse (reviewed by (Fuller et al., 2003)). The most studied of these proteins is the guanine nucleotide exchange factor (GEF) Vav1, a prominent activator of Rho GTPases. Notable examples of the family of Rho GTPases involved in the regulation of T cell signalling and functions are Rac and cdc42. Upon Rac and cdc42 KO, defects in T cell development and activation are observed (Tybulewicz and Henderson, 2009). Vav1 activates Rho family GTPases, and Vav1 deficient T cells exhibit abnormal TCR signalling, calcium responses and cytoskeletal re-organisations (Kumari et al., 2014).

Notably, co-stimulation through the CD28 molecule through its binding to CD80 and CD86 expressed on the surface of the APC is an important aspect of T cell activation (Beyersdorf et al., 2015). This receptor-ligand binding process is critical, as TCR ligation alone is not sufficient for complete activation, thus

a secondary signal generated via CD28 binding prevents an anergic response (Andrews et al., 1997). CD28 increases actin polymerisation and the assembly of actin rich protrusions (Salazar-Fontana et al., 2003). Indeed, functionalised CD28 plays an important role in actin re-organisation at the immunological synapse, generating downstream signals independent of the TCR activation pathway. Vav1 is proposed to serve as the messenger for CD28 induced actin remodelling, through its binding to GRB2 (a signalling protein with Src homology 2 domain) and recruitment to the CD28 receptor, thus enhancing Vav1 polymerisation (Wu et al., 1997, Boomer and Green, 2010, Tavano et al., 2006). This increased phosphorylation leads to more interactions of Vav1 with LAT (Salojin et al., 1999), thus forming more signalosomes which further mediate actin re-organisation through cdc42 activation by Vav1 (Salazar-Fontana et al., 2003).

1.4.4.2 Actin mediated T cell spreading

Post initial contact with an APC bearing its cognate antigen, the architecture of the T cell drastically changes. The T cell reabsorbs its uropod and extends actin rich pseudopodia and lamellipodia governed by actin polymerising and binding proteins, towards the APC membrane (Burkhardt et al., 2008). It is this polymerisation that enables the TCR to bind to the pMHC, by bringing the two membranes ~15 nm apart (Kumari et al., 2014).

Actin mediated T cell spreading can be characterised by two temporally distinct processes. Firstly, adhesion-based molecules (integrins), for example LFA-1, embedded in the T cell membrane bind their ligand, for example Intercellular adhesion molecule 1 (ICAM-1) expressed on the APC membrane, thus stabilising the T cell-APC contact (Dustin and Cooper, 2000, Wang et al.,

2009). LFA-1 also plays a critical role in T cell migration and LFA-1 deficiencies have been linked to reduced IL-2 production (Wang et al., 2009). LFA-1 binding to ICAM-1 brings the two membranes into local proximity (up to 40 nm separation). Secondly, WASP activation enables Arp 2/3 mediated actin nucleation, generating branched actin networks at the cell edge thus inducing cell spreading, along with CD28 co-stimulation (Dustin and Cooper, 2000). Generally, the promotion of additional membrane protrusions and the lamellipodium greatly facilitates T cell spreading, allowing an expansive engagement of the APC membrane and the close contact between membranes (~ 15 nm separation) required.

In unison with actin driven radial growth of the synapse, the MTOC begins to translocate towards the T cell – APC contact site, which is recognised as a hallmark of T cell engagement (Grakoui et al., 1999). MTOC re-orientation is accompanied by synchronized translocation of the Golgi apparatus and vesicles, thus allowing the polarised delivery of cellular mediators such as cytokines to the APC membrane (Ritter et al., 2015, Kloc et al., 2013, Kupfer et al., 1991). The microtubule system is commonly referred to as an intracellular highway, serving as the tracks for myosin mediated vesicle trafficking. In T cells, vesicle delivery has been shown to be an important process in the regulation of activation (Das et al., 2004, Soares et al., 2013). Various signalling molecules such as LAT, can be recycled or indeed transported to the immunological synapse through vesicles. Vesicles typically residing up to several microns away from the synapse interface are recruited upon TCR triggering, where they interact with the plasma membrane associated molecules. For example, vesicular LAT has been shown to interact with pre-existing clusters of plasma membrane LAT during the late stages of activation (Williamson et al., 2011). As such, MTOC polarisation is considered

fundamental in maintaining the specificity of cytotoxic and secretory responses. In terms of CD4+ T cells, the function of the MTOC polarisation is to direct Golgi apparatus derived vesicles. For example, CD4+ T cell - B cell interactions induce a polarisation of the MTOC, directing secretory vesicles containing B cell growth factors and lymphokines (Kupfer et al., 1987). Upon disruption of the motor protein driven translocation of the MTOC post T cell activation, levels of ZAP-70, LAT and Vav1 phosphorylation and receptor recycling are reduced (Martín-Cófreces et al., 2008) and contrariwise, ZAP-70, LAT and SLP-76 are required for MTOC polarisation upon TCR triggering (Kuhné et al., 2003).

Arp 2 and Arp 3 deficient T cells have been shown to exhibit impaired cytoskeletal spreading upon stimulation. The overall concentration of actin at the immunological synapse is also reduced upon Arp 2 and Arp 3 silencing (Burkhardt et al., 2008). Protrusions however still extend and span the APC membrane, although the nucleation factor facilitating this remains unknown, demonstrating that Arp 2/3 independent actin nucleation is important at the immunological synapse (Gomez et al., 2007). Arp 2/3 silencing does not however interfere with MTOC polarisation (Gomez et al., 2007). WASP, a NPF that activates the Arp 2/3 complex, recruitment to the immunological synapse is orchestrated by its interaction with adaptor proteins Nck and PST-PIP (Zeng et al., 2003, Badour et al., 2003). Upon WASP recruitment, cdc42 binding alters its conformational state, thus enabling the formation of branched filaments via WASP dependent Arp 2/3 activation (Zeng et al., 2003, Kim et al., 2000). Upon WASP KD IL-2 secretion is impaired (Burkhardt et al., 2008), however, the definitive role of WASP in the polymerisation of actin at the synapse remains unclear, perhaps owing to the partially overlapping functions of the many actin regulatory proteins at the interface. Another activator of the Arp 2/3

complex is HS1, which acts to stabilise pre-existing branched networks (Uruno et al., 2003). HS1 deficient T cells exhibit abnormal lamellipodium when activated via the TCR pathway and possess transient actin responses at the immunological synapse (Gomez et al., 2006). The effector for Rac1, WAVE2, also influences actin architecture at the immunological synapse. WAVE2 silencing significantly reduces the abundance of actin at the T cell - APC interface and is required for integrin-based adhesion post TCR crosslinking (Nolz et al., 2006).

Arp 2/3 independent actin regulatory proteins further contribute to the spatio-temporal organisation and signalling activity of the immunological synapse. FMNL-1, a highly expressed formin in T cells, for example plays an interesting role at the immunological synapse. In FMNL-1 deficient Jurkat T cells, actin accumulation and the formation of protrusions at the synapse remains unchanged however, MTOC polarisation is impaired, indicating a more complex role for formins other than regulation of the actin cytoskeleton alone at the immunological synapse (Gomez et al., 2007). Recently, it has been demonstrated in HeLa and Jurkat T cells that FMNL-1 KD results in a significant increase in cellular actin and a fragmentation of the Golgi apparatus (Colón-Franco et al., 2011). As such, a highly abundant actin meshwork could impede MTOC re-orientation. A simplified schematic illustrating the signalling cascades that induce actin remodelling post TCR activation is presented in Figure 11.

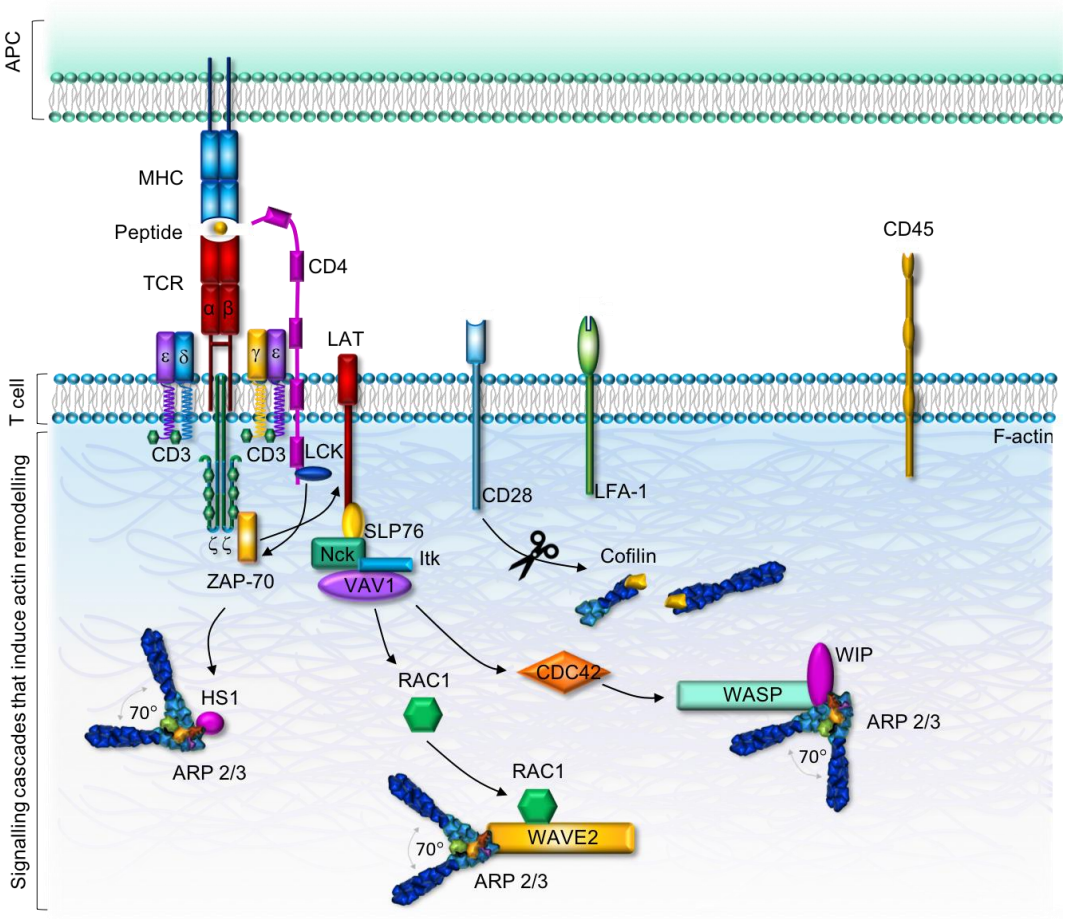

Figure 11: Simplified schematic depicting various signalling pathways that regulate the actin cytoskeleton upon TCR engagement with pMHC expressed on the surface of APCs. Upstream actin regulators such as Vav1, cdc42 and RAC1, transduce signals to NPFs such as WAVE2, WIP, HS1 and WASP that can mediate the formation of branched actin networks via activation of the Arp 2/3 complex. A secondary, co-stimulatory signal is generated via CD28 binding to its ligand on the surface of APCs, which is linked to cofilin activation. Whilst cofilin severs pre-existing filaments, new barbed termini are created upon cofilin binding, thus promoting polymerisation at the synapse. Note that numerous other actin regulatory proteins are localised to the synapse, however, their mechanistic role in T cell activation is comparatively unknown.

1.4.4.3 Actin retrograde flow and the formation of supramolecular activation clusters (SMACs)

Once the actin polymerisation driven radial growth of the synapse has reached a plateau, actin towards the synapse periphery begins to flow towards the synapse centre in a retrograde fashion. This retrograde flow is mainly driven by actin polymerisation pushing against the membrane, however myosin motors also contribute to this net translocation, by pulling against branched actin networks (Babich et al., 2012, Yi et al., 2012). Importantly, halting actin polymerisation via pharmacological treatments results in a rapid loss in downstream signalling at the T cell synapse (Babich et al., 2012), further highlighting the integrated role of actin in T cell signalling.

Actin retrograde flow is coupled with the formation of supramolecular activation clusters (SMACs), first coined by Kupfer, as the synapse reaches a maturation stage (Monks et al., 1998). The prototypical mature synapse exhibits three radially distinct zones of molecular and cytoskeletal organisation: the central (c)SMAC, peripheral (p)SMAC and the distal (d)SMAC regions. The dSMAC is actin rich and contains molecules associated with the downregulation of T cell activation that typically possess large extracellular domains, such as CD45 and CD43 (Grakoui et al., 1999). Actin flows at the dSMAC at a velocity of ~ 6 μm/min (Kaizuka et al., 2007, Yi et al., 2012) and serves as the origin of the actin retrograde flow across the synapse. The pSMAC contains a concentric series of acto-myosin rings that flow inwards towards the synapse centre at a slower velocity (~ 2 μm/min) than that of the dSMAC (Yi et al., 2012) . Contractile forces are readily generated in this zone. The pSMAC is also enriched in adhesion molecules such as LFA-1, which contributes to the synapse stability. Molecules associated with T cell signalling, for example CD3, Lck and CD28, are abundant at the cSMAC of the

mature synapse, although, these molecules are no longer co-localised with TCR complexes (Dustin, 2014). At the inner border of the pSMAC, a sharp drop off and subsequent arrest of actin flow occurs, generating a clear distinction between the actin rich pSMAC and the actin poor cSMAC, observable by conventional fluorescence microscopy. This loss in actin abundance at the cSMAC is thought to facilitate MTOC polarization, and subsequent delivery of associated vesicles towards the APC membrane (Fooksman et al., 2010, Ritter et al., 2015).

Co-ordinated with actin retrograde flow and the formation of SMAC zones is the transportation of protein clusters, which has important implications for T cell signalling. Indeed, actin dynamics are considered indispensable for microcluster dynamics at the immunological synapse. Protein microclusters of the TCR and its associated signalling molecules form throughout the spreading phase of synapse formation and begin to migrate towards the cSMAC in an actin dependent fashion upon synapse maturity (Yi et al., 2012). This linked translocation can be explained in various ways. For example, the actin rich dSMAC could exert a mechanical force on the microclusters thus pushing them inwards towards the cSMAC (Grakoui et al., 1999, Basu and Huse, 2017). Another hypothesis suggests that the series of acto-myosin arcs observed in the pSMAC of the synapse provides a contractile force, capable of traversing microclusters across the synapse, in addition to the dSMAC mediated translocation (Yi et al., 2012). Studies using Jurkat T cell synapses demonstrated that microcluster dynamics were reduced upon treatment with blebbistatin, which acts to disrupt myosin II function (Yi et al., 2012). This finding is also consistent with the active composite model, in which acto-myosin dynamics influence clustering at the plasma membrane (Gowrishankar et al., 2012). Other studies however demonstrate that the

velocity of the translocating microclusters is not impacted upon myosin II inhibition, rather, that their flow directionalities are scrambled (Kumari et al., 2012). This acto-myosin mediated translocation occurs multiple times, as TCR signalling is sustained by the appearance of new TCR microclusters at the dSMAC, which are subsequently corralled to the pSMAC. Similarly to the actin flow, the velocity of TCR microclusters upon translocation from the dSMAC (5.6 – 8.4 μm/min) to the pSMAC (2.3 μm/min) is reduced (Yi et al., 2012, Kaizuka et al., 2007). The flow speeds of the cortical actin mesh and the TCR microclusters are consistent with a frictional coupling mechanism, promoting translocation from the dSMAC to the pSMAC (DeMond et al., 2008). A schematic illustration of the stages of synapse formation is presented in Figure 12. Besides its mechanical role in propagating effector functions, the actin cytoskeleton delimits the plasma membrane per the picket fence model of Kusumi and induces protein clustering via the active composite model. Thus, altering the density of the cortical actin meshwork by polymerisation, nucleation or actin crosslinking for example, has profound consequences for protein clustering. For example, the clustering behaviours of MHC molecules, integrins and the previously discussed TCR complexes are influenced by the actin cytoskeleton, which acts to corral and compartmentalise these signalling complexes. Numerous proteins that act to sever, cap, crosslink and bundle actin filaments at the immunological synapse exist and have been studied using various techniques.

The actin crosslinking protein α-actinin for example, is enriched underneath clustered surface proteins at the immunological synapse (Geiger and Singer, 1979). α-actinin is also thought to facilitate the translocation of membrane receptors across the synapse (Hoessli et al., 1980). Although, its

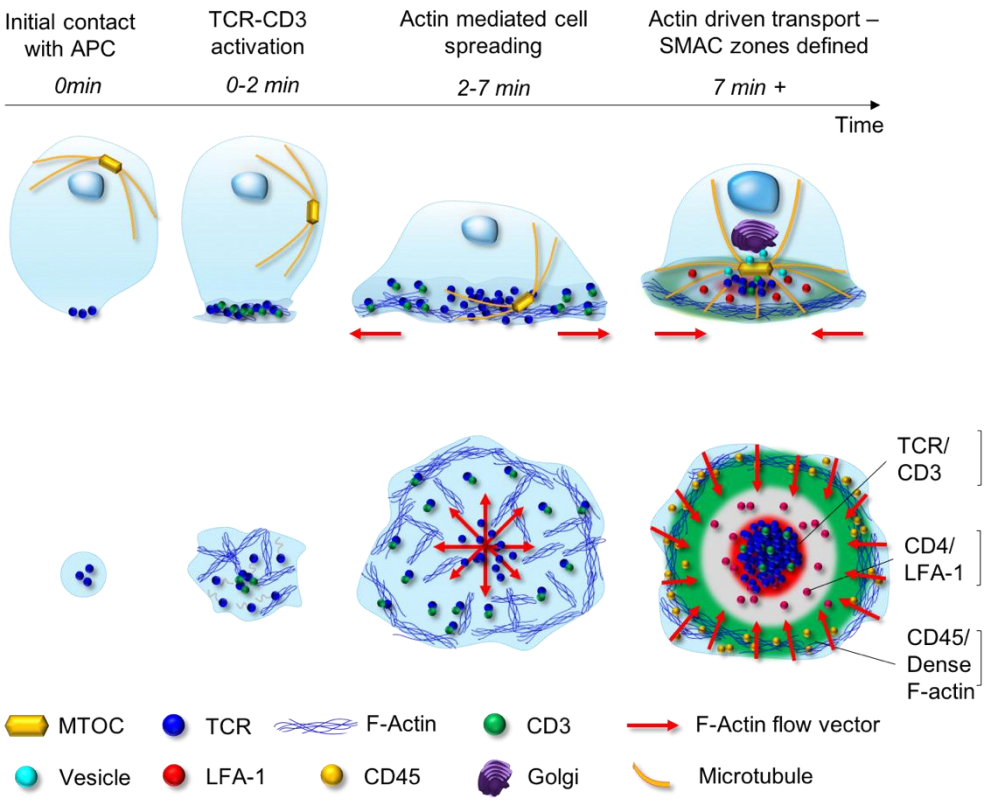

Figure 12: The organisational structure of the immunological synapse, depicted from a side and surface view. In the initial contact phase, the TCR has recognised its cognate pMHC expressed on the surface of its target. TCR-pMHC binding leads to the activation of TCR-CD3 complexes, which are localised to the engagement site. The TCR signalling pathway is thus activated, and a signalling cascade involving numerous signalling proteins is propagated downstream. The T cell extends actin rich protrusions, mediated by Arp 2/3 activation at the cell periphery, to spread across the APC membrane. Actin begins to flow in a retrograde fashion once actin polymerisation has reached a plateau, driving the translocation of protein clusters towards the synapse centre. Synonymous with synapse maturation is the formation of SMAC regions, in which molecules and actin are spatially organised to facilitate effector functions.

deterministic role in the activation of T cells remains to be fully understood, since α-actinin silencing has been demonstrated to increase IL-2 secretion yet reduces the accumulation of actin at the T cell – APC interface (Gordón-Alonso et al., 2012). Gordon-Alonso et al. demonstrate that upon α-actinin silencing, a disrupted organisational architecture of the synapse occurs. The cSMAC and the pSMAC of the synapse were dispersed compared to those of the prototypical synapse, although this did not appear to impair its ability to signal (Gordón-Alonso et al., 2012). More recently, a live cell fluorescence microscopy study provided the quantification of the actin flow speed in the presence and absence of α-actinin. The flow velocity of cortical actin was found to be similar to that of α-actinin, and upon α-actinin KO, the actin flow velocity was significantly increased (Ashdown et al., 2017). The authors state that loss of α-actinin at the immunological synapse results in a less ordered actin retrograde flow, as the orientations of the flowing filaments become more variable. The authors suggest that α-actinin KO facilitates the rapid translocation of actin filaments from the dSMAC to the pSMAC, however these fibres lack a co-ordinated organisation with the remaining cortical meshwork. As such, the authors postulate that α-actinin is an important linker and regulator of actin retrograde flow at the immunological synapse. The authors further investigate the flow of the plasma membrane itself, which was found to be correlated with actin at α-actinin rich regions of the synapse. Upon α-actinin KO, the velocity of the plasma membrane was not significantly altered however its flow directionalities were scrambled. Given a higher velocity of actin flow in α-actinin KO synapses, it was suggested that α-actinin functions as a mediator of linked plasma membrane and cortical actin flow.

The cSMAC was first thought to be the primary signalosome at which signal transduction occurs, owing to the accumulation of numerous signalling

molecules such as TCRs, LAT and Lck. TCR microclusters effectively segregate downregulators of T cell signalling, such as CD45, and contribute to calcium flux (Bunnell et al., 2002). However, the cSMAC does not effectively segregate CD45, and is rich in lysobisphosphatidic acid (LBPA), which acts to degrade TCRs (Varma et al., 2006). It is now thought that the cSMAC is the site of TCR internalisation however, the role of the cSMAC in signal sustention and termination is not fully understood.

The characteristic bull's-eye SMAC structures of the immunological synapse have been observed in many systems such CD4+ T cell synapses activated through B cell lymphoma tumour cell lines, ICAM-1 and MHC containing lipid bilayers and anti-CD3 anti-CD28 coated coverslips. However, the formation of SMACs is not universal, and is not a pre-requisite for signalling. There exists numerous occasions of which mature immunological synapses do not present SMAC structures or indeed exhibit a variation on the prototypical organisation, and their existence in vivo remains an open question. Recent work suggest that many factors contribute to the SMAC organisation of T cells such as their differentiation state and contact with APCs (Brossard et al., 2005, Hailman et al., 2002). Various organisational topologies of the immunological synapses of NK cells have also been observed, ranging from an entirely diffuse organisation to a multifocal structure (Davis et al., 1999, Davis and Dustin, 2004, Carlin et al., 2001). Interestingly, although actin retrograde flow has not been directly quantified in the synapses formed by NK cells, clusters of killer immunoglobulin-like receptors (KIR) appear to undergo centripetal translocation from the cell periphery to the centre, suggesting an actin-driven translocation mechanism similar to that of T cells.

Interestingly, the role of the APC actin cytoskeleton in the formation of the immunological synapse is less well studied. The APC cytoskeleton was initially thought to play a passive role in immunological synapse formation, with the T cell cytoskeleton bearing much of the workload. In contrast to results observed in B – T cell synapses, at the synapses of dendritic cells and CD4+ T cells, the dendritic actin cytoskeleton actively polarises and induces clustering and activation of the resting CD4+ T cells (Al-Alwan et al., 2001, Comrie et al., 2015, Al-Alwan et al., 2003).

1.4.4.4 Post synapse

The final stage in the T cell activation cycle is disassembly of the immunological synapse. The disassociating structure, or kinapse, and its transition from active to inactive remains poorly understood. Actin is most likely involved in this transition, owing to its interaction with multivalent synapse stabilising proteins, although the exact mechanism driving kinapse onset remains unknown.

In the context of this Thesis, the role of actin at the immunological synapse will be investigated via a model system. For this, artificial synapses of an immortalised T cell line (Jurkat E6.1) will be used. Activation is induced through crosslinking of CD3 receptors (and through CD28 co-stimulation), which has been demonstrated to render the T cells receptive to IL-2 in the absence of APCs (Zhang et al., 2002, Watson et al., 2008, Tsoukas et al., 1985). Artificial synapses generated on antibody coated coverslips offer the benefit of TIRFM studies, which facilitates certain super resolution microscopy methods. Whilst there are concerns regarding the immobilisation of certain proteins and receptors upon forming such artificial synapses, the dynamic

behaviours of these molecules nor their downstream effector functions will be interrogated in the context of this Thesis. Rather, the organisation of the actin cytoskeleton on the nanoscale will be quantified using super resolution microscopy methods.

Chapter 2 Super-resolution microscopy

2.1 Introduction

The phenomenon of luminescence has fascinated mankind since it was first observed in the 16th century. Luminescence, as etymology suggests, refers to the emission of light by a substance, typically due to photon absorption. Other stimuli such as chemical reactions can also lead to luminescence, an effect which is manifested in bioluminescent organisms. The process of luminescence was repeatedly observed over the centuries since its discovery, however, the phenomenon was not fully understood until the 19th century (Stokes, 1852, Herschel, 1845). Since its inception, fluorescence microscopy has become an invaluable tool for the study of structural and biochemical processes occurring within living organisms owing to its unparalleled specificity, sensitivity and non-invasive nature. For much of its history however, the fluorescence microscope has been fundamentally limited in terms of its achievable spatial resolution, owing to the wave nature of light. Nonetheless, the fluorescence microscope has become a routinely used instrument across the life sciences, offering insight into diverse cellular organisations and functions. In this Chapter, the basic principles of fluorescence and their application to fluorescence microscopy will be detailed. The advent of super-resolution fluorescence microscopy, through means of

breaking of the classical diffraction limit of light will be discussed, with an emphasis on single molecule localisation microscopy (SMLM) methods.

2.2 Basic principles of fluorescence

The basic physics of fluorescence can be understood through use of the Jablonski diagram, first proposed in 1935. This schematic illustrates the many possible transitions an electron within a molecule can undertake post-excitation (typically through photon absorption) and thus the mechanism of emission. Per convention, electronic energy levels are depicted on the vertical axis whilst the series of horizontal lines account for electron spin multiplicity, or vibrational states. Upon excitation, there are a multitude of pathways of de-excitation and energy dissipation, highlighted in Figure 13.

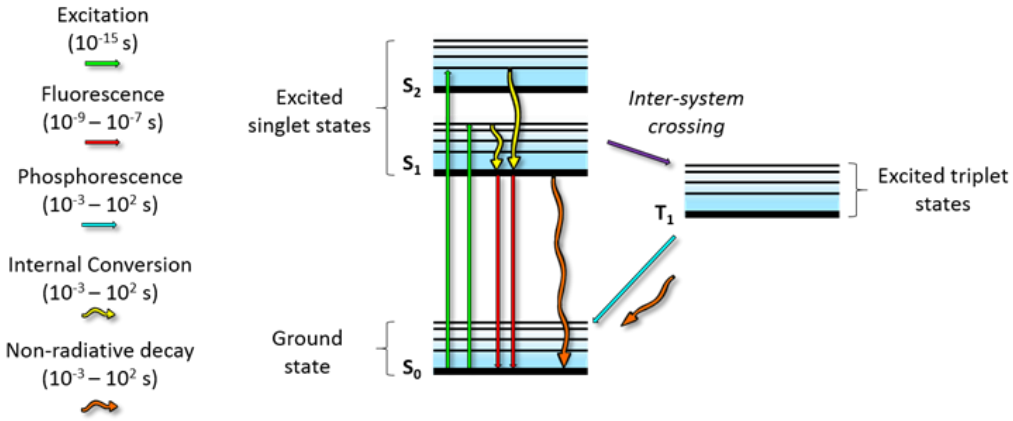

Figure 13: Schematic Jablonski diagram in which possible electronic transitions post excitation are depicted.

The electronic ground state (S_0) represents the energy state in which the electron resides in the steady-state, pre-excitation. When this ground state electron is excited to a higher energy state by photon absorption, either a singlet (S) or triplet (T) excited state will form. A singlet electronic state insists that all electron spins, or intrinsic angular momenta, are paired such that the total spin s=0 via the Pauli exclusion principle. The excited triplet state however, allows symmetric electron pairs with s=1. Upon absorption, the ground state electron transitions to the first excited singlet state, S_1, at an increased vibrational energy level. The electron can then revert to the lowest (most stable) vibrational level in S_1 in a process called internal conversion. The mechanism of internal conversion conserves spin multiplicity and the excess energy is converted into heat. The electron now has the possibility to either decay to the ground state S_0 non-radiatively, or via the emission of a photon in a phenomenon termed fluorescence. Transitions that do not conserve spin multiplicity are also possible; to the triplet state via intersystem crossing (Lakowicz, 2006). The transition from S_1 - T_1 requires a flip in electron spin, and thus has a lower probability of occurrence. Internal conversion often follows intersystem crossing, as relaxation to the ground state is forbidden. The metastable electron has a longer lifetime at the lowest vibrational level of the excited triplet state, and eventual de-excitation via phosphorescence can occur. Fluorophores can undergo the process of excitation and de-excitation multiple times before being irreversibly damaged (photobleached), owing to their weakly bound delocalised electrons. Generally, fluorophores absorb in the visible region of the electromagnetic spectrum and the energy difference between their lowest unoccupied molecular orbital and their highest occupied molecular orbital corresponds to the energies of visible quanta.

The triplet state has important consequences for certain super resolution microscopy methods. Molecules that enter the triplet state are dark but will return to the ground state to re-enter the fluorescence cycle. In the triplet state, molecular oxygen plays an important role in fluorophore bleaching. Firstly, molecules in the dark triplet state can transfer energy to molecular oxygen thus forming excited singlet oxygen species. Secondly, the transfer of electrons from the fluorophore in the triplet state to molecular oxygen results in the formation of superoxide radicals (Blythe et al., 2013). The generation of singlet oxygen and superoxide radials, together with other oxidizing species, is thus synonymous with a diminished fluorophore intensity and photobleaching. Prolonging this dark state through depleting the system of oxygen through oxygen scavenging buffers is a fundamental tactic for triplet state mediated SMLM methods.

When irradiated with a light source of the appropriate wavelength (close to the excitation maximum), the light emitted from the fluorophore is necessarily of a longer wavelength due to internal conversion. This effect is known as Stoke's shift, depicted in Figure 14. Stoke's shift is a valuable measure for fluorescence studies since it allows the distinction between the incident light (excitation source) and the subsequent fluorescence of the fluorochromes via filtration.

A multitude of information can be elucidated based upon the fluorescent emission of a species. For example, the efficiency of the fluorescence process can be determined through the ratio of emitted to absorbed photons, in a measurement termed the quantum yield (QY). The QY is an important indicator of the quality of the fluorophore for biological applications since a high fluorescence efficiency is desirable. Importantly, the QY is expected to

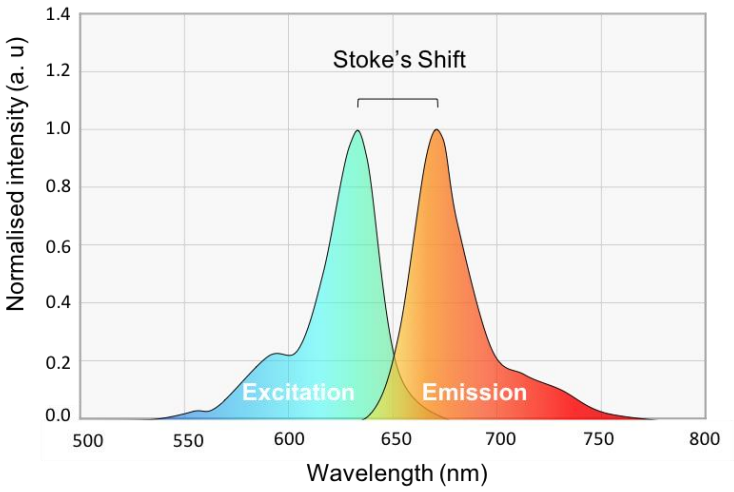

Figure 14: Schematic illustration of the Stoke's shift of a fluorophore. Upon excitation by photon absorption, the fluorophore emits photons of a longer wavelength due to energy loss. The Stoke's shift (nm) is given by the difference in energy between the emission and absorption (excitation) maxima and can be used for detection via filters.

be constant through time and space for identical fluorophores, meaning that the emission intensity is directly proportional to the fluorophore concentration (Lakowicz, 2006). The absorption cross section of a fluorophore is also a highly important parameter, as together with the QY, this defines the brightness of the fluorophore. An ideal fluorophore for fluorescence microscopy possesses a high absorption cross section, and thus brightness.

Another fluorophore characteristic that can be determined is the fluorescence lifetime; the average time that the electron remains in the excited singlet state before returning to the stable ground state either non-radiatively or via photon emission. Fluorescence lifetime imaging (FLIM) uses the lifetimes of fluorescent molecules as a reporter, rather than the intensity of

emission, to produce an image. Since the fluorescent lifetime depends on a plethora of biological parameters such as the local pH, oxygen levels and calcium ion concentrations, numerous FLIM functional studies exist (see review by (Becker, 2012)). In the context of this Thesis, intensity-based methods of extracting quantitative information will be solely used, and thus will be the principal focus.

2.3 Fluorescent probes for biological applications

Fluorophores can act as fluorescent motifs of the functional system. In general, fluorophores can be attributed to one of two groups: organic dyes and fluorescent proteins. Encapsulated quantum dots (QDs) have also been presented as a potential label for biological studies due to their high photo-stability and high QYs, however most commercial QDs induce toxic responses upon excitation and are comparatively large, thereby limiting their use for the study of biological systems (Granada-Ramírez et al., 2018). More recently, the use of organic nanoparticles with functionalised coating surfaces have been proposed for cellular studies, although this approach remains relatively unexplored. Light microscopy studies also report the use of sample auto-fluorescence (intrinsic fluorescence) as a reporter for functional information such as cellular metabolic states (Stringari et al., 2011). It is important to note that sample auto-fluorescence is often considered as a hindrance as it reveals non-specific target structures.

Synthetic fluorescent dyes were first utilised over a century ago, one of the most common being fluorescein. Early studies (1871) highlighted its use in circularity systems; 10 kg of fluorescein diluted in the river Danube could be

detected over 300 miles away in the river Rhine three days later (Cohen, 1958). Fluorescein has also successfully been applied to the vascular system as a fluorescent marker for imaging the optic disc during stages of glaucoma development. Various commercialised organic dyes exist to date, derivatised to suit microscopy studies enabling both specific staining of targets and the possibility of multiple colour acquisitions through distinct excitation and emission spectra (Giepmans et al., 2006, Demchenko et al., 2009). Common dyes include 4',6-diamidino-2-phenylindole (DAPI) (Barcellona and Gratton, 1990), which selectively labels deoxyribonucleic acid (DNA), the family of AlexaFluors (Panchuk-Voloshina et al., 1999), cyanine dyes such as Cy5, oxazine derivatives such as Nile red and rhodamine dye families.

A common strategy for specific labelling involves immunostaining. This technique exploits the specificity of fluorescently labelled antibodies to their endogenous epitope thus allowing the detection of the spatial distribution of endogenous targets within the sample via microscopy. Immunostaining can be achieved either directly or indirectly (Figure 15). Direct immunostaining makes use of a single primary antibody that binds its cellular target conjugated to a fluorescent label whereas indirect immunostaining uses two antibodies; the primary which binds to its specific epitope, and the secondary which binds to the primary and is chemically conjugated to a fluorophore for detection. The major disadvantages of immunostaining are the limited number of target specific antibodies available and their physical size. Whilst in the context of conventional microscopy the impact of the antibody size may not be significant, for super resolution methods their size becomes comparable to the spatial resolution achievable and thus is a limiting factor for high-fidelity target reconstruction (Mikhaylova et al., 2015). A possible alternative labelling strategy for high resolution microscopy is to use an antigen-binding

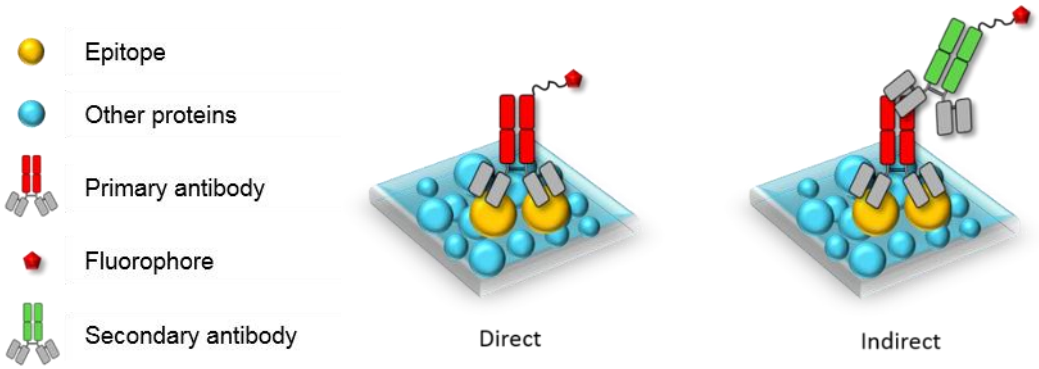

Figure 15: Schematic illustrating direct and indirect immunostaining techniques for fluorescence microscopy studies.

fragment (termed F(ab)), a cleaved portion of the immunoglobin protein structure (Andrew and Titus, 2003). F(ab)s are desirable for microscopy studies due to their relatively small size, which offers both greater accessibility and resolution whilst maintaining target specificity.

A more versatile labelling strategy relies upon the expression of fluorescent proteins within the cell or organism, either through transient expression driven through a plasmid or through stable expression, for example, through clustered regularly interspaced short palindromic repeats (CRISPR-Cas9) mediated gene editing, to be discussed. A revolutionary discovery was made in 1962: Green fluorescent protein (GFP). The first bioluminescent protein (aequorin) was isolated and purified from the jellyfish species *Aequorea Victoria* (Shimomura et al., 1962). During the isolation of aequorin, another protein with green fluorescence emission upon ultra-violet (UV) excitation was observed, henceforth known as GFP. The discovery of this natural phenomenon ultimately heralded a new age of cellular biology, yet its

utility as a tool for the life sciences was not truly recognised until the early 1990s. A pioneering study in the early 1990s reported the cloning and sequencing of the wild-type GFP gene (Chalfie et al., 1994). The discovery that expression of cloned GFP in other organisms resulted in fluorescence emission of the same photophysical properties as the original GFP and the generation of a fluorescence fusion protein revolutionised cellular biology, paving the way for numerous derivatives of GFP and coral fluorescent proteins routinely used as reporters of expression today (Tsien, 1998, Shimomura, 1979, Chalfie et al., 1994).

Over the last few decades, a multitude of fluorescent fusion proteins have become available and the wide spectrum of biological processes on which they can report has diversified. Introducing a single point mutation to the GFP gene for example produces a modified excitation spectrum, with a maximum at 488 nm; a wavelength more suited to live cell studies. This mutation is observed in the most common GFP derivative, Enhanced-GFP (EGFP)(Cormack et al., 1996). Many fluorescent proteins spanning the entire electromagnetic spectrum have been engineered, with varying success (Day and Davidson, 2009). Transiently expressing the appropriately tagged fluorescent fusion protein, directed through a plasmid, can however have adverse effects on cell function if the protein is over-expressed. It has also been reported that GFP for example can induce apoptosis, although the literature is divided regarding cytotoxicity (Liu et al., 1999a). Over-expression is not a consideration when performing immunostaining, however, immunostaining can induce artefacts (reviewed by (Schnell et al., 2012)) that the fluorescence protein approach eliminates. Further, fluorescent proteins often produce present lower photon counts compared to their synthetic probe counterparts, which has important implications for high resolution methods (to be discussed).

The targeted insertion of fluorescent labels into eukaryotic cells, under the control of endogenous promoters, has had a significant impact on the field of microscopy. CRISPR-Cas9 mediated gene editing allows for stable expression under the influence of normal cellular regulation, resulting in healthy cell morphologies and functionalities (Khan et al., 2017). Questions remain to be answered regarding the functional impact of endogenous protein tagging via CRISPR-Cas9 mediated knock ins, however, with careful design this labelling strategy is likely to become a powerful technique routinely used to investigate nanoscale protein distributions and functions.

The choice between a synthetic approach, immunostaining or transfecting fluorescent proteins to achieve a fluorescent motif for the target of interest is naturally a balance between live/fixed cells, the importance of multi-colour acquisition, the resolution acceptable for the biological study and the materials currently available.

2.4 Fluorescence microscopy

Owing to its unparalleled sensitivity, the fluorescence microscope has been at the centre of innumerable discoveries in cell biology for decades. The fluorescence microscope is principally an optical detector, capable of selective excitation and detection of fluorescent molecules within a sample over a vast range of space (from single cell to whole organism) and time scales, dependent upon the approach. The remainder of this Chapter is dedicated to a brief scientific history of the development of the fluorescence microscope, from the diffraction-limited to the evolved super-resolution systems available today.

2.4.1 Conventional fluorescence microscopy: the diffraction barrier

The simplest case of image formation in the widefield diffraction-limited microscope involves a single molecule (the source), emitting photons which travel in all directions in a spherical wavefront away from their source. As the wavefront interacts with optical apertures it experiences Fraunhofer diffraction, and the resultant intensity distribution at the back focal plane of the objective is the Fourier transform of the object. The Fourier transform of a point source is uniform at all frequencies, i.e. the field at infinity exhibits constant amplitude. As the light emanating from the point source encounters a circular aperture (i.e. the objective lens), its manifestation at the Fourier plane will appear as a top-hat function in frequency space, owing to the boundaries imposed by the lens. The inverse Fourier transform of a top hat function (in this case produced by the tube lens), produces an amplitude which is a sinc function and therefore the intensity is a sinc squared function at the detector: The Airy disk. The three-dimensional intensity distribution of this diffraction pattern is aptly termed the point spread function (PSF) (Bianco and Diaspro, 1989), and is an indicator of the resolving power of the optical system. The PSF is elongated along the optical (z) axis, owing to the asymmetry of the wavefront originating from the microscope objective and as a result, axial resolution in optical microscopy systems is significantly worse than that of the lateral.

Despite harmonious advances in hardware, optics and image processing methods, the resolving power of the fluorescent microscope is fundamentally limited due to the diffraction of light. Resolution in this case is defined as the smallest distance at which two point sources can be separated and distinguishable as two independent objects (Airy, 1834). Whilst the resolution

of an optical system can be enhanced by geometrical optics and alignment, there is a physical barrier imposed by the wave nature of light, beyond which information becomes inaccessible. This diffraction barrier and thus the resolving capability of the optical system, was principally described by Ernst Abbe in 1873:

$$R_{x,y} = \frac{\lambda}{2N_A} \quad (1)$$

$$R_z = \frac{2\lambda}{{N_A}^2} \quad (2)$$

Where λ is the wavelength of the excitation and N_A is the numerical aperture of the objective lens, i.e. its light gathering ability. The achievable resolution of the system can thus be influenced by the wavelength of light used. In practice, most systems adopt objective lenses of $N_A \leq 1.5$, and when under UV excitation for example, the resolution in ideal conditions that one can achieve is inherently limited to ~160 nm in the lateral and ~360 nm in the axial plane. These fundamental limitations were also described by Rayleigh (Rayleigh, 1879), whose criterion states that if the first order minimum of the diffraction pattern formed by one point source coincides with the maximum of another point source the imaging process is deemed diffraction-limited (Figure 16).

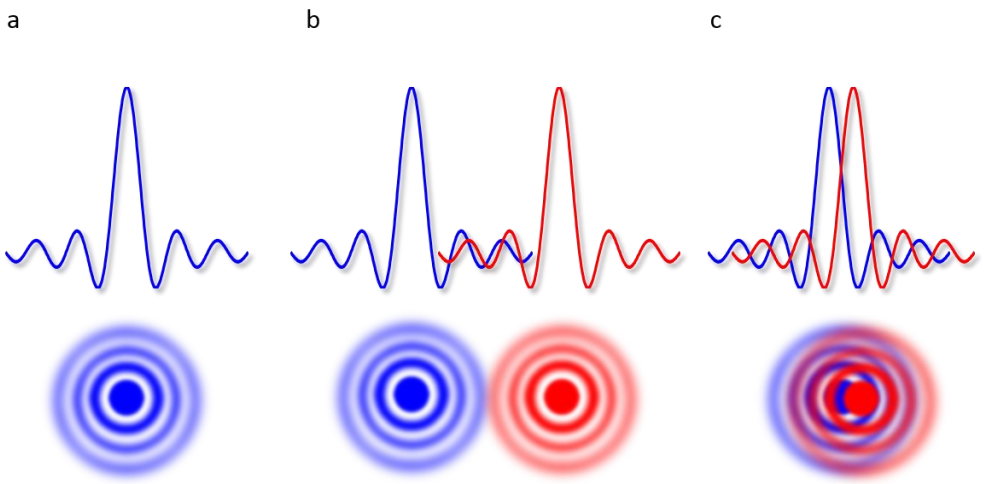

Figure 16: Visualisation of the Airy disk for a single point source (a), two point sources which are resolvable (b) and two point sources that cannot be resolved as two objects (c). The Airy disk patterns highlight superposition of point source emission via Rayleigh's criterion. Note that each point source is pseudo coloured solely for visualisation purposes.

2.4.2 Extending resolution

Several strategies have been proposed to improve the lateral and axial resolution of the widefield system including confocal microscopy (Minsky, 1961), 4Pi microscopy (Hell et al., 1994), total internal reflection fluorescence (TIRF) microscopy (Axelrod, 1981), and selective plane illumination microscopy (SPIM) (Huisken et al., 2004).

In the standard confocal microscope, a coherent source of excitation (typically a laser) is focused by an objective lens of high N_A to form a diffraction limited spot of illumination on the sample. A pinhole is placed before the detector in an optically conjugate plane, thus creating the confocal

volume of fluorescence detection. Typically, the pinhole size is set to match the size of the Airy disk such that only the first harmonic can pass through to the detector. This configuration eliminates the detection of out of focus fluorescence, which otherwise degrades axial resolution, and thus presents a vast improvement to conventional wide-field techniques (Figure 17). In terms of lateral resolution, a modest improvement can be achieved through confocal microscopy. For an ideally small pinhole, the Airy disk is typically narrower by a factor of 1.4, compared to that of the widefield microscope. As such, only a modest improvement in lateral resolution is achievable with confocal microscopy. Optical sectioning of thick biological samples is however possible due to the confocal configuration. Since confocal microscopy is a point scanning method however, image formation is typically a time-consuming process as a raster scan of the sample is required, whilst also considering signal-to-noise and contrast requirements.

It is important to note that the optical sectioning capability of a diffraction-limited optical system can be significantly improved without the need for cost and instrument complexity, through image deconvolution. Image deconvolution is mostly used for wide-field microscopy images although can in theory be applied to any digitally acquired image. Numerous deconvolution algorithms exist and can achieve improvements in both lateral and axial resolution (Cotte et al., 2010, Swedlow, 2013).

Another strategy to improve resolution is through TIRF microscopy, by exploitation of an evanescent wave at the plane of focus, typically at the glass coverslip-sample interface. TIRF microscopy facilitates certain super-resolution methods producing a well-defined axial volume of excitation, thereby selectively confining fluorescence emission. TIRF microscopy relies

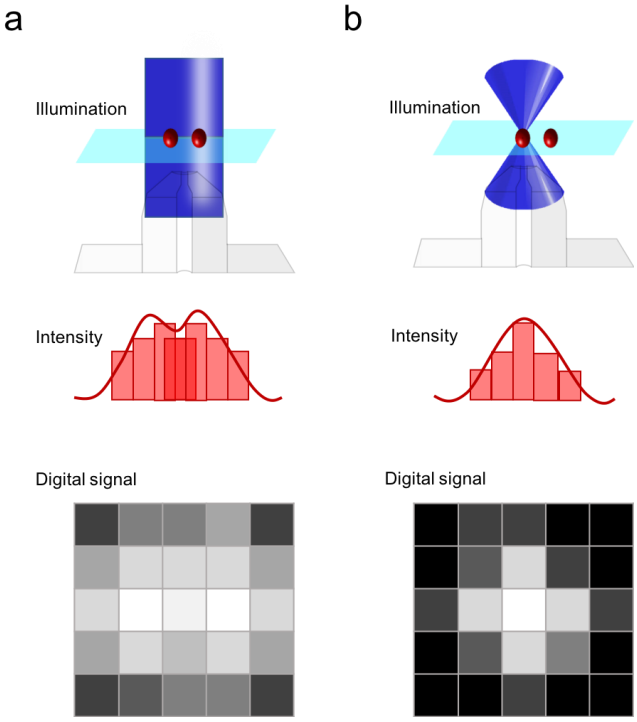

Figure 17: Detection volumes of conventional wide-field microscopy (a) and confocal point scanning methods (b). The illumination is depicted dark blue and molecules to be imaged, and their 2D intensity distributions, are depicted red. Whilst both methods can use the same excitation source and detect fluorescence through an objective lens, the use of a pinhole aperture enables optical sectioning in the confocal configuration.

upon the total internal reflection (TIR) of the incident light at the interface between differentially refractive materials, governed by Snell's Law:

$$n_1 Sin\theta_1 = n_2 Sin\theta_2 \qquad 3$$

Where n_1 is the higher refractive index, n_2 is the lower refractive index, θ_1 represents the angle of the incident illumination with respect to the interface normal and θ_2 is the angle formed between the refracted light and the interface normal. When the excitation is inclined at angles greater than the critical angle,

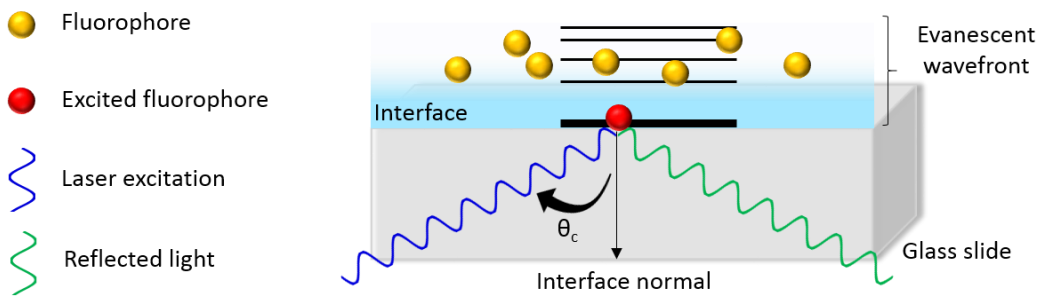

Figure 18: Schematic illustration of the basic principles of TIRF microscopy. Laser excitation at the critical angle induces an electromagnetic field at the interface, which decays exponentially in the axial dimension, thus providing optical sectioning. Only fluorophores within ~100 nm of the interface may be excited and therefore detected in TIRF mode.

termed θ_c, the wave no longer crosses the boundary between refractive indices, rather, the light is entirely reflected though n_1 internally. For TIR to occur, the incident light must encounter a high to low refractive index mismatch, Figure 18. At the high-low refractive index boundary, an electromagnetic wavefield is generated in the low-refractivity medium, of the same wavelength of incident light. The intensity of the induced evanescent wavefield decreases exponentially with increased distance from the boundary, resulting in a highly specific axial region of fluorophore excitation, typically extending ~ 100 nm into the sample. The exponential decay in intensity can be expressed as:

$$I(z) = I_0\, e^{-z/d} \qquad 4$$

For which

$$d = \frac{\lambda_0}{4\pi}(n_2{}^2 sin^2\theta_1 - n_1{}^2)^{-1/2} \qquad 5$$

Where I(z) is the intensity perpendicular to the interface, I_0 is the intensity at the interface (for which z = 0), d is the penetration depth, z is perpendicular distance from the interface and all other parameters remain per equation 3. This method of achieving optical sectioning again reduces out of focus background fluorescence, as such, TIRFM is particularly suited to the study of surface regions. TIRFM alone however possesses limited lateral resolution, akin to that of conventional microscopy systems. In terms of the biological context presented in this Thesis, imaging of the T cell immunological synapse via TIRFM is a suitable approach as once activated, T cells spread to form a flat surface with their stimuli (the antibody coated coverslip in this Thesis). TIRFM thus enables imaging of the synapse alone, avoiding the background associated with a deeper sample illumination.

Despite various technical and mathematical solutions presented to improve the resolution of the optical microscope, a physical barrier to resolution persists. Although diffraction-limited microscopy can elucidate biological insight, these methods do not enable a nanoscale description of the system. It is for this reason that a concerted effort was made in the 1990s to circumvent the diffraction barrier and produce the first "super-resolution" microscope to unravel the nanoscopic features of the cellular machinery.

2.5 The advent of super-resolution

Synergistic technological advances in optical physics, organic chemistry, labelling strategies and image analysis has propelled the field of fluorescent microscopy into nanoscale detection, enabling unprecedented access to diverse biological systems. The various strategies of achieving super resolved

images can be largely grouped into two categories: deterministic (ensemble) and stochastic (single-molecule) methods.

2.5.1 Deterministic methods of achieving super resolution

The first super-resolution system was proposed by Stefan Hell in 1994, for which he gained a Nobel prize. The principle of stimulated emission depletion (STED), proposed theoretically in 1994 (Hell and Wichmann, 1994) and verified experimentally in 1999, circumvents the diffraction limit by controlling photophysical properties of fluorescent molecules. A physical suppression of the effective PSF size is achieved by superimposition of a toroidal depletion beam (the STED beam) with a typical excitation laser. The STED beam forces excited electrons to the ground state, thereby the fluorescence signal is depleted in this region, and only those fluorophores within the centre of the excitation spot will emit. The energy of the STED photons is lower than that of the excitation laser and is tuned to match the energy difference between the singlet excited state and the highest orbital of the ground state. Increasing the power of the STED beam will increase the region of depletion, and further narrow the effective PSF thus improving lateral resolution. Axial resolution however is not improved in conventional STED.

Practically, the STED set-up is similar to that of the standard scanning confocal microscope, although its mechanism of illumination is modified to force stimulated emission. First implementations of STED used pulsed lasers, with the delay between pulses in part governing the probability of stimulated emission, however more recent versions incorporate continuous wave lasers. As with confocal microscopy, STED images are formed through a raster scan

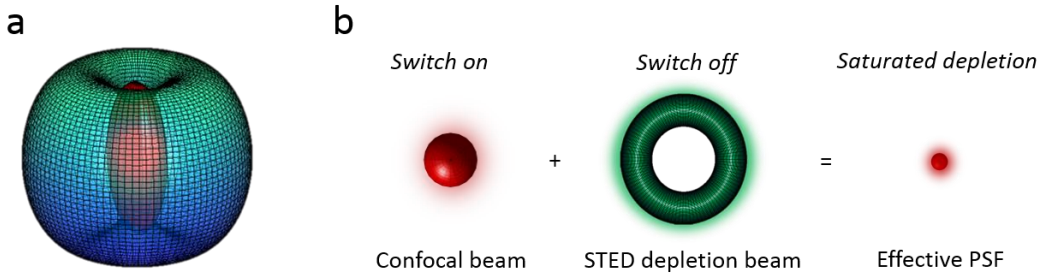

Figure 19: Principle of STED microscopy. The 3D PSF (a) is formed through superposition of the diffraction-limited excitation beam (depicted red) and the toroidal depletion (STED) beam. The depletion beam forces peripheral fluorophores into the ground state via stimulated emission (b). Due to this configuration, only central fluorophores are detected, at a high-resolution due to the effective narrowing of the PSF at the focal point.

of the sample. Unlike SMLM methods, ensemble-based methods such as STED do not require extensive post-processing to produce the super-resolved image, and only one acquisition is required to form the full spatial distribution of sample fluorophores. However, there is often a high cost associated with STED techniques owing to the high-powered lasers (~200 mW) used to achieve the best possible resolution. Nonetheless, STED has been utilised at biologically compatible laser powers for the study of live cells (Wegner et al., 2017, Heine et al., 2018) reaching ~ 80 nm spatial resolution.

2.5.1.1 Structured Illumination Microscopy

Engineering the PSF shape by use of patterned illumination is another common strategy to subvert the diffraction barrier in ensemble-based methods. Structured illumination microscopy (SIM) typically employs a movable diffraction grating to produce a well-defined pattern of high

frequencies, which is projected onto the sample via the objective lens (Gustafsson, 2000). The superimposition of the patterned light and fluorescence produces Moiré fringes due to interference. Whilst subject to homogenous illumination, proximal fine details within the sample are unresolvable. By application of structured excitation however, the high spatial frequency sample information overlaps with the high-frequency components of the illumination pattern thus producing an emission distribution of a low spatial frequency which in turn can be detected via the objective lens. To create a SIM image, the diffraction grating is moved (rotation and translation dependent upon 2D/3D modality) and post-processing preformed. Indeed, SIM relies heavily on post-processing for image reconstruction, by mathematically extracting fluorophore positions by deconvolution.

Original SIM systems achieve a two-fold improvement in lateral (~ 100 nm) and axial (~ 250 nm) resolution per equations 2 and 3, and recent SIM modifications such as the introduction of dual objective systems or saturated SIM achieve up to ~100 nm axial resolution. A major advantage to the SIM approach is temporal resolution; SIM images do not require raster scanning (as with STED or confocal microscopy) to produce high resolution images. Further, due to its comparatively lower exposure to laser power, SIM is an attractive live cell imaging modality. SIM also does not require complex labelling or manipulating of photophysical properties of fluorescence compounds, however, SIM is prone to image artefacts (Schaefer et al., 2004). A schematic of the SIM imaging process is depicted in Figure 20.

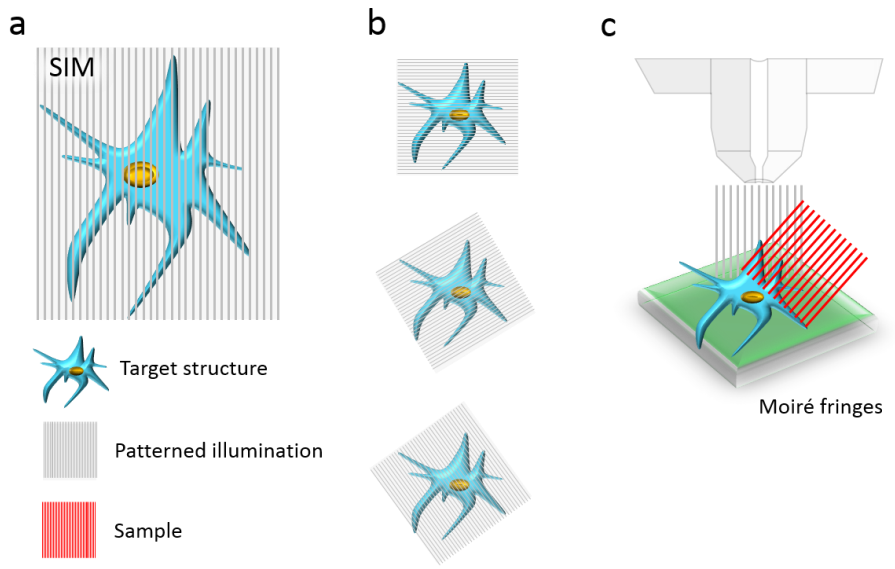

Figure 20: SIM methodology. The sample is subject to a patterned widefield illumination (a) of known characteristics. Through a series of translations and rotations (b), several raw images are acquired. The light originating from the sub-diffraction limit target structure interferes with the structured incident illumination, thus forming Moiré fringes, such that originally high spatial frequency information is shifted to a lower spatial frequency and can be readily collected via the objective (c). Following mathematical operations, the super-resolved SIM image is formed.

2.5.2 Stochastic based methods of achieving super resolution

A family of closely related single molecule techniques have recently emerged, each exploiting photophysical switching properties of fluorescent compounds. Eric Betzig shared the 2014 Nobel prize for Chemistry with Stefan Hell and William E. Moerner, for the development of photoactivatable localisation microscopy (PALM), although the principles underpinning the localisation of individual emitters were described as early as the 1980s (Bobroff, 1986, Moerner and Kador, 1989). An inspirational study by Bobroff

et al. (1986), demonstrated that although the physical size of the observed target is limited by the resolving power of the microscope, its centre of mass can be determined at an arbitrary precision given sufficient photons (Bobroff, 1986). Thompson et al. applied this theoretical framework to the study of individual fluorescent probes via confocal microscopy. It was demonstrated that the pixelated PSF of the individual point source could be recapitulated by a Gaussian function, whose centre position provides an estimation of the spatial position of the emitter and whose standard deviation is a measure of the uncertainty of localisation (Thompson et al., 2002). Although these fundamental principles that form the foundations of localisation based super-resolution microscopy have been known for decades, tactics to temporally separate the individual PSFs and thus avoid ensemble activation of multiple fluorophores within the same diffraction limited volume, were not realised until 2005. Lidke et al (2005) performed the localisation of individual QDs, separated through time and space, via exploitation of fluorescence intermittency or blinking properties of point sources (Lidke et al., 2005). Lidke et al. further postulated that the temporal separation of individual fluorophores through their intensity fluctuations could be applied to cellular studies, and through the localisation process the underlying structure could be reconstructed by painting the fluorophores in a pointillist fashion.

2.5.2.1 PALM methodology

SMLM strategies to achieve temporal separation and thus avoid overlap of multiple PSFs at the detector vary, although all methods limit the probability of PSF overlap by stochastically activating only a sparse subset of fluorophores per image frame (Figure 21). PALM relies on photo-activation/conversion of fluorescent proteins to achieve temporal separation in fluorophore emission (Betzig et al., 2006, Hess et al., 2006). When subject to illumination, certain

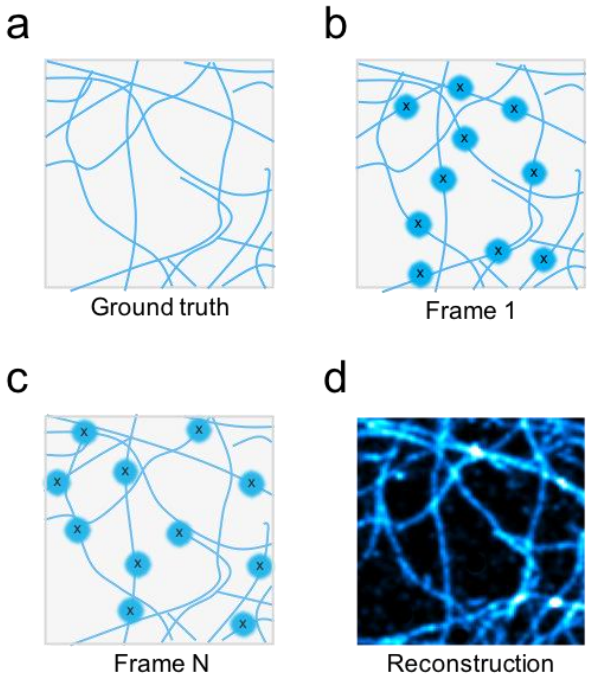

Figure 21: The basis of SMLM. Localisation based methods of super resolution microscopy rely upon the serial activation, localisation and de-activation of a sparse subset of sample fluorophores per image frame. This process is repeated over multiple frames (b-c), such that the full fluorophore population can be reconstructed and rendered as an image (d). Various factors influence the quality of the reconstruction, i.e. how faithful the reconstruction is to the ground truth (a).

fluorescent proteins can undergo a photoswitch to longer excitation and emission wavelengths in a controlled fashion. This photochromism serves as a basis for serial single molecule detection, in a cycle of activation, detection (localisation) and de-activation. Unlike conventional fluorophores, which fluoresce when subject to a specific wavelength of illumination, photoactivatable fluorescent proteins (PA-FPs) require an initial photoactivation to engage the mechanism of emission. The underlying mechanisms driving photoswitching is thought to be conformational changes in the PA-FPs upon excitation, for example, cis-trans isomerisation of the

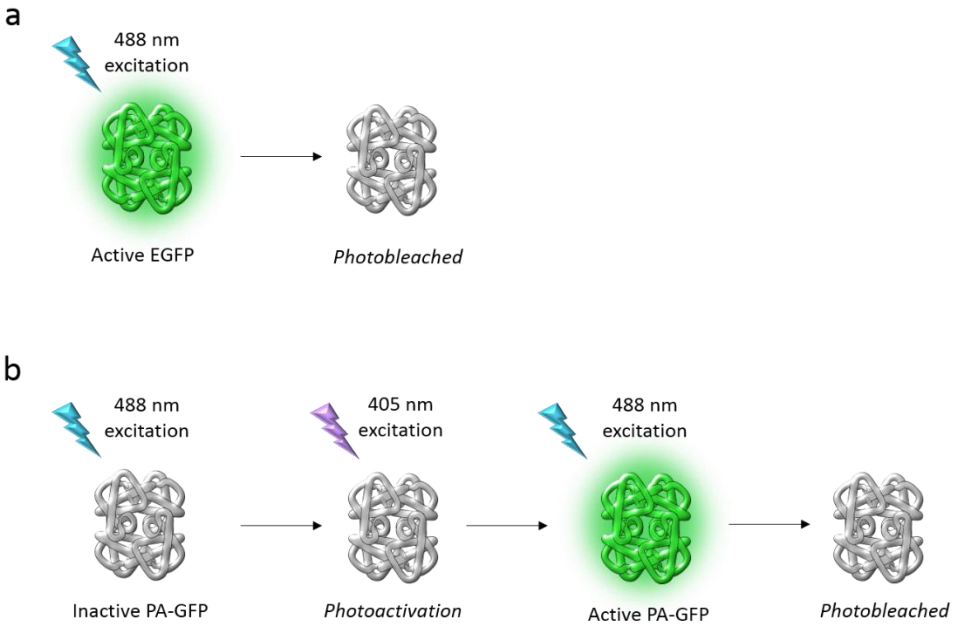

Figure 22: The basis of PALM signal generation. Unlike conventional FPs which are excited to fluoresce when subject to a specific wavelength of light (a), PA-FPs require an initial photoactivation to trigger their normal fluorescence behaviour (b). Photoactivation is typically achieved through UV excitation, and post-photoactivation, the fluorophores undertake the fluorescence process by conventional means, until the population of fluorophores are irreversibly damaged. The number of fluorophores activated per cycle is a crucial determinant to the success of the PALM experiment.

fluorophore methylene bridge between the two rings of the fluorophore of the PA-FP Dronpa and GFP derivatives. In a conventional PALM experiment, the sample is subject to a low-powered continuous UV excitation which acts to stochastically switch a small subset of PA-FPs into the active state. These activated fluorophores are typically separated by a distance greater than that of their PSFs and are thus resolvable. This subset is then photobleached, i.e. forced into the inactive/off state via a high-powered excitation laser (at 488 nm

in the case of Figure 22b). The individual PSFs from the image frame can be localised with nanometre precision, and a new set of sample fluorophores imaged in the next frame. This cyclical process is repeated over many image frames, until the entire population of fluorophores is depleted. The full population of sample fluorophores can therefore be reconstructed by combining the frame-wise localised PSFs. This molecular map of x-y coordinates enables a full quantification of the millions of single molecules within the cellular structure, which are otherwise indistinguishable as an array of point sources via conventional microscopy (Sage et al., 2015).

2.5.2.2 STORM methodology

Stochastic optical reconstruction microscopy (STORM), developed by Xiaowei Zhuang in 2006, is closely related to the PALM technique (Rust et al., 2006). STORM however employs a different tactic to PALM in generating a photoswitchable signal, by use of dye-pairs (and more recently single dyes) rather than proteins. The STORM concept was first demonstrated using the cyanine dye pair Cy3 – Cy5, termed the cyanine switch. Cy5 alone can be forced into a dark (non-fluorescent) state in a controlled and reversible manner, however the addition of a proximal Cy3 molecule greatly facilitates the switching of Cy5 as it aids recovery to the fluorescent state by acting as an energy donor. In principle, any fluorophore capable of optical photoswitching can be used to perform STORM (Figure 23a). A popular variant of the STORM methodology, direct-STORM (dSTORM), relies upon a manipulation of the triplet state to produce fluorophore blinking (Figure 23b) (van de Linde et al., 2011, Heilemann et al., 2008, Heilemann et al., 2009). In contrast to STORM, dSTORM does not require the use of a donor molecule to facilitate photoswitching. Rather, the prolonged triplet state is thought to involve

photoreduction, by use of primary thiols such as β-mercaptoethylamine to generate stabilised radical ions.

In a typical dSTORM experiment, all sample fluorophores are forced into a dark state by use of high power laser illumination and thiol agents and remain in this stable off state for a prolonged lifetime. This prolonged dark state lifetime can also be enhanced through use of an oxygen scavenging buffer, interchangeably termed a reducing buffer (Heilemann et al., 2008, Olivier et al., 2013b). Free-radical formation is a major source of photobleaching in fluorescent systems, therefore by reducing the population of reactive oxygen species within the sample via glucose oxidase and catalase-based conversions for example, the dark state lifetime can be extended (discussed in Section 2.2). By application of a low powered UV laser (the switching signal) a small subset of fluorophores can be activated into the on state, akin to the PALM method. To convert the fluorophore back to the fluorescent state, oxygenation of the reduced radical occurs, promoted by redox buffers. The nature of this process is stochastic; provided that the labelling of target structures is optimised (primarily fluorophore concentration), the molecules that switch are likely to be separated by a distance greater than their PSFs, and thus are resolvable as point sources. Once the PSFs of the activated subset of molecules have been detected, these molecules are typically photobleached and a new subset of fluorophores can be sampled. Importantly for the dSTORM technique, the chemical composition of the reducing buffer is a fundamental determinant of the off state lifetime, and numerous compositions have been derived to date to facilitate SMLM methods (Olivier et al., 2013a).

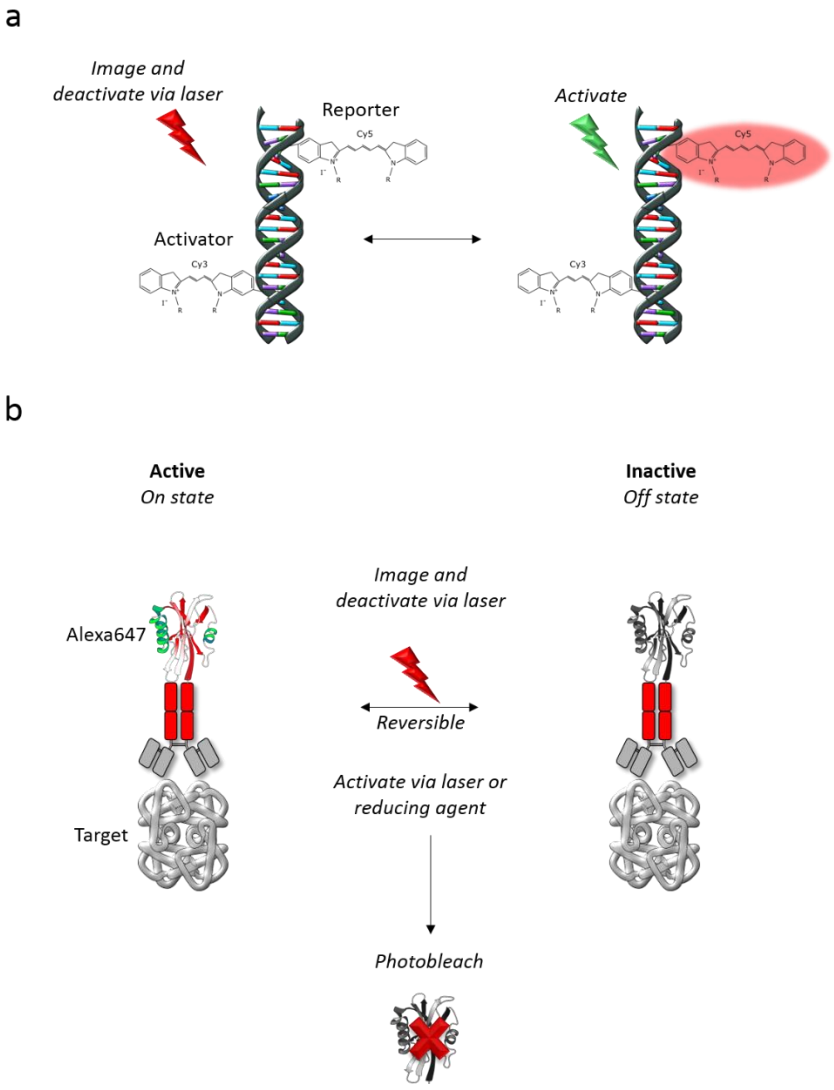

Figure 23: Principle of signal generation in STORM. Originally, the cyanine switch of Cy5 on DNA (a – reporter) was used to generate a photoswitchable signal. A red laser excites fluorescence from the reporter and deactivates Cy5 into the dark state. A green laser (activation) is then applied to return the reporter to the excited state, the recovery of which highly depends upon the propinquity of the Cy3 molecule. dSTORM however uses a single dye (b), Alexa647 in this schematic, and relies heavily upon the thiol-based imaging buffer to facilitate photoswitching, without the need of a donor molecule.

For both PALM and STORM, the activated subset of fluorophores should be photobleached post-detection under ideal conditions. In practice, a long-lived activation can render a molecule detectable across sequential acquisition frames, and thus a single molecule can be localised multiple times. Fluorophores can also possess the ability to undergo on/off switching cycles many times, in an effect termed multiple- or photo-blinking (Annibale et al., 2010, Dickson et al., 1997). This effect is most prominent in dyes used for STORM however, the effect of multiple blinking on SMLM quantification is a universal issue (Shivanandan et al., 2014). In terms of the analysis of clustered distributions of target proteins, multiple blinking adversely affects the analysis due to the induced self-clustering owing to the detection of a single molecule as multiple point sources, each with a unique localisation precision. In terms of structurally focused analysis however, the issue of multiple blinking is comparatively minor if one is not concerned with absolute quantification, for example molecule counting (Shivanandan et al., 2014). For example, analysing a fibrous distribution of single molecules is greatly facilitated by a high sampling rate of the underlying structure, for accurate reconstruction and the opportunity to reject poorly localised molecules without significant loss of structural information.

Defining the resolution of a sub-diffraction limited image is complex. Rayleigh's criterion does not consider photon counts in its assessment of image resolution for example (Ram et al., 2006), and parameters unique to SMLM data such as the localisation uncertainty contribute to the image resolution. Labelling density further defines the resolution achievable by SMLM, although these parameters alone are not sufficient to describe the resolution of SMLM images. Nieuwenhuizen et al. thus proposed a novel tool for the assessment of SMLM image resolution termed Fourier image

resolution (FIRE), based on Fourier ring correlation (FRC). For this, the localisations are assigned at random into two sub-sets, each forming a new image and their Fourier transforms computed (Nieuwenhuizen et al., 2013). The correlation between the two Fourier transforms as a function of frequency, up to a maximum fixed value, is then calculated thus providing a FRC curve. The image resolution is the inverse of the spatial frequency at which the FRC curve drops below a fixed threshold.

Although instrumentation for ensemble-based methods is typically more complex than that required for localisation-based microscopy, the complexity lies within controlling the blinking behaviour of the fluorophores for stochastic modalities. Achieving optimal imaging conditions often means testing a variety of parameters, for example the probe itself, buffer conditions, excitation intensity and their various permutations result in a manifold of blinking behaviours (Dempsey et al., 2011). Exploiting photophysical pathways and the complexity of controlling these processes can also contribute to error in quantification. One of the current limitations of SMLM methods is the probes available, whether this be their brightness, photostability, compatibility for live cell studies, specificity or their capacity for multiplexing. The major implication of this is limited photon counts (hence high uncertainty – to be discussed) and often poor labelling density; two fundamental contributors to the image resolution (Nieuwenhuizen et al., 2013). A brief summation of presented modalities is presented in Figure 24, the choice of which ultimately depends upon the relative strengths and weaknesses of each system in light of the biological question at hand.

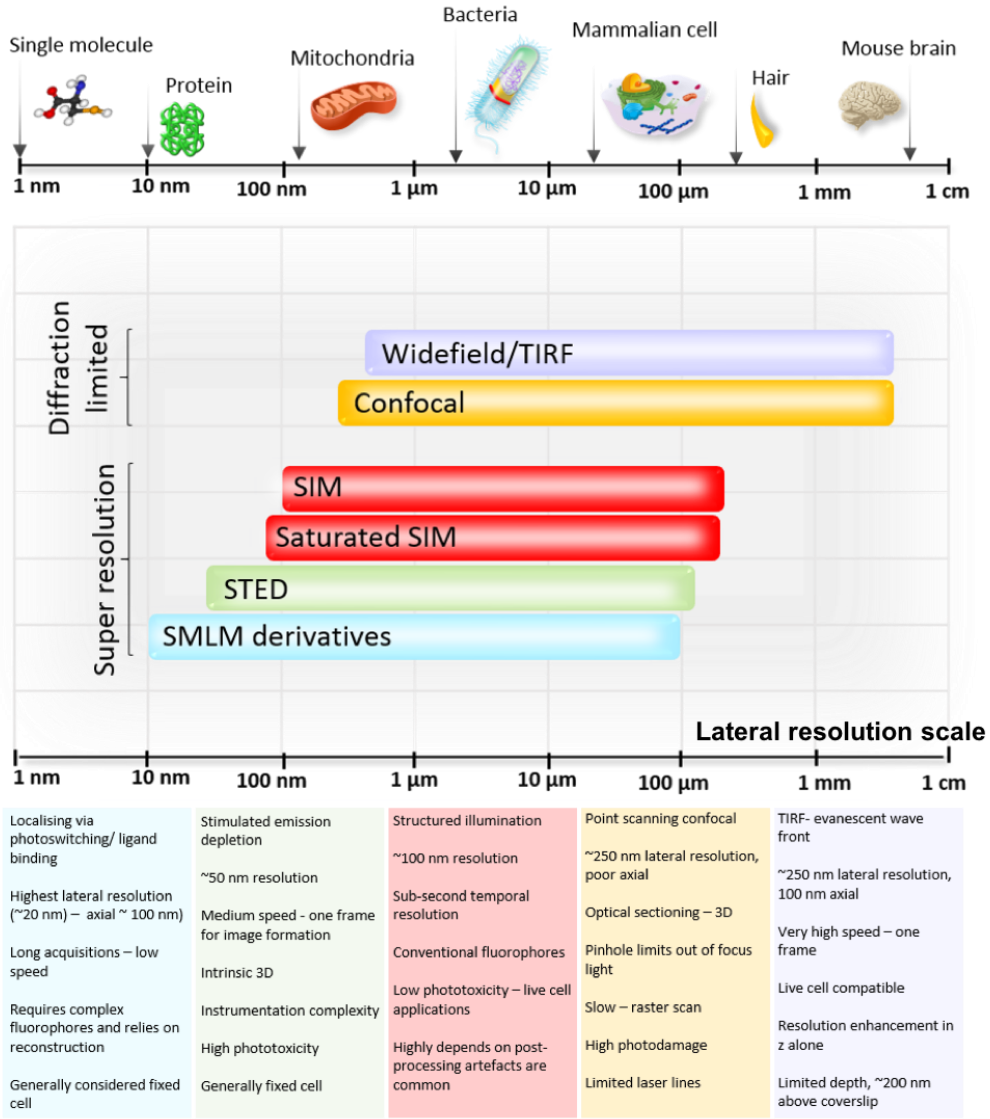

Figure 24: Summation of the scope of the discussed conventional microscopy methods and ensemble and stochastic methods of achieving super resolution.

2.5.2.3 Alternative stochastic approaches

Numerous alternative stochastic methods exist to date that produce SMLM data sets, a notable example is point accumulation for imaging in nanoscale topography (PAINT) and its many derivatives (Sharonov and Hochstrasser, 2006, Giannone et al., 2010, Jungmann et al., 2014). Generally, the PAINT principle exploits the immobility of a probe when bound to its target to produce a signal that can be localised with extremely high precision. Recent methods inspired by the PAINT technique include universal-PAINT (uPAINT) (Giannone et al., 2010), DNA-PAINT (Jungmann et al., 2010) and image reconstruction by integrating exchangeable single-molecule localisation (IRIS) (Kiuchi et al., 2015). For all three modalities, freely diffusing probe can reversibly and repeatedly bind/unbind its intracellular target in a transient manner, producing the blinking necessary for SMLM. In the bound state, the probe remains immobile for a prolonged period such that the detector can accumulate a significant number of emitted photons for detection. The probe binding kinetics can be modulated, and the sparseness of activation is achieved through the concentration of the probe, rather than the activation laser. This renders PAINT based methods of SMLM extremely flexible, and multiplexing becomes readily achievable since serial imaging with the same fluorophore can be easily performed.

IRIS employs small protein fragments that bind and unbind to their specific targets in an exchangeable fashion, producing a highly labelled map of localisations (Kiuchi et al., 2015). An exemplar IRIS probe consists of the small F-actin-binding peptide LifeAct (17 aa) conjugated to the fluorescent molecule Atto-655, which transiently binds to F-actin. The IRIS approach to SMLM is most suited to ultrastructural studies; individual molecules are sampled multiple times as the probe transiently diffuses in the imaging

solution. In practice, IRIS imaging is performed on a microscope capable of TIRF, providing optical sectioning and crucially limiting signals originating from the freely diffusing unbound probe. Prevention of overlap of multiple PSFs at the detector and thus the production of a SMLM data set is realised through controlling the concentration of the dye, rather than through exploiting photophysical properties of fluorophores or complex imaging buffer solutions. IRIS permits long acquisition times, since the pool of LifeAct-Atto655 molecules exist in the imaging solution, the absolute number of which is dependent upon the concentration. Owing to the large numbers of localised molecules, one can afford to apply a strict filtering process when using the IRIS approach, retaining molecules with the best estimated precision and photon counts to produce high quality SMLM reconstructions (Peters et al., 2017, Peters et al., 2018a, Schätzle et al., 2018, Tas et al., 2018).

The use of IRIS for the study of the actin cytoskeleton offers multiple advantages over previous methods. Firstly, the physical size of the probe is small and thus the SMLM reconstruction is more faithful to the true underlying structure. Larger markers for F-actin, including actin itself, also present the problem of competing with their endogenous counterpart population which can subtly influence actin structure and dynamics (Feng et al., 2005) , an effect that IRIS overcomes. The use of Phalloidin for the study of the cytoskeleton can be limited due to its toxicity and actin stabilising properties, however for fixed cells this is not a concern (Cooper, 1987). Further, Phalloidin binds actin structures with high affinity and low disassociation rates (De La Cruz and Pollard, 1996), such that once a dye molecule interacts with its target the F-actin binding site becomes unavailable for further binding. The nature of this interaction fundamentally limits the density at which the underlying structure may be sampled, and thus can provide an

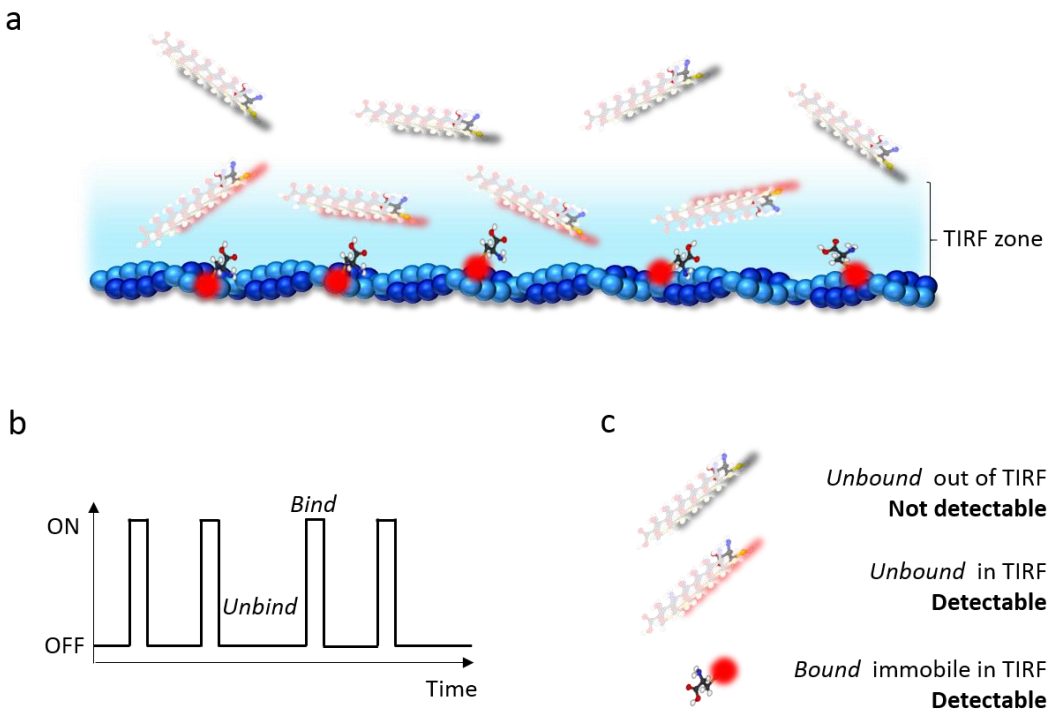

Figure 25: IRIS methodology. Freely diffusing probe transiently binds and unbinds its target structure (a). When imaged in TIRF mode, upon binding the probe remains immobile and can be detected as a point source (b). Whilst some unbound probe can be detected in the TIRF zone, thus degrading image quality (c), it is possible to filter these molecules based upon their emission characteristics.

incomplete reconstruction of continuous structures. Transfection of genetically encoded proteins to tag intracellular actin also presents drawbacks; cells expressing variants demonstrate altered actin behaviours (Feng et al., 2005) and functions and again the physical size of the fluorescent compound is comparable to the resolution limit of localisation based methods. Not only does IRIS surmount the labelling density problem often faced when employing previous methods, but also the number of observable targets is essentially unlimited regardless of spatial proximity; a fundamental

advantage. It is for these reasons that IRIS probes and derivatives thereof are attractive candidates for the study of the actin cytoskeleton.

2.5.2.4 Current challenges in quantitative SMLM

The performance of pointillist super-resolution methods highly depends upon the labelling density of the target structure, for high-fidelity reconstruction. Indeed, the labelling density has a pronounced effect on the resolution of the SMLM data set. The Nyquist-Shannon sampling criteria outlines this principle, in which continuous data is sampled by a series of digitised points (Nyquist, 1928, Shannon, 1949). To accurately reconstitute the continuous structure, the sampling interval must be greater than at least twice that of the highest spatial frequency of the sample, to preserve spatial resolution. If the labelling density is lower than the Nyquist interval, the underlying structure will be under sampled producing error prone analysis. It is for this reason that high localisation precisions alone are not sufficient to produce high quality SMLM reconstructions; if the density of labelling is below the Nyquist criteria the structure cannot be fully recapitulated. Critically, for structural SMLM analyses, over-sampling is beneficial, as even though the extra information does not contribute to enhanced resolution, the extra signals can improve accuracy in reconstruction.

Currently, achieving 3D SMLM with both high resolution in both lateral and axial planes and high sample depth remains a challenge. Whilst methods that engineer the PSF through astigmatism for example, or via the double helix point spread function (DHPSF) (Pavani et al., 2009), can achieve up to 15 μm – thick cell volumes (Carr et al., 2017), the highest reported axial resolution is ~ 100 nm. Interferometric methods such as iPALM (Betzig et al., 2006) however

offer isotropic resolution, routinely reporting localisation precisions in the range of 10 – 30 nm. This is achieved via a dual objective and camera system. Briefly, the emission from a fluorophore is captured on both cameras, thus producing two optical paths. Owing to interference, the axial positional information is encoded in the combination of these two paths, and post-processing can reveal the z position of the fluorophore (Shtengel et al., 2009). This method however can only retrieve information up to ~ 600 nm away from the interface, thus the study of whole cells is currently limited. Light sheet microscopy is a promising imaging technique for achieving optical sectioning and deep sample volumes. Lattice light sheet for example can produce ~ 1 μm thick optical sections over a 50 μm field of view (FOV), by use of astigmatic lenses to encode axial positions, achieving localisation precisions of 9 nm and 45 nm in the lateral and axial dimensions respectively, under ideal conditions. This method has been successfully applied to reconstruct the entire nuclear lamina for example (Gustavsson et al., 2018).

Errors in labelling such as unspecific binding and the physical size of the labelling motif can also have a profound effect for quantitative studies. It is important to note that all SMLM methods involve the imaging of the fluorescent tag, rather than the protein itself. For PALM studies for example, the size of a typical PA-FP is of the order of ~5 nm, combined with the linker to the specific protein of interest (~ 5 nm) such that the vector sum of these markers can contribute to ~10 nm offset in a randomised orientation (Deschout et al., 2014, Enderlein et al., 2006). For distance based quantitative studies, especially co-localisation, this can render labels further apart, or indeed closer together than the true protein distribution (Shivanandan et al., 2016). For indirect immunostaining methods, this effect is compounded by use of primary and secondary antibodies, contributing to error in true localisation.

The fluorescent moiety can reside up to ~30 nm from its target structure, comparable to the resolution of SMLM methods. This effect can be somewhat ameliorated by use of F(ab) fragments, as previously discussed, and more recently by use of nanobodies (Ries et al., 2012).

Absolute quantification, for example protein counting, is also currently limited due to poor detection efficiency of single targets. For example, during the transfection of PA-FPs, errors such as misfolding can lead to the production of non-fluorescent proteins, which combined with incomplete photoconversion leads to a low proportion of fluorescent cells (Shivanandan et al., 2014). Generally, a low detection efficiency can be ascribed to any process that prevents a molecule from being detected, whether this be due to premature photobleaching, epitope masking or quenching, sample drift during acquisition or incomplete activation of fluorophores. Previous studies claim that the detection efficiency can range from 40-74%, dependent upon the approach (Durisic et al., 2014). For example, for the case of the PA-FP mEos2 only 60% of the sample population are photoconverted (Annibale et al., 2012). A lower detection efficiency can lead to underestimation of sample fluorophores, therefore whilst positional information is readily and reliably extracted via SMLM, the true number of target molecules remains uncertain.

Arguably, the most important parameter to consider when performing SMLM is the choice of fluorophore, which is highly dependent on the imaging modality, availability and instrumentation (Dempsey et al., 2011). The ideal fluorophore for SMLM applications remains in an inactive state, is activated and emits many photons, before being photodamaged permanently. Two fluorophore characteristics are integral to the super resolution image quality: the number of emitted photons per event and the duty cycle, i.e. the duration

of time the fluorophore resides in the active state. The higher the number of photons, the better the estimate of its position owing to the inverse square root dependency in the Thomson formula (to be discussed). The collected number of photons, which varies drastically among fluorophores, is thus the limiting factor to the resolution attainable with SMLM approaches. A fluorophore with a low duty cycle is desirable, as the number of detectable point sources within a diffraction limited volume is inversely related to the duty cycle and thus the density of detectable fluorophores is inherently related to the duration of the active state.

Stochastic approaches require thousands of sequential frames to fully reconstruct the sample fluorophore distribution, and thus long acquisition timescales. It is for this reason that STORM/PALM is generally considered a fixed-cell modality, however a select few live cell studies exist (Klein et al., 2011, Manley et al., 2008, Shroff et al., 2008). Fixation itself is a controversial topic, as many studies claim that the chemical process disturbs the spatial distribution of proteins and their configurations (Annibale et al., 2012, Tanaka et al., 2010). Further, long acquisitions exacerbate the effect of sample drift, caused by thermal fluctuations and instrument vibration, although many algorithms exist to correct for this common artefact (Geisler et al., 2012, Mlodzianoski et al., 2011).

A summation of the current challenges and limiting factors to achieving high quality SMLM data is presented in Figure 26.

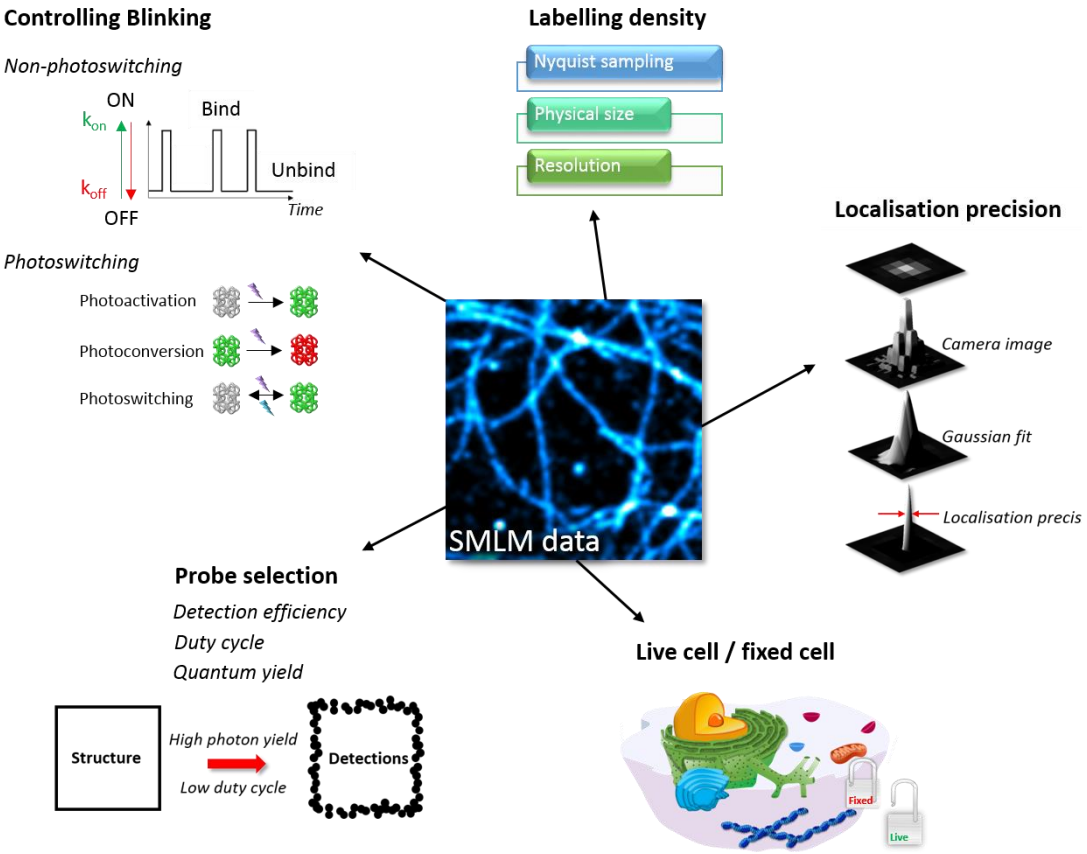

Figure 26: Summation of challenges and factors contributing to high fidelity SMLM data. A delicate balance lies within sampling the underlying structure with a high degree of accuracy, preserving its native state and imaging at the resolution scale appropriate for the biological system.

2.5.3 Data analysis for SMLM methods

Despite the numerous methodologies employed to achieve the temporal separation of PSFs, the nature of the data produced through SMLM is shared: a spatial point pattern (SPP). SMLM relies upon heavy post-processing of raw images, to reconstruct the full population of detected fluorophores, perhaps its major disadvantage.

2.5.3.1 Image reconstruction of SMLM data

Each raw SMLM image frame consists of multiple PSFs, whose position must be estimated to provide a localised spatial coordinate map. Various localisation algorithms exist to this end, a common method is the ImageJ plug-in ThunderSTORM (Ovesný et al., 2014). In the context of this Thesis, all SMLM image reconstruction was performed using ThunderSTORM due to its high performance (Sage et al., 2015).

Pre-processing can be firstly performed to enhance features within the image, such as low pass filtering. The approximate position of molecules is next estimated, typically through local maxima in intensity values within a connected 8 neighbouring pixel range. For local maxima, the sub-pixel localised values are calculated by fitting of PSF models to the intensity distributions of point sources; though either a weighted-least squares method or maximum likelihood estimation. Extracting the central position of the fitted Gaussian enables an accurate estimation of the nanoscale localisation of a single point source, and its standard deviation provides information pertaining to the uncertainty in localisation. Specifically, the localisation uncertainty can be estimated via the Thompson formula:

$$\langle \Delta x^2 \rangle = \frac{s^2 + \frac{a^2}{12}}{N} + \frac{8\pi s^4 b^2}{a^2 N^2} \quad 6$$

In which N is the number of photons per point source, a is the pixel size of the detector, the term $a^2/12$ is the variance of the top hat distribution of a, b is the background noise and s is the standard deviation of the PSF (Thompson et al., 2002). Whilst in theory the distribution should be fit to an Airy disk for the PSF, a Gaussian function is mathematically more tractable and has been shown to exhibit minor deviations from the Airy distribution. Processing the entire image sequence results in a map of molecular co-ordinates, each with a unique localisation uncertainty, from which a super-resolved image can be constructed. Ultimately the super-resolved data resides within the SPP, and thus images are provided purely for visualisation purposes. ThunderSTORM further enables the fitting of up to five overlapping PSFs, retaining accuracy (Holden et al., 2011, Huang et al., 2011).

Various post-processing stages are typically implemented to achieve high quality reconstructions. ThunderSTORM offers various built-in modules, for example filtration on the basis of poor localisation precision, merging of molecules that appear within a given number of sequential frames to palliate the multiple blinking issue (Annibale et al., 2011b, Annibale et al., 2011a) and correction for lateral drift experienced during acquisition.

2.5.4 Quantitative tools for the study of SPPs generated via SMLM

Owing to the statistical nature of the data produced via SMLM, new challenges have been faced in terms of analysis. Whilst conventional microscopy produces pixelated images representing the intensity distribution of the array of sampled fluorophores, SMLM methods produce SPPs. As such, the analysis of such data requires a switch from traditional image processing to point pattern analyses.

The field of SPP analysis is diverse, yet whilst various methods exist for the study of clustered distributions the complimentary analysis of fibrous pointillist structures remains comparatively understudied. Extracting biologically relevant, accurate descriptions of the underlying point process constituting the SPP is indeed a challenge – however existing statistical methods can be readily adapted to suit the study of continuous pointillist structures generated via SMLM. The first quantification tools for the study of SPPs in the context of super resolution microscopy were inspired by Ripley's K-function methodology (Ripley, 1977). The use of the K-function for spatial descriptive statistics however predates super resolution commercialisation, having been initially used in the field of ecology (Haase, 1995) and more recently applied to electron micrograph studies (Hess et al., 2005, Prior et al., 2003). The K-function measures the spatial association between point co-ordinates i and j in a given SPP by drawing a series of concentric circles (2D, spheres 3D) centred on each point, and counting the number of neighbouring points extended at a distance d less than that of the radius r of the encompassing circle (Figure 27). Mathematically, the K-function is expressed:

$$K(r) = \frac{A}{n^2}\sum_{i=1}^{n}\sum_{j=1,i\neq j}^{n}\delta_{ij} \qquad 7$$

$$\delta_{ij} = 1 \; for \; d < r \, , \qquad else \; \delta_{ij} = 0$$

Where n is the number of points within the area of interest A. Ripley's K-function offers the advantage of characterising the dominance of a point process over a vast range of distances; a crucial feature for the study of single molecules to whole cells. The linearized version of the K-function, termed the L-function, is typically reported for ease of comparison across multiple length scales and a normalised version termed the H-function can be easily computed:

$$L(r) = \sqrt{\frac{K(r)}{\pi}} \qquad 8$$

$$H(r) = L(r) - r \qquad 9$$

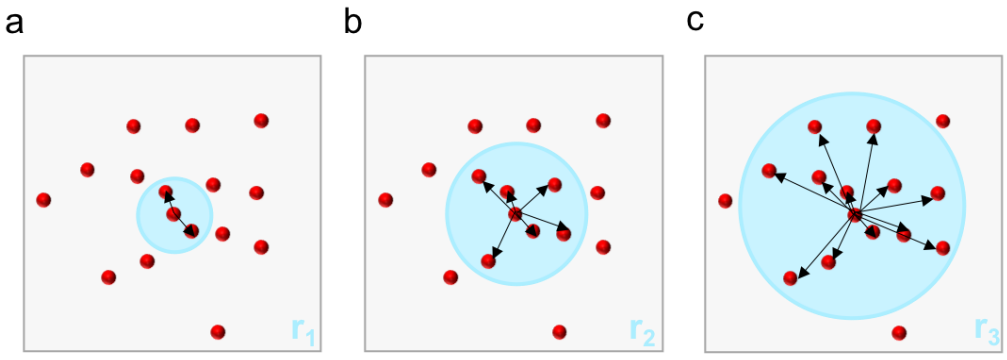

Figure 27: Ripley's K-function methodology. A series of concentric circles of radii r_1 to r_n (a-c) are drawn, centred on the localisation of interest i. Euclidean distances from the i^{th} point to every other point are calculated, and those which satisfy d < r contribute to the K(r) function.

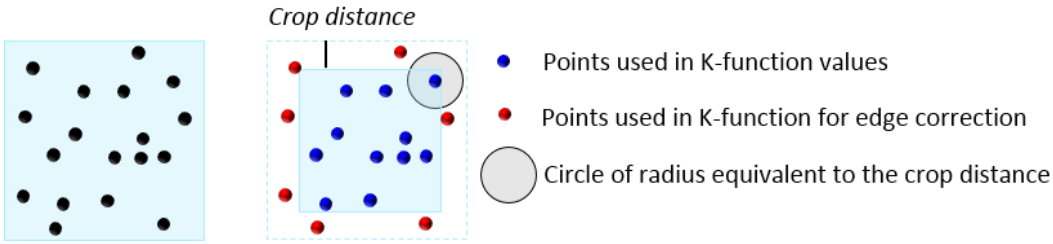

Figure 28: Principle of reducing the analysis area for edge correction. The analysis region is reduced by a crop distance equivalent to the largest radius used in the calculation of the K-function, to ensure that the circle never encounters a ROI boundary. The K-function will not be calculated for points existing outside of the crop distance band, rather, these points will be considered for the calculation of the K-function in the analysis region (depicted blue).

For completely spatially random (CSR) SPPs, the expectation value of the K-function is equivalent to the area of the encompassing circle and therefore the expectation value of the linearized L-function is simply the radius r (Ripley, 1979). As such, the L-function scales with the radius, rather than the area. Edge effects must be accounted for to eliminate erroneous K-function estimates, which occur when the search area encounters a ROI boundary. The simplest edge correction method is to crop the ROI to a smaller region post-analysis, for which K-values are correctly assessed (Figure 28). Comparing the K-function output to that expected for an equivalent randomly distributed data set provides an indication of the scale of dispersion, clustering or indeed spatial randomness, depicted in Figure 29.

A similar approach to Ripley's K-function is pair correlation (PC) analysis, which has been applied to SMLM data sets (Sengupta et al., 2013). PC is related to the K-function in the sense that rather than circles, tori are used to

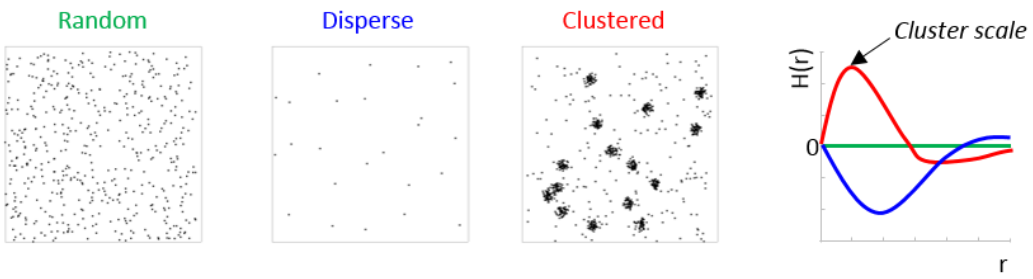

Figure 29: H-function methodology. For an input SPP, the H-function is calculated across a supplied radial range. The linearized and normalised versions are often easier to interpret graphically, since for CSR, L(r)=r for all r, and H(r)=0 (depicted green). Thus, for a disperse or clustered SPP (depicted blue and red respectively) one can compare H-function curves to the CSR reference.

determine local densities. This strategy was applied to SMLM data to attempt to account for the effects of overcounting arising from multiple blinking for example, as the magnitude of the apparent clustering does not depend on the number of times an average molecule is counted.

The K-function provides a robust overview of the global properties of the SPP data is computationally fast and is statistically principled. The method has inspired many cluster analysis methods, particularly in SMLM data (Owen et al., 2010, Williamson et al., 2011), although the K-function alone cannot provide a full description of the clustering on a cluster per cluster basis. Methods that can extract the full clustering behaviour of SPPs such as DBSCAN (Ester et al., 1996) and Bayesian cluster analysis (Rubin-Delanchy et al., 2015) were thus developed. Whilst DBSCAN is highly effective in identifying highly dense clusters from sparsely populated clusters for example, is computationally fast and requires no *a priori* knowledge, the method however relies upon user definable parameters. The Bayesian

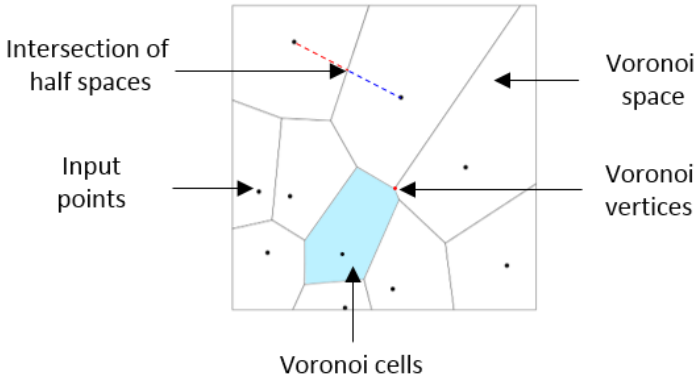

Figure 30: Components of a Voronoi diagram. The Voronoi diagram becomes more complex as the number of unique points increases.

framework however, relies upon a fully generative model for a clustered SPP. The authors use the Ripley's K-function to analyse the clustered SPPs, varying the radius R over which the K-function is calculated, and the threshold T at which molecules are assigned to clusters. The quality of the cluster assignments is then compared to its posterior probability, to determine the best combination of R-T for each SPP. Whilst this method is thus free of user definable parameters, its major drawback is the computational time required to generate the many analysed combinations of R–T.

Geometrical approaches to assess the local density of points within SPPs have recently been proposed, a notable method being Voronoi tessellation (Okabe et al., 2000)(Figure 30). When constructing a Voronoi tessellation, points are segmented according to their spatial organisation alone, without the need for radial or toroidal based scanning. This feature is particularly suited to SPPs that do not consist of circular clusters of points, as topological bias is reduced when assessing local density with respect to the K-function. Moreover, the use of Voronoi tessellation as a density parameter is robust to sparse, non-uniform or extremely dense data (Levet et al., 2015, Andronov et

al., 2016). Briefly, a Voronoi tessellation involves the partitioning of the Euclidean plane into Voronoi cells or polygons, based upon the location of the points supplied. In the simplest case, for two distinct points (seeds) in the plane the Voronoi construction involves drawing their perpendicular bisector such that two Voronoi cells are formed. Generally, the Voronoi construction is formed through the intersection of half-spaces for all points, and is thus a convex polygon (Okabe et al., 2000). Voronoi segmentation has been previously applied to SMLM data (Levet et al., 2015), and more recently for co-localisation studies (Andronov et al., 2016), however this approach is currently understudied in the context of fibrous SPP analysis. Information can be extracted via the Voronoi construction, for example, the area of each Voronoi cell is inherently related to the local density. Further, by analysing neighbouring cells, a scale over which each point is clustered can be estimated. The Voronoi approach offers rapid multi-scale segmentation and classification within each ROI and has been shown to be a powerful tool for the study of non-uniform clusters of points. However, to obtain a full description of the underlying point process, user-definable parameters must be applied, as with the K-function. Nonetheless, tessellation is computationally fast, has a strong theoretical underpinning and does not introduce radial/circular bias in density measurements.

Despite finding use in the analysis of clustered SPPs generated via SMLM, the Voronoi approach is arguably more suited to fibrous, non-uniform structures (Figure 31) and will serve as a basis for fibre identification in the upcoming Chapters. Fibrous structures generated via SMLM are near ubiquitous in the field, and yet analysis tools dedicated to such data remain understudied. Indeed, the field of conventional microscopy image analysis is mature, several algorithms exist to date for the study of pixelated fibrous

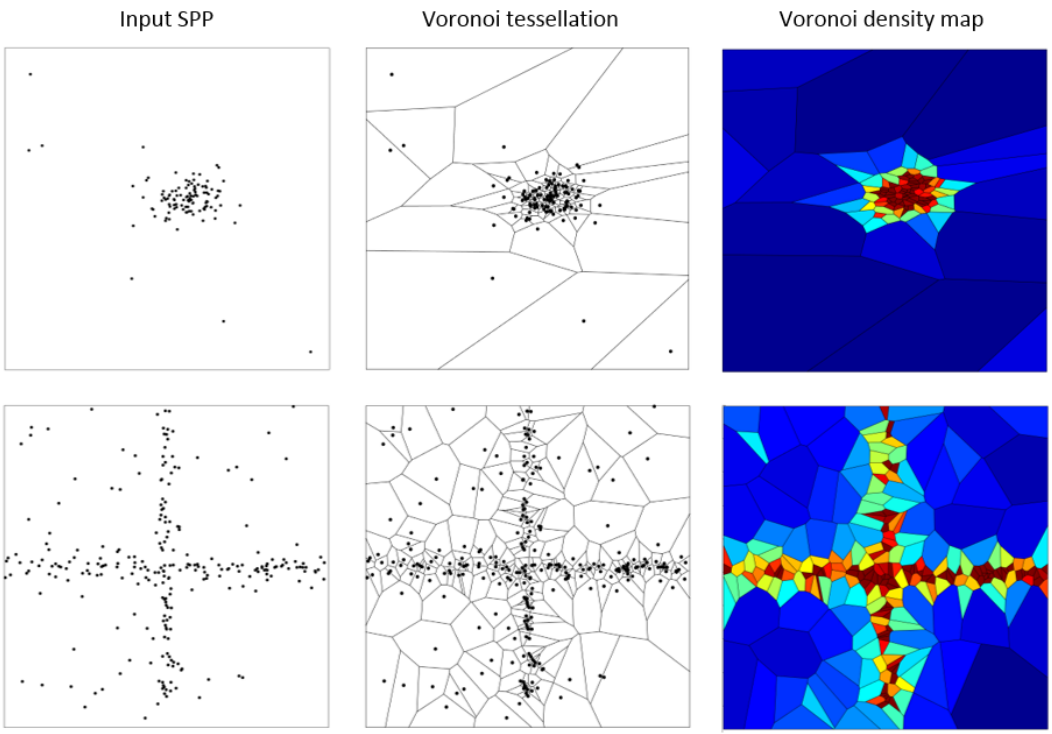

Figure 31: Voronoi tessellation applied to either clustered (top) or fibrous (bottom) data. The Voronoi density map can be calculated from the tessellation, in which the Voronoi cells are pseudo coloured according to their area. The densest regions are depicted red, often indicative of clustered or fibrous points. This map can then be used to produce a binary map, in which only those Voronoi cells (and their corresponding seeds) with an area greater than a pre-defined threshold remain.

structures (Boudaoud et al., 2014, Alioscha-Perez et al., 2016, Eltzner et al., 2015, Herberich et al., 2010, Elosegui-Artola et al., 2014). Most methods report pre-processing stages to remove blurring and feature enhancement filters, then directionality enhancements from which the fibres are segmented (binarized) and individual fibres extracted. Various descriptors can be extracted from the fibrous traces, such as the location, directionality, length and estimated width enabling both a global and local analysis. Most methods are semi-automated and rely upon a plethora of user-definable parameters and are prone to producing false positives if the image is blurred, inhomogeneous in brightness/contrast, has proximal parallel fibres and if the

background noise is high. Indeed, the analysis of fibrous SPPs shares similar problems, compounded by labelling density and localisation uncertainty.

Previous studies have reported on the directionality of SPPs, in the context of co-localisation studies. Nieuwenhuizen et al. extract the orientational information termed I (x, ϕ) from pixelated SMLM data, directly interpretable as the expected density of localisations in one image channel at a position x belonging to filaments of orientations φ (Nieuwenhuizen et al., 2015). The authors employ a cross correlation method to determine the co-orientation of two channel fibrous data. This involves a series of convolutions with orientation selective filters, to first provide the orientational space, from which the co-orientation plot can be determined via cross correlation. The method faces the same issues as those for conventional microscopy: blurring, noise, auto fluorescence and cross-talk between image channels. Moreover, the density of filaments, the microscope PSF and localisation error are shown to affect co-orientation significance. Whilst this method is a useful tool for the study of biological co-orientation, it does not attempt to provide information on the individual fibrous networks.

Investigating the orientational order of biological networks has also attracted attention from an instrumentation standpoint. Valades Cruz et al. employed polarized super resolution detection to quantify the molecular localisation and orientation of DNA, microtubules and actin filaments (Valades Cruz et al., 2016). Using the signals acquired through polarisation microscopy, the extent of the fluorescent tag orientational translation/rotation and the local disorder of its target can be elucidated. The method can report the localisation of single molecules and simultaneously assess the local heterogeneity in structures, providing the averaged fluorophore orientation

and the angular aperture of each pixel. Again, whilst this method is an important advance for the study of structural order in biomolecular assemblies, no attempt is made to reconstruct the fibrous SPPs generated.

Tracing of SMLM fibrous structures has been demonstrated, albeit at the cost of sacrificing the pointillist nature of the data, that is, by rendering the SPP as an image and performing conventional image analysis (Zhang et al., 2017). Zhang et al. developed a computational tool for the study of microtubule networks imaged via SMLM. The method termed SIFNE, is similar to that of previous conventional microscopy image analysis methods; the authors begin by feature enhancement of the rendered image, and then produce a binary map of filaments from which individual fibres are extracted. Individual identification numbers are assigned to fibres at intersection points, constrained by angle and radius parameters suitable to microtubules. The authors acknowledge several limitations and challenges faced when performing filament tracing. For example, for dense networks and highly curved structures manual intervention is required. Further, their imposed constraints do not account for fibre branching. Since the SIFNE method is essentially a conventional image processing algorithm, the authors warn of the issue of inhomogeneity in illumination intensity across the ROI, owing to the gaussian beam excitation profile. The authors state that the uneven background levels and the inhomogeneous fluorescence often encountered with SMLM greatly affects the analysis, and as a result, the analysis of complex networks such as the actin cytoskeleton is currently unachievable. The authors further state that for smaller filaments such as F-actin, which are often extremely dense, fluorophore photophysics and instrumentation should be improved to assist in the complimentary analysis.

Directly analysing the pointillist data is an important advance. With numerous options available for the rendering of SMLM SPP data, and no clear consensus on the best approach, pixilation induces variability on the derived image (Baddeley et al., 2010). This variability makes the comparison of tracing algorithms that use pixelated data as input problematic as they are likely to perform differently with pixelated images of differing statistical compositions and constructions.

2.6 Conclusions and outlook

This Chapter highlights the various approaches used to achieve super resolution images of biological samples, with an emphasis on SMLM techniques. A prevalent theme within the field is the need for complimentary analysis tools for SMLM data. Whilst technological advances are indeed the powerhouse of SMLM, due importance must be placed upon the data itself. Super resolution images are in fact statistical entities rather than pixelated images in the true sense of the word and must be treated as such to elucidate biological insight on the nanoscale. Importantly, owing to the diversity and multidisciplinary nature of the SMLM field, many topics remain understudied. As such, the remainder of this Thesis is dedicated to the development of novel data analysis methods for the study of filamentous structures by SMLM. Specifically, the developed methods will be used to interrogate the nanoscale organisation of the actin cytoskeleton at the T cell immunological synapse, whose structure and function is vital for orchestrating the immune response.

Chapter 3 On the use of Ripley's K-function to quantify fibrous spatial point patterns

Following results and figures adapted from published work:

Peters, R. et al. *Quantification of fibrous spatial point patterns from single-molecule localization microscopy (SMLM) data*. Bioinformatics 33, 1703-1711 (2017).

Peters, R and Owen, D. M. *On the use of Ripley's K-function to quantify fibrous spatial point patterns.* Microscopy & Analysis, Life Sciences Supplement September/October (2017).

3.1 Introduction

Unlike conventional microscopy which produces pixelated images, SMLM produces data in the form of a SPP. As such, a new set of challenges are posed in terms of data analysis. Often, such SPPs are analysed using cluster analysis algorithms to quantify molecular clustering within, for example, the plasma membrane. While SMLM cluster analysis is now well developed, techniques

for analysing fibrous structures in SPPs remain poorly explored. Inspired by localised Ripley's K-function, routinely used in the cluster analysis field, an analogous statistical methodology for fibrous SPP analysis has been developed. In this Chapter, using simulated data, the underlying theory to describe fibrous spatial and angular arrangements and how these descriptors can be quantitatively derived from such pointillist data sets will be demonstrated. Using experimental data acquired via the IRIS and dSTORM approach to SMLM, the 2D distribution of the actin cytoskeleton at the mature immunological synapse will be analysed, by use of Ripley's K-function and the novel modification, termed the Angular K-function, thereof.

3.2 A novel modification of Ripley's K-function

Ripley's K-function was first applied to SMLM datasets in 2010, providing a quantitative study into the distribution of surface bound proteins in the HeLa cell line (Owen et al., 2010). The K-function strategy has also been implemented in full clustering algorithms, for example generating density estimations for a Bayesian cluster analysis framework. The K-function, as previously described, relies upon a series of circular (in the case of 2D data) regions to determine the local density of points over a specified spatial range. The method is intrinsically suited to a clustered distribution of molecules in which there is on average, no angular relationship between localisations. By implementing a variant of Ripley's K-function based upon angular dispersion, one can extract analogous information regarding a fibrous distribution of molecules. This involves computing the K (r = 200 nm)-function within specific angular intervals, relative to a reference vector ⟨0,1⟩ for each point in the fibrous SPP. The Angular K-function is therefore mathematically comparable to the K-function but incorporates a correction term for the differing angular

regions in which localisations are detected. Mathematically, the Angular K-function is expressed:

$$K = \frac{360}{\alpha}\frac{A}{n^2}\sum_{i=1}^{n}\sum_{j=1,\ i\neq j}^{n}\delta_{ij} \qquad 10$$

Where δ_{ij} is unity if the Euclidean distance of the i^{th} and j^{th} events is less than radius r and lies within the given angular range specified by α, and n is the number of events in area A, for $i \neq j$. The border cropping method described in Section 2.4.4 will be used for edge correction. The Angular K-function (and the normalised Angular H-function) method simply exploits the preferential directionality of certain localisations; a fibrous feature.

3.3 Results on simulated SPP data

To test the methods capability of discerning fibrous characteristics in diverse SPPs, numerous simulations were performed.

3.3.1 CSR SPPs

The method was initially validated against SPPs consisting of CSR points, for which the expectation value of the H(r)-function is known. For this, points are drawn from a uniform distribution, defined between the ROI edges. For CSR distributed SPPs, $\langle K(r)=\pi r^2 \rangle$, $\langle L(r)=r \rangle$ and $\langle H(r)=0 \rangle$ for all radii r. A representative example (n=50 simulations) of a CSR distribution of points and the resultant H(r)- and H(α)-function analysis is presented in Figure 32. The power spectral density of a physical process encompasses fundamental

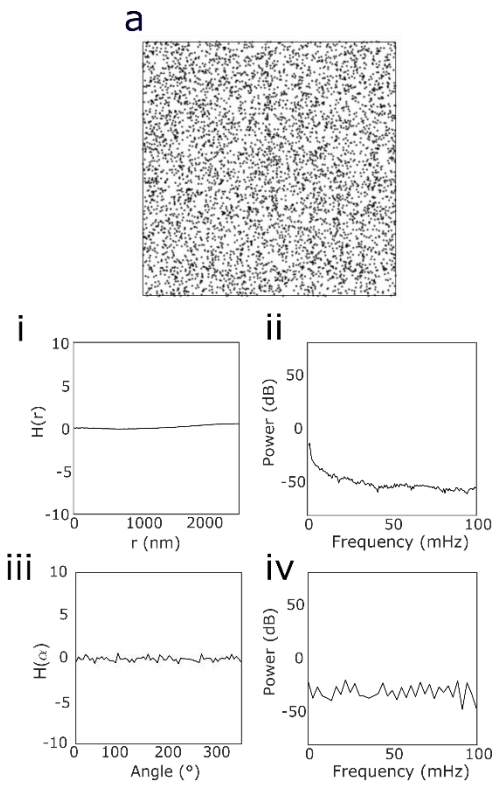

Figure 32: Ripley's H(r)- and H(α)-function analysis of a CSR distributed set of points. An example of a CSR distributed SPP (a) and resultant H(r)-function analysis (i) and power spectrum (ii), averaged from n=50 simulations. H(α)-function analysis (iii) and its power spectrum (iv) were also computed to ascertain angular information in the SPP.

information pertaining to the H(r)- and H(α)-function. By traversing to the frequency domain, one can estimate the distribution of the signal power to obtain an understanding of its statistical characteristics. Note that the power is calculated by the square of the amplitude of the Fourier transform. As expected, H(r) and its power spectrum (Figure 32i-ii respectively) demonstrate a lack of spatial regularity and for all radii H(r)=0 on average. The H(α)-function demonstrates a lack of angular features in the SPP, as expected for a random distribution of points (Figure 32iii-iv).

3.3.2 Clustered SPPs

To highlight the suitability of the method for pointillist fibre analysis compared to the conventional H-function, simulated data sets of clustered rather than fibrous SPPs were generated of pre-defined clustering characteristics. The simulated ROI consists a set of discrete localisations, of which 50% are assigned to one of 15 clusters and the remainder assigned to the background, thereby producing a pointillist map of co-ordinates. More precisely, central positions of clusters are randomly generated across a square ROI, from which associated clustered co-ordinates are drawn from a normal distribution with a standard deviation of 50 nm. The SPP is then subjected to a CSR distribution of background localisations, to reflect an assemblage of un-clustered molecules. All co-ordinates are then disturbed by Gaussian noise, the mean and variance of which was determined by a gamma distribution with shape, k, and scale, θ, parameters to simulate a maximum of 15 nm localisation uncertainty (Figure 33a). These parameters were chosen to reflect the data achievable with the IRIS approach to SMLM, for the study of fibrous SPPs.

The resultant H(r)- and H(α)-functions (Figure 33i, iii respectively) provide a description of the underlying spatial point process. Spatial clustering at all distances is statistically significant. The H(r)-function exhibits a maximum at ~70 nm (Figure 33ii). A careful interpretation must be applied to this maximum: 70 nm is not the cluster radii, rather, the distance over which the data is most clustered. This estimation accounts for all points within the ROI, such as background noise and an average over all ROIs is presented. Further, Ripley's K-function does not consider the localisation uncertainties of individual molecules. Computing the H(α)-function and the shift corrected analogue (Figure 33iii-iv respectively) indicates that the underlying process

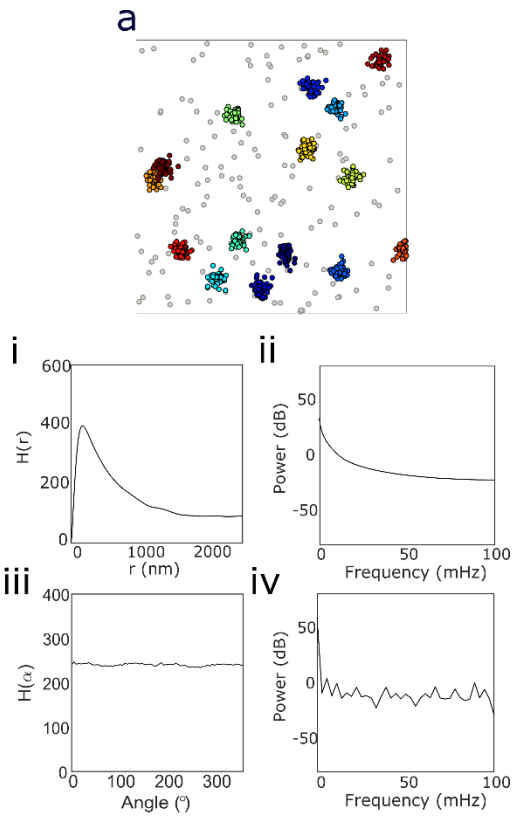

Figure 33: H(r) and H(α) analysis of a clustered SPP. A representative (n = 50 simulations) cluster map (a), in which input clusters are pseudo coloured, and resultant conventional H(r)-function analysis (i) and power spectrum (ii) is presented. H(α)-function analysis (iii) and its power spectrum (iv) were also computed to ascertain angular information in the SPP.

generating the SPP is not of a fibrous nature. There is no preferential directionality between localisations, evidenced by the lack of maxima in H(α) and its power spectrum (Figure 33iv).

3.3.3 Regular, perpendicular, fibrous SPPs

The method was next validated on various fibrous SPPs, classified as either regular, random or bundled. Firstly, the case of a regular, perpendicular arrangement of fibrous structures is considered. For this, an equal number of horizontal and vertical fibres were simulated, orthogonal to one another and to their axis of intersection (Figure 34a-c). Events were attributed to each fibre at a regular spacing of 15 nm, which were then subject to a random perturbation in cartesian space of up to a maximum 15 nm displacement, to simulate localisation uncertainty. A CSR distribution of events, contributing to 30% of the total number of fibrous localisations, was then applied to the fibrous SPP. Such a simulation is referred to as the standard condition henceforth.

Several inter-fibre spacings were examined using both conventional and H(α)-function analysis (Figure 34a-c) and a total of n=50 simulations were computed for robust statistics. A limited description of the underlying fibrous SPP can be recovered through the H(r)-function, in which the minimum depicts the radius at which the events are most disperse, i.e. the inter-fibre spacing, and its periodicity demonstrates spatial regularity. This periodicity in H(r) can be quantified by the power spectral density of the point process, displayed in the frequency domain. The time-period is inherently related to the occurrence of fibres within the SPP: the time-period of the power spectrum is the inverse of the inter-fibre spacing. For example, in the case of fibres regularly arranged at intervals of 1250 nm (Figure 34a), the power spectrum (Figure 34aii) exhibits a time-period of 0.8 mHz corresponding to the input inter-fibre distance.

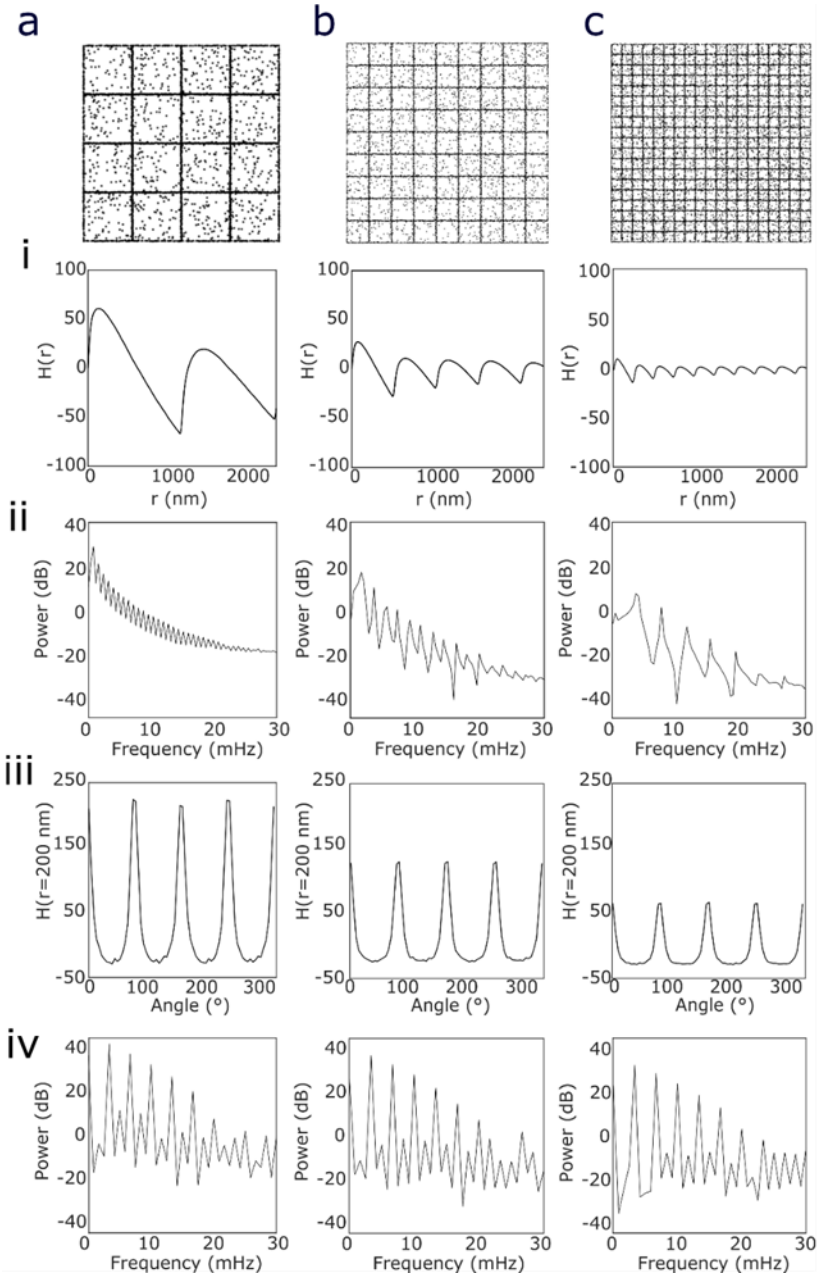

Figure 34: Ripley's H(r)- and H(α)-function analyses of regular, orthogonal fibrous point patterns of various simulated inter-fibre spacings (1250 nm 555 nm and 260 nm a - c respectively). Three representative input data sets (a - c) from n=50 simulations, from which Ripley's H-function was calculated (i) and concomitant power spectra (ii). Ripley's H(α)-function curves (iii) and their spectra (iv) were also computed for each condition.

Further information can however be extracted through use of the H(α)-function. For the regular, perpendicular SPPs, one would expect maxima in H(α) at intervals of 90° with respect to ⟨0,1⟩. Despite localisation uncertainty, background noise and various intersections, the method accurately evaluates the angular regularity of the SPP, for various inter-fibre spacings (Figure 34iii-iv.).

3.3.4 Spatially random, perpendicular, fibrous SPPs

To examine the specific effect of irregularity in inter-fibre spacings, simulations of spatially random perpendicular fibres were performed. In this case, the random positioning of each fibre, per axis, is defined by a 1D CSR distribution. An equal number of fibres per axis was simulated. All other simulation parameters remain per the standard condition. A representative example (from n=50 simulations) of such an arrangement is presented in Figure 35a. This specific case in which there is irregularity in the spatial component, whist preserving the regularity in the angular component of the fibrous SPP, clearly demonstrates the power of the H(α)-function analysis. Computing the H(r)-function and its power spectrum (Figure 35ai-ii) reveals the lack of regularity in the spatial arrangement of the fibres, evidenced by the lack of periodicity in the frequency domain for all arrangements. Thus, the conventional H(r)-function provides a method for distinguishing between spatially regular and randomly arranged fibres within a SPP. Further information however is obtained through H(α)-function analysis. Similarly to the previous case (Figure 34-iv), H(α) reveals that the fibres are orthogonal to one another and to their axis of intersection (Figure 35iii-iv).

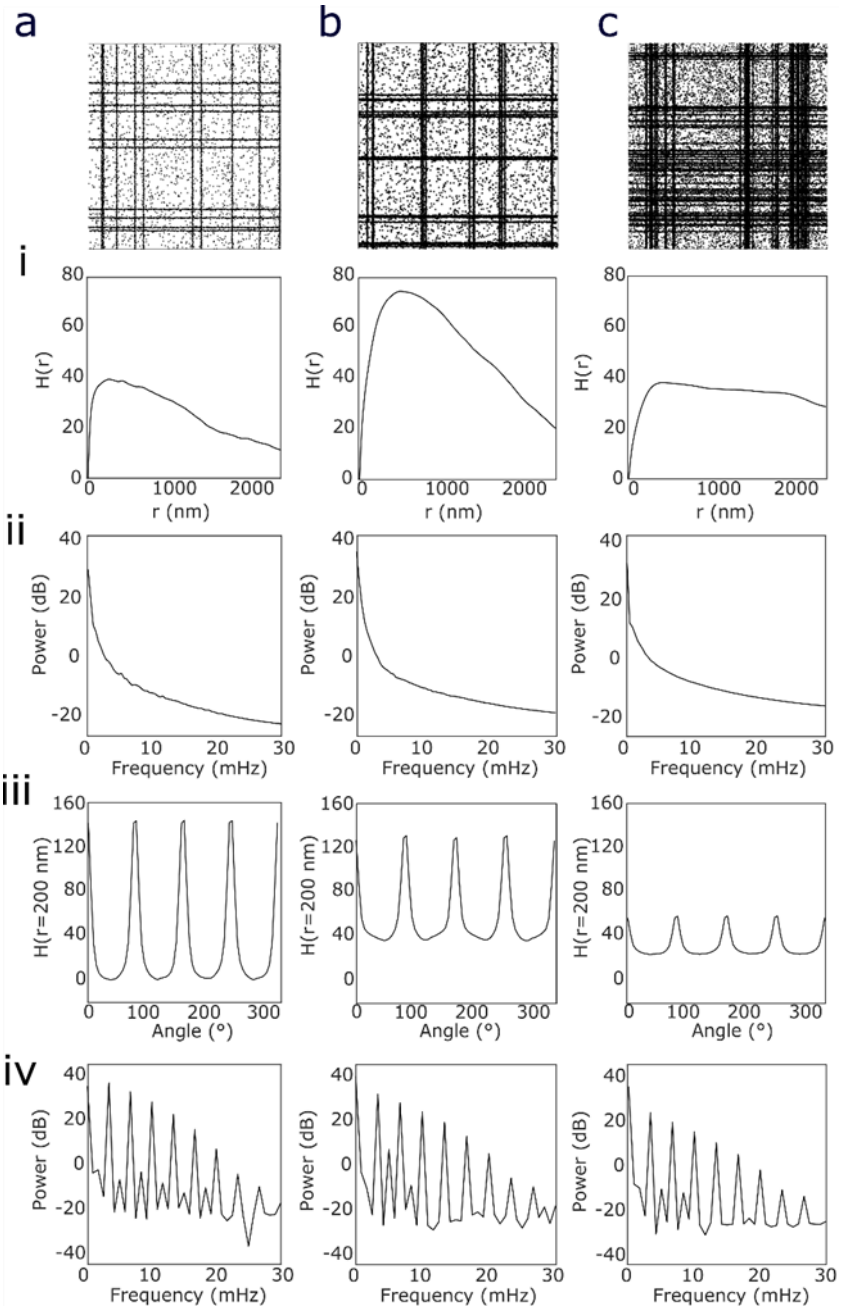

Figure 35: Ripley's H(r)- and H(α)-function analysis of fibrous SPP of varying bundling properties. Representative examples of randomly generated orthogonal fibres (a), low-bundling fibrous SPPs (b), and a highly bundled fibrous SPPs (c). Ripley's H-function was calculated (i) and their associated power spectra (ii). Ripley's H(α)-function curves (iii) and their spectra (iv) were also computed for each condition, from n=50 simulations.

The final case of interest for linear, perpendicular fibres is those that form bundles. The bundled fibrous SPP is constructed by first defining the number of bundles per axis (5 per axis in Figure 35b and 10 per axis in Figure 35c) and the number of fibres assigned to form each bundle. The bundling behaviour of F-actin, has been reported to play an important role in multifarious cellular processes. Therefore, to obtain a quantitative knowledge regarding such behaviour could be of interest across diverse biological systems. The fibre bundles are initiated by drawing a random coordinate, the seed, from a 1D CSR distribution. The seed coordinate is referred to as the bundle centre. For individual fibres assigned to each bundle (3 fibres per bundle in Figure 35b. and 5 per bundle in Figure 35c), a random initial coordinate is generated from a normal distribution with mean parameter μ (the bundle centre) and standard deviation σ (the bundle width, typically σ=100 nm). All other parameters were generated per the standard condition, for n=50 simulations. In the case of low bundling (Figure 35b), the conventional H(r)-function maximum is increased (Figure 35bi.), compared to that of the singular fibre case (Figure 35ai) demonstrating an increased clustering of points. As the bundle density increases (Figure 35c) however, the H(r)-function maximum decreases in magnitude and it becomes broader (Figure 35ci), since the ROI becomes more fibre abundant. By performing H(α)-function analysis (Figure 35iii.), the perpendicular nature of the fibrous bundles is evidenced by the periodicity in their associated power spectra (Figure 35iv).

The effect of increased bundle widths was also examined, using both H(r)- and H(α)-analysis. An example of the standard low bundling case is shown in Figure 36b for ease of comparison. Firstly, the simulated bundle widths were reduced to 50 nm, a representative example (from n=50 simulations) is shown in Figure 36a. As the bundle width increases, the H(r)-function curves present

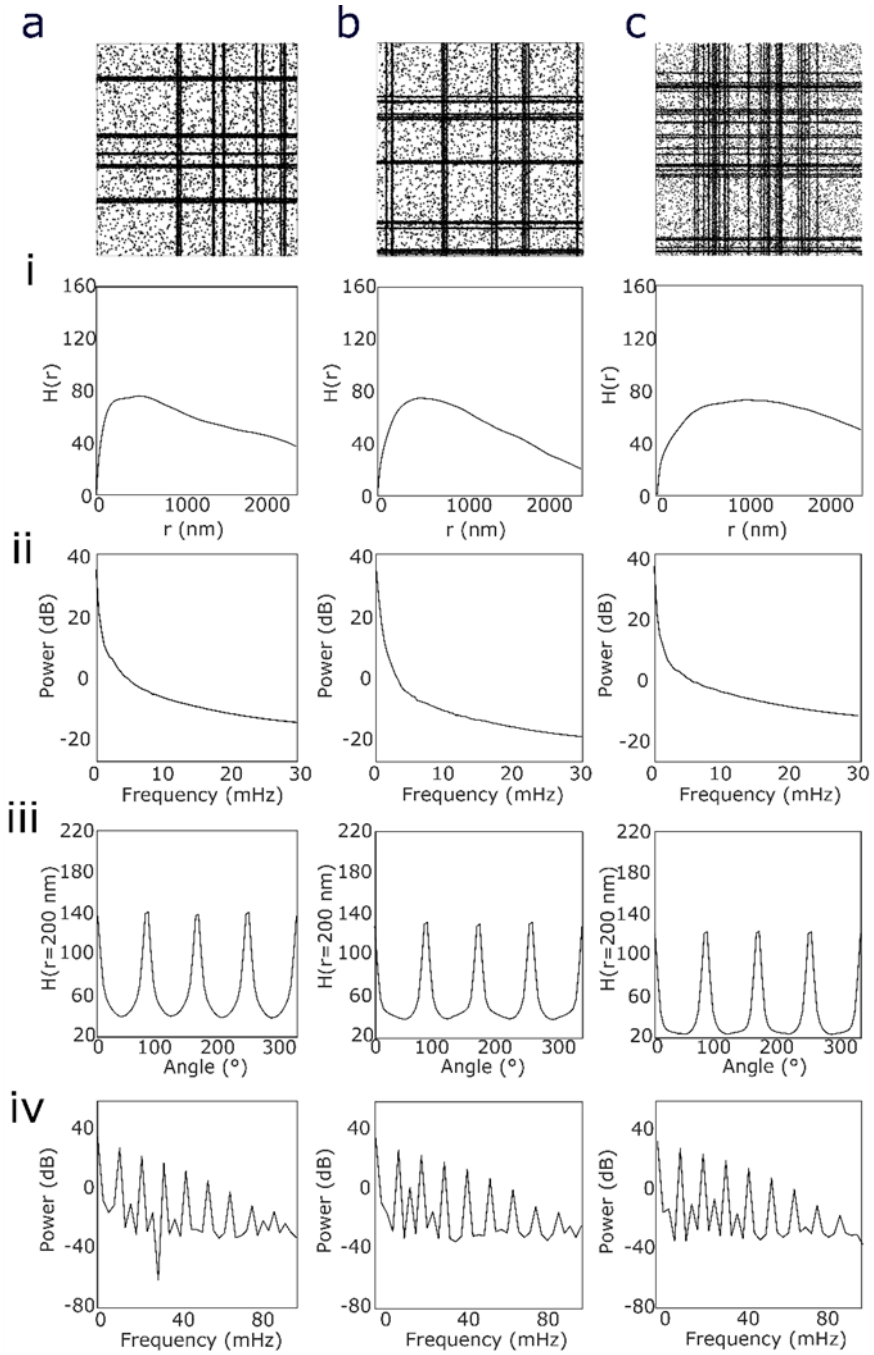

Figure 36: Ripley's H(r)- and H(α)-function analysis of fibrous SPP of varying bundling widths. Representative examples of bundle widths of 50 nm, 100 nm, 250 nm (a - c respectively). Ripley's H-function was calculated (i) and their associated power spectra (ii). Ripley's H(α)-function curves (iii) and their spectra (iv) were also computed for each condition, from n=50 simulations.

a broadening and a shift to higher radii, evidence of the increased distance over which that data demonstrates the most clustered behaviour. The most extreme example of which is in the case of 250 nm fibre bundles (Figure 36c). H(α)-function analysis again demonstrates angular periodicity in the SPP.

3.3.5 Fibrous SPPs consisting of both orientational heterogeneity and curvature

The next level of complexity involves the introduction of multiple directionalities for both linear and curved structures. For this, one must correct for fibre directional heterogeneity with respect to the reference vector as information can be lost in the H(α)-function due to the maxima detected at multiple angles. To correct for this and recover the fibrous information, one can calculate a "shift-corrected H(α)" curve. Shift correction is involves computing the H(α)- function per localisation, extracting the first maximum H(α)'$_{Max}$, and translating all H(α) values by - H(α)'$_{Max}$, such that H(α)'$_{Max}$ has intrinsic start at α=0°. Shift correcting H(α) curves enables a clear discrimination between fibrous and non-fibrous SPPs, since the former are expected to exhibit maxima in shift corrected H(α) with a period of ~180° (Figure 37a).

Consider first the case of linear fibres exhibiting random directionalities. This condition is achieved through generating two seed (x, y) coordinates from a uniform distribution, within the square ROI, for each fibre. Each fibre is constructed per the standard condition and is placed to intersect both random seeds and is then extrapolated across the ROI. A typical example of

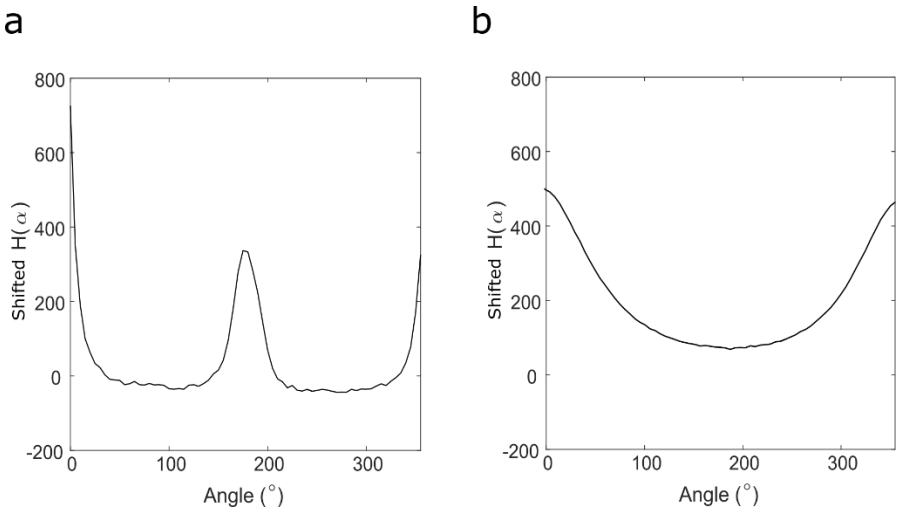

Figure 37: Shift correction reveals a hallmark of fibrous SPPs. For a fibrous SPP input (the standard condition in this case), shift correction produces a single peak in H(α) at 180° whereas for a clustered SPP (data shown in Figure 33a) the shifted curve does not exhibit a maximum at 180°.

such a simulation is presented in Figure 38a (n=50 simulations), in which 15 fibres are randomly generated both spatially and orientationally. As expected, no spatial periodicity is achieved in the conventional H(r)-function (Figure 38ai-ii.), due to the lack of spatial regularity in the SPP. By computing the H(α)-function and its power spectrum (Figure 38iii-iv), the lack of angular periodicity in the SPP also becomes evident, since the fibres are no longer perpendicular to one another and to the axis of intersection. Thus, H(α) is a useful tool to distinguish between angular periodicity and random orientations of fibres within a SPP.

Introducing the aforementioned shift-correction process can however extract more information when analysing SPPs of various fibrous orientations. Briefly, by correcting for the angular disparity between the first maxima in H(α) and the reference vector ⟨0,1⟩, for each point, one can ensure

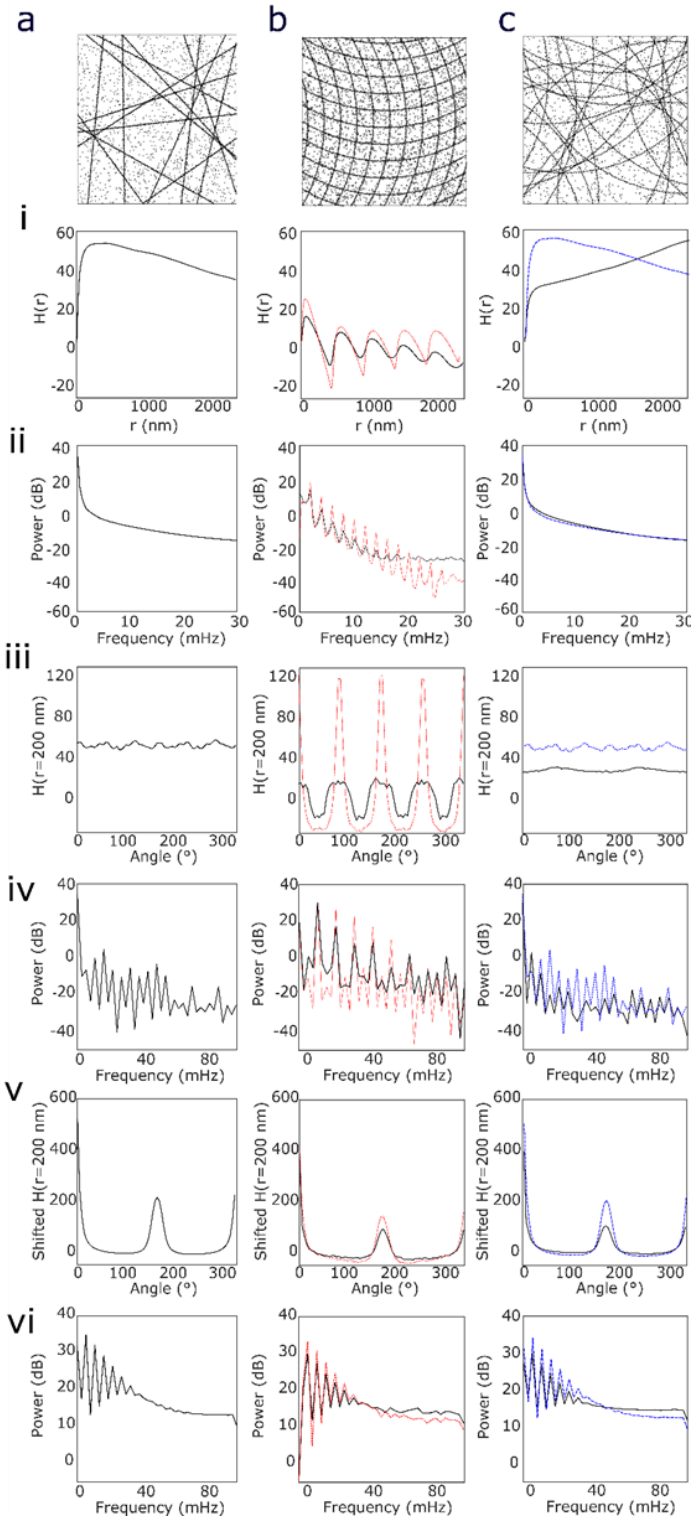

Figure 38: Ripley's H(r)- and H(α)-function analyses of SPPs of various architectures. Representative examples of a spatially and orientationally random, linear SPP (a) and its curved analogue (c) and a regular curved SPP (b). Ripley's H(r)-function (i) and its power spectra (ii) were calculated and H(α)-function analysis (iii) and its power spectra (iv) computed. Shift-corrected H(α) curves (v) and their corresponding power spectra (vi) are also presented from n=50 simulations.

that each H(α) curve has intrinsic start at α=0°. This stage is necessary when averaging multiple H(α)-function curves to assess the global nature of the fibrous SPP. Thus, by implementation of the shift-correction process, regardless of heterogeneity in fibre orientation, one can identify the presence of fibrous structures due to the single characteristic peak at α=180° in the shift-corrected curve. Indeed, for the randomly orientated fibrous structures generated (Figure 38a), a single maximum at α=180° is computed by use of the shift-corrected H(α)-function (Figure 38v-vi).

Fibres of a known curvature and a regular spatial arrangement were next examined, to investigate the methods capability of discerning non-linear structures. A series of horizontal and vertical fibres are generated by constructing counter-clockwise arcs at equally spaced intervals (500 nm) along the x and y axis, across the ROI. The radius of curvature R = 5000 nm, remained constant and all other parameters set per the standard condition. An example of this input SPP is demonstrated in Figure 38b, from n=50 simulations. The spatial regularity, as assessed by Ripley's H(r)-function and its power spectrum (Figure 38bi-ii respectively), remains accurate despite curvature, localisation uncertainty and background noise, in the same way as for linear structures. However, in comparison to its linear counterpart (red dash lines, Figure 38biii.), the height of the H(α)-function curve, defined as the distance from the curve minimum to its maximum, is significantly reduced from 162.40 ± 0.31 nm to 64.46 ± 0.33 nm (S.E.M, n = 50, $P < 0.0001$). This decrease is evidence for the presence of high density points at a greater spread of angular positions; the hallmark for curvature. This behaviour is mirrored in the shift-corrected H(α)-function curves, in which the height of the characteristic peak at α=180° is decreased relative to its linear counterpart ($P < 0.0001$) (Figure 38bv).

In the final case, an assemblage of spatially random curved fibres was considered. For this, the radius of curvature was globally set to R=5000 nm, and two random seed coordinates were generated from a uniform distribution, within the ROI. A clockwise or counter-clockwise arc was selected at random to intersect the seed coordinates for each fibre and extrapolated across the region. Fibres were otherwise constructed per the standard condition (Figure 38c). Analogous to the case of linear fibres of heterogenous orientations, the H(r)-function and its power spectrum (Figure 38ci-ii respectively) revealed a lack of spatial periodicity between the fibres. Similarly, the H(α)-function and its associated spectrum (Figure 38ciii-iv respectively) demonstrate no dominance in fibre orientation. However, the shift-corrected curve (Figure 38cv) exhibits a characteristic maximum at α=180°, the height of which (64.46 ± 0.33 nm) is significantly lower than that of its linear analogue (blue dashed lines, 112.30 ± 0.99 nm, S.E.M, n=50, $P < 0.0001$), indicative of fibre curvature.

3.4 Sensitivity of methodology to simulation parameter variation

To test the sensitivity of the method, simulations involving increased levels of background noise, reduced labelling density of fibres and poor localisation precisions were performed. For this the standard condition data set was examined.

3.4.1 Increased level of non-fibrous localisations

The effect of an increased level of background noise on the H(r)- and H(α)-function analysis was examined. Consider the spatially regular, linear, perpendicular fibrous SPP, an example of which is presented in Figure 39a. This standard condition data set encompasses 30% non-fibrous localisations, and both spatial and angular features of the underlying point process can be distinguished using H(r)- and H(α)-function analysis. Increasing the level of non-fibrous localisations to 60% (Figure 39b) and further to 90% (Figure 39c), and subsequently performing H(r)- and H(α)-function analysis for n=50 simulations, reveals that both analysis methods remain robust to such conditions.

3.4.2 Reduced and inconsistent labelling density

Achieving a high enough labelling density for high-fidelity target reconstruction, in this case the actin cytoskeleton, is one of many factors to consider when performing SMLM data analysis. The choice of fluorescent probe has a significant impact on the labelling density achievable, hence, to validate the methods capability to discern fibrous structures in pointillist data, simulations of a degraded labelling of the fibres were performed, whilst keeping all other simulation parameters per the standard condition. Consider the case of a spatially regular series of orthogonal fibres, in which the labelling density is initially set to 100% (Figure 40a) and then degraded at random to 50% (Figure 40b) and 25% (Figure 40c) of the standard condition. Examples of such a simulation is presented in Figure 40a-c respectively. Despite the decreased number of fibrous points, both H(r)- and H(α)- function methods remain robust to poor labelling density, background noise and localisation uncertainty. The presence of spatially regular fibres is evidenced through

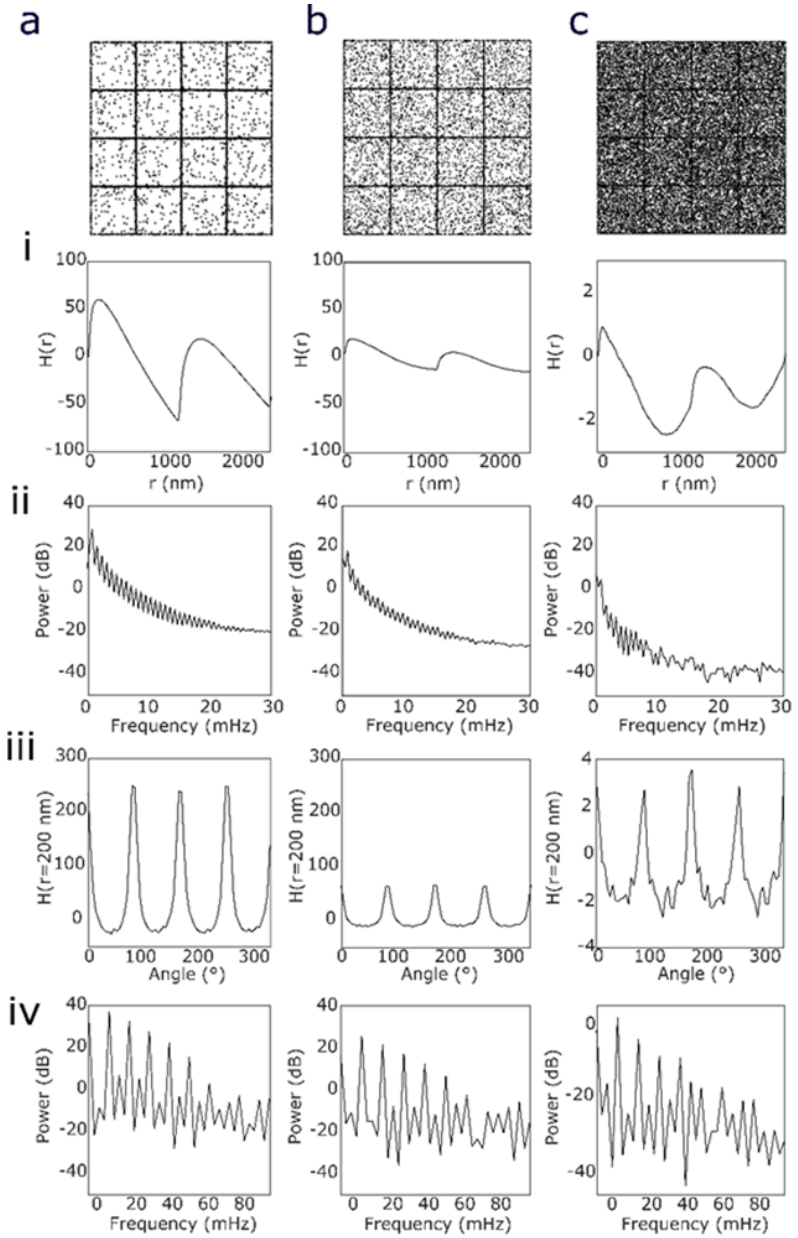

Figure 39: The effect of an increased percentage of non-fibrous localisations on the H(r)- and H(α)-function analysis. Representative examples (n=50 simulations) of 30%, 60% and 90% of localisations assigned to the background (a-c respectively). H(r)-function analysis (i) and corresponding power spectra (ii), H(α)-function analysis (iii) and its power spectra (iv) were computed.

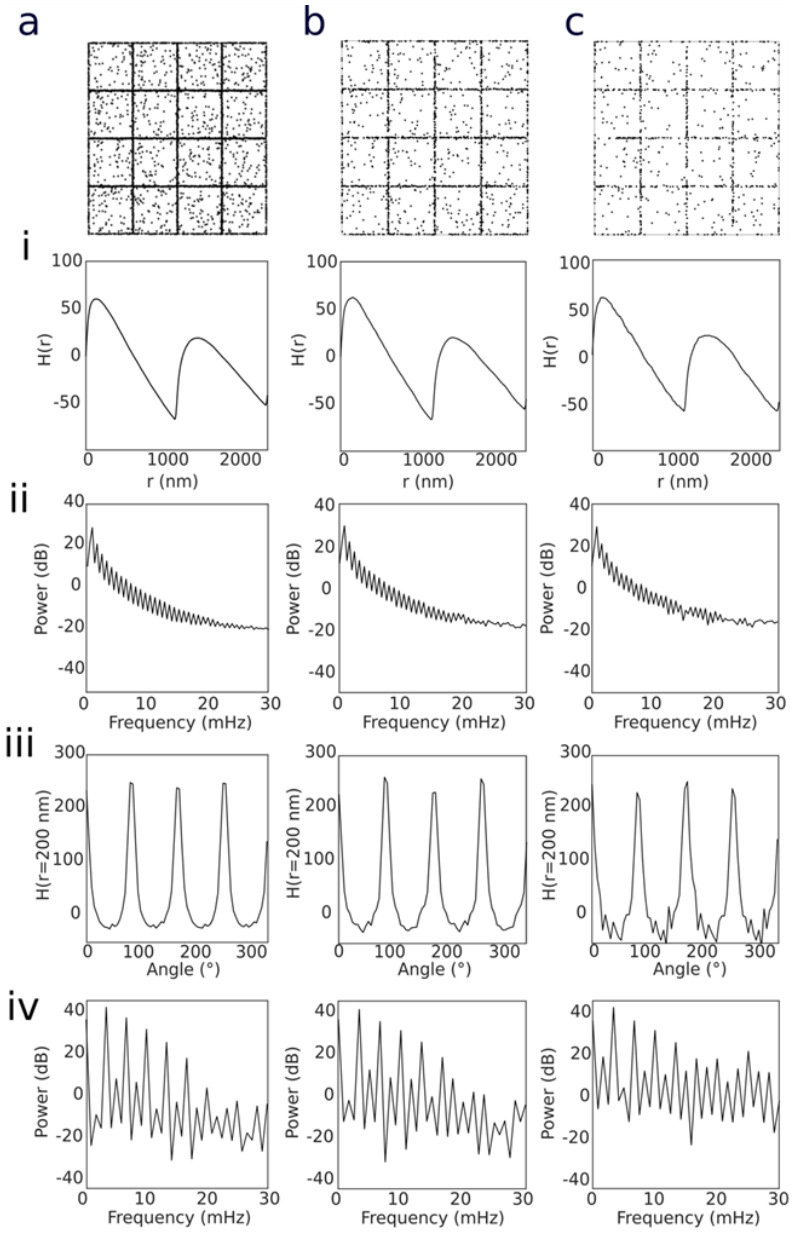

Figure 40: Examining the effect of reduced labelling density of fibrous structures on H(r)- and H(α)-function analysis. Simulations (n=50) of the regular, orthogonal, fibrous SPP with 100% (a), 50% (b) and 25% (c) of the standard condition labelling density. Ripley's H(r)-function (i) and its power spectra (ii) demonstrate spatial regularity whereas Ripley's H(α)-function (iii) and its power spectra (iv) demonstrate angular periodicity for the three conditions.

periodicity in the H(r)-function (Figure 40i-ii), and their perpendicular nature through the H(α)-function (Figure 40iii) and its spectra (Figure 40iv).

3.4.3 Poor localisation precision of fibrous localisations

The effect of artificially degrading the localisation precision at which the fibrous points are localised on the H(r)- and H(α)-function analysis was examined. Consider the case of a spatially regular series of orthogonal fibres, exhibiting three progressively poorer localisation uncertainties (0 nm, 30 nm and 50 nm for Figure 41a-c respectively), simulated otherwise per the standard condition. The case of perfectly localised fibrous points was first considered (Figure 41a). Both H(r)-function (Figure 41ai) and its spectrum (Figure 41aii) demonstrate the presence of spatially regular fibres. In this case, at all radii exclusive of the inter-fibre spacing (1250 nm), the H(r)-function is above that expected for an equivalent distribution of CSR points. At the simulated inter-fibre spacing of 1250 nm however, the H(r)-function is zero indicative of the background localisations which are simulated to occupy completely spatially random positions within the region, as expected. The angular periodicity of the SPP is evidenced by the H(α)-function analysis (Figure 41aii) and its corresponding power spectrum (Figure 41aiii). In the case of perfectly localised fibrous points, there is a sharp transition in H(α) at intervals of 90°, indicating a narrow distribution of fibrous points within each fibre as expected for a 0 nm localisation precision. As the localisation precision is artificially degraded, for both cases (30 nm and 50 nm for Figure 41b - c respectively), the H(r)-function and its spectra remain robust in the detection of spatial periodicity. Further, the H(α)-function (Figure 41b-ciii) and its spectra (Figure 41b-civ) demonstrate the angular periodicity of the SPP, albeit, a slight broadening and lowering of the characteristic peaks separated by 90° in the

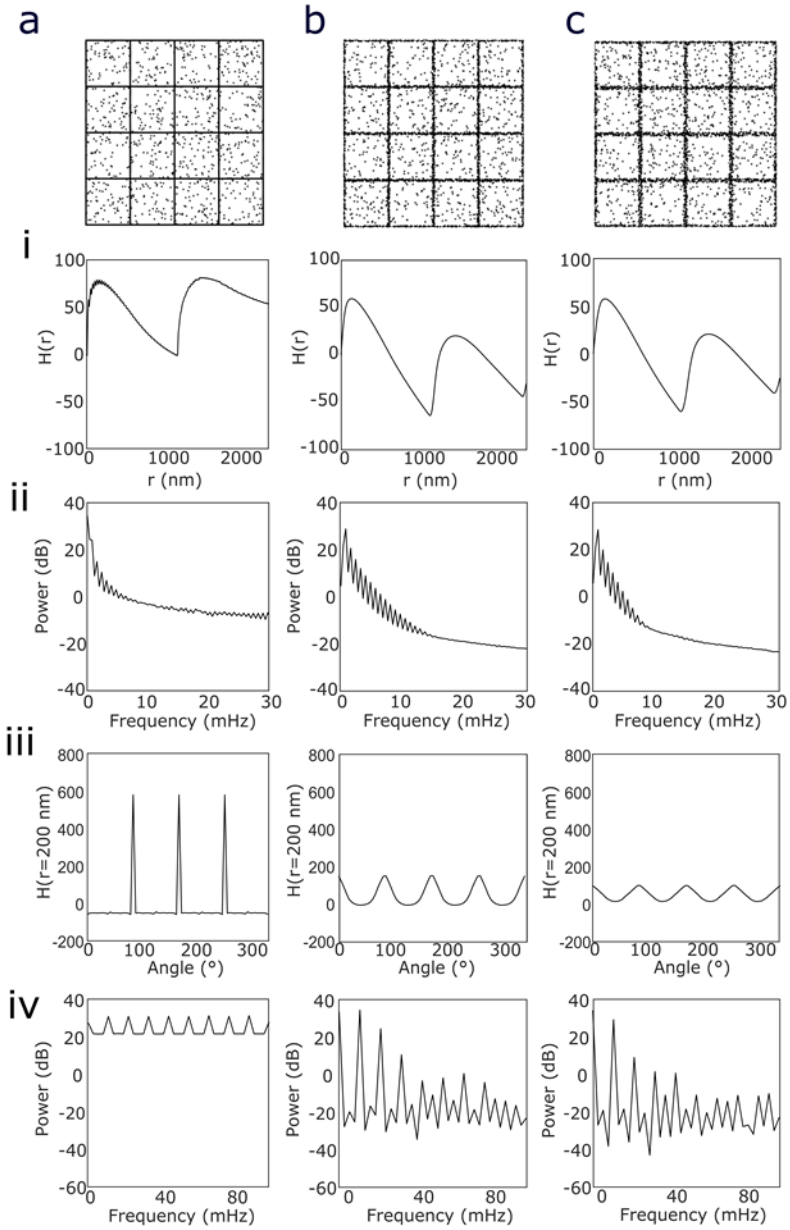

Figure 41: The effect of degraded localisation precision on H(r)- and H(α)-function analysis. Example SPPs (a-c) from n=50 simulations of fibres simulated with 0 nm (a), 30 nm (b) and 50 nm (c) localisation uncertainty on average. Conventional H(r)-function analysis was performed (i) and its spectra reveals spatial periodicity for all three conditions (ii). Angular periodicity was determined through H(α)-function analysis (iii) and its corresponding spectra (iv).

H(α)-function curves are evidence for the wider range of angles at which the fibres are detected due to the higher localisation uncertainty.

3.5 Robustness to analysis parameters

Throughout this Chapter, all data presented was analysed using the default analysis parameters of fixed radius = 200 nm and angle increment = 5°. To test the robustness of the method to changes to both radial and angular input parameters, simulations of increasing radius and increasing angular increments were performed.

3.5.1 The effect of the radius on the H(α)-function analysis

Consider the case of the spatially regular, orthogonal series of fibres generated per the standard condition at an inter-fibre distance of 500 nm, an example of which is presented in Figure 43a. The effect of increasing the radius over which the H(α)-function is calculated was examined, whilst fixing the angle increment to 5°. The contour plot (Figure 43b) demonstrates that the calculated values of H(α) are largely insensitive to this choice of parameter, up to 700 - 750 nm. At this radius (equivalent to √2 of the inter-fibre spacing), the diagonals of the regular fibrous mesh are detected at intervals of 45°.

3.5.2 The effect of angular incrementation on the H(α)-function analysis

The exemplar fibrous SPP (Figure 43a) was analysed using the H(α)-function with increasing angular increments and the default radius

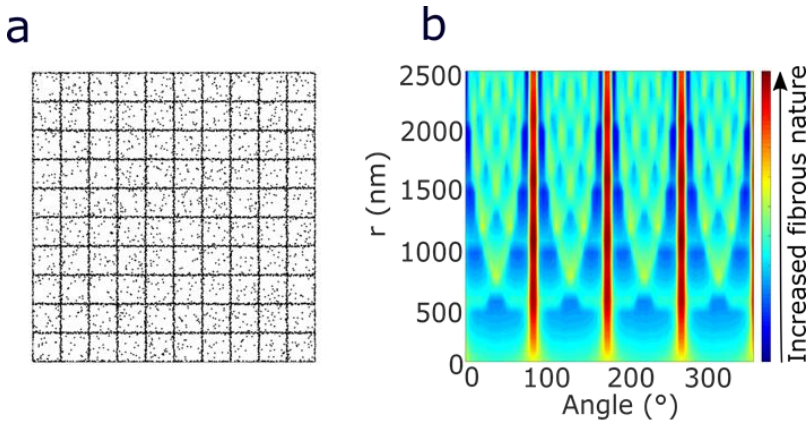

Figure 43: Studying the effect of varying the fixed radius on the H(α) analysis of a fibrous SPP. H(α) analysis was performed on a standard condition data set (a) for radii 0 – 2500 nm. The corresponding contour plot of all H(α) values is presented with H(α) value maxima depicted red and H(α) minima depicted blue (b).

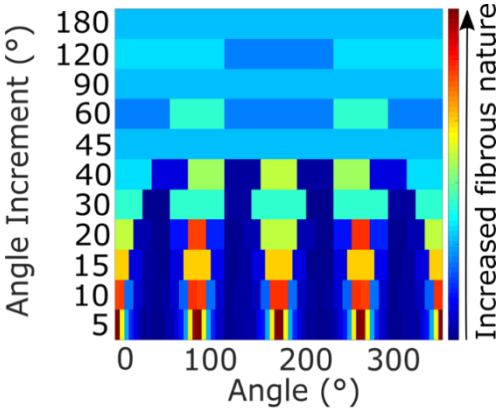

Figure 42: The effect of increasing the angular increment over which the H(α)-function is calculated for fixed radius r=200 nm. Integers of 360° were used as angular increments to determine the robustness of the method to this choice of input parameter. H(α) maxima are depicted red and H(α) minima are depicted blue (b).

(r = 200 nm) to study the importance of the angular input parameter on the analysis method. The working range of the angular increment is relatively large – the method is robust to this choice of parameter. However, as depicted in Figure 42, once the angular increment over which the H(α)-function is calculated exceeds 45°, the fibrous nature of the SPP is no longer evident. Hence, the default parameter of 5°, is indeed suitable for extracting accurate information.

3.6 Results on experimental data

The methodology was next applied to the study of the actin cytoskeleton at the mature T cell immunological synapse. For this, IRIS and dSTORM imaging was firstly performed using a commercial N-STORM system operating in TIRF mode (see Methods). SMLM images were reconstructed using the ThunderSTORM plug-in to ImageJ, as previously discussed (see Methods). A representative IRIS image of cortical actin at the mature synapse is presented in Figure 44i, from which three peripheral ROIs were selected for analysis Figure 44ii. The conventional Ripley's H-function demonstrates that there is no spatial periodicity in the arrangements of actin filaments at the synapse periphery (Figure 44iii-iv), indicating a non-regular arrangement of cortical actin. The Angular H-function curves and their power spectra (Figure 44v-vi) demonstrate that the fibres are not perpendicular to one another, nor to the axis of intersection. However, there is a non-random orientation of fibres, evidenced by two prominent peaks in the non-shifted curves (Figure 44v), for example at ~20° and ~200° relative to the y-axis for case Figure 44aii. This suggests a preferential directionality of fibres at the synapse periphery. To confirm the presence of fibrous structures, the previously discussed shift correction stage was implemented. A single peak at 180° is observed in the shift corrected curves (Figure 44vii), which is low and broad (77.66 ± 8.22 nm), earlier discussed as a hallmark of fibre curvature.

To validate the methods capability of discerning fibrous actin networks despite poorer labelling density and localisation uncertainty (Section 3.4), dSTORM imaging via Phalloidin was performed. A representative dSTORM image is presented in Figure 45i, from which three ROIs were selected for analysis Figure 45a-cii. The results confirm the lack of spatial periodicity

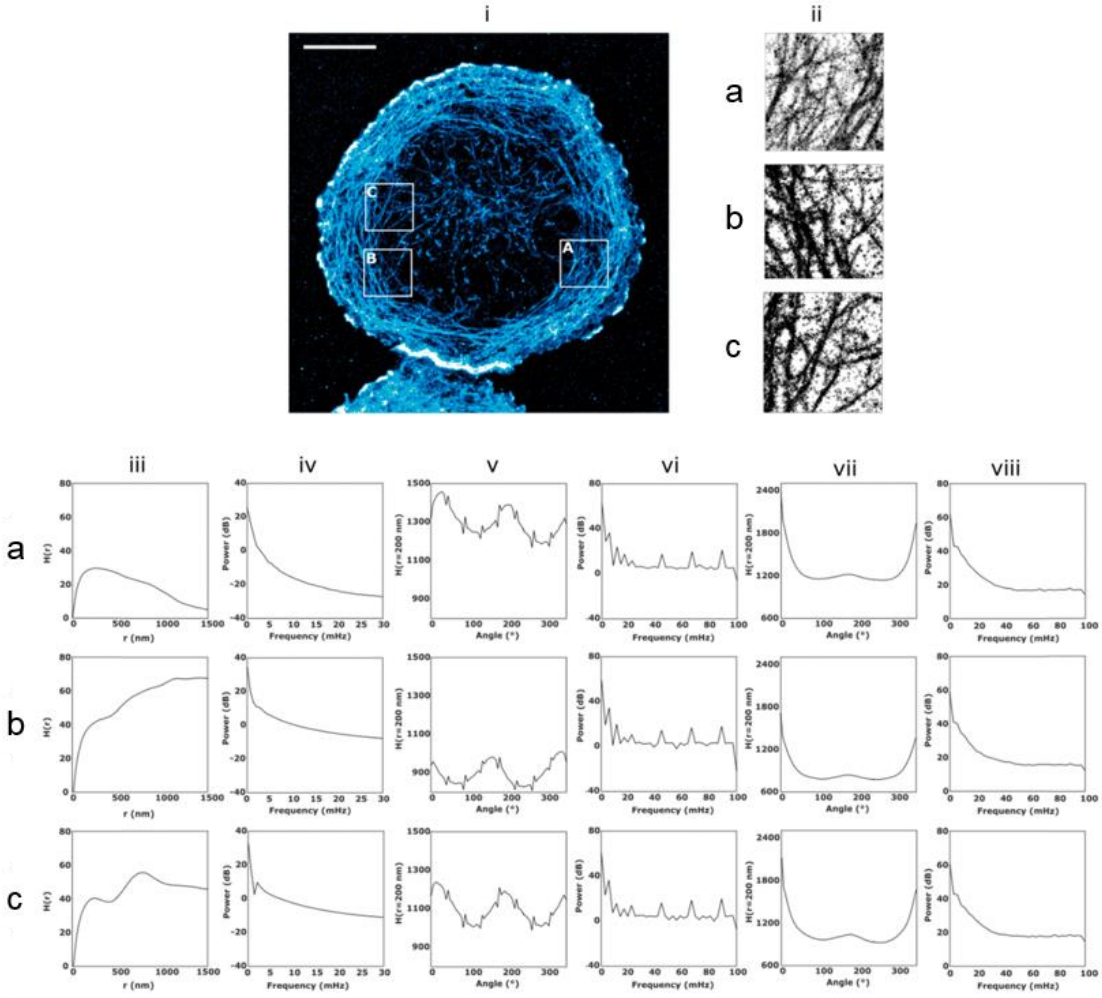

Figure 44: Application of Ripley's H-function and the Angular H-function to the study of cortical actin at the T cell synapse acquired via IRIS. A representative IRIS image (i), from which three peripheral ROIs were selected for analysis (a-cii). Conventional H(r)-function analysis (iii) and its spectra (iv), Angular H-function analysis (v) and its spectra (vi), and shift corrected Angular H-function analysis (vii) and its spectra (viii) are presented. Scale = 5 μm.

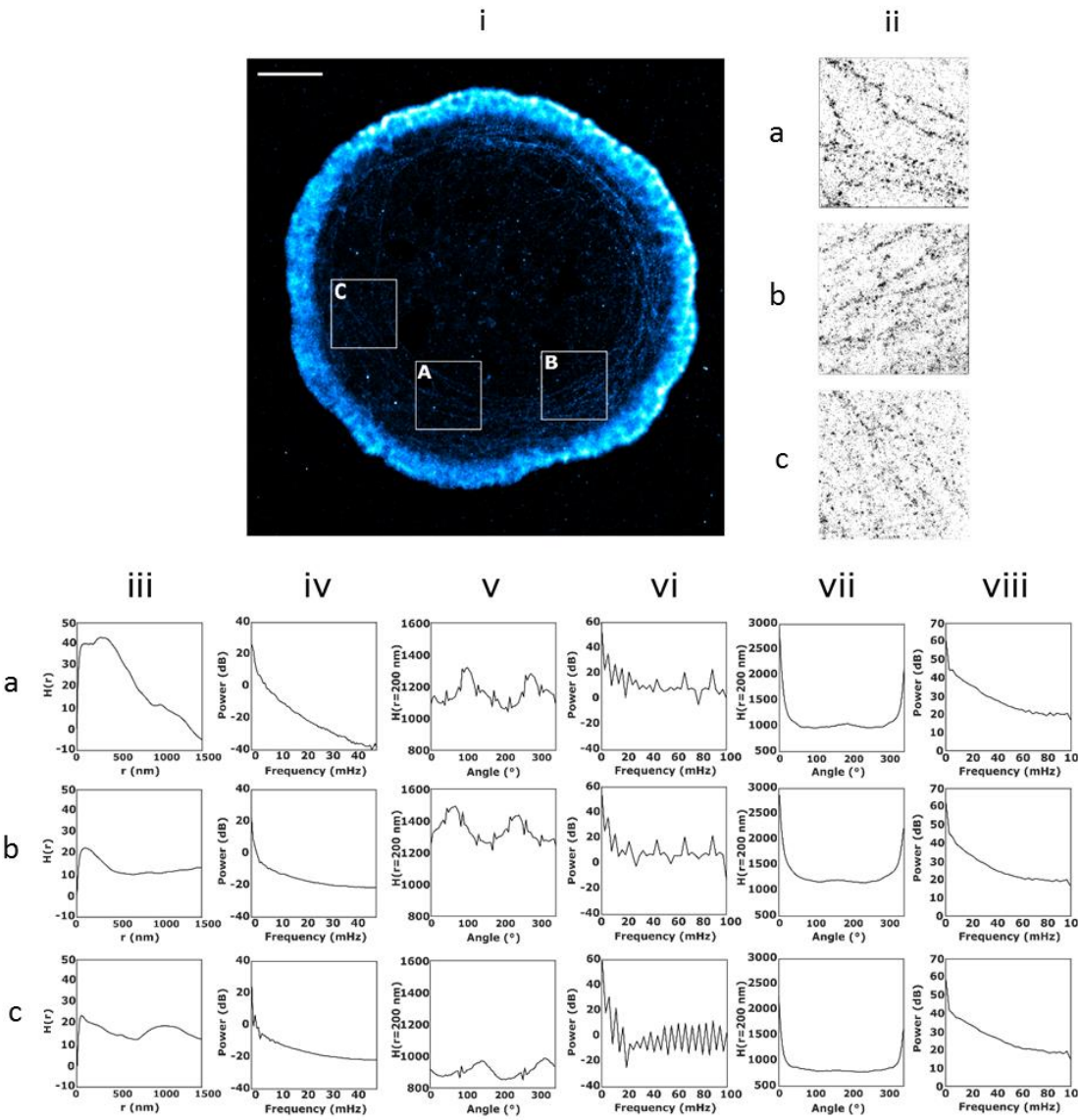

Figure 45: Application of Ripley's H-function and the Angular H-function to the study of cortical actin at the T cell synapse acquired via dSTORM. A representative IRIS image (i), from which three peripheral ROIs were selected for analysis (a-cii). Conventional H(r)-function analysis (iii) and its spectra (iv), Angular H-function analysis (v) and its spectra (vi), and shift corrected Angular H-function analysis (vii) and its spectra (viii) are presented. Scale = 5 μm.

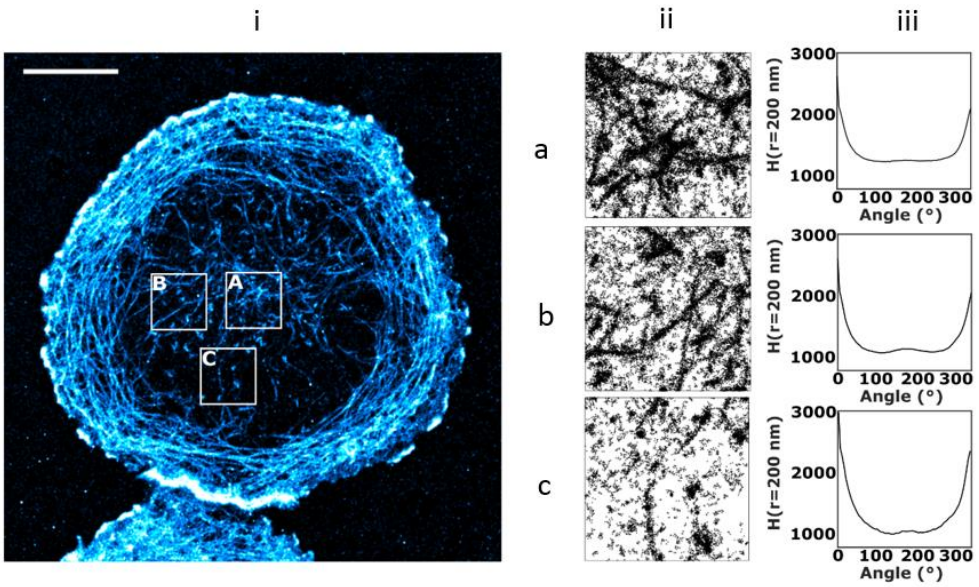

Figure 46: Shifted Angular H-function of central ROIs of the mature T cell immunological synapse. Selected ROIs from the synapse centre are presented (a-cii) with corresponding shifted Angular H-function analysis (iii). Scale = 10 μm.

(Figure 45iii-iv) in actin networks observed via IRIS, and their non-random orientations Figure 45v.

To test the methods ability to evaluate changes in actin organisation across the distinct zones of the synapse, ROIs from the synapse centre were analysed (Figure 46) and compared to those of the periphery (Figure 44). Compared to the actin abundant peripheral regions, the cSMAC of the mature synapse is actin poor which is thought to encourage TCR internalisation, as previously discussed. The series of actin rings at the cell periphery have been visualised by numerous T cell biology groups, as previously discussed and the radial flow of actin towards the synapse centre is a well characterised behaviour of mature synapses. A decrease in the maxima of the shifted Angular H-function

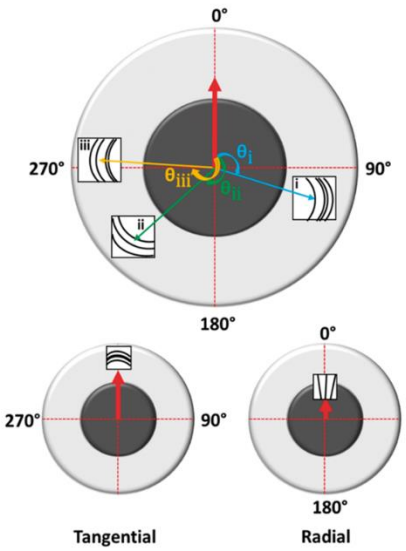

Figure 47: Schematic depicting the post-processing stage of the Angular H-function analysis to extract preferential fibre directionalities. For tangential like structures, upon performing post-processing, fibre directionalities are out of phase by 90° with the cell reference vector, whereas for radial like structures, the fibre directionalities align with the cell reference vector.

was observed (38.55 ± 11.07 nm) in central regions compared to those of the periphery ($p=0.047$) indicating a change in fibre curvature within the same cell.

To extract the preferential fibre directionalities in the cell periphery, suggested by the presence of prominent peaks in the non-shifted Angular H-function curves (Figure 44v), a post-processing stage was implemented. This involves determining the angular discrepancy between the cell centre and the centre of each ROI. The cell centre reference vector is defined as the x co-ordinate of the centre of the cell, pointing in the y axis. The angle between each ROI centre and the cell reference vector, termed θ_i, is first computed for each i^{th} ROI. These θi values are then used to translate the Angular H-values to align

with the cell reference vector, to compensate for angular discrepancies owing to the ROIs position within the cell. This allows for the assessment of the preferential directionality of fibres across different ROIs within the same cell. A schematic depicting the post processing methodology is presented in Figure 47.

For the peripheral ROIs of the mature T cell immunological synapse one would expect a dominance in tangential structures, owing to the presence of F-actin concentric rings previously discussed. Indeed, this population of tangential fibres was demonstrated by the post-processing stage of the Angular H-function, evidenced by maxima in the post-processed curves at 90° and 270° with amplitude (0.98 ± 0.25 nm) (Figure 48a). Interestingly, no peaks were observed at 0° and 180°, suggesting that a secondary population of radial fibres was not dominant. Central ROIs however present a significantly different organisation (p=0.0307). Radial fibrous orientations dominate the

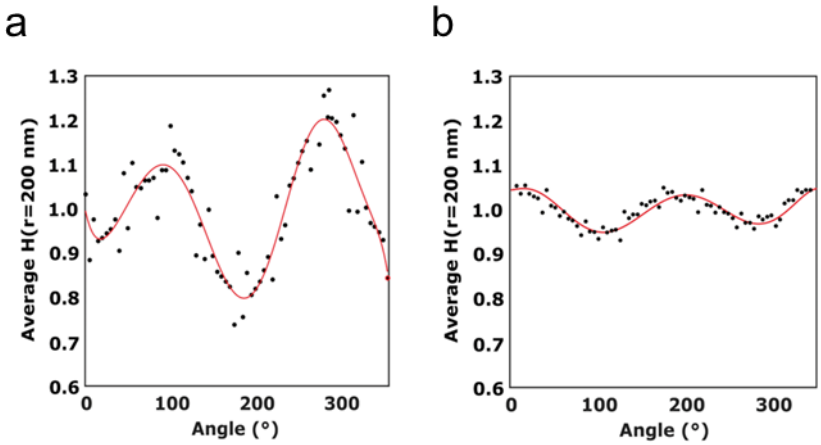

Figure 48: Post-processing of the Angular H-function reveals distinct directionalities of fibrous populations at the mature T cell immunological synapse. A summation of post-processed curves for the synapse peripheral (a) and central (b) ROIs is presented normalised by their average Angular H values.

cSMAC, evidenced by peaks in the post-processed curves at 0° and 180° with amplitude (0.17 ± 0.03 nm) (Figure 48b). The method thus can detect significant differences between differing fibre architectures within the same cell.

3.7 Summation of results

In this Chapter, the use of Ripley's H(r)-function and the proposed novel modification thereof, H(α), for the study of fibrous SPPs has been examined. Using a variety of simulated fibrous pointillist data sets, information pertaining to spatial regularity and angular features of the SMLM like data sets has been extracted using both the H(r)- and H(α)-function. Both methods are capable of discerning fibrous structures in SPPs despite complex intersections, background noise (i.e. non-fibrous localisations) and localisation uncertainty. The H(α)-function however, can provide additional information to the conventional H(r)-function in the context of fibre curvature, co-orientation and angular periodicity despite heterogeneity in fibre orientation.

The method is also robust to variety in both simulation and analysis parameters. Simulated results indicate that the method can distinguish fibrous structures despite the presence of up to 90% non-fibrous localisations, poor and inconsistent labelling and poor localisation precisions. Further, the H(α)-function analysis is largely insensitive to the radial and angular input parameters, as detailed previously.

The experimental results in this Chapter highlight that the cortical actin meshwork at the peripheral regions of the mature T cell immunological

synapse are not spatially regularly arranged. The peripheral meshwork is curved but possesses co-linearity, presenting an organised architecture in which fibres are not randomly orientated. Fibrous structures at the cell periphery demonstrate a preferential, tangential directionality, quantitatively assessed by the Angular H-function. The comparatively actin poor central region of the mature synapse however, was found to be populated by radial actin fibres, of a differing curvature.

Whilst the statistical analysis of clustered distributions of molecules in SMLM data sets is currently mature, the analogous study of fibrous point patterns remains comparatively understudied. This makes the proposed Angular H-function methodology an important advance in the field of pointillist data analysis of fibrous structures generated by means of localisation-based microscopy. However, this analysis remains limited to the assessment of the global nature of the data. It is not possible using this method alone to extract fibre descriptors on a local scale, for example, the number of fibres or the fibre lengths. Nonetheless, analysis methods enabling a quantitative description, either global or local, will enable SMLM methods to evolve from visual illustrations of nanoscale structures to a reliable, statistical study of the biology of interest.

Chapter 4 Quantitative fibre tracing in SMLM data

Following results and figures adapted from published work:

Peters, R., Griffié, J., Burn, G.L., Williamson, D.J. & Owen, D.M. *Quantitative fibre analysis of single-molecule localization microscopy data*. Scientific Reports 8, 10418 (2018).

4.1 Introduction

The H(α)-function method to extract global statistics of fibrous SPPs provides information regarding spatial and angular periodicity, fibre co-orientation and curvature. Whilst such a method is useful for the study of the general properties of a fibrous meshwork, information on a fibre per fibre basis is not quantifiable. Numerous studies detailing the importance of the nanoscale architecture of fibrous structures exist, for example the Picket Fence model of Kusumi. In this model, the spatial organisation of cortical actin ultimately effects cell signalling, through the regulation of protein diffusion and microclustering at the cell membrane. Understanding and quantifying such structures, without sacrificing the pointillist nature of the data acquired by SMLM, could therefore prove invaluable for the study of biological phenomena on the nanoscale. In this Chapter, a novel strategy for the tracing of fibrous structures in data generated by SMLM is presented. The algorithm outputs various fibre descriptors, such as the number of fibres, fibre lengths,

areas of enclosed meshwork, and locations and angles of branched fibres. The approach is validated using a variety of simulated data sets, presenting various complex fibre nanoarchitectures and tested using experimental data acquired via the IRIS approach to SMLM.

4.2 Defining a novel strategy for the tracing of fibrous structures in pointillist data

Previous methods of tracing fibrous structures in data acquired using super resolution microscopy methods involved rendering the pointillist data as a conventional image and applying conventional image analysis techniques for the study of fibrous networks. Using this approach, local properties of the mesh can be extracted, albeit at the expense of the true nature of pointillist data. Directly analysing the fundamental pointillist data is an important advance. Whilst there are several methods for rendering and visualising pixelated images from pointillist data, there is no ideal method to do this, and no consensus on the best approach. Thus, pixelation introduces variability on the derived image meaning that such an input into a fibre tracing algorithm is further from the ground truth. Additionally, this variability makes the comparison of tracing algorithms that use pixelated data as input intrinsically difficult as they perform differently with pixelated images with different statistical composition and construction. Analysing the fundamental, pointillist data removed this layer of variability ensuring high fidelity, un-manipulated input data with well-known statistical properties.

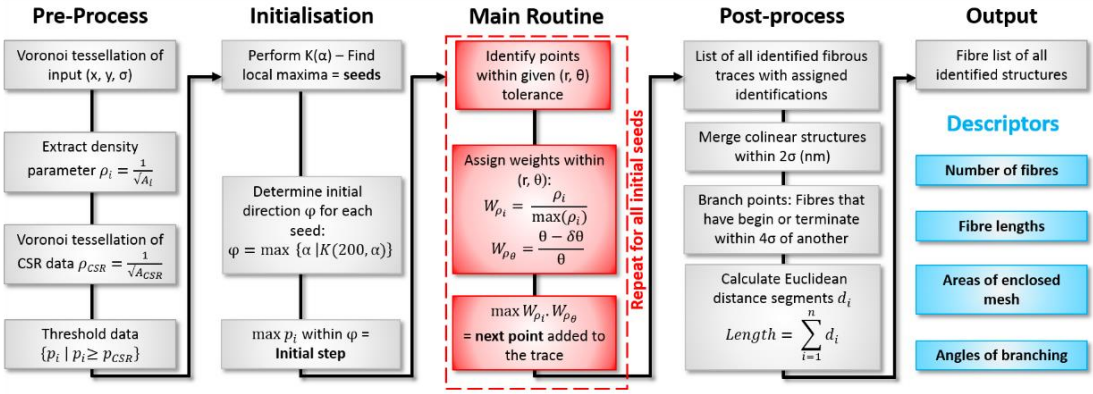

Figure 49: Summation of the workflow for the fibre tracing algorithm.

Utilising only the raw localisations as input for the tracing routine, the method accurately extracts fibrous structures, despite the presence of background noise, localisation uncertainty and complex intersections, thereby providing a full system characterisation on a fibre per fibre basis. The algorithm can be split into distinct stages: Pre-processing, initialisation, the main routine (tracing) and post-processing, Figure 49.

4.2.1 Pre-processing

The first stage of the algorithm involves assigning each point an initial local density parameter. For this, localisations are segmented by means of Voronoi tessellation (Figure 50a-c), without the need of radial or toroidal based scanning, therefore limiting topologically biased assignments. This form of segmentation is particularly suited to SMLM data, as the input can be sparse, non-uniform or extremely dense. The use of tessellation and triangulation has been applied to SMLM data, although most notably to clustered SPPs. Recent work demonstrated the use of mesh diagrams for the segmentation of clusters

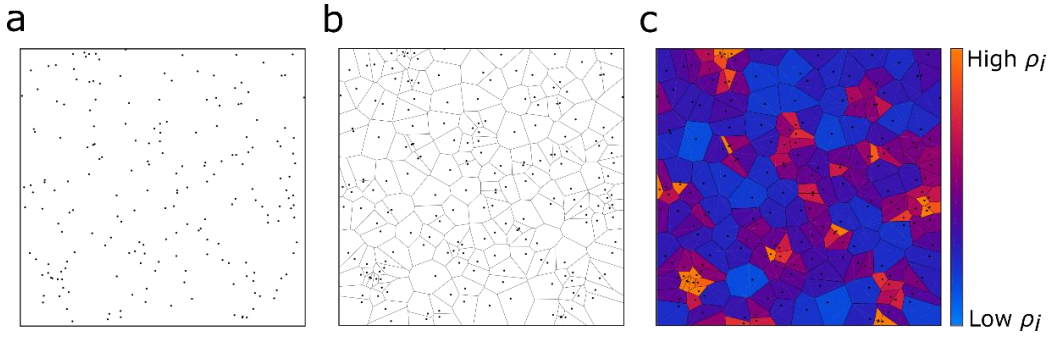

Figure 50: The principle of Voronoi tessellation in the context of SMLM data. A list of localisations, completely randomly distributed in the case of (a), are segmented by their Euclidian distance from neighbouring "seeds" (b); the Voronoi tessellation or mesh. By computing the area of each Voronoi cell for example, one can determine a density parameter ρ_i (c) for each seed.

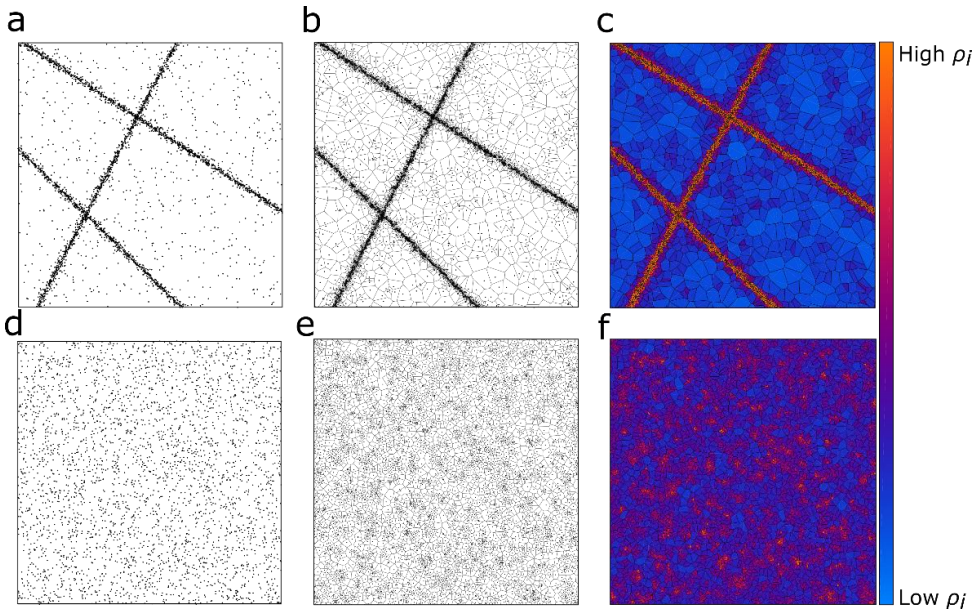

Figure 51: The strategy of identifying background points within a fibrous SPP. For a given fibrous SPP (a), the points are segmented by performing a Voronoi tessellation (b) from which density parameters are calculated (c). This process is repeated for an equivalently dense CSR distribution (d-f) of points, such that an average density parameter for CSR can be determined for each SPP input.

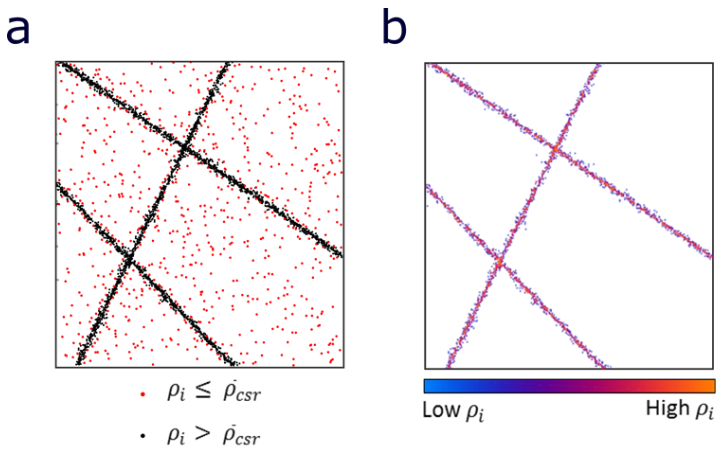

Figure 52: Thresholding effectively removes background of non-fibrous points. By application of a density parameter threshold, the fibrous and background localisations, depicted black and red respectively (a), are distinguished. The remaining points (b) can now be considered for fibre assignment.

in SMLM data through thresholding and performing Monte Carlo simulations, although such methods are relatively understudied in the context of super resolution image analysis (see Section 2.5.4).

Performing a Voronoi tessellation of a fibrous SPP involves a partitioning of a plane into Voronoi cells (for all localisations) (Figure 51b), based upon the spatial organisation of input points or seeds (Figure 51a) alone. In the simplest case of two distinct points in the Euclidean plane, the Voronoi cells are calculated per the intersection of half-spaces and is thus a convex polygon. In this example, line segments are formed via the perpendicular bisector, given the Euclidean metric. As the system becomes more complex, a clearer distinction between sparser, background points and denser fibrous points becomes evident. To characterise this behaviour, a density parameter per $\rho_i = \frac{1}{\sqrt{A_i}}$ is assigned for each localisation in the SPP, where A_i is the area of the ith Voronoi cell (Figure 51c). All points within the SPP are then subject to a

threshold, such that only those possessing local density parameters greater than that of the average calculated by an equivalent distribution of simulated CSR points remain (Figure 51d-f). The data now contains all points that have been identified as possible fibrous structures for subsequent tracing (Figure 52).

4.2.2 Initialisation

An important part of the tracing strategy is to initialise each fibre trace at the points possessing the most fibrous nature. For this, the Angular H-function (r=200 nm, α=5° per Section 3.5) was implemented to ascertain local fibrous maxima. The modulation depth of the Angular H-function is defined as the difference between absolute maximum and minimum in H (r, α). For each point, the modulation depth is calculated, from which local maxima can be found by implementing a radial search (r = 50 nm) for maxima in modulation depth or equivalently, the most fibrous points. This approach offers the advantage that such maxima are routinely located on isolated fractions of fibres, rather than at complex fibre intersections, in which points resemble clustered behaviour. Consequently, the tracing routine is initialised in a region in which the fibres are well characterised, enabling a clearer estimation of the fibre direction.

Once local fibrous maxima have been identified, the initial direction of the trace, φ, is estimated. To estimate the initial direction of the fibre, a local Angular H (r=200 nm, α=5°)-function is performed, to determine which angular range with respect to a reference vector $\langle 0,1 \rangle$ exhibits the highest value in H (r, α) and thus is most likely to be the direction of fibre. The localisation with the next highest Voronoi density parameter ρ_i within the distance

specified is chosen as the first step in the trace. Using this initial vector as the direction of the fibre, the algorithm can continue to search for more localisations in the trace through the main routine (Figure 53).

4.2.3 The main routine

Once initial density parameters and local fibrous maxima are identified, the main tracing routine can begin. The tracing takes as input, the list of molecular coordinates that satisfy $\{\rho_i | \rho_i \geq \rho_{CSR}\}$, their initial density parameters $(\rho_i, \rho_{i+1} \ldots \rho_N)$ and finally the list of local fibrous maxima. Given a fixed radius and angle tolerance (r, θ), points that are identified along the initial fibre direction are assessed. Default analysis parameters are set to r=100 nm, θ=15°. For all localisations that satisfy both radial and angular constraints, a weighted density parameter based upon both directionality $W_{\rho\theta}$ and local density $W_{\rho i}$ is calculated. The angular disparity between the absolute vector of the fibre direction termed θ and that of the query localisation termed δθ is determined for all points, which is then normalised by the angular tolerance specified. Mathematically $W_{\rho\theta}$ is expressed:

$$W_{\rho\theta} = \frac{\theta - \delta\theta}{\theta} \qquad 11$$

A weighted Voronoi density parameter $W_{\rho i}$ is also calculated for each point identified within the (r, θ) search region. For this, each parameter $(\rho_i, \rho_{i+1} \ldots \rho_N)$ is weighted by that of the maximum identified within the search area:

$$W_{\rho i} = \frac{\rho_i}{\max(\rho_i, \rho_{i+1} \dots \rho_N)} \quad 12$$

The highest product of the two weighted parameters (max $W_{\rho\theta} \,.\, W_{\rho i}$) provides the next localisation to be added to the trace, Figure 53. A two-point moving average for the calculation of the fibre direction is performed throughout, to limit the probability of spurious directions. The fibre direction is updated, and the process continues until there are no more localisations to consider along the fibre direction within the supplied constraints (r, θ). At this stage, the search returns to the initial seed from which the trace was initiated and the tracing routine is repeated in the opposite direction to the initial fibre direction (-180°). The entire process is repeated for all identified fibrous maxima, until a list of fibrous structures recognised by an identification number is generated.

4.2.4 Post-processing

Once a list of all fibrous structures has been generated, several post-processing stages can be performed to obtain the complete fibre landscape, from which key fibre descriptors can be extracted. The post-processing begins with a process termed stitching, in which certain fibres may be concatenated, based upon specific constraints.

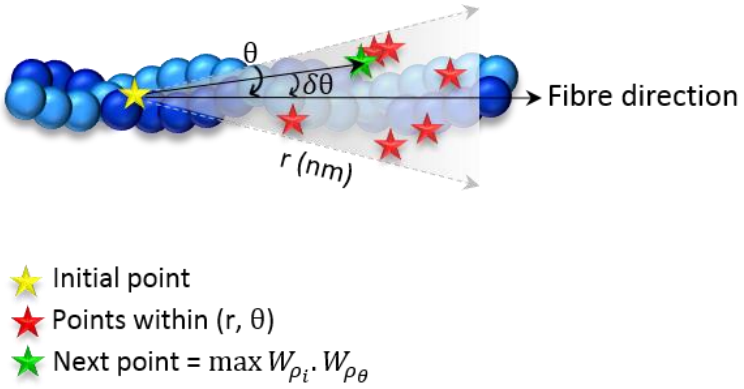

Figure 53: Schematic representation of the main tracing routine. Query points (red) are first identified. The vector between the previous point (yellow) and each query point is determined, to obtain the angular deviation δθ of the query localisation to the fibre direction. Weighted density parameters $W_{\rho i}$ and $W_{\rho\theta}$ are calculated per equations 11-12 and the next point (green) is added to the trace.

4.2.4.1 The stitching processes

There exists a strong possibility that the same fibre is identified across multiple traces. This is indeed conceivable as there exists multiple paths to trace a fibre from different seed points, based upon the nature of the data itself. To correct for this type of over-sampling, co-linearity stitching based upon strict radial and angular criteria (Figure 54) is performed. The algorithm begins with the longest traced fibre. For each input fibre, if any another fibre lies within four times the average uncertainty of all localisations (4σ (~ 60 nm)) of the start or end co-ordinate of the input fibre, the query fibre is considered for stitching. The angle between the input and the query fibre is calculated across three sampling ranges of the fibre, Φi-iii, and fibres satisfying (Φi, Φii, Φiii, ≤ 5°) are concatenated. Three sampling ranges are defined as those

containing 20%, 50%, and 80% of the localisations of the fibre. This process is repeated iteratively, such that all fibres are considered for stitching based on co-linearity.

It is necessary to further account for fibres with spurious start and finish directions. This arises particularly in shorter fibres at complex intersections; regions of dense localisations in which the initialisation of the fibre direction may be poorly estimated. For each fibre, the average nearest neighbour distance to all other fibres, λi is determined. Further, the angular disparity between the given fibre and all others is determined, across the three sampling ranges (20%, 50%, 80%), βi-iii. Fibres that satisfy ($\lambda i \leq 4\sigma$) and (βi, βii, $\beta iii \leq 15°$) are further concatenated. A smoothing algorithm performs (up to a maximum of) a ten-point moving average on all identified traces, and the absolute lengths of the fibres is calculated as the sum of individual steps. A schematic of the stitching process is presented in Figure 54.

The output comprises a list of Cartesian co-ordinates, representative of all fibrous traces, along with their associated localisation precisions and assigned identification number. Notably, the output takes the same form as that of the input data; a SPP. Without the need to render the pointillist data as a conventional image, the method can produce accurate traces of fibrous nanoarchitectures whilst preserving the true nature of the data. Indeed, the multifarious methods of SMLM data rendering provide different images, and a comparison between approaches is not quantitatively evaluated. Several parameters contribute to achieving accurate visualisation of SMLM data, from convolution methods to sampling criterion. As such, by exploiting the localisation co-ordinates as input alone for data analysis, one can ensure a fairer comparison not only between conditions but across all SMLM data.

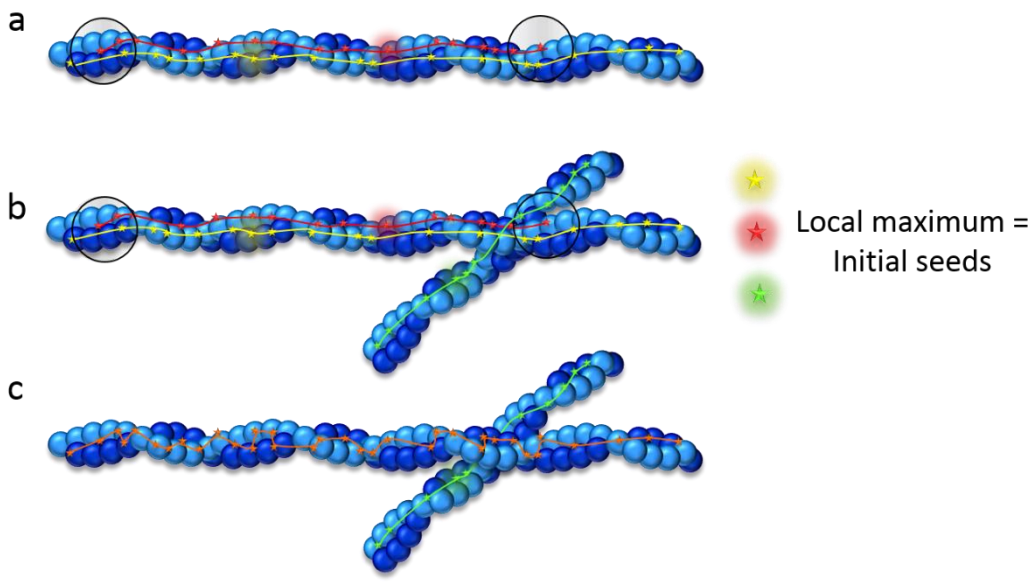

Figure 54: Schematic representation of the stitching process based on co-linearity. For a given fibre (red trace, (a)), the start and end points are identified and any points lying within 4σ are identified (points within the black circles). In the case of (a), the two traces satisfy the co-linearity constraints. However, in case (b), whist the new fibre (green) satisfies the proximity constraint, the angular requirement for co-linearity is not met, therefore this fibre is not added to the original trace (c). This process is repeated for all fibres.

4.2.4.2 Extracting key fibre descriptors

The final stage of the analysis workflow is to use the fibre landscape to extract detailed information on the nanoscale organisation of the fibrous SPP. Several fibre descriptors can be determined from the analysis method including the number of fibres, fibre lengths, areas of enclosed meshwork, and the locations and angles of branch points. Similarly to the stitching process, a possible branch point is identified by searching for fibres that have starting or terminating positions within 4σ of any other fibre, excluding a distance of 4σ from the ROI boundaries. The method performs smoothing, and co-ordinates

assigned to fibre traces are not evenly spaced. By fitting each trace to a parametric spline for example, and defining a set of nodes, one could attempt to extract the persistence length. However, one must be careful regarding the order of spline used. It is not clear if all traces within the fibre landscape can be fit to the same order of spline and increasing the order to suit more oscillating traces does not necessarily improve accuracy per Runge's phenomenon (Fornberg and Zuev, 2007). A degree of fibre curvature can however be estimated from the analysis, by computing the ratio of fibre length to the Euclidean start-end distance, per fibre. A workflow of the algorithm is summarised in Figure 49.

4.3 Results on simulated data sets

To validate the methodology, a variety of SMLM like data sets of known fibre architectures were simulated. Each condition comprises of n=30 simulated data sets for robust analysis regarding distributions of fibre descriptors including the number of fibres, fibre lengths, areas of enclosed regions and angles subtended by branched fibres.

Whilst the simulated fibre organisations presented are diverse, the methodology in the context of labelling density, localisation uncertainty and background noise is consistent and as such, is referred to as the standard condition. Specifically, the standard condition comprises of a square (3 x3 μm^2) ROI, in which localisations are initially placed at intervals of 3.4 nm, to mimic the structure of F-actin. The extent of sampling was varied, to represent non-uniform fluorophore labelling and possible multiple blinking of labels: 30% of localisations received no label, 40% one label, 25% two labels and the

remaining 5% received up to a maximum of six labels. All points were then subject to a Gaussian noise spatial perturbation, the mean and variance of which were drawn from a Gamma distribution with shape and scale parameters (k, θ), chosen such that the average simulated localisation uncertainty was 16 nm, to represent results achieved in experimental data sets. The Gamma distribution was purposely chosen to emulate the typical distribution of localisation error when performing IRIS imaging. Finally, the entire SPP was subject to a CSR distribution of non-fibrous background localisations.

4.3.1 Spatially regular linear fibrous SPPs

Consider the case of a series of orthogonal fibres of a known inter-fibre spacing, regularly distributed across the ROI. A representative example of such a fibre arrangement (Figure 55a) and its corresponding fibre landscape (Figure 55b) is presented, from which key fibre descriptors are evaluated. In this case, the method routinely and accurately traces the fibrous structures, despite the presence of localisation uncertainty and background localisations. The distribution (from n=30 simulations) of the number of fibres (Figure 55c), fibre lengths (Figure 55d), areas of enclosed meshwork (Figure 55e) and branching angles (Figure 55f) demonstrate close alignment with simulated values. A notable result is the distribution of areas formed through enclosed mesh regions (Figure 55e), in which the regularity of the input data set is evident through its narrow profile.

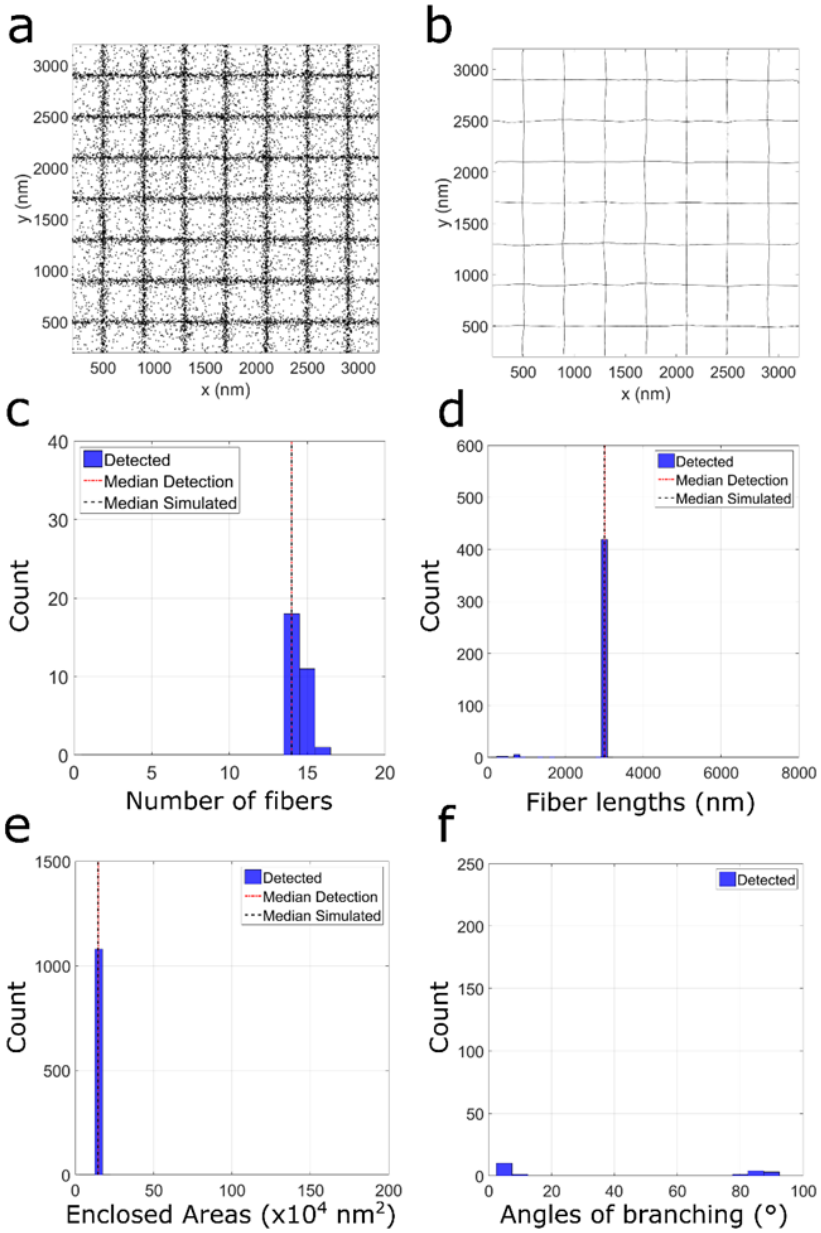

Figure 55: Fibre analysis (n=30 simulated) of regular fibrous SPPs generated using the standard condition. A representative input (a) of all localisations and resulting fibre analysis (b) output. Histograms of the distribution of the detected number of fibres (c), fibre lengths (d), areas of enclosed regions (e) and angles of identified branching points (f) are presented.

4.3.2 Fibrous SPPs exhibiting randomised spatial co-ordinates and orientations

The method was further tested by simulating a more complex fibrous input, consisting of 15 linear fibres of randomised directionality spanning the ROI, otherwise simulated per the standard condition. A representative example of such a simulation (Figure 56a) and its corresponding fibre analysis (Figure 56b) output is presented. Despite heterogeneity in fibre orientation and complex sites of multiple fibre intersections, the method can identify the fibrous localisations and reproduces an accurate organisation of simulated fibres. On a fibre per fibre basis, the fibre tracing routine can determine key characteristics, for example fibre lengths, in close agreement with simulated values. Moreover, as in the Angular K-function, global properties of the fibrous SPP can be elucidated by analysis of the distribution of certain descriptors. For example, inspecting the distribution of enclosed regions formed through random fibre intersections, reveals that the fibres in the SPP are not periodically arranged, as in the case of Figure 55.

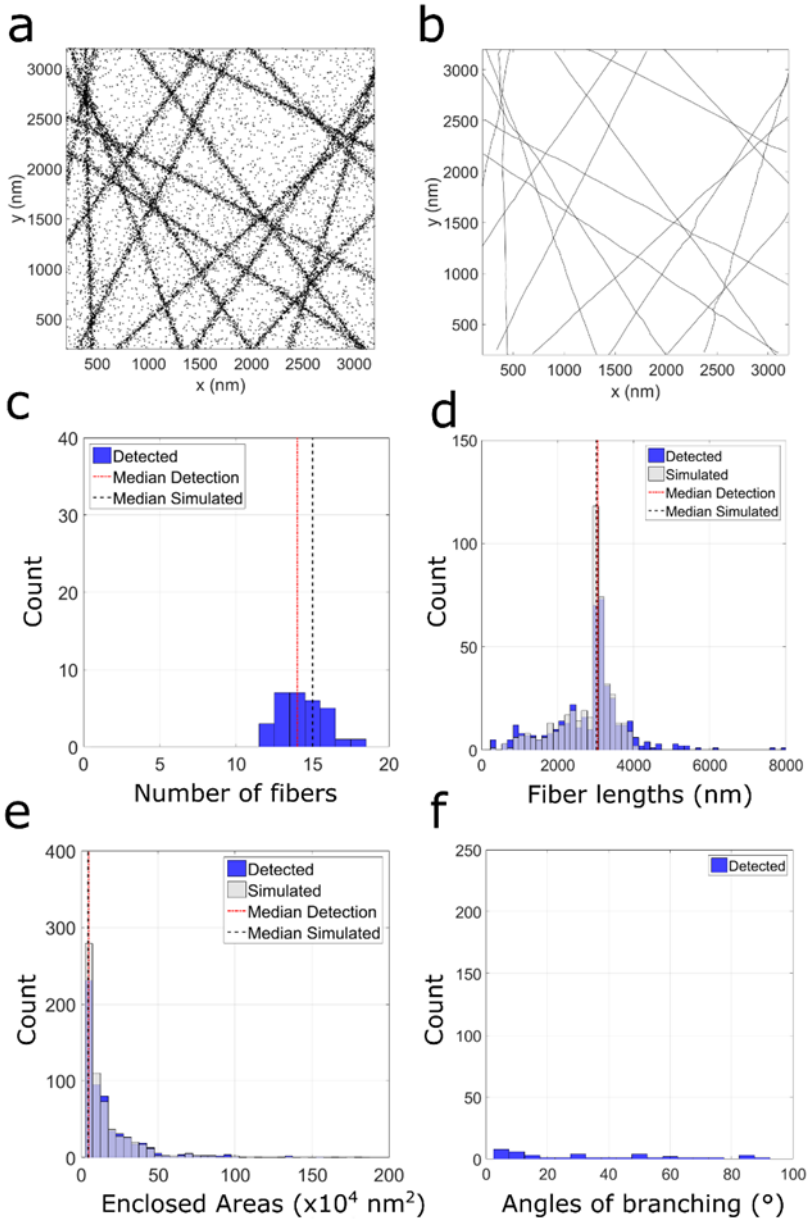

Figure 56: Fibre analysis (n=30 simulations) of 15 randomly distributed linear fibrous structures generated per the standard condition. A representative fibrous SPP (a) and its corresponding output (b) via the algorithm. Histograms of number of fibres (c), fibre lengths (d), areas of enclosed regions (e) and angles of identified branching points (f) are presented.

4.3.3 Branched filamentous networks

Consider the case in which daughter filaments have grown from mother filaments at a characteristic 70° angle. In the context of the biological system presented in this Thesis, in which Arp 2/3 serves as nucleation sites on pre-existing filaments, branched fibrous networks are prominent. Moreover, in many biological systems dense meshworks of branched fibres play an important role in cellular mechanics, as previously discussed. To construct a branched network of fibres, 7 mother filaments were first simulated, from each of which a nucleation site was randomly designated. Growth of a daughter filament, orientated at 70° from its mother was then simulated per the standard condition (Figure 57a). The method can accurately trace such a complex network of branched fibres, providing results that closely agree with simulated values. The area of enclosed mesh regions (Figure 57e) further demonstrates that the network is not regularly arranged, as per simulation. The angles of branched fibres (Figure 57f) exhibits a prominent peak at 70°, as per simulation.

4.3.4 Fibrous SPPs exhibiting shorter lengths

To evaluate the methods capability of tracing fibres that do not span the entire ROI, point patterns of shorter fibres at two different fibre densities were simulated. For this, two random co-ordinates within the ROI were generated, from which the equation of the straight line is determined via the slope and intercept. Fibres of a maximum 1 μm Euclidean length were then extracted and initialised from a random point along the line. Note that fibres were initialised at any point within the ROI, such that one would expect in some cases the fibre to intersect a ROI boundary. All other simulation parameters remain per the standard condition.

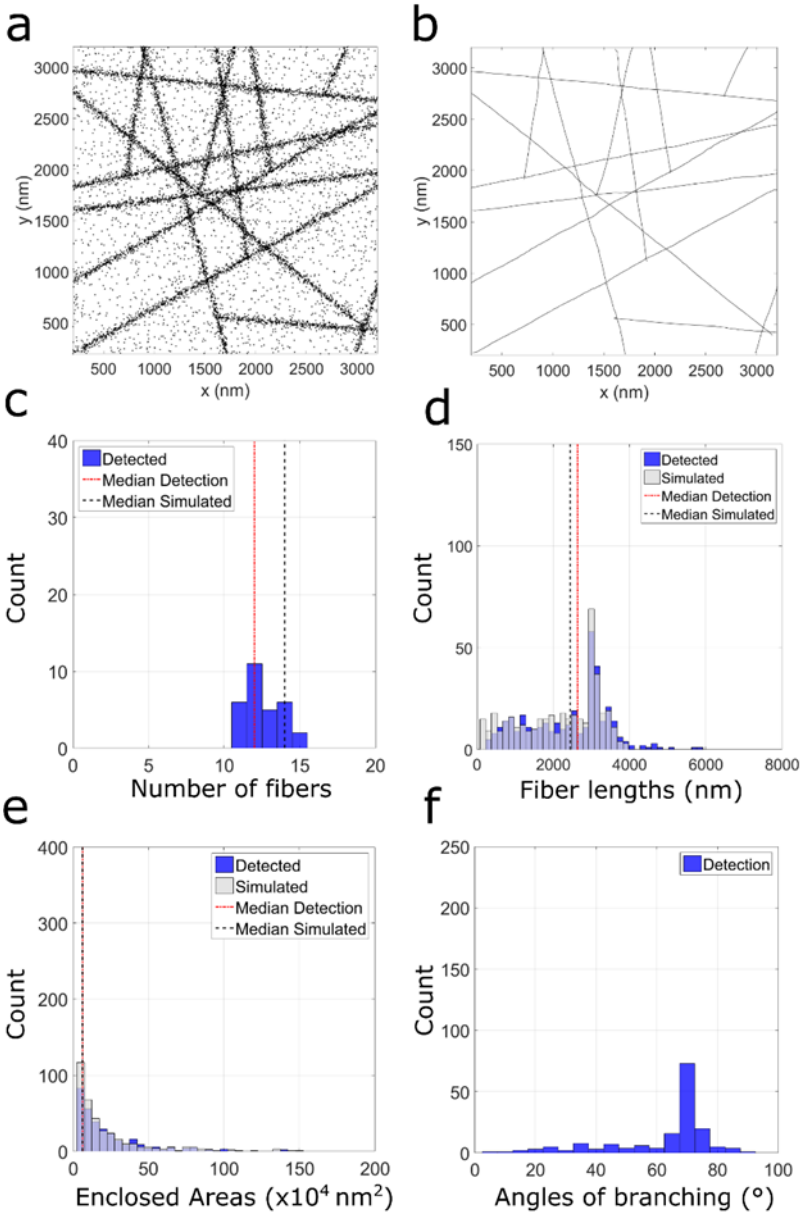

Figure 57: Fibre analysis (n=30 simulations) of a branched fibrous network generated per the standard condition. A representative input (a) of a branched fibrous network and resulting fibre landscape (b) output. Histograms of number of fibres (c), fibre lengths (d), areas of enclosed regions (e) and angles of identified branching points (f).

Firstly, 15 linear fibres were generated (n=30), from which fibre descriptors were evaluated (Figure 58). The median detected number of fibres, fibre lengths and enclosed areas are in close agreement with simulated values demonstrating an accurate tracing. The analysis of branching points however is over-estimated by the method. A proposed explanation for this inaccuracy lies within the method of simulation. Since a branching point is defined as any fibre whose start or end lies within 4σ (60 nm) of any other fibre (see 4.2.4.2), it is likely that for shorter fibres such a condition is readily met in comparison to the simulations in which the fibres span the entire ROI. Encouragingly however, there is no prominent angular maxima exhibited in the branched network (Figure 57).

To account for the disparity in point density, the case of 45 (1 μm maximum length) fibres generated per the standard condition was considered (Figure 59). Specifically, 45 fibres were selected within a 3 × 3 μm^2 ROI as this number is representative of the dissection of 15 fibres than span the entire ROI. In this case, the method performs reasonably well, however there are failures. For example, the method under-estimates the number of fibres. This can be explained by the merging of shorter fibres that are orientationally similar and spatially proximal, as in the case of Figure 59a. Despite some inaccuracies in the absolute number of fibres detected, other descriptors remain relatively faithful over n=30 simulations. Again, the number of detected branch points is over-estimated by the method, despite a lack of specific angular features.

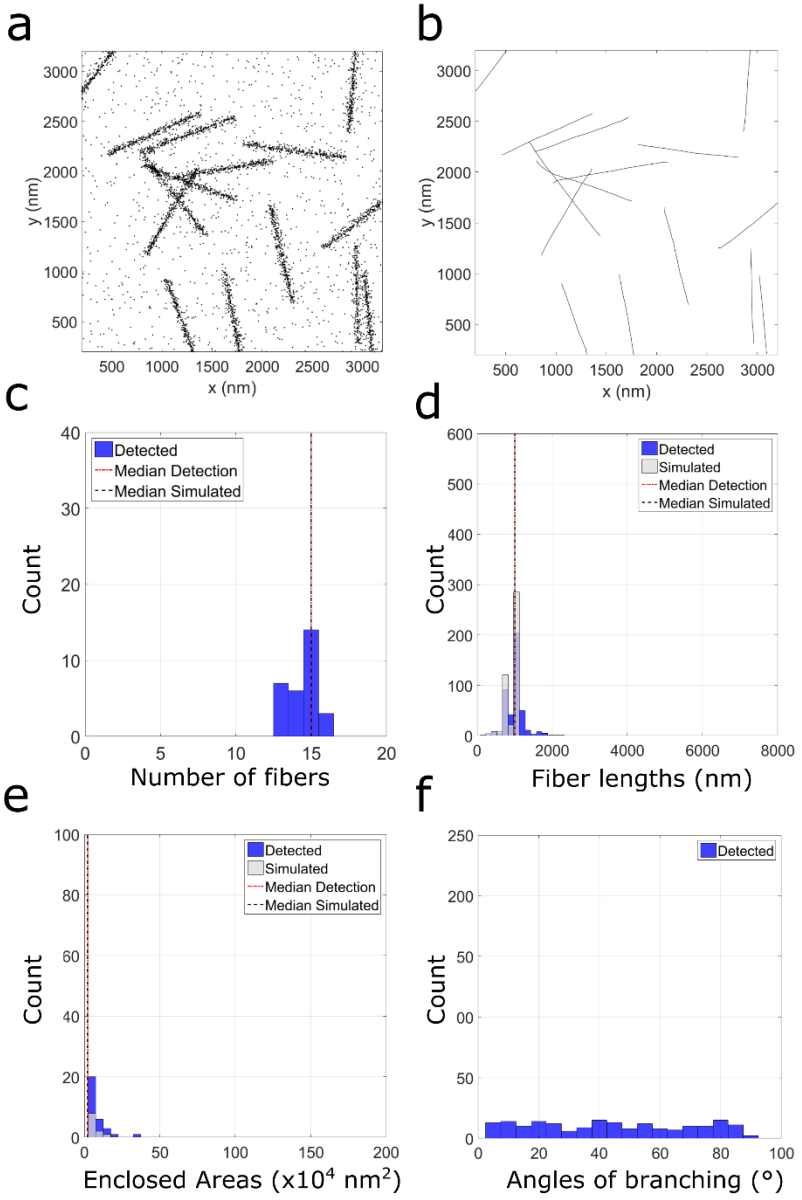

Figure 58: Fibre analysis (n=30 simulations) of 15 fibres of 1µm maximum length randomly placed within the ROI, generated using the standard condition. A representative input (a) of localisations and resulting fibrous (b) output. Histograms of number of fibres (c), fibre lengths (d), areas of enclosed regions (e) and angles of identified branching points (f).

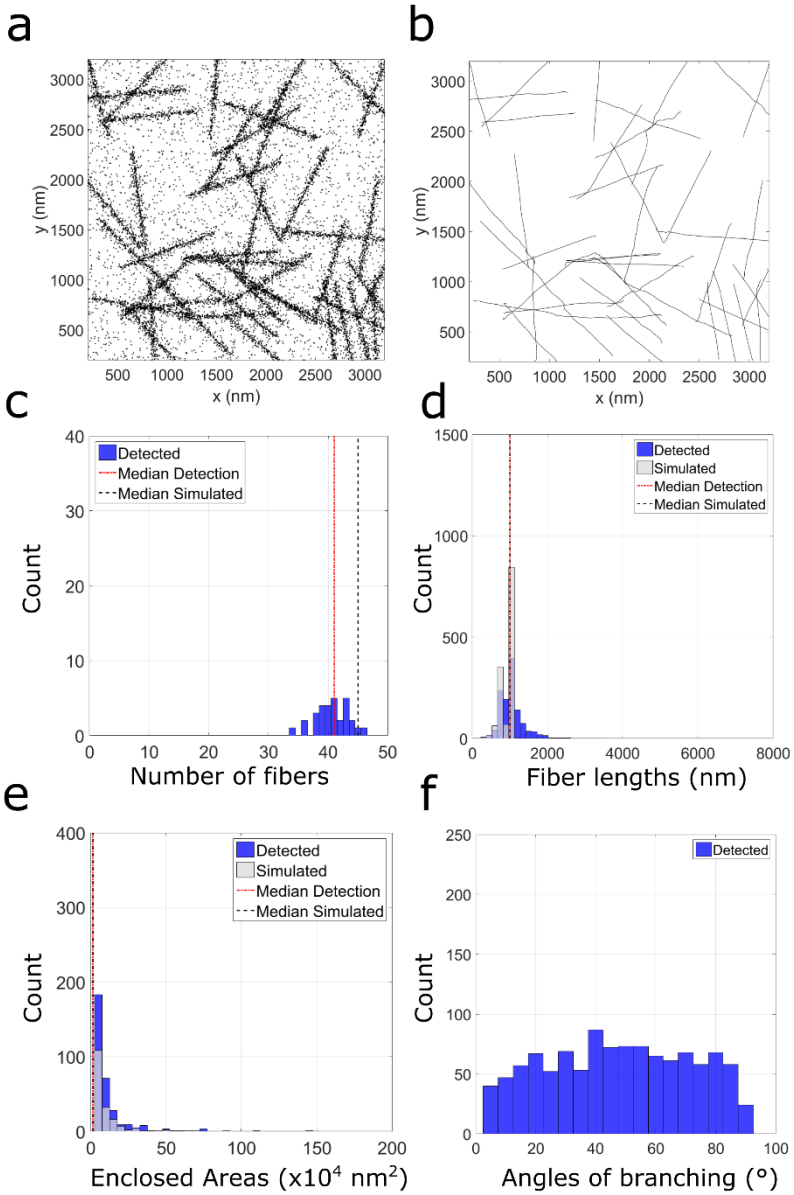

Figure 59: Fibre analysis (n=30 simulations) of 45 fibres of 1µm maximum length randomly placed within the ROI, generated using the standard condition. A representative input (a) of localisations and resulting fibrous (b) output. Histograms of number of fibres (c), fibre lengths (d), areas of enclosed regions (e) and angles of identified branching points (f).

4.3.5 Fibrous SPPs exhibiting curvature, randomised directions and orientations

The next level of complexity involved generating fibres exhibiting curvature. For this, the curved analogue of Figure 56a was generated, in which a global radius of curvature (R=8000 nm) was predefined. Fibres were randomly assigned either a clockwise or anticlockwise direction of arc propagation, generated per the standard condition. A typical input and analysed example are presented in Figure 60. The method is successful in following the curves of the fibres, as detected descriptors closely align with those simulated. A measure of the fibre curvature was also extracted, per Section 4.2.4.2, demonstrating that the method can accurately distinguish between linear and curved fibrous structures (Figure 61).

4.3.6 Clustered SPPs

To validate the methods performance of selectively tracing fibrous structures in pointillist data, simulations of a clustered distribution of molecules were performed. For this, 30 cluster maps were simulated (described in detail in Section 3.3.2), and the results summarised in Figure 62. The method seldom detects the presence of fibres in clustered SPPs, however in select cases fibres are indeed traced through multiple clusters. Despite simulating spatially random clusters, there exists an occasion that clusters will appear somewhat aligned, as in the case of Figure 62a. For this, the method identifies this preferential directionality of input points as a fibrous characteristic and thus traces a single fibre at this location (Figure 62b). Note that the areas of enclosed regions and the angles of branching fibres are not reported. This is due to no detections of these descriptors, owing to a lack of any enclosed regions or branching points detected.

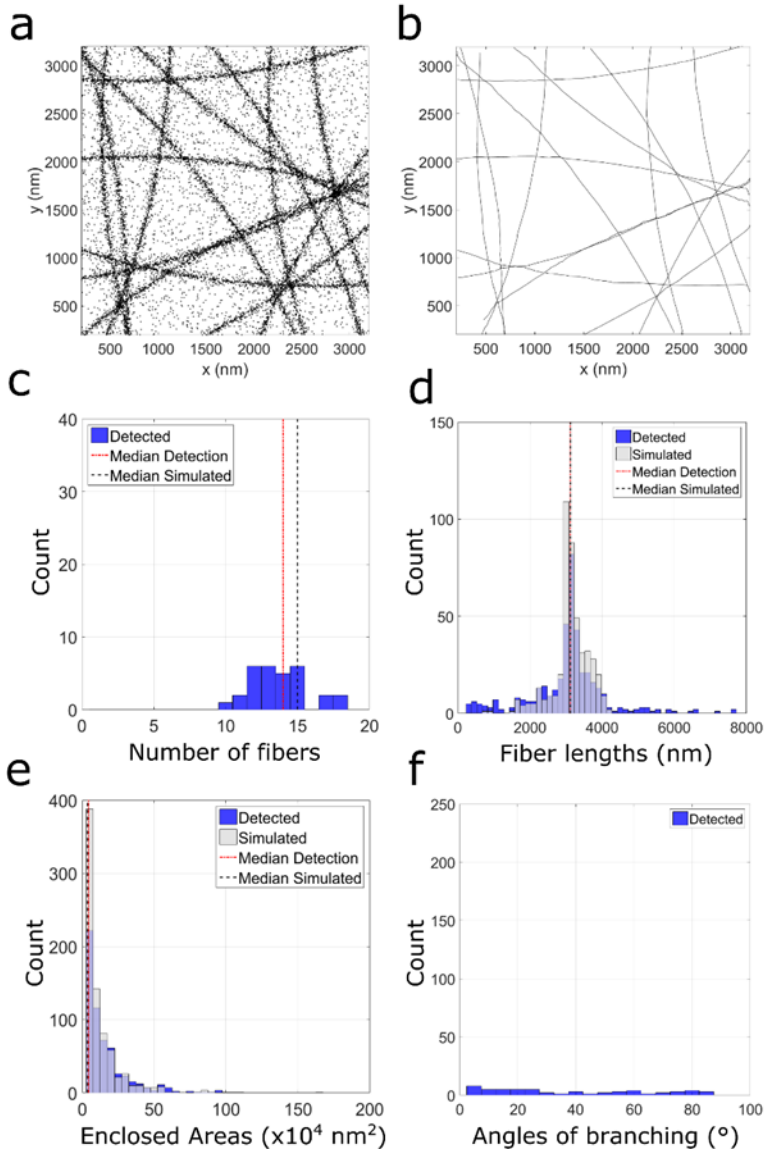

Figure 60: Fibre tracing (n=30 simulations) of fibrous SPPs with curvature, generated per the standard condition. A typical fibrous SPP (a) in which fibres possess heterogeneous directionalities and their concomitant output traces (b). Histograms of the number of fibres (c), fibre lengths (d), areas of enclosed regions (e) and the angles of branched fibres (f) are presented.

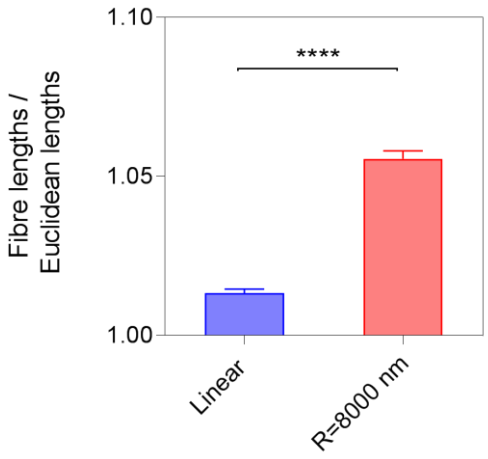

Figure 61: Estimating the degree of fibre curvature. Fibre curvatures were estimated for both the linear case (Section 4.3.2) and its curved analogue (Section 4.3.5). * = $p \leq 0.05$, ** = $p \leq 0.005$, *** = $p \leq 0.0005$, ****= $p < 0.0001$, ns = non-significant. Error bars represent the 95% confidence interval of the mean.

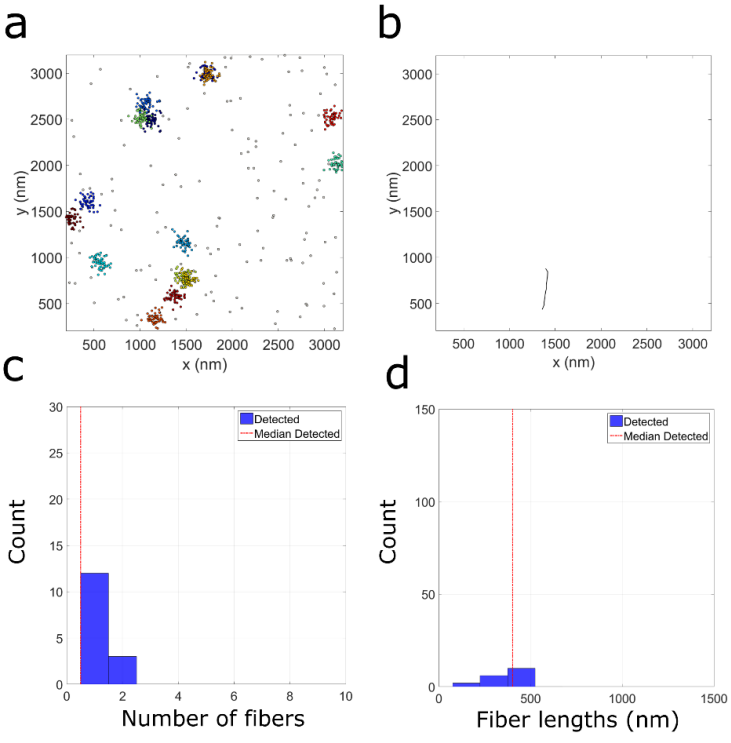

Figure 62: Fibre tracing (n=30 simulations) of clustered SPPs. A representative cluster input (a), in which clusters are pseudo coloured by simulated identification number and the resultant fibre landscape (b). The number of fibres detected (c) and the lengths of these detected fibres (d) is also presented.

4.4 Sensitivity of methodology to simulation parameters

To evaluate the performance of the method for various data inputs to account for diverse biological conditions, simulations of an increased CSR background noise, an increased number of fibrous localisations, poor labelling density and high localisation uncertainties were performed. For sensitivity analyses, the case of linear fibres spanning the entire ROI (Figure 56a) was considered.

4.4.1 Increased number of fibres

Simulations in which the number of fibres was incrementally increased were performed, whilst keeping all other parameters per the standard condition. The method was tested using simulations of 5 to 60 fibres (n=10 simulations per condition), with maximum lengths equal to 4.2 μm. The analysis revealed that the method is largely robust to this parameter, as most fibre descriptors align with simulated values (Figure 63a-c). The angle of branched fibres descriptor however is the least accurate (Figure 63d), despite there being a lack of signature branching angle.

4.4.2 Poor and inconsistent labelling density

The sensitivity of the method to a variety of labelling densities was also evaluated (Figure 64). For SMLM, this is an important experimental consideration, as differing techniques offer variable labelling of target structures, as previously discussed. To assess both poorly labelled structures and uneven densities, fibrous points were deleted at random at various

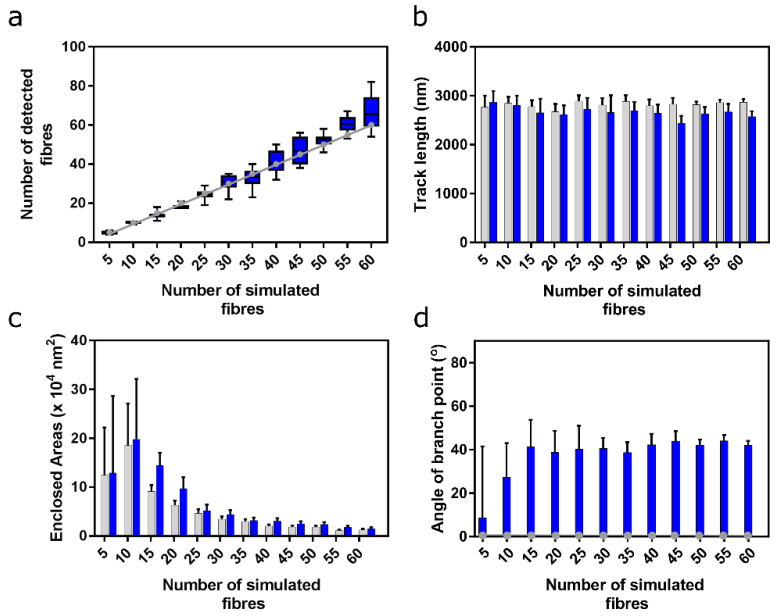

Figure 63: The effect of increasing the number of fibres within the ROI on the analysis. Errors represent the 95% confidence interval of the median for n=10 data sets per condition. For all cases (a-d) simulated and detected values are depicted grey blue respectively.

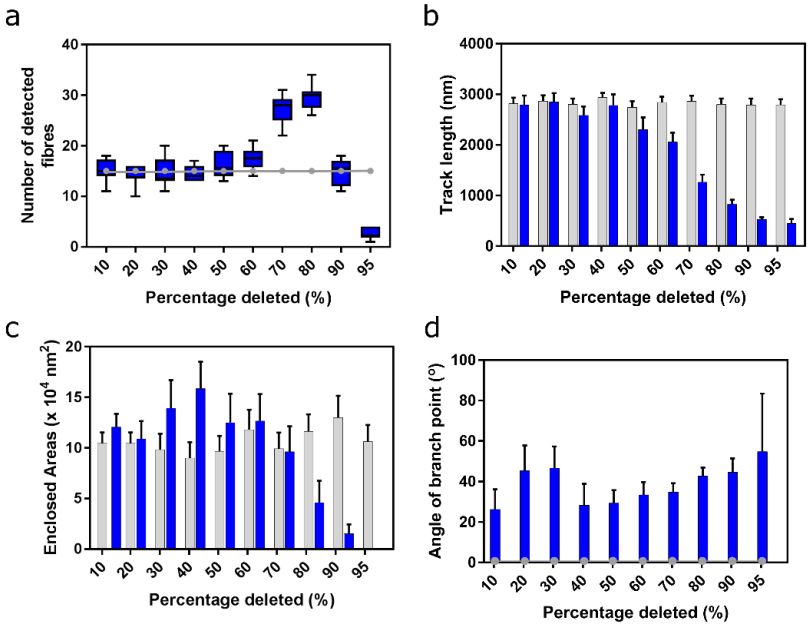

Figure 64: The effect of poor and uneven labelling density of fibrous structures on the analysis. Errors represent the 95% confidence interval of the median for n=10 data sets per condition. For all cases (a-d) simulated values and detected values are depicted grey and blue respectively.

percentages (10 - 95%) from the standard condition data set. Descriptors fail to accurately align with simulated values at ~ 60% deletion. Notably, the number of fibres detected as the percentage of labelling is reduced displays interesting behaviour. At 70 - 80% deletion, the number of detected fibres significantly increases as the poorer labelling has the effect of splitting fibres into smaller segments. At 90% onwards however, the number of detected fibres begins to decrease, as the simulated SPP begins to lose fibrous signatures.

4.4.3 Increased CSR background level

The method was further tested for simulations of an increased level of CSR background noise. Starting with a purely fibrous SPP (0% CSR) and rising to 70% noise, the limits of detection were evaluated (Figure 65), whilst keeping all other parameters per the standard condition. For most descriptors (Figure 65a-c), the method begins to fail at CSR percentages greater than 60%. At this level, fibrous signatures become indistinguishable from CSR localisations. In terms of experimental conditions, IRIS imaging typically produces a higher level of background signal, owing to the freely diffusive probe that remains in solution. dSTORM imaging however produces a low degree of background signal, when appropriate sample preparation is undertaken (outlined in Chapter 7). In both approaches however, the background signal is minimal compared to the cellular signals.

To demonstrate this, a representative IRIS and dSTORM image of the distribution of F-actin at the mature T cell immunological synapses were subject to a 3D intensity profile (Figure 66), thus highlighting the low background signals achievable with both methodologies. For both cases, the

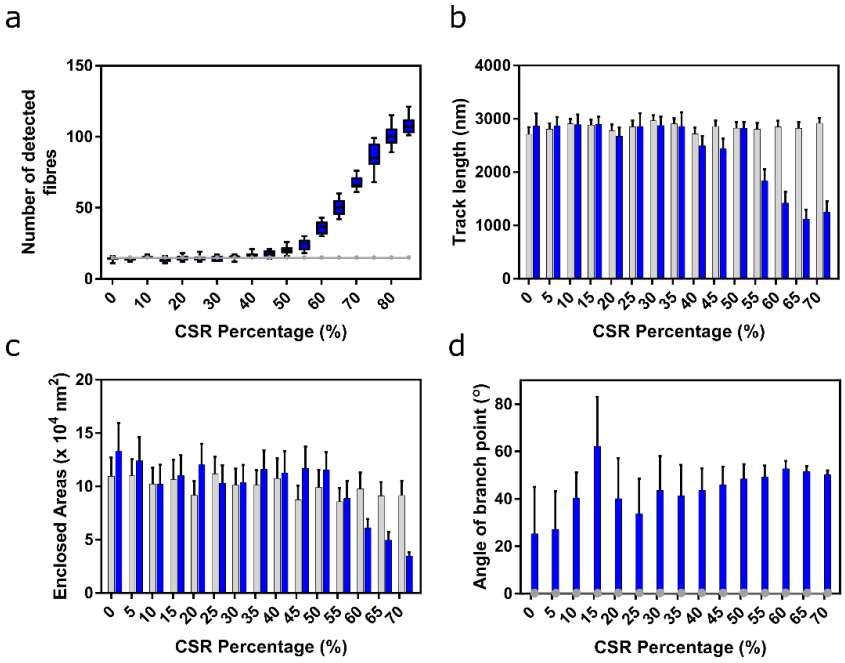

Figure 65: Examining the effect of an increased level of CSR background on the analysis. Errors represent the 95% confidence interval of the median for n=10 data sets per condition. For all descriptors (a-d) simulations and detections are depicted grey and blue respectively.

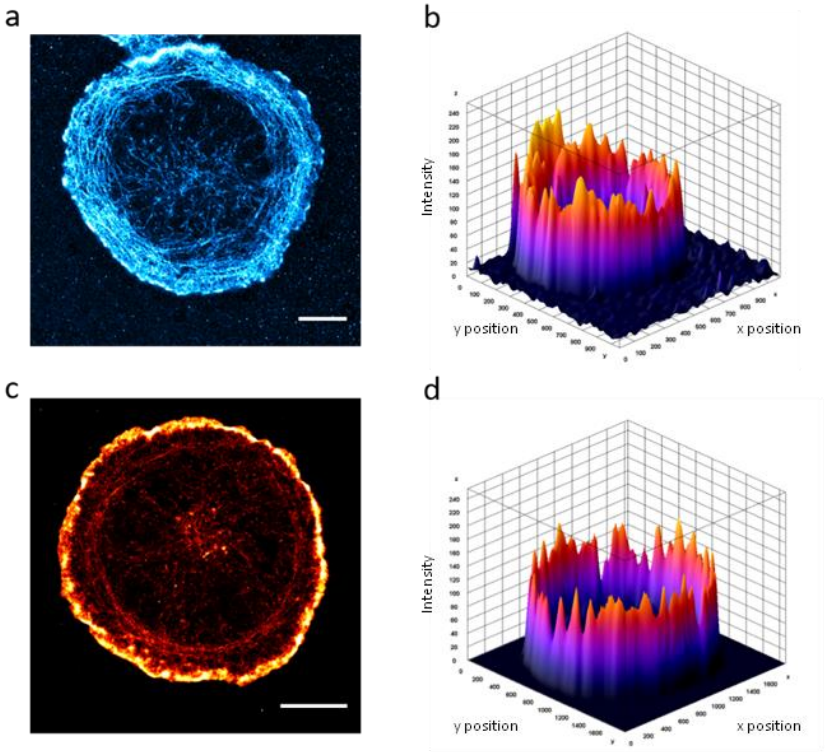

Figure 66: Background signal in experimental fibrous SPPs generated by SMLM. A representative dSTORM (a) and IRIS (b) image of actin at the mature T cell immunological synapse and their 3D intensity profiles (b, d respectively) are presented. Scale = 5 μm.

background intensity (calculated per pixel in ImageJ software) was < 60% of the total image intensity, and as such the analysis remains valid for both approaches. The intracellular contribution of background signal however is impossible to quantify.

4.4.4 Increased localisation uncertainty

Whilst the standard condition data sets present an average localisation precision of 16 nm (to align with experimental methods), other localisation-based methods of super resolution, for example dSTORM, often produce higher uncertainties in molecular positions. As such, the fibre analysis method was tested using simulations of increasing average localisation uncertainty, Figure 67. Results indicate that the method remains accurate up to ~ 40 nm localisation uncertainty, after which more fibres of shorter lengths are detected, as the labels err from their intended position (the target structure).

To demonstrate the methods suitability for both IRIS and dSTORM data, the distribution of localisation uncertainties across representative IRIS and dSTORM SMLM data sets was evaluated (Figure 68). Note that the IRIS acquisition produces significantly more localisations (as previously discussed), compared to the dSTORM method. For IRIS images of the actin cytoskeleton at the mature T cell synapse presented in this Thesis, the average localisation uncertainty was typically ~ 16 nm, whereas for dSTORM images ~ 25 nm localisation uncertainty is achieved. As such, the analysis method presented in this Chapter is capable of accurately tracing fibrous structures in both IRIS and dSTORM data sets.

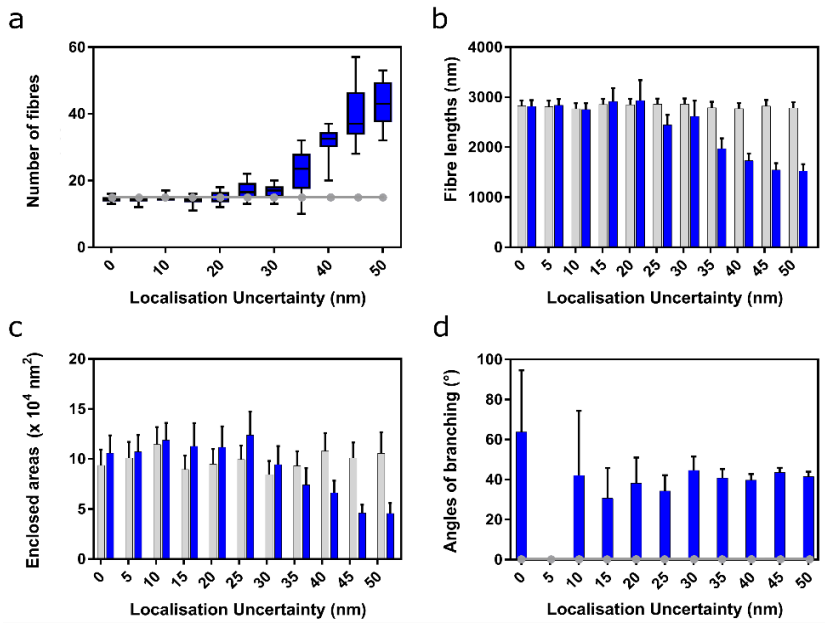

Figure 67: The effect of an increased localisation uncertainty on the fibre analysis method. Errors represent the 95% confidence interval of the mean for n=10 data sets per condition. For all cases (a-d) simulated values and detected values are depicted grey and blue respectively.

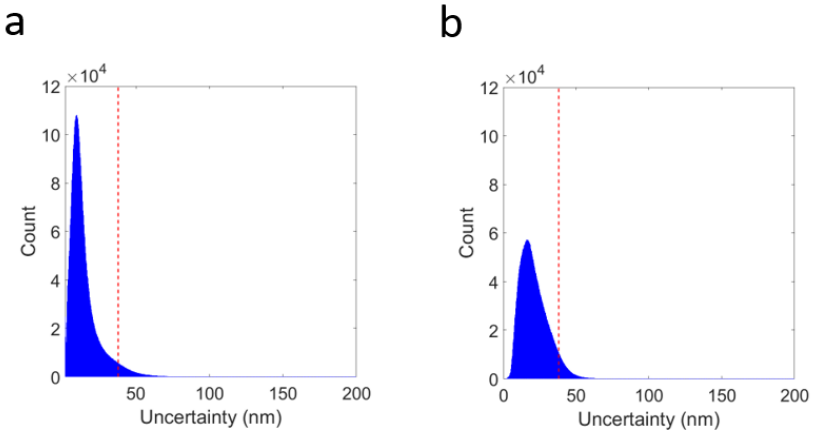

Figure 68: Histograms of the localisation uncertainties calculated in the ThunderSTORM plug-in to ImageJ. Localisation uncertainties of representative IRIS (a) and dSTORM (b) acquisitions (visually depicted in Figure 66a, c respectively). The red dashed line represents the maximum localisation uncertainty beyond which the analysis becomes inaccurate.

4.5 Results on experimental data

The methodology was next applied to the distribution of F-actin at the T cell immunological synapse, Figure 69. SMLM imaging was performed on a commercial N-STORM system operating in TIRF mode (see Methods), and images were reconstructed using ThunderSTORM software (see Methods). A total of n=30 regions were selected from either peripheral or central zones of the mature synapse and analysed. The results suggest a statistically significant doubling of the fibre density (Figure 69i) in peripheral regions compared to central regions ($p<0.005$). The peripheral fibres were also significantly longer than those detected within the central synaptic area (Figure 69ii, $p<0.0005$). No statistically significant difference in the average areas of enclosed regions was observed (Figure 69iii), however the number of enclosed regions in the peripheral ROIs was larger. No characteristic branching angle was detected within either peripheral or central regions (Figure 69iv), however significantly more branching points were detected in peripheral regions (Figure 69iv, $p<0.0005$).

As expected, the actin meshwork is denser in the peripheral regions of the mature T cell immunological synapse compared to the actin poor cSMAC. The longer fibres detected in the cell periphery compared to the centre could be explained by their differing curvatures, and the polymerisation activity of actin towards the cell periphery. As the number of fibres and their lengths are significantly smaller in the cSMAC, the number of regions of which the network encloses is significantly lower than those of the periphery. The analysis did not detect a characteristic 70° Arp 2/3 branching angle for central or peripheral ROIs. This could be due to the projection of the 3D information

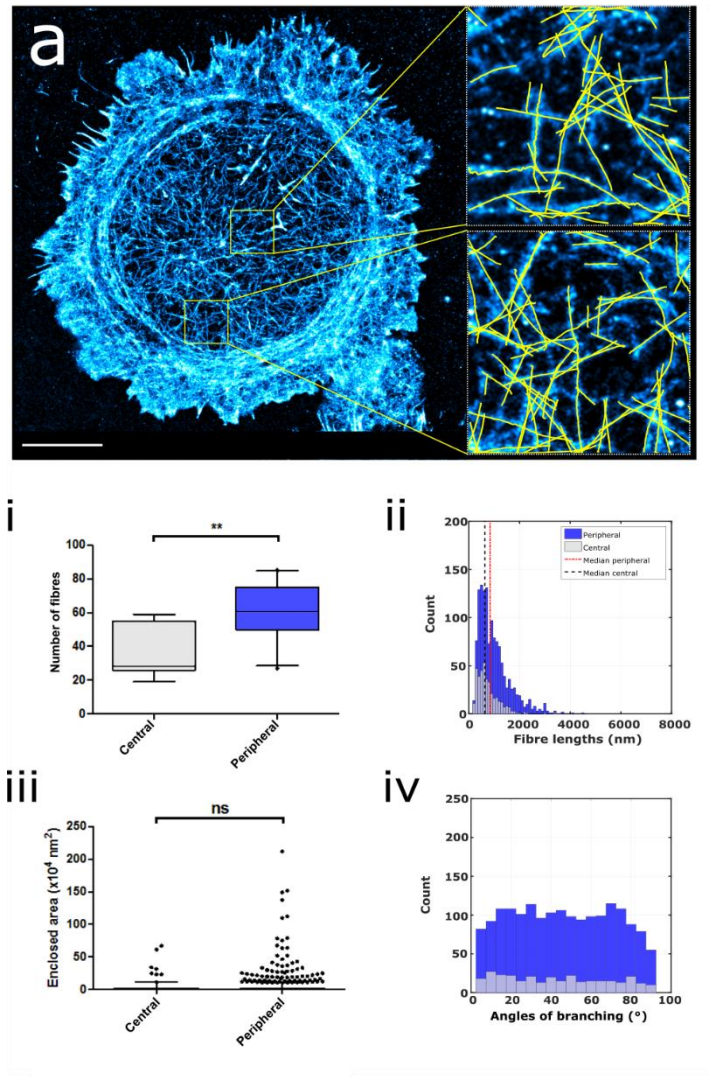

Figure 69: IRIS imaging and tracing quantification of the F-actin cytoskeleton at the mature T cell synapse. A representative IRIS image (a) of the T cell synapse with exemplar ROIs depicted with traces (yellow). The number of fibres (i), their lengths (ii), areas of enclosed regions (iii) and branching angles (iv) are presented for central (grey) and peripheral (blue) regions. N=3 cells, n=30 ROIs. Scale = 5 μm. * = $p \leq 0.05$, ** = $p \leq 0.005$, *** = $p \leq 0.0005$, ****= $p < 0.0001$, ns = non-significant. Error bars represent the 95% confidence interval of the median.

onto a 2D plane, thus producing differing branching angles. The number of branch points was however increased at the cell periphery, the location at which Arp 2/3 and its NPFs are enriched.

To test the methods capability of detecting differing actin architectures, the control (Figure 69) Jurkat T cells were pharmacologically perturbed by use of Cytochalasin D (see Methods). As previously discussed Cytochalasin D results in a net depolymerisation of actin networks and has found use in cancer therapy for example. A representative IRIS image of a Cytochalasin D treated mature T cell synapse is presented in Figure 70a. A total of n=30 regions were selected from either peripheral or central zones of Cytochalasin D treated mature synapses and analysed. Similarly to the control condition, the number of fibres in the peripheral regions of Cytochalasin D treated cells was significantly increased compared to central regions (Figure 70i). The fibre lengths in the peripheral regions were modestly increased (Figure 70ii, $p<0.05$) and the areas of enclosed regions were not significantly different across the synapse zones (Figure 70iii). No characteristic branching angle was detected for both peripheral and central regions of the treated synapse (Figure 70iv), and no significant difference in the number of branching points across the synapse zones was detected.

Compared to untreated synapses, Cytochalasin D treated synapses presented significantly fewer fibres ($p<0.05$ and $p<0.0005$ for central and peripheral regions respectively) which are shorter in length ($p<0.0005$ for both central and peripheral regions). These shorter fibres that are sparser thus enclose significantly less regions than those of the control synapse ($p<0.05$ for both central and peripheral regions) and fewer branch points are detected ($p<0.005$).

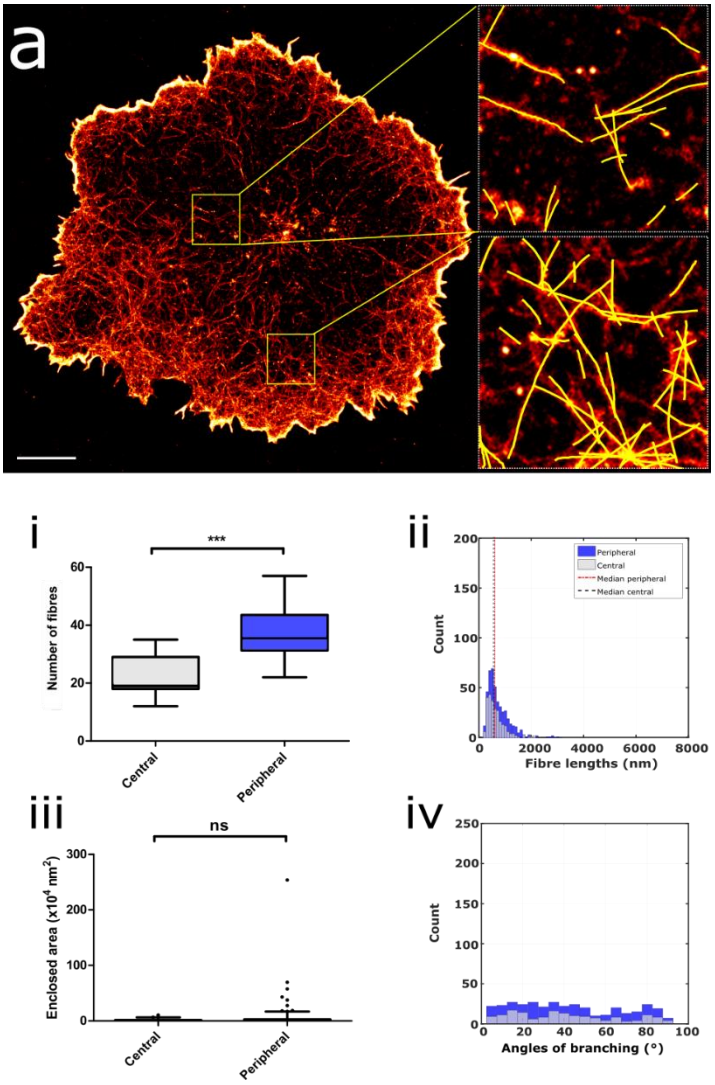

Figure 70: Examining the effect of Cytochalasin D on the F-actin network of the mature T cell immunological synapse. A representative IRIS image (a) of the Cytochalasin D treated T cell synapse with exemplar ROIs depicted with traces (yellow). The number of fibres (i), their lengths (ii), areas of enclosed regions (iii) and branching angles (iv) are presented for central (grey) and peripheral (blue) regions. N=3 cells, n=30 ROIs. Scale = 5 μm. * = $p \leq 0.05$, ** = $p \leq 0.005$, *** = $p \leq 0.0005$, ****= $p < 0.0001$, ns = non-significant. Error bars represent the 95% confidence interval of the median.

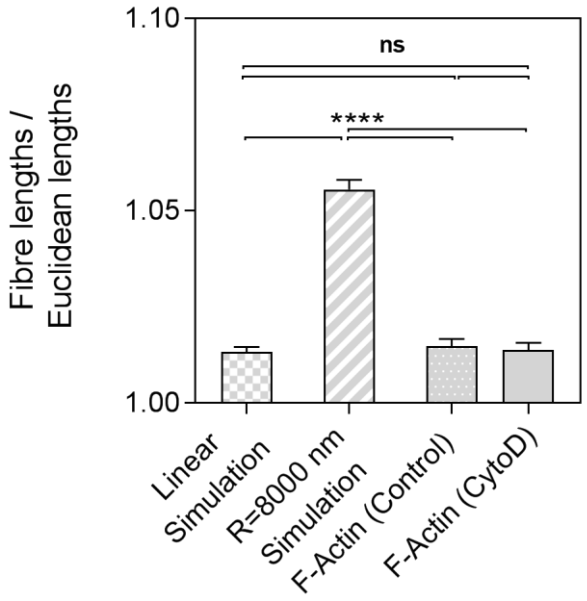

Figure 71: Estimations of fibre curvatures. Curvatures of fibres detected in the linear simulation (Section 4.3.2), curved simulation (for which R = 8000 nm, Section 4.3.5), all n=30 ROIs of peripheral and central ROIs of the control (Figure 69) and Cytochalasin D treated (Figure 70) synapses. * = $p \leq 0.05$, ** = $p \leq 0.005$, *** = $p \leq 0.0005$, ****= $p < 0.0001$, ns = non-significant. Error bars represent the 95% confidence interval of the median.

A measure of curvature can be extracted from the analysis, as previously discussed. Briefly, this consists of calculating the ratio of the fibre detected length and the Euclidean distance from its start and end co-ordinates. In terms of the biological study, the addition of Cytochalasin D did not appear to impact the fibre curvature. Within the ROI size selected, ($3 \times 3\ \mu m^2$), the fibrous network is largely composed of linear fibres, Figure 71.

4.6 Summation of presented results

In this Chapter, an analysis method capable of tracing fibres through pointillist data has been developed. This method takes as input the list of localised molecular co-ordinates, rather than a pixelated image, and is thus fundamentally different to other fibre tracing methods routinely used in pixelated data sets. As such, judging its performance against pre-existing methods is challenging. Analysing the pointillist data directly is an importance advance and will allow for more flexibility for future SMLM data sets. The method presented in this Chapter builds upon the previously described Angular K-function, enabling a local description of the fibrous SPP. The method was validated against numerous simulations of varying actin architectures, providing accurate descriptions of the number of fibres, fibre lengths, areas of enclosed regions and numbers/angles of branching points.

The method is largely robust to an increased CSR background level, localisation uncertainty and poor and inconsistent labelling density and is thus suitable for the study of the actin cytoskeleton via either dSTORM or IRIS. Importantly, whilst the nanoscale distribution of actin is the focus of this Thesis, the developed methods are readily applicable to other structures such as microtubules, provided that the input remains an SPP. Further, the ThunderSTORM plug-in to ImageJ was chosen for image reconstruction owing to its comparatively high performance, as previously discussed, however localisations generated by alternative fitting algorithms can be readily applied to the methods.

The experimental results in this Chapter highlight the methods ability to discern differing actin architectures, within the same cell, and upon

pharmacological disruption via Cytochalasin D. At the peripheral regions of the mature T cell synapse of untreated cells, the method detected a denser population of fibres which were of longer lengths, compared to those detected within central regions. Together, these more numerous and longer fibres enclosed more regions in the cell periphery than in the cell centre. A characteristic 70° Arp 2/3 driven branching angle was not however detected in experimental data. This could be due to the projection of the 3D network onto the 2D plane for TIRFM imaging. These key trends remained within the Cytochalasin D treated synapses, excluding the number of detected branching points which remained unchanged across the synaptic area of treated cells. Compared to control cells, Cytochalasin D treated cells displayed fewer, shorter fibres that together enclosed less regions. The number of detected branching points was also significantly reduced upon Cytochalasin D mediated actin disruption, compared to the untreated cells. These results agree with the net depolymerising function of Cytochalasin D and provide quantitative measures, on the nanoscale, of the local effects of pharmacological treatment upon the actin cortex.

Chapter 5 The interplay between F-actin, α-actinin and LAT at the T cell synapse

5.1 Introduction

A suite of analysis tools dedicated to the study of fibrous structures generated by SMLM have been developed in previous Chapters. These tools will be applied to the study of F-actin at the T cell immunological synapse in E6.1 Jurkat T cells (control) and α-actinin KO cells in the forthcoming Chapter. Both control and α-actinin KO cells are first subject to a macroscale analysis, deciphering the effect of α-actinin KO on cell proliferation and rates of successful synapse formation in 2D, fixed samples. Diffraction limited methods are firstly employed to provide a general overview of the organisation of F-actin in both cell types. By use of super resolution microscopy and fibre analysis methods developed in the context of this Thesis, the precise quantification of the actin cytoskeleton in control and α-actinin KO immunological synapses will be presented.

Dynamic and precise remodelling of the actin cytoskeleton plays a critical role in immunological synapse formation and has been shown to be important in the regulation of membrane protein diffusion and clustering of

transmembrane proteins via the Picket Fence model. Owing to its importance in T cell activation, its long cytoplasmic tail and controversy surrounding its recruitment to the immunological synapse, the spatial organisation of the transmembrane protein LAT will be subject to a macroscale and nanoscale analysis in the final sections of this Chapter, in control and α-actinin KO cells.

To investigate the co-organisation of actin and LAT at the immunological synapse of control and α-actinin KO cells, dual colour SMLM will be performed on 2D, fixed samples. Such information could provide information pertaining to the Picket Fence model of Kusumi, in which transmembrane proteins such as LAT can be corralled by the actin meshwork and temporally confined into specific microdomains. Specifically, the effect of the ABP α-actinin upon the delimiting function of the actin membrane skeleton will be assessed in the context of LAT clustering at the T cell immunological synapse.

5.2 A macroscale study of F-actin at the T cell immune synapse in control and α-actinin KO cells

To investigate the role of α-actinin on the macroscale organisation of F-actin at the T cell immunological synapse, the ACTN1 gene of Jurkat E6.1 T cells was knocked out via CRISPR-Cas9. The α-actinin KO cells were provided by Dr. David Williamson, and characterised by Dr. George Ashdown (Ashdown et al., 2017). The authors found that when screened for ACTN1 expression by Western blot, ACTN1 expression was substantially reduced, Figure 72.

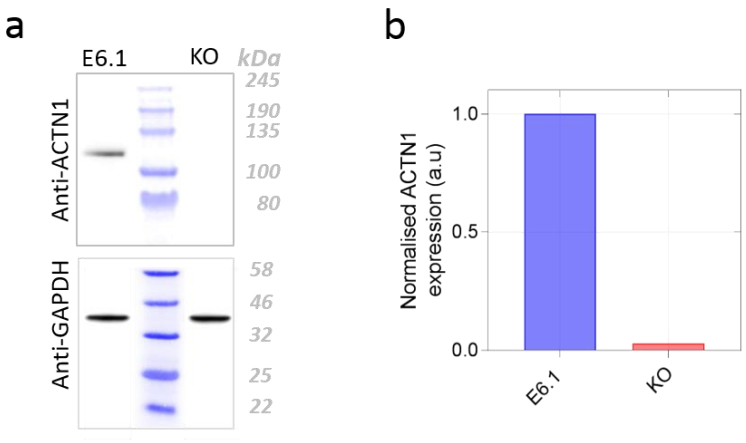

Figure 72: CRISPR-Cas9 KO of ACTN1 in Jurkat E6.1 T cells. Control and α-actinin KO cells were screened for ACTN1 expression via Western blot (a) and results normalised to the control expression levels (b). The loading control anti-Glyceraldehyde 3-phosphate dehydrogenase (GAPDH) was used owing to its high and ubiquitous expression. Figure modified from (Ashdown et al., 2017).

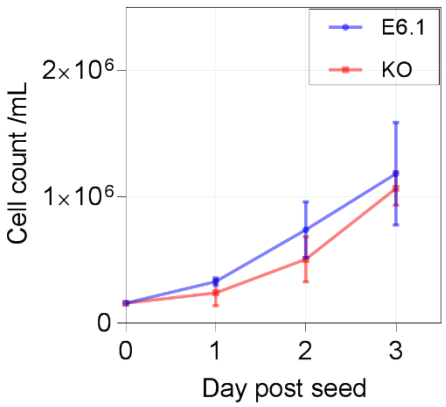

Figure 73: The effect of α-actinin KO on cell proliferation. Control (Jurkat E6.1) and α-actinin KO cells were initially seeded to the same density, and growth was monitored via a haemocytometer for up to 3 days post seeding. Results originate from 3 independent experiments. Error bars represent the 95% confidence interval of the mean.

5.2.1 Cell proliferation and synapse characterisation

To assess the effect of the α-actinin KO on cell proliferation, cells were counted using a haemocytometer in 3 independent experiments (Figure 73). The concentration of control cells doubled per day, a trend which was recapitulated in the α-actinin KO cells, despite a slight lag.

5.2.2 Macroscale analysis of the organisation of F-actin in control and α-actinin KO cells via TIRFM

To verify that α-actinin KO did not impair the mechanism of synapse formation, both the control and α-actinin KO cells were activated. To facilitate TIRFM, artificial T cell synapses were formed against anti-CD3 and anti-CD28 antibody coated coverslips (see Methods). Both control and α-actinin KO cells were allowed to form mature immunological synapses and were chemically fixed 8 minutes post-activation. After permeabilisation, cells were stained for F-actin using Alexa Fluor® 647 Phalloidin and imaged (see Methods). Both brightfield and standard single channel TIRFM was performed (Figure 74). Whilst both control and α-actinin KO cells were able to form synapses (96% and 87% synapse success rate for control and α-actinin KO respectively), α-actinin KO synapses presented significantly different morphologies (n=50 cells in 3 independent experiments). Quantification of brightfield images via the ImageJ measure tool revealed that α-actinin KO synapses were of smaller areas and smaller perimeters (Figure 75a, b). Although, the ellipticities of α-actinin KO synapses were unchanged compared to controls (Figure 75c).

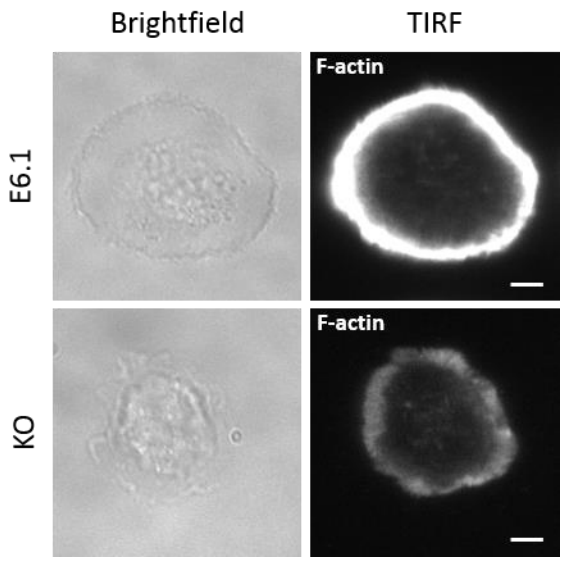

Figure 74: Representative (from n=50 cells) Brightfield and TIRF images of both control (E6.1) and α-actinin KO (KO) synapses. Scale = 5 μm.

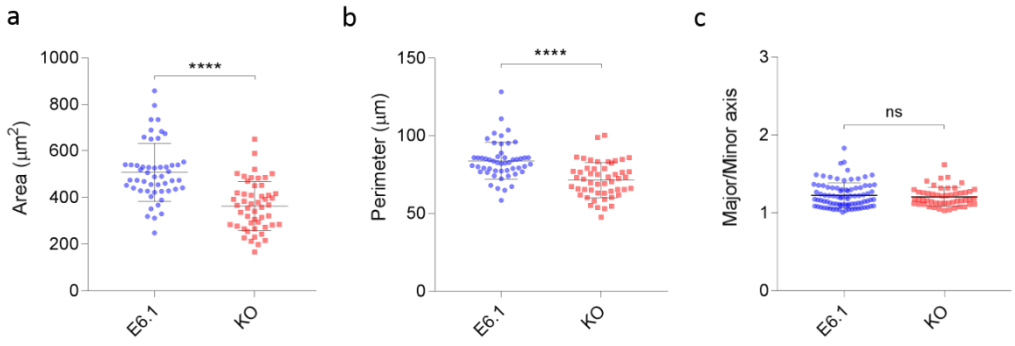

Figure 75: Synapse characterisation in control (E6.1) and α-actinin KO cells. In 2D, fixed samples, synapse areas (a), perimeters (b) and ellipticities (c) were quantified for n=50 cells in 3 independent experiments using the ImageJ measure tool. * = $p \leq 0.05$, ** = $p \leq 0.005$, *** = $p \leq 0.0005$, ****= $p < 0.0001$, ns = non-significant. Error bars represent the 95% confidence interval of the mean.

Owing to the crosslinking ability of α-actinin and its ability to simultaneously interact with the actin cytoskeleton and several transmembrane proteins, such as CD3, synapse morphology is altered upon α-actinin KO. The area of the mature synapse was significantly reduced from 508.4 ± 17.5 μm^2 (for control cells) to 363.9 ± 14.7 μm^2 (for α-actinin KO cells). The perimeter of α-actinin KO synapses was also significantly reduced from 84.8 ± 1.7 μm for control synapses to 71.5 ± 1.6 μm for α-actinin KO synapses. Synapse ellipticities were not however impacted upon α-actinin KO. By silencing α-actinin, which is known to co-localise with F-actin at the immunological synapse, it is suggested that the spreading phase of synapse maturation is perturbed. The mechanical properties of the cytoskeleton can be in part attributed to the linkage of α-actinin and F-actin, and by removing this physical linkage the cytoskeleton the α-actinin KO cells are proposed to produce less force when interacting with the anti-CD3/anti-CD28 coated coverslip, thus resulting in smaller synapses of smaller perimeters.

To investigate the global distribution of F-actin at the immunological synapse, TIRFM images were next quantified (Figure 74). For this, the Radial Intensity Profile (RIP) plugin to ImageJ was used to determine the intensity of F-actin as a function of the distance from the cell centres, in both control and α-actinin KO cells (Figure 76). At the synapse centre, there was no significant difference in the intensity of F-actin for control and α-actinin KO cells on the macroscale. Since the cSMAC is actin-poor, and α-actinin is known to translocate to the synapse periphery upon synapse maturation, α-actinin KO does not appear to alter the macroscale organisation of actin at the cSMAC. Traversing to the synapse peripheral and distal (p- and dSMAC) regions however, there was a significant reduction in F-actin intensity in α-actinin KO cells compared to the control. This finding is consistent with prior studies, in

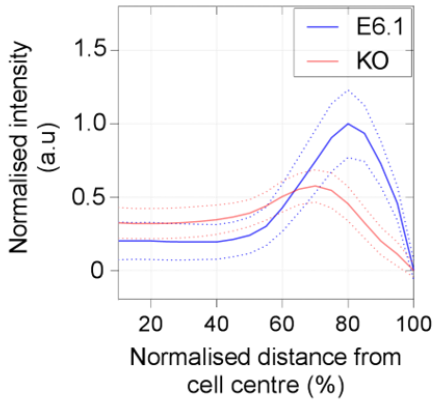

Figure 76: Quantification of F-actin intensity in control (E6.1) and α-actinin KO cells. Cells were stained for F-actin using Alexa Fluor® 647 Phalloidin and imaged via Brightfield and TIRF microscopy (Figure 74). Scale = 5 μm. RIPs were calculated for normalised distances to cell centres, and fluorescence normalised by that of the control maximum (b). Error bars represent the 95% confidence interval of the mean for n=50 cells in 3 independent experiments.

which α-actinin strongly co-localises with F-actin at the immunological synapse and as such, α-actinin KO results in a loss of intensity in actin rich regions such as the p- and dSMAC. Moreover, α-actinin KO appears to subtly disperse the SMAC organisation of the immunological synapse, resulting in a global loss of F-actin intensity and a disrupted architecture. α-actinin has been previously shown to be a regulator of T cell activation and immunological synapse formation, and as such, appears to influence the architecture of F-actin and SMAC formation, consistent with previous reports (Gordón-Alonso et al., 2012).

During immunological synapse formation, cortical actin is highly dynamic and plays multifarious roles that ultimately influence cell signalling and response. As a regulator of actin dynamics, the presence of α-actinin at the

immunological synapse has been found to be important in the formation of SMAC zones. Although historically SMAC formation was considered as a pre-requisite for sustained TCR signalling, these radially symmetric domains are not universally observed, as previously discussed. As such, although α-actinin KO disrupts SMAC compartments, α-actinin KO cells remain capable of forming effective synapses, albeit of differing actin organisation.

5.3 The global nanoarchitecture of F-actin at the T cell immune synapse in control and α-actinin KO cells

To assess the disruption of the actin cytoskeleton in α-actinin KO cells on the nanoscale, super resolution microscopy was employed. For this, dSTORM imaging of Alexa Fluor® 647 Phalloidin in control and α-actinin KO cells was performed (see Methods). Although the IRIS approach to SMLM provides a superior labelling density to that achievable with dSTORM, acquisition time is increased by ten-fold when performing IRIS experiments. Further, IRIS probes are not commercially available, nor have they been extensively used for the study of the actin cytoskeleton at the T cell synapse. Since the analysis methods developed in the context of this Thesis have been validated using both IRIS and dSTORM data, dSTORM was chosen as the preferred technique for the remainder of this Chapter. To obtain an overall description of the nanoscale disruption of F-actin in α-actinin KO cells, the conventional Ripley's H-function and the Angular H-function (Section 2.5.4 and Chapter 3 respectively) were first applied to the pointillist data, providing information on the global properties of the actin meshwork.

5.3.1 α-actinin KO does not affect the overall fibrousness of F-actin at the T cell immunological synapse

For SMLM images, n = 30 (3 x 3 μm^2) ROIs were selected for analysis (from n = 5 cells). A representative example of the distribution of F-actin in control (Figure 77a) and α-actinin KO (Figure 78a) immunological synapses is presented. The H(r)-function demonstrates that the data is clustered for both control and α-actinin KO cells (Figure 77i, Figure 78i respectively). The power spectral density reveals that there is no periodicity in the conventional H(r)-function (Figure 77ii, Figure 78ii), indicating a spatially non-regular arrangement of actin at the immunological synapse of control and α-actinin KO cells. Examining the non-shifted H(α)-function curves (Figure 77iii, Figure 78iii) and their spectra (Figure 77iv, Figure 78iv) reveals that whilst the fibres are not perpendicular to one another, there is a non-random organisation of F-actin in both control and α-actinin KO cells. The shifted H(α)-function curves (Figure 77v, Figure 78v) and their spectra (Figure 77vi, Figure 78vi) provide evidence for a fibrous distribution, evidenced by a single peak at 180°. Note that this peak is low and broad, a hallmark of fibre curvature (see Chapter 3). Interestingly, no significant difference in the height (defined as the distance from the curve minimum to its maximum) of the shifted H(α) peaks of control and α-actinin KO conditions was calculated, suggesting that α-actinin KO does not affect the global fibrousness of F-actin, or indeed the fibre curvature (p = ns), at the immunological synapse.

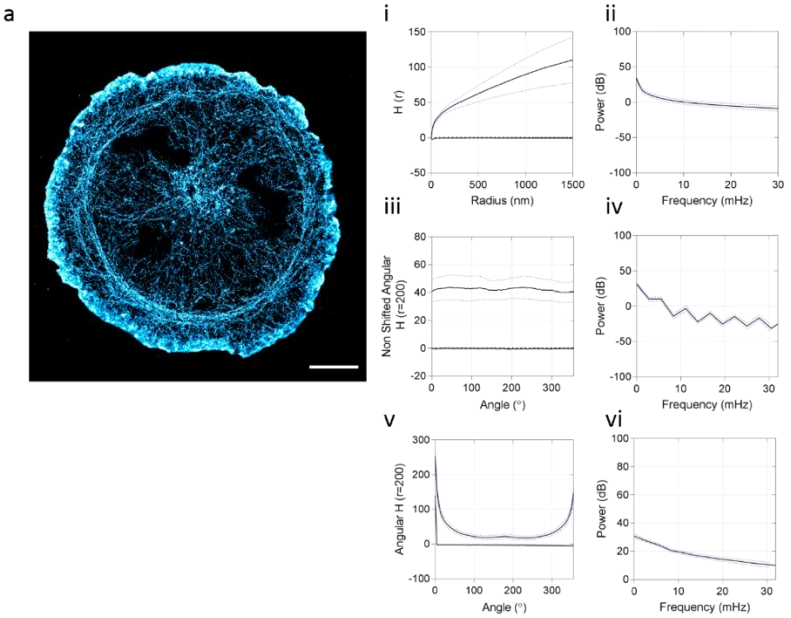

Figure 77: Quantification of the global nanoscale organisation of F-actin in control synapses. Representative dSTORM reconstruction, scale = 5µm (a). Conventional H(r) analysis was performed (i) and power spectra generated (ii). Ripley's H(α) curves (iii), their power spectra (iv) and their shift corrected analogues (v) and (vi) are also displayed. CSR envelopes are also depicted (i, iii, v) to test randomness.

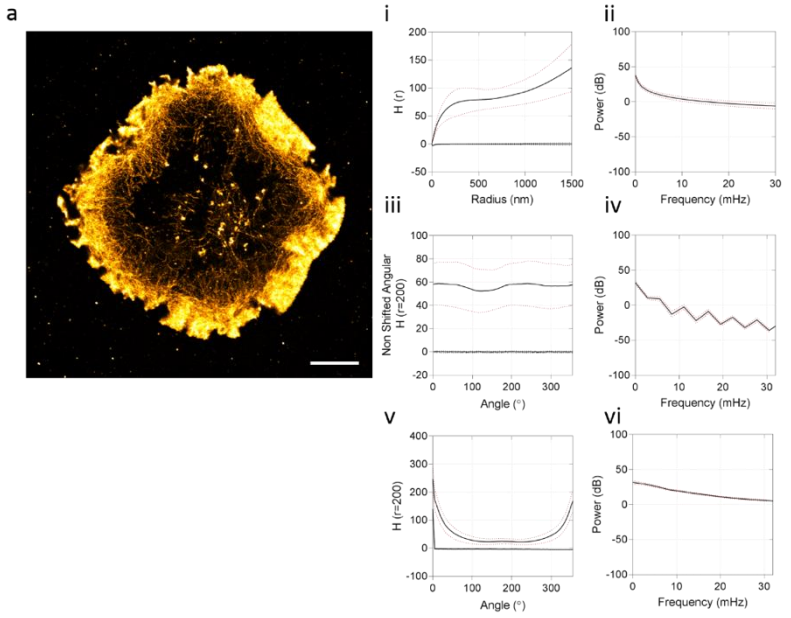

Figure 78: Quantification of the global nanoscale organisation of F-actin in α-actinin KO synapses. Representative dSTORM reconstruction, scale = 5µm (a). Conventional H(r) analysis was performed (i) and power spectra generated (ii). Ripley's H(α) curves (iii), their power spectra (iv) and their shift corrected analogues (v) and (vi) are also displayed. CSR envelopes are also depicted (i, iii, v) to test randomness.

5.3.2 α-actinin KO disrupts the preferential directionality of F-actin at distinct zones of the T cell immunological synapse

In control, mature immunological synapses, cortical actin at the synapse periphery is abundant, whereas towards the cSMAC actin is depleted, as previously discussed. Moreover, F-actin has been shown to form a series of concentric ring like structures towards the synapse periphery, whose structure has been recently implicated in TCR microcluster dynamics (Murugesan et al., 2016). To demonstrate the methods capability of detecting this dual population of actin fibres at the synapse centre and periphery, the post-processing of the non-shifted H(α)-function curves stage was implemented (described in Section 3.6). Briefly, the angular discrepancy between the cell centre and the ROI centre is calculated, and the H(α) values are translated by this discrepancy, to align with the reference vector <0,1>. The translated H(α) curves are summed and normalised, to assess the preferential directionality of fibres with respect to the reference vector. In this way, multiple ROIs within the synapse centre or periphery can be compared, and the dominance of radial or tangential fibrous structures across the entire data set can be evaluated.

For control cells, a dominance of radial fibrous structures was observed at the synapse centre, consistent with previous reports. This preferential directionality is evidenced by peaks in the translated H(α) curves at 0° and 180°, Figure 79a. For peripheral regions however, a dominance in tangential structures was observed, evidenced by peaks in the translated H(α) curves at 90° and 270° (Figure 79b). For the α-actinin KO cells however, this preferential directionality was disrupted at the synapse centre and periphery, with no district preferential orientation of F-actin fibres (Figure 79c, d). Previous live cell super resolution studies have reported a reduction in orderedness in actin flow upon α-actinin KO in Jurkat T cells, via SIM and spatiotemporal image

correlation spectroscopy (STICS) analysis (Ashdown et al., 2017). Whilst actin appeared to be flowing in a retrograde fashion in the α-actinin KO cells during mature synapse formation similarly to the control cells, the flow of actin was increased, and flow vectors of a more disordered nature compared to the control synapses. The authors hypothesise that through its crosslinking function and ability to stabilise pre-existing actin filaments, α-actinin KO results in individual filaments of higher velocities and scrambled directionalities. The authors further state that owing to loss of α-actinin, actin fibres can be more readily transported inwards from the dSMAC to the synapse centre in a polymerisation driven fashion, albeit, such fibres lack co-organisation with the cortical actin mesh. Although the evidence presented in this Thesis cannot directly report on the dynamic nature of actin, the results presented in this section are indeed consistent with the observation of scrambled, less ordered actin flows upon α-actinin KO, evidenced by the perturbation of preferential directionalities of actin fibres at the mature T cell immunological synapse of α-actinin KO cells.

On the macroscale, upon α-actinin KO, a global loss of intensity of F-actin at the immunological synapse was observed, resulting in synapses of smaller areas and perimeters. Further, α-actinin KO appeared to significantly disrupt SMAC zones at the immunological synapse, producing a more dispersed cSMAC and a significantly depleted actin dSMAC. On the nanoscale, whilst α-actinin KO did not alter the degree of fibrousness of the actin cytoskeleton on the global scale, preferential directionalities (tangential for the peripheral and radial for the central regions) were disrupted. Whilst global properties of the actin nanoarchitecture were successfully extracted using the Angular H-function, information on the local scale is inaccessible. As such, the following

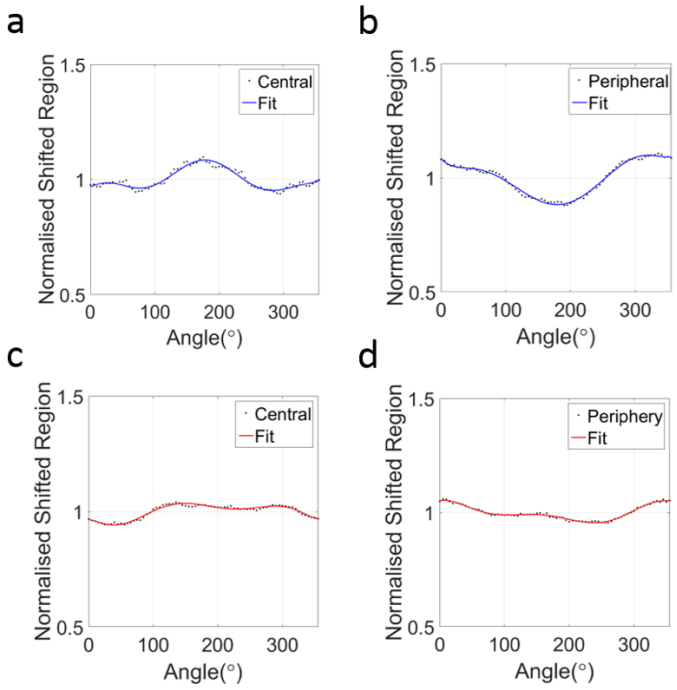

Figure 79: Quantification of the dominance in fibrous directionality in distinct zones of the immunological synapse for control and α-actinin KO synapses. An average of all post-processed H(α) curves for central (a, c) and peripheral ROIs (b, d) of control (depicted blue) and α-actinin KO (depicted red) synapses is presented. All data was fit to an 8th order polynomial.

sections will be dedicated to the study of individual filaments comprising the complex actin mesh via the fibre tracing method presented in Chapter 4.

5.4 The local nanoarchitecture of F-actin at the T cell immune synapse in control and α-actinin KO cells

To provide a local description, on a fibre by fibre basis, of the actin cytoskeleton in control and α-actinin KO cells, the presented fibre tracing algorithm (Chapter 4) was used for the data presented in Section 5.3. This method extracts the number of fibres, fibre lengths, areas of enclosed regions formed by actin fibre networks and filament branching angles.

A representative example (n=5 cells, n=30 regions) of the actin nanoarchitecture in control immunological synapses is presented in Figure 80a. Localisations from the selected ROI are presented, and the fibre traces overlaid, Figure 80b. Histograms for the number of fibres, fibre lengths, areas of enclosed regions and branching angles for all analysed regions are presented (Figure 80c-f). Central and peripheral regions were further separated to compare local differences in fibrous make-up across the spatially distinct synapse zones (Figure 81). A statistically significant doubling of the fibre density was observed in the synapse periphery compared to the central regions (Figure 81a). Fibres were also significantly longer in the synapse periphery (Figure 81b), which can be attributed to the continual polymerisation at the cell edge after the synapse has been established and matured. Together, these longer and more numerous fibres enclose more regions in the synapse periphery than the synapse centre ($p<0.005$), and the areas in which these networks enclose (Figure 81c) is smaller on average.

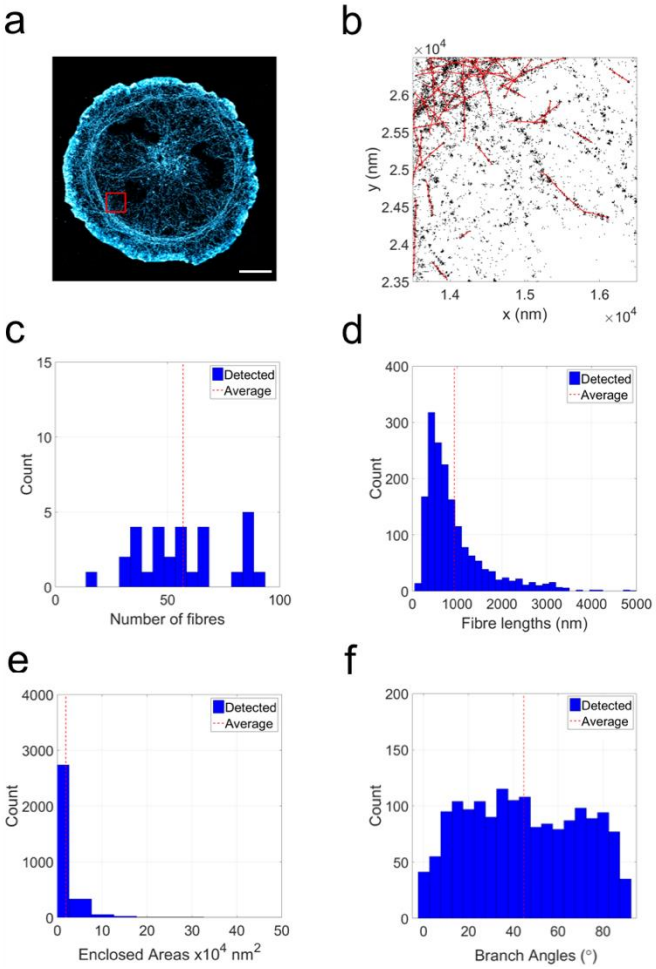

Figure 80: Quantification of the local nano organisation of F-actin in control synapses, n=30 ROIs. A representative dSTORM reconstruction, from which an exemplar ROI was extracted, and localisations plotted for method demonstration (b). Resulting fibre traces are depicted red (b). Histograms of number of fibres (c), fibre lengths (d), areas of enclosed regions (e) and angles of identified branching points (f) are presented with median values overlaid (red dashed line).

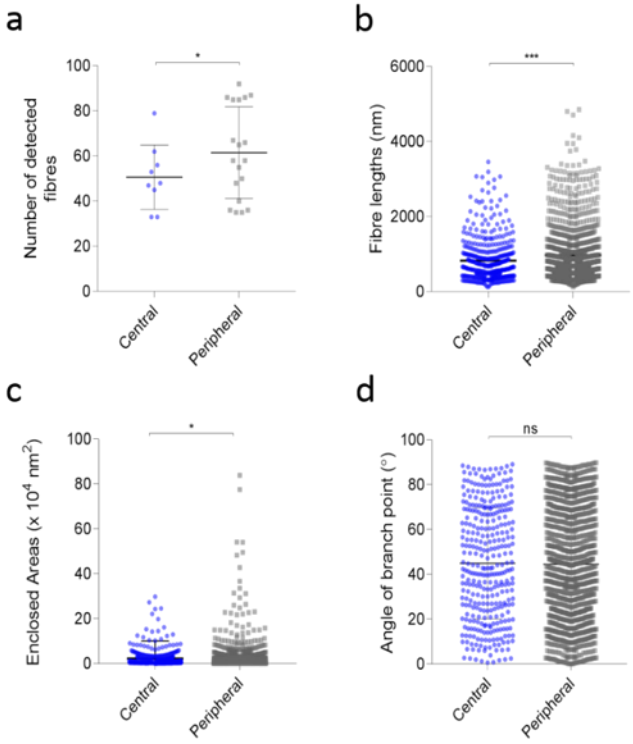

Figure 81: Comparison between central and peripheral ROIs at the immunological synapse of control cells. The number of detected fibres per ROI (a), the fibre lengths (b), areas of enclosed regions (c) and angles of branch points (d) are presented for the central and peripheral ROIs. * = $p \leq 0.05$, ** = $p \leq 0.005$, *** = $p \leq 0.0005$, ****= $p < 0.0001$, ns = non-significant. Error bars represent the 95% confidence interval of the mean.

A representative SMLM image (n=5 cells, n=30 regions) of the nanoscale distribution of F-actin at the immunological synapse of α-actinin KO cells is presented in Figure 82a. Localisations from the selected ROI are presented, and the fibre traces overlaid, Figure 82b. Histograms for the number of fibres, fibre lengths, areas of enclosed regions and branching angles for all analysed regions are displayed (Figure 82c-f). Central and peripheral regions were again separated to infer local properties of the actin mesh at these distinct synapse zones. Similarly to that of the control condition, the number of fibres was significantly increased at the synapse periphery for α-actinin KO cells

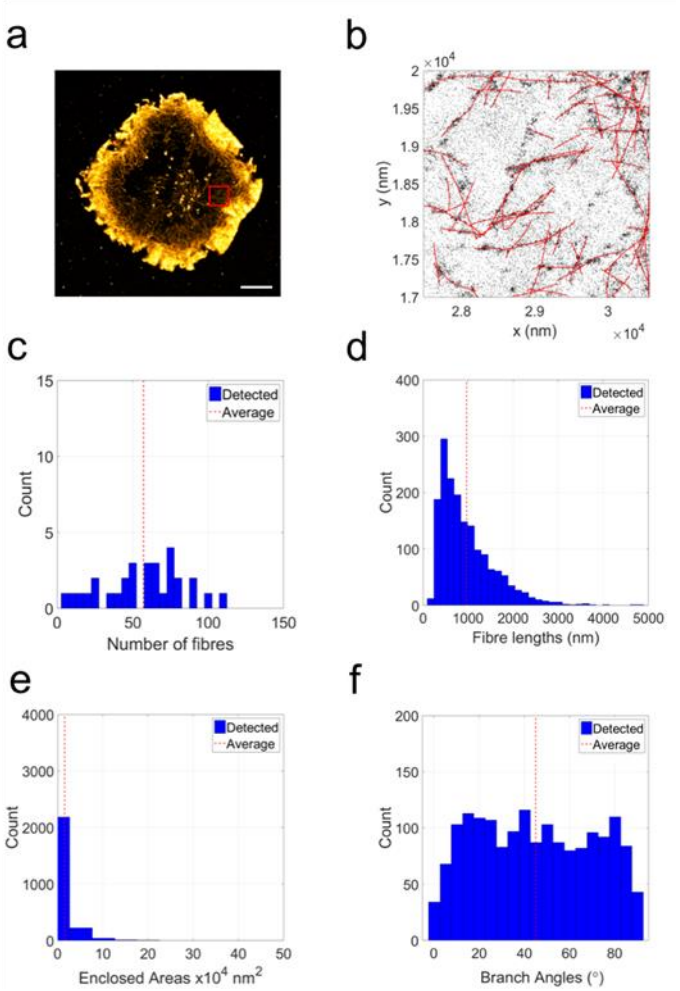

Figure 82: Quantification of the local nanoscale organisation of F-actin at the immunological synapse of α-actinin KO cells, n=30 ROIs. A representative dSTORM reconstruction, from which an exemplar ROI was extracted, and localisations plotted for method demonstration (b). Resulting fibre traces are depicted red (b). Histograms of number of fibres (c), fibre lengths (d), areas of enclosed regions (e) and angles of identified branching points (f) are presented with median values overlaid (red dashed line).

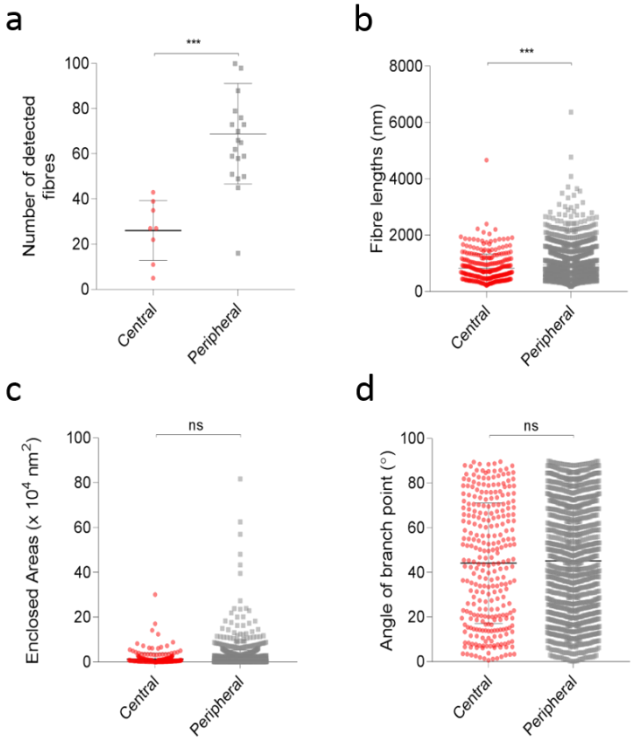

Figure 83: Comparison of central and peripheral regions at the α-actinin KO immunological synapse. The number of detected fibres per ROI (a), the fibre lengths (b), areas of enclosed regions (c) and angles of branch points (d) are presented for the central and peripheral ROIs. * = $p \leq 0.05$, ** = $p \leq 0.005$, *** = $p \leq 0.0005$, ****= $p < 0.0001$, ns = non-significant. Error bars represent the 95% confidence interval of the mean.

(Figure 83a). Furthermore, these fibres are significantly longer than those detected in the synapse centre, despite the areas of which they enclose remaining unchanged (Figure 83b, c respectively).

A comparison of the total fibrous population of actin between control and α-actinin KO cells revealed subtle differences in nano organisation (Figure 84). The number of detected fibres was significantly lower in α-actinin KO cells (Figure 84a). Whilst the total number of localisations per ROI was slightly higher for control cells (Figure 85), this did not translate to a substantially higher actin population. Since α-actinin acts to crosslink fibres into bundled

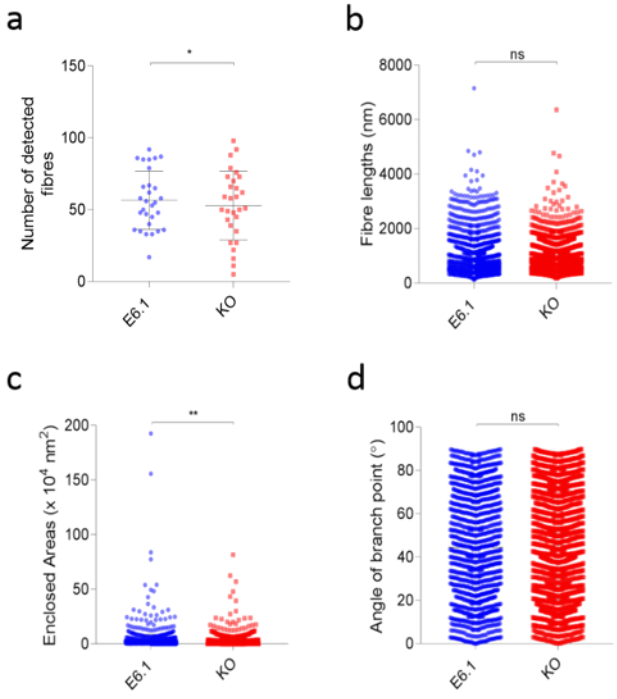

Figure 84 : Comparison of the local F-actin nanoarchitecture in control and α-actinin KO synapses. The number of detected fibres per ROI (a), the fibre lengths (b), areas of enclosed regions (c) and angles of branch points (d) are presented for the central and peripheral ROIs. * = $p \leq 0.05$, ** = $p \leq 0.005$, *** = $p \leq 0.0005$, ****= $p < 0.0001$, ns = non-significant. Error bars represent the 95% confidence interval of the mean.

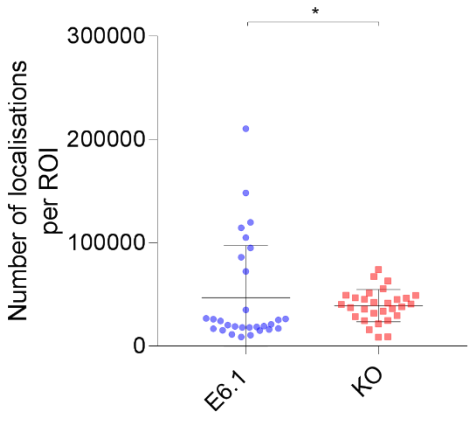

Figure 85 : Total number of localisations per ROI for all 30 analysed ROIs for control (E6.1) and α-actinin KO (KO) synapses. * = $p \leq 0.05$, ** = $p \leq 0.005$, *** = $p \leq 0.0005$, ****= $p < 0.0001$, ns = non-significant. Error bars represent the 95% confidence interval of the mean.

networks, it is suggested that upon α-actinin KO detected fibres are individual filaments, compared to the complex and multifarious architectures observed in the control cells, and are perhaps less likely to be concatenated in the post-processing stage of the algorithm. Hence, whilst consistent with the macroscale analysis, in which the intensity of F-actin is reduced upon α-actinin KO, only a subtle difference in the number of fibres detected was observed, as the method can essentially trace these individual filaments more successfully than those belonging to fibrous bundles. The fibre lengths also remained unchanged across all ROIs of control and α-actinin KO cells, Figure 84b. Since α-actinin does not act to promote polymerisation or conversely act to sever or depolymerise actin, α-actinin KO does not alter fibre lengths. A significant difference in the areas of enclosed regions was however observed upon α-actinin KO across the synaptic contact zone, on average (Figure 84c).

Comparing all central regions of control and α-actinin KO cells, significantly more fibres were detected for control cells (Figure 86a) despite their lengths remaining consistent (Figure 86b). The areas formed through the intersection of the actin mesh remained however unchanged (Figure 86c). Interestingly, in this case the number of enclosed regions for control and α-actinin KO cells was not statistically significantly different, despite there being more fibres in the control cells. This could be explained by the lack of preferential directionality of fibres within the synapse centre of α-actinin KO cells. Upon α-actinin KO, live cell studies have demonstrated that the actin flow speed is increased, and at the synapse centre, the directionality of filament flow vectors is scrambled, with respect to control cells (Ashdown et al., 2017). In this way, whilst the actin fibres are more numerous and indeed more ordered in the control synapse centre, owing to the scrambled directionalities of filaments in the α-actinin KO synapse centre, the number

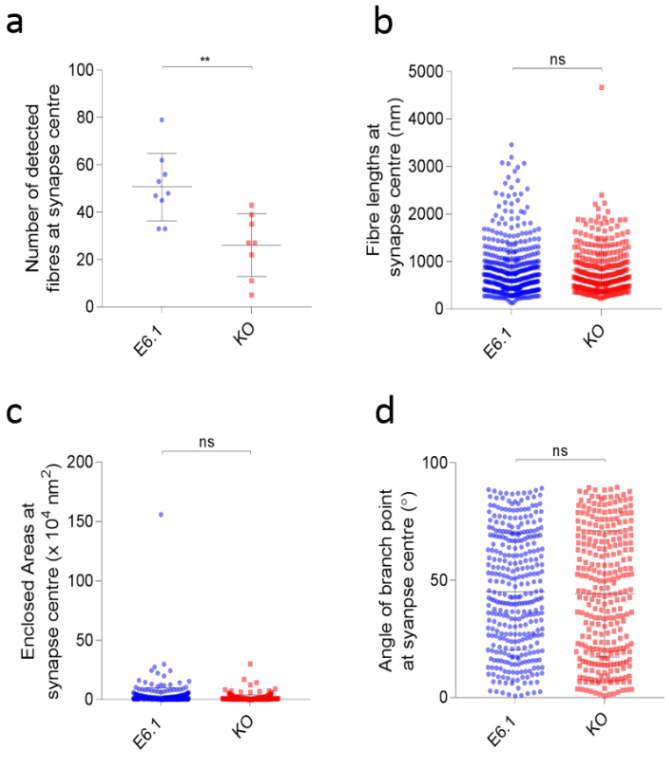

Figure 86: Comparison of the local F-actin nanoarchitecture in central regions of control and α-actinin KO synapses. The number of detected fibres per ROI (a), the fibre lengths (b), areas of enclosed regions (c) and angles of branch points (d) are presented for the central and peripheral ROIs. * = $p \leq 0.05$, ** = $p \leq 0.005$, *** = $p \leq 0.0005$, ****= $p < 0.0001$, ns = non-significant. Error bars represent the 95% confidence interval of the mean.

and areas of enclosed regions remains unchanged. Traversing to the cell peripheral regions, the number of fibres and their lengths remained unchanged upon α-actinin KO (Figure 87a, b respectively). The actin mesh size however was slightly but significantly altered in α-actinin KO cells, Figure 87c.

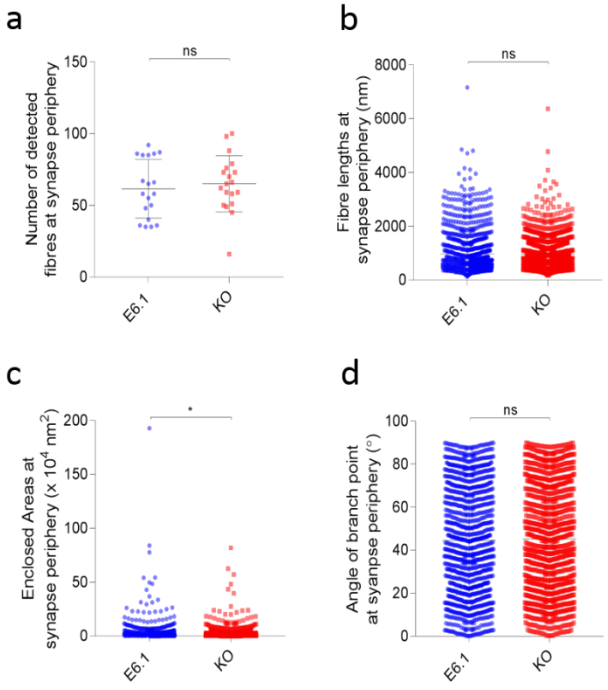

Figure 87: Comparison of the local nanoscale organisation of F-actin in peripheral regions of control and α-actinin KO synapses. The number of detected fibres per ROI (a), the fibre lengths (b), areas of enclosed regions (c) and angles of branch points (d) are presented for the central and peripheral ROIs. * = $p \leq 0.05$, ** = $p \leq 0.005$, *** = $p \leq 0.0005$, ****= $p < 0.0001$, ns = non-significant. Error bars represent the 95% confidence interval of the mean.

5.5 A macroscale analysis of the distribution of LAT in control and α-actinin KO cells at the T cell immune synapse

The adaptor protein LAT is essential for signalling through engaged TCRs, serves as a docking site for other adaptor and effector proteins and kinases and is critical for T cell development. As previously discussed, the phosphorylation of several molecules such as SLP-76 and Vav is LAT dependent, and the nanoscale organisation of transmembrane proteins such as LAT is influenced by the actin cytoskeleton at the T cell immunological synapse. Whilst it is recognised that LAT is indispensable for T cell signalling, it's vesicular and plasma membrane associated populations, and their roles in early and late T cell activation, remains a current subject of debate. Moreover, the influence of particular ABPs on the nanoscale organisation of LAT at the mature immunological synapse remains to be studied.

To examine the effect of modulating the organisation of the actin cytoskeleton via ABPs on the clustering behaviour of LAT at the immunological synapse, the macroscale distribution of LAT in control and α-actinin KO cells was firstly analysed. For this, artificial synapses were formed for control and α-actinin KO cells against anti-CD3 and anti-CD28 antibody coated coverslips, to facilitate TIRFM. Synapses were allowed to mature before being chemically fixed and permeabilised (see Methods). Both brightfield and standard single channel TIRFM was performed (Figure 88a).

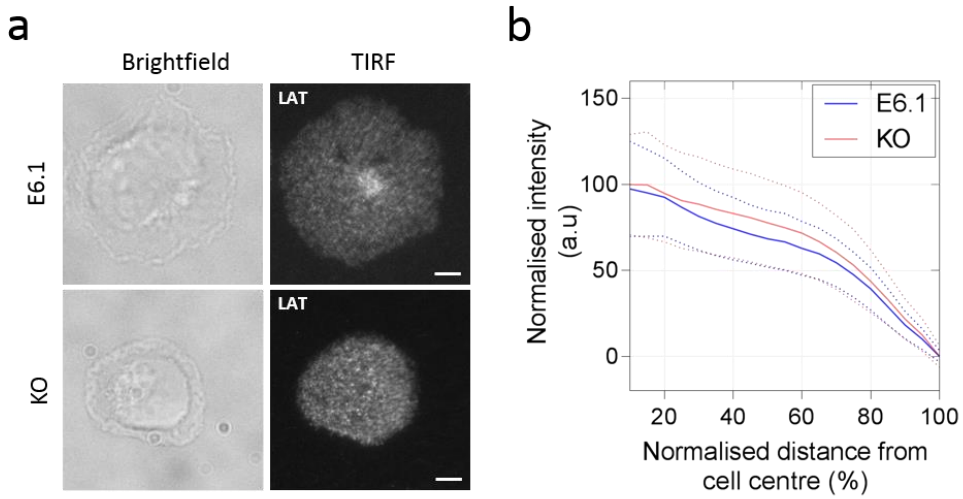

Figure 88: Quantification of LAT intensity in control (E6.1) and α-actinin KO (KO) cells. Cells were stained for LAT and imaged via Brightfield and TIRF microscopy (a). Scale = 5 μm. RIPs were calculated for normalised distances to cell centres, and fluorescence normalised by that of the maximum (b). Error bars represent the 95% confidence interval of the mean for n=50 cells in 3 independent experiments.

The intensity of LAT at the immunological synapse of control and α-actinin KO cells as a function of the distance from the cell centre was quantified via RIPs, for n=50 cells in 3 independent experiments (Figure 88b). The distribution of LAT does not appear to change upon α-actinin KO, on the macroscale. Moreover, LAT appears to be evenly distributed across the synapses. LAT containing signalling microclusters have been previously shown to be of 200 – 500 nm diameter, when assessed by diffraction limited microscopy (Balagopalan et al., 2015). Since this diameter corresponds to the best theoretical lateral resolution of a diffraction limited system, super resolution methods must be employed to estimate the size and distribution of LAT clusters at the immunological synapse.

5.6 The global nano organisation of LAT at the T cell immune synapse in control and α-actinin KO cells

To assess the nanoscale organisation of LAT at the immunological synapses of control and α-actinin KO cells, PALM was employed. For this, cells were transfected with the photoswitchable fusion construct LAT-mEos2 (see Methods) and allowed to recover for 36 hours prior to imaging. Synapses were again formed against anti-CD3 and anti-CD28 antibody coated coverslips and allowed to mature before being chemically fixed. A total of n = 30 (3 x 3 μm^2) ROIs from n = 5 cells per condition were chosen for analysis. Representative PALM images of LAT in control and α-actinin KO synapses are presented in Figure 89a and Figure 89d respectively. Localisations from a representative ROI are also presented for both conditions (Figure 89b and Figure 89e respectively). The distribution of LAT was assessed by Ripley's H-function (Figure 89c, f for control and α-actinin KO conditions respectively) for all ROIs. In agreement with previous studies, LAT appears to be clustered at the control immunological synapse. Whilst LAT appears to also be clustered at the α-actinin KO immunological synapse, the extent to which the localisations are clustered is significantly lower than that of the control cells. This is evidenced by the significantly lower H(r) value for r ≈ 100 nm, for the α-actinin KO cells. The spatial scale over which the data is clustered however appears to be similar for both conditions, despite a slight broadening of the H(r) curve for the α-actinin KO data. This could suggest that LAT clusters in the α-actinin KO cells present larger radii, or that there is more variation in the clustered nature of LAT for this condition.

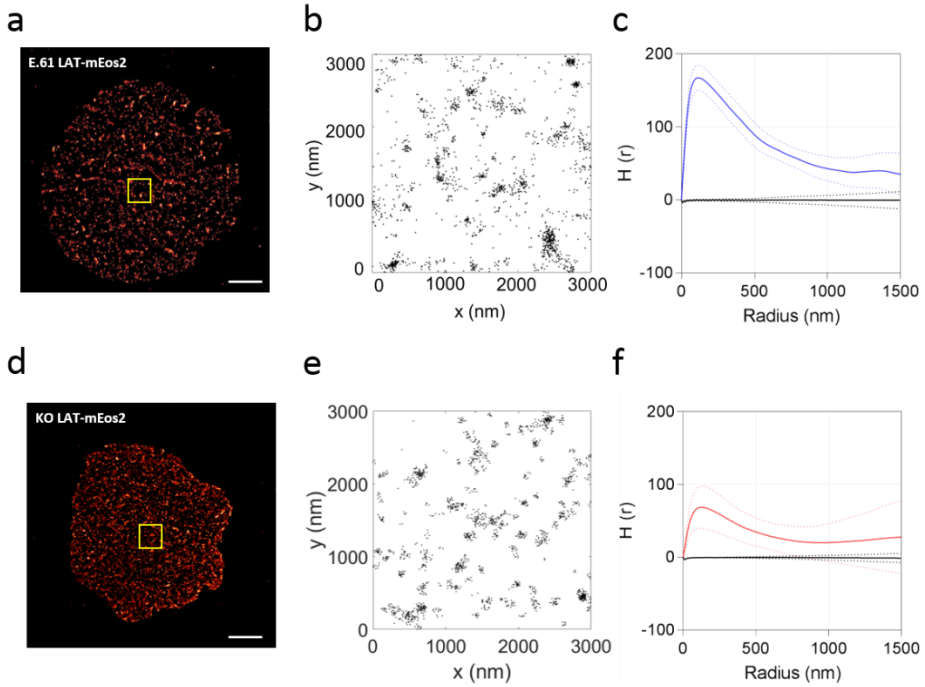

Figure 89: Quantification of the global nanoscale organisation of LAT in control and α-actinin KO cells. Representative examples of PALM reconstructions of LAT at the control (a) and α-actinin KO (d) synapses, scale = 5µm. Localisations of the exemplar ROIs are plotted (b, e) and Ripley's H(r)-function analysis, with CSR envelopes depicted black, presented (c, f). Errors represent the 95% confidence interval of the mean.

5.7 The local nano-organisation of LAT at the T cell immune synapse in control and α-actinin KO cells

To provide a local description of the distribution of LAT in control and α-actinin KO cells, a Bayesian cluster analysis algorithm was used for the same data presented in Section 5.6. This method extracts the number of clusters, cluster radii, number of localisations per cluster and the percentage of localisations in clusters. By use of this method, the clustering behaviour of LAT in the presence or absence of α-actinin can be quantitatively assessed, on a cluster by cluster basis.

A representative PALM image (n = 30 ROIs, n = 5 cells) of the distribution of LAT at the control immunological synapse is presented in Figure 90a, from which the selected ROI was chosen for method demonstration. Localisations from the selected ROI were plotted (Figure 90b), and the Bayesian score heat map (Figure 90c) from which the highest scoring R-T combination was extracted and used for cluster identification presented (Figure 90d) (methodology detailed in Section 2.5.4). Histograms of the number of clusters, cluster radii, number of localisations per cluster and the percentage of total localisations in clusters is presented for all ROIs (Figure 90e-h respectively). The average number of clusters per 3 x 3 μm^2 was reported as 32.23 ± 2.45, of 29.96 ± 3.25 nm average radii. The average number of localisations per cluster was measured as 37.25 ± 3.79, with 63.49 ± 2.85% of localisations attributed to clusters. The number of clusters per μm^2 was slightly higher than that of previous reports (27 ± 1 cluster/ 3 x 3 μm^2), although a different analysis strategy was adopted in this particular study, and the absolute values remain reasonably similar. Central and peripheral regions of the synapse were next separated to compare local differences in LAT clustering across the spatially distinct synapse zones (Figure 91). Consistent with the macroscale analysis, no significant differences were found in the number of clusters, cluster radii, number of localisations per cluster and the percentage of total localisations in clusters detected in the synapse centre and periphery (Figure 91a-d respectively). Whilst LAT clusters follow an outward flow from the cSMAC to the pSMAC upon maturation, they also exhibit an inward flow from the synapse periphery towards recycling endosomes located at the synapse centre. As such, this net translocation of LAT clusters could result in a lack of preferential localisation of LAT clusters at the mature synapse.

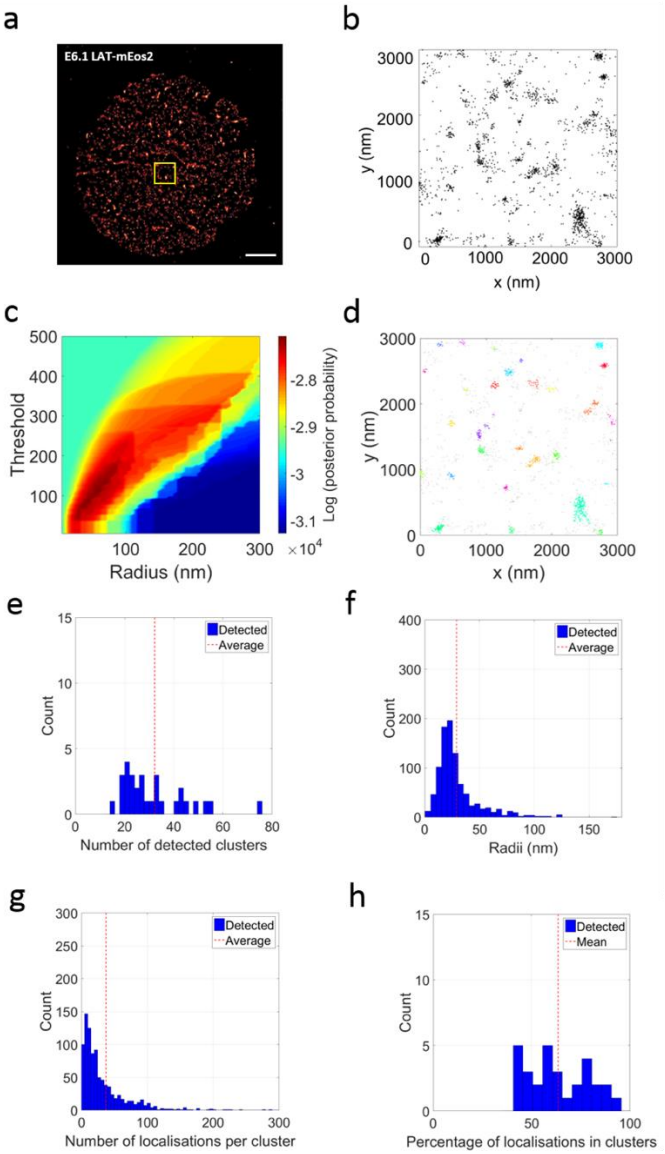

Figure 90: Quantification of the nanoscale clustering of LAT at the control immunological synapse via PALM and Bayesian cluster analysis. A representative PALM reconstruction is presented (a), scale = 5μm, and an exemplar ROI depicted. Localisations from this given ROI are presented (b) and analysed, producing a heat map (c) of the cluster proposals. The highest scoring combination of the radius and threshold was extracted and used to produce the cluster map (d), in which clusters are pseudo coloured. Histograms of the number of clusters (e), cluster radii (f), number of localisations per cluster (g) and the percentage of molecules in clusters (h) is presented.

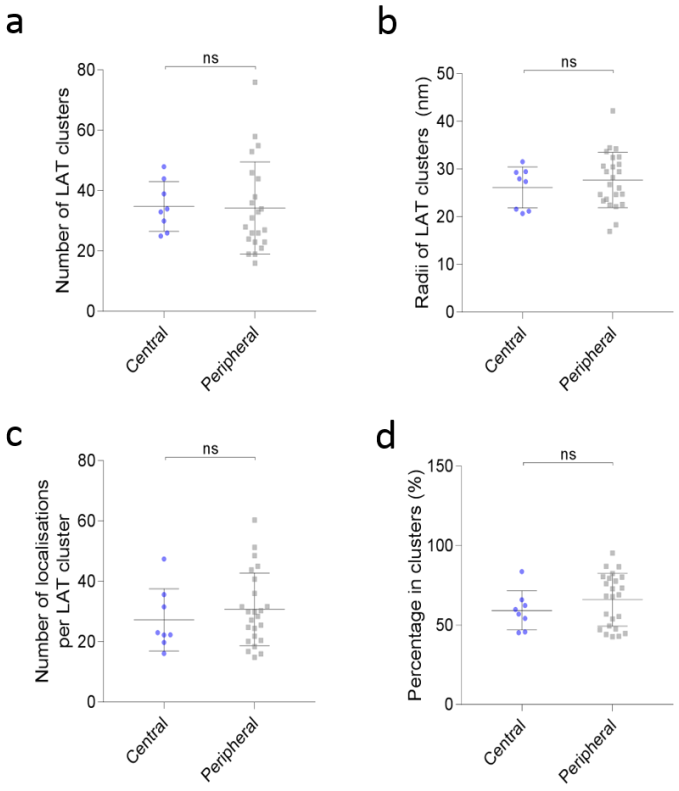

Figure 91: Evaluation of LAT clustering across the central and peripheral regions of the control T cell synapse. The number of detected clusters per ROI (a), cluster radii (b), number of localisations per cluster (c) and percentage of localisations in clusters (d) are presented for the central and peripheral ROIs. * = $p \leq 0.05$, ** = $p \leq 0.005$, *** = $p \leq 0.0005$, ****= $p < 0.0001$, ns = non-significant. Error bars represent the 95% confidence interval of the mean.

The distribution of LAT in α-actinin KO cells was next investigated via PALM and Bayesian cluster analysis. A representative example (n = 30 ROIs, n = 5 cells) is presented (Figure 92a), with localisations from the selected region plotted for method demonstration (Figure 92b). The heat map for this ROI and resultant cluster identification is also presented (Figure 92c, d respectively). Histograms of the number of clusters, cluster radii, number of localisations per cluster and the percentage of total localisations in clusters are shown for all ROIs analysed (Figure 92e-h respectively). The average number of clusters

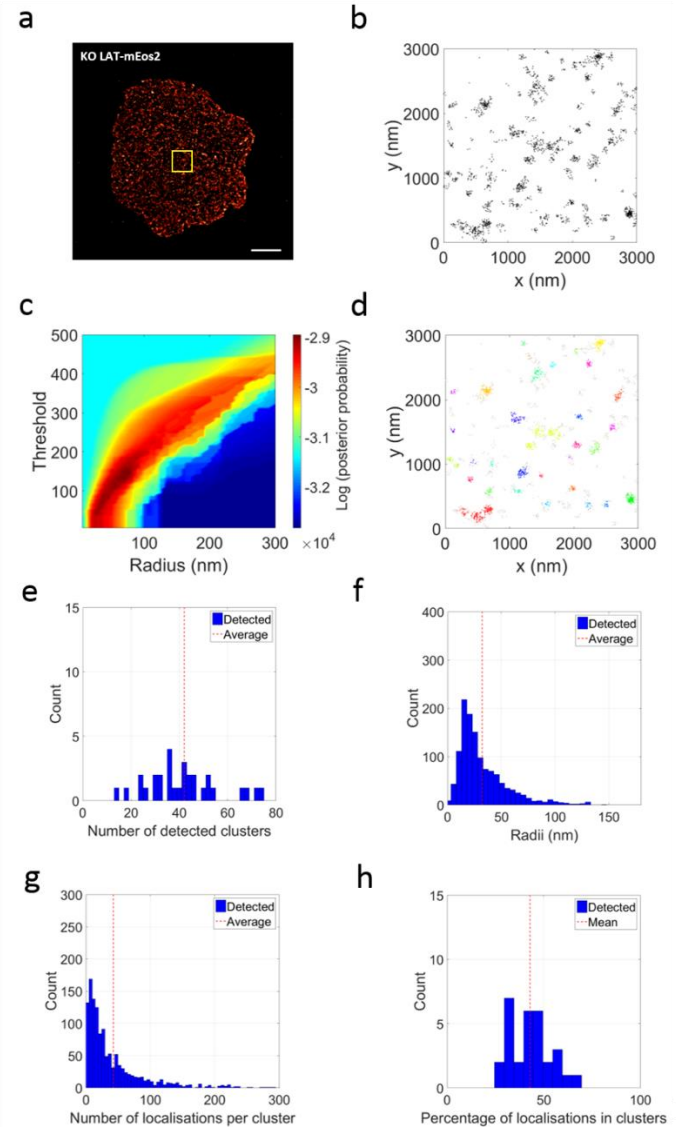

Figure 92: Quantification of the nanoscale clustering of LAT at the α-actinin KO immunological synapse via PALM and Bayesian cluster analysis A representative PALM reconstruction is presented (a), scale = 5µm, and an exemplar ROI depicted. Localisations from this given ROI are presented (b) and analysed, producing a heat map (c) of the cluster proposals. The highest scoring combination of the radius and threshold was extracted and used to produce the cluster map (d), in which clusters are pseudo coloured. Histograms of the number of clusters (e), cluster radii (f), number of localisations per cluster (g) and the percentage of molecules in clusters (h) is presented.

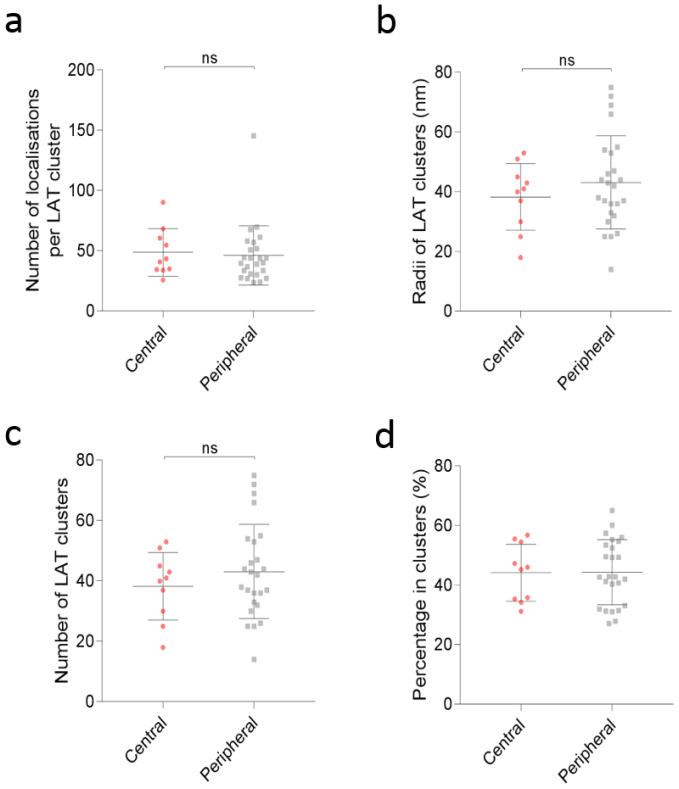

Figure 93: Comparison of LAT clustering across central and peripheral zones at the α-actinin KO immunological synapse. The number of detected clusters per ROI (a), cluster radii (b), number of localisations per cluster (c) and percentage of localisations in clusters (d) are presented for the central and peripheral ROIs. * = $p \leq 0.05$, ** = $p \leq 0.005$, *** = $p \leq 0.0005$, ****= $p < 0.0001$, ns = non-significant. Error bars represent the 95% confidence interval of the mean.

was measured as 42.00 ± 2.78, of 32.16 ± 0.65 nm cluster radii. The average number of localisations per cluster was evaluated as 42.50 ± 1.56, with 42.86 ± 1.88% of total localisations being attributed to clusters, on average.

To evaluate the local LAT clustering in α-actinin KO synapses, the analysed ROIs were further separated into those corresponding to either central or peripheral regions of the synaptic area. Similarly to the control condition, the number of clusters, cluster radii, number of localisations per LAT cluster and the percentage of localisations per cluster were not significantly different in the central and peripheral regions (Figure 93). This could infer that the

translocation of LAT at the immunological synapse was not impaired by loss of α-actinin, although live cell studies would be required to substantiate this.

A comparison of the total population of LAT clusters between control and α-actinin KO cells however, revealed significant differences in nano organisation (Figure 94). There were significantly more LAT clusters in α-actinin KO synapse (Figure 94a), of significantly larger radii (Figure 94b). The number of localisations per LAT cluster was also slightly enhanced upon α-actinin KO (Figure 94c), whilst the percentage of localisations assigned to clusters was lower (Figure 94d). These findings agree with the global Ripley's H-function analysis, in which the LAT appeared to be less clustered (% of localisations in clusters decreased), evidenced by the comparatively lower amplitude of the H(r)-function maximum, in α-actinin KO cells (Figure 89). Further, the observed increase in LAT cluster radii for α-actinin KO cells was subtly proposed in the H-function curve (though a broadening of this maximum) and the Bayesian method was able to provide precise numerical values to this suggestion.

The slightly increased number of LAT clusters in the α-actinin KO synapses could be explained by the changes in the actin meshwork (Figure 87). For example, modulating the actin meshwork could facilitate traffic of intracellular vesicles containing LAT to the immunological synapse. Whilst subsynaptic vesicles typically reside up to a micron away from the synapse interface, previous studies have reported their successful translocation to the interface upon stimulation. Moreover, this vesicular recruitment has been proposed to precede the phosphorylation of LAT, suggesting that this translocation is rapid, as previously discussed. Hence, whilst vesicular LAT may be recruited to the immunological synapses of control cells, it could be

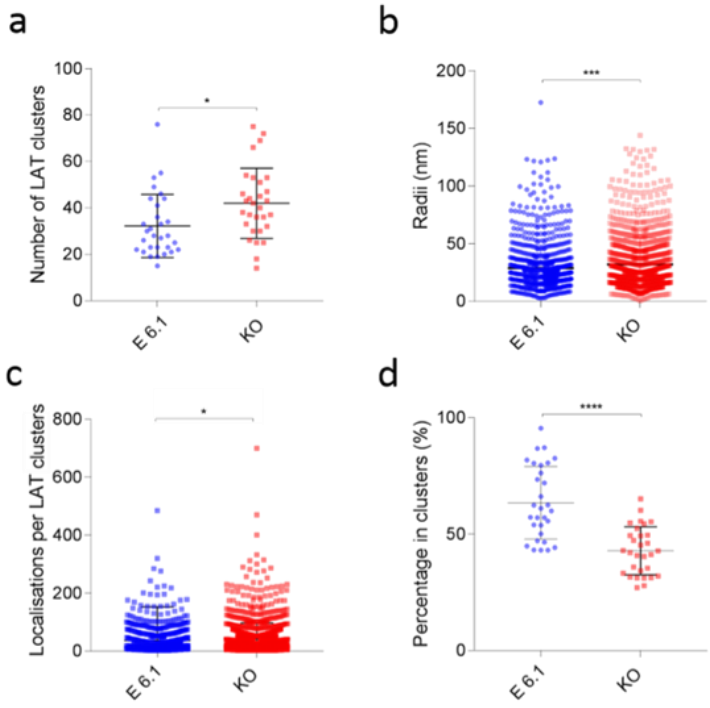

Figure 94: Comparison of LAT clustering across the synaptic area of control and α-actinin KO synapses. The number of detected clusters per ROI (a), cluster radii (b), number of localisations per cluster (c) and percentage of localisations in clusters (d) are presented for all ROIs of the control and α-actinin KO conditions. * = $p \leq 0.05$, ** = $p \leq 0.005$, *** = $p \leq 0.0005$, ****= $p < 0.0001$, ns = non-significant. Error bars represent the 95% confidence interval of the mean.

possible that loss of α-actinin facilitates this process by reducing the number of actin obstacles vesicles encounter upon translocation, resulting in more LAT clustering activity at the interface. On the other hand, since the actin cytoskeleton serves as a delimiter of the plasma membrane into compartments, by disrupting this organisation plasma membrane residing transmembrane LAT could diffuse more freely in the membrane. The probability of interaction with other LAT molecules could therefore increase, and more LAT clusters could be formed. Indeed, in one recent study by Magenau et al. a similar behaviour was observed. The authors evaluate the

clustering of several model membrane proteins such as Lck10, Src15 and LAT34, the transmembrane domain of wild type LAT, fused to mEos2 in HeLa cells (Magenau et al., 2015). The authors demonstrate that upon actin disruption by Latrunculin B, the radius of clusters and the number of molecules per cluster was enhanced. The authors suggest that by perturbing the actin mediated membrane compartmentalisation, the lateral mobility of such proteins is enhanced and as a result, an increased probability of protein-protein interactions occurs.

The radii of LAT clusters and the number of localisations per cluster was significantly increased upon α-actinin KO. The percentage of localisations attributed to clusters was however significantly reduced in α-actinin KO synapses, compared to the control condition. Whilst LAT does not directly interact with the actin cytoskeleton, LAT clustering at the immunological synapse forms part of a complex multivalent assembly of various proteins and kinases, some of which directly influence the organisation of the actin cytoskeleton. As such, subtly altering the nanoscale organisation of F-actin can result in a significant impact on the clustering of transmembrane proteins such as LAT. It is suggested that a loss of α-actinin, which in turn disrupts the actin mesh, results in a more freely diffusive nature of LAT, resulting in a lower percentage of localisations assigned to clusters. Whilst the number of localisations per LAT cluster increases for α-actinin KO cells, the radii also increases in such a way that the average cluster density (number of localisations per LAT cluster/area of LAT cluster) remains unchanged, with respect to that of the control condition. Hence, the LAT clusters in α-actinin KO cells appear to be more diffuse, despite their similar molecular composition. This again could be attributed to the perturbation in spatial

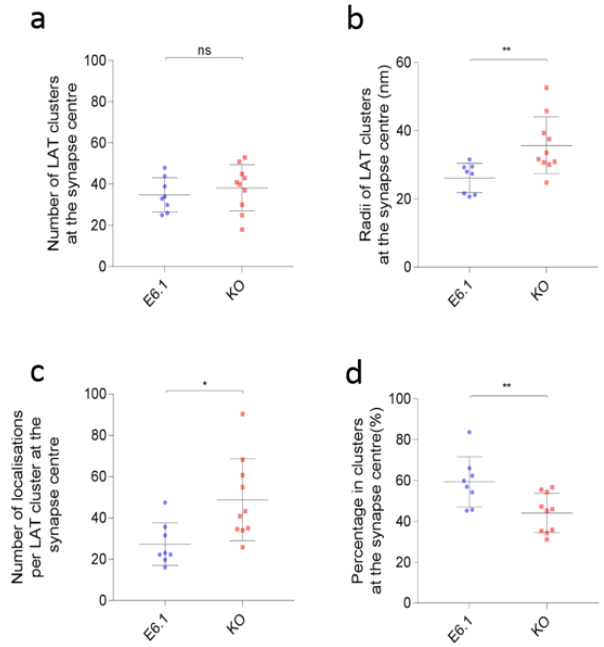

Figure 95: Comparison of LAT clustering at the synapse centre for control and α-actinin KO cells. The number of detected clusters per ROI (a), cluster radii (b), number of localisations per cluster (c) and percentage of localisations in clusters (d) are presented for the central ROIs of control and α-actinin KO ROIs. * = $p \leq 0.05$, ** = $p \leq 0.005$, *** = $p \leq 0.0005$, ****= $p < 0.0001$, ns = non-significant. Error bars represent the 95% confidence interval of the mean.

confinement, owing to the differing topologies and organisation of the actin cytoskeleton in the control and α-actinin KO synapses.

To investigate the impact of α-actinin KO on LAT clustering in distinct regions of the immunological synapse, the analysed data was again separated into central (Figure 95) and peripheral (Figure 96) ROIs. For both the synapse centre and periphery, the same trends in LAT clustering was observed between the control and α-actinin KO conditions. The number of LAT clusters in the central and peripheral regions of the α-actinin KO and the control cells was not significantly different. The radii of LAT clusters and the number of

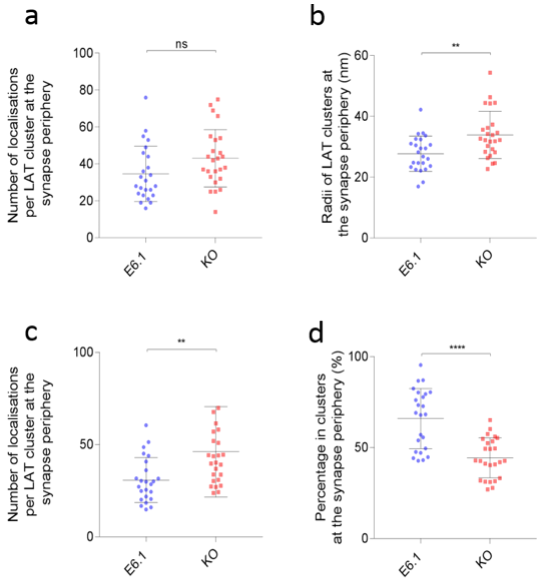

Figure 96: Comparison of LAT clustering at peripheral regions of the control and α-actinin KO synapses. The number of detected clusters per ROI (a), cluster radii (b), number of localisations per cluster (c) and percentage of localisations in clusters (d) are presented for the peripheral ROIs of control and α-actinin KO ROIs. * = $p \leq 0.05$, ** = $p \leq 0.005$, *** = $p \leq 0.0005$, ****= $p < 0.0001$, ns = non-significant. Error bars represent the 95% confidence interval of the mean.

localisations per LAT cluster in the α-actinin KO cells in the synapse centre and periphery was enhanced in the α-actinin KO cells. The percentage of localisations in clusters was however decreased, for central and peripheral regions in α-actinin KO cells compared to their corresponding control regions.

5.8 The spatial co-localisation and co-alignment of LAT and F-actin at the T cell immunological synapse

It has been demonstrated that α-actinin KO impacts the clustering of the transmembrane protein LAT at the T cell immunological synapse. To investigate the co-organisation of actin and LAT at the immunological synapse

of control and α-actinin KO cells, dual colour SMLM was performed on 2D, fixed samples. The spatial correlation of actin and LAT was quantified using a bivariate Ripley's K-function, to provide an indication of the interaction of actin and LAT on the global scale. Briefly, the bivariate (interchangeably the cross) K-function reports the number of type j events within a given radius of type i events, described in Section 2.5.4. In this case, the type j events refer to those of the LAT localisations and the type i events refer to the F-actin localisations. Further, the co-alignment of the two molecular species will be then evaluated, using an angular version of the bivariate K-function (Peters et al., 2018b). This method can provide additional information such as if LAT resides in proximity to actin fibres or resides in the central regions of the actin meshwork, in effect, exhibiting anticorrelated behaviour.

5.8.1 Co-localisation and co-alignment of LAT and F-actin at the immunological synapse of control and α-actinin KO cells

A representative dual colour SMLM image of F-actin and LAT at the mature T cell immunological synapse is presented in Figure 97a (n = 5 cells, n = 30 3 x 3 μm^2 ROIs). The bivariate H-functions (Figure 97i, ii) demonstrate that there is a lack of spatial co-localisation between LAT and F-actin at the mature immunological synapse, as their H-values remain within the CSR envelopes at the spatial scales indicated. The angular bivariate H-functions (Figure 97iii, iv) demonstrate a lack of co-alignment of LAT and F-actin at the mature T cell immunological synapse, evidenced by a lack of angular features in the curves. If for example, LAT clusters were residing on actin filaments, one would expect a peak at 180° in the LAT cross F-actin Angular H-function. Thus, in relation to the actin meshwork, LAT clusters appear to be randomly orientated. In terms of the current literature, LAT has no demonstrated direct

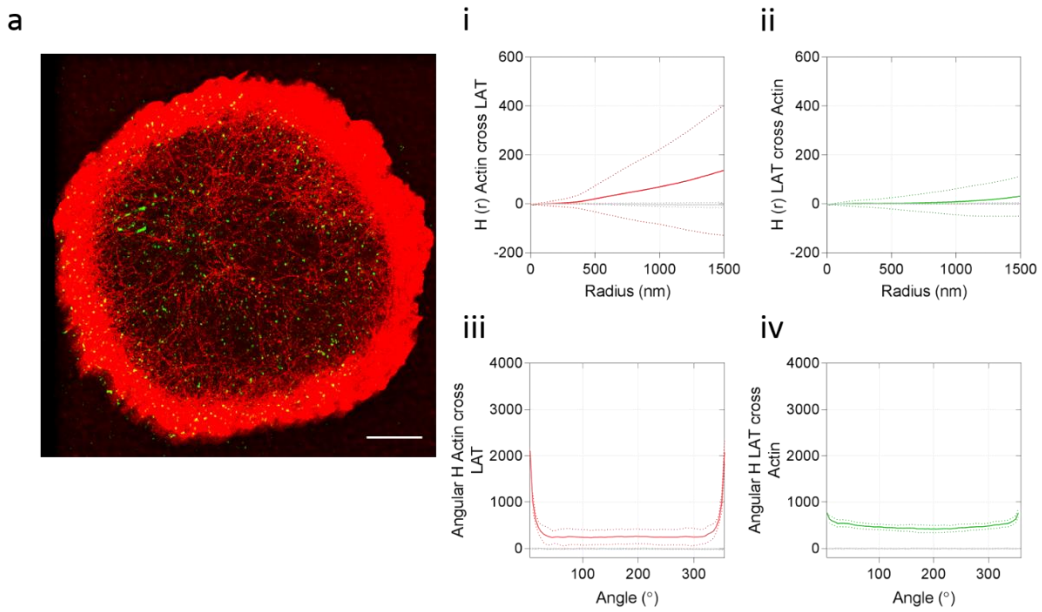

Figure 97: The co-localisation and co-alignment of F-actin and LAT at the T cell immunological synapse. A representative 2-colour SMLM image of LAT (green) and F-actin (red) acquired via PALM/dSTORM sequentially (a), scale = 5μm. The bivariate H-functions (i, ii) and angular versions (iii, iv) are reported for which the F-actin cross LAT data is depicted red and the LAT cross F-actin data is depicted green. CSR envelopes were computed to test randomness and are depicted grey.

interaction with actin. Upon LAT recruitment to the T cell synapse however, several kinases become activated and downstream responses initiated, that ultimately involve the re-organisation of the actin cytoskeleton.

The co-localisation and co-orientation of LAT and F-actin at the T cell immunological synapses of α-actinin KO cells was next investigated by use of the bivariate K-functions (Figure 98). Similarly to the control condition, a lack of spatial or indeed angular relationship was detected between LAT and F-actin at the T cell immunological synapse of α-actinin KO cells. Again, LAT clusters were not located on actin structures, nor were they spatially anti-correlated with the actin meshwork. Thus, whilst the spatial clustering of LAT

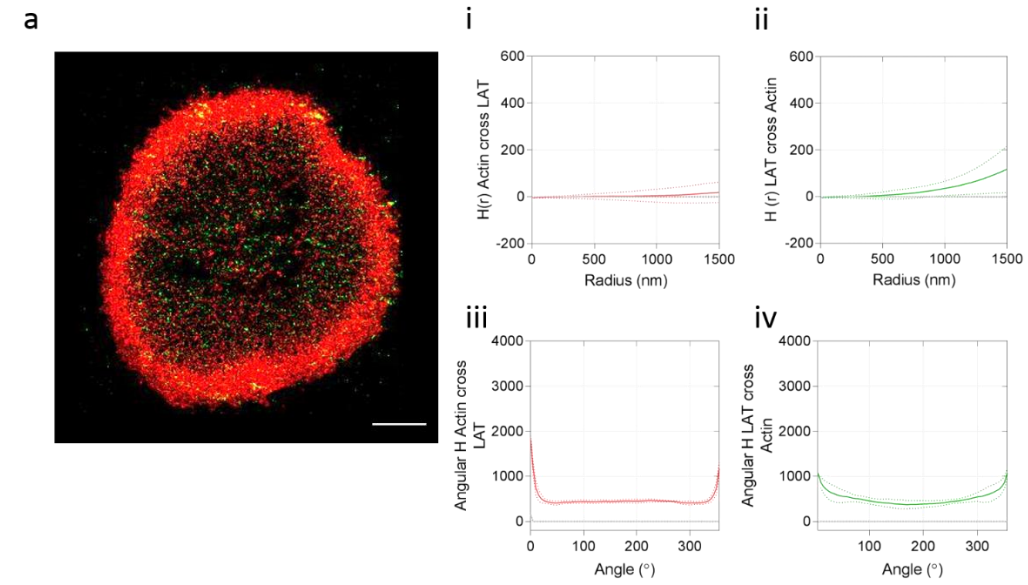

Figure 98: The co-localisation and co-alignment of F-actin and LAT at the T cell immunological synapse of α-actinin KO cells. A representative 2-colour SMLM image of LAT (green) and F-actin (red) acquired via PALM/dSTORM sequentially (a), scale = 5μm. The bivariate H-functions (i, ii) and angular versions (iii, iv) are reported for which the F-actin cross LAT data is depicted red and the LAT cross F-actin data is depicted green. CSR envelopes were computed to test randomness and are depicted grey.

appears to be α-actinin-F-actin dependent, the co-localisation of LAT and actin does not appear to be altered upon α-actinin KO.

5.9 Summary of presented results

In this Chapter, the analysis methods developed in the context of this Thesis were applied to experimental data of the actin cytoskeleton at the T cell immunological synapse. The effect of α-actinin KO on the distribution of F-actin on both the macro and nanoscale was quantified. Upon α-actinin KO, synapses formed via antibody coated coverslips were found to be of a significantly smaller area and perimeter compared to control conditions. This

could be due to a perturbation in the protrusive forces generated by the α-actinin-F-actin network located at the cell periphery during the synapse spreading phase, for example. The nanoscale distribution of actin was further assessed on the global and local level, by use of the developed analytical methods. Upon α-actinin KO, the distinct SMAC zones of the mature synapse were altered, and the series of tangential rings observed at the synapse periphery and the radial fibre populations of control cells were no longer dominant features of the α-actinin KO synapses. In agreement with the macroscale analysis, the number of detected fibres in the α-actinin KO cells was reduced compared to that of the control synapses, and together, the average area of enclosed regions formed through the actin meshwork was significantly impacted.

The spatial organisation of the transmembrane protein LAT at the T cell immunological synapse was next subject to a macro and nanoscale analysis in both control and α-actinin KO cells. LAT was found to be clustered in both control and α-actinin KO cells. The percentage of clustered molecules was significantly higher for control cells, although the LAT clusters of α-actinin KO cells were found to be significantly larger and containing more molecules per cluster. A modest increase in the number of LAT clusters was detected at the α-actinin KO synapse, which could be explained by the modulation of the actin meshwork. For example, by the mesh becoming looser, this could allow for more vesicles to become transported to the interface. On the other hand, by opening the actin mesh via α-actinin KO one could be enhancing the lateral mobility of plasma membrane associated LAT, thus increasing the probability of protein-protein interactions and thus the local protein density.

The final section of this Chapter assesses the co-localisation and co-alignment of LAT and actin at the T cell immunological synapse via 2D SMLM. For this, bivariate K-functions were implemented. A lack of spatial co-localisation between LAT and actin was measured for both the control and α-actinin KO synapses. This indicates a subtle role for α-actinin in the clustering of LAT: The presence or absence of α-actinin does not directly affect the organisation of LAT relative to actin at the immunological synapse, however, its linkage with F-actin and thus its role in membrane compartmentalisation, significantly alters the clustering behaviour of LAT.

Chapter 6 Discussion

6.1 Summary of presented results

Fluorescence microscopy has become an invaluable tool for the study of biological phenomena since its inception over a century ago. The field has evolved remarkably over the last decade, and several techniques of surpassing the diffraction limit of light have been adopted worldwide. Awarded the Nobel Prize in Chemistry in 2014 for its discovery, super resolution microscopy has now become a central tool in the life sciences, allowing unprecedented access to the nanoscale features and dynamics of diverse cellular specimens. Whilst initially motivated by the generation of impressive images provided with nanometric detail, the field has now progressed to acknowledge the quantitative information encompassed within the reconstructed images. Localisation based methods of super resolution microscopy (SMLM) present a technical challenge for the extraction of meaningful, reliable and robust biological conclusions, owing to their data outputs: SPPs. The field of spatial descriptive statistics has thus been widely adopted for the study of SPPs generated by SMLM, and numerous analysis methods have been developed to address the need for SMLM quantification. This Thesis aims to add to the available toolkit of SMLM analysis methods, in particular, for the study of fibrous SPPs which remains understudied compared to its clustered counterparts.

One of the first studies concerning the quantitative analysis of SMLM data sets was inspired by a long-standing analytical tool in ecology: Ripley's K-function. Ripley's K-function has been widely used to analyse the distribution of protein clusters assessed by SMLM methods. This method provides information pertaining to the nature of the pointillist distribution, whether this be clustered, dispersed or random. Lacking however, is information on a per point basis, and as such, numerous analysis methods have been proposed to overcome this deficiency. Notable methods include DBSCAN, Bayesian methods and more recently, Voronoi tessellation. These methods are not suited to the study of fibrous structures, and their implementation could result in a misclassification of fibres into a series of punctate clusters, partially owing to the circular bias imparted by some of these methods or indeed their comparison against a clustered model. Inspired by the progression of cluster analysis methodologies, this Thesis aims to provide a complimentary approach for the study of fibrous, rather than clustered, SPPs.

A novel modification of Ripley's K-function, which was specifically adapted to suit fibrous data, was firstly presented (Chapter 3). This method was utilised alongside a traditional Ripley's K-function and validated using numerous simulations, providing information on spatial periodicity, angular periodicity, linearity and dominant orientations of the underlying fibrous structures (Peters et al., 2017). The Angular H-function was applied to the distribution of actin filaments at the T cell immunological synapse, whose structure and dynamics is critical for mounting an immune response. Global information pertaining to the actin meshwork was presented, such as spatial and angular periodicities. Moreover, specific features of the cytoskeleton of the mature synapse were provided, such as the quantitative evidence for the concentric series of actin arcs at the cell periphery (Peters et al., 2017). Upon

disruption of the meshwork using the actin disrupting agent Cytochalasin D, the analysis method was further able to detect significant differences in canonical actin organisation. Whilst this method remains useful for garnering information pertaining to the global actin architecture on the nanoscale, quantifying the actin meshwork on a per fibre basis remains inaccessible. Further, whilst the method is robust to the user definable parameters (radius, angular range), a bias could be induced in the analysis if these parameters were to be changed per experimental condition.

To address the incomplete description of fibrous SPPs provided by the Angular H-function, a novel fibre tracing strategy was developed (Chapter 4). Validated by use of simulated data, the method is capable of tracing filamentous structures within a SPP generated by SMLM. The method provides a wealth of information, without resorting to pixelation, allowing the precise characterisation of the actin meshwork at the mature immunological synapse (Peters et al., 2018a). Specifically, the effect of Cytochalasin D on the actin meshwork was extracted on a per fibre basis. In pharmacologically treated cells, fewer fibres of shorter lengths were detected which enclose fewer compartments compared to non-treated cells. Similarly to the Angular H-function, this method relies on user definable parameters. The method however appears to be robust to variations in such parameters.

Finally, the importance of the actin crosslinking protein α-actinin on the architecture of the actin cytoskeleton at the T cell synapse was elucidated, by use of both the Angular H-function of Chapter 3 and the fibre tracing method of Chapter 4. For this, the distribution of actin in CRISPR-Cas9 α-actinin KO cells was quantified, on the macro- and nanoscale. Together, the results indicate an important role for α-actinin in maintaining SMAC zones of the

mature immunological synapse. Differences in the actin mesh topology upon α-actinin KO suggested a possible important role for α-actinin in actin mediated membrane compartmentalisation. To test this theory the clustering behaviour LAT, a crucial signalling molecule at the T cell immunological synapse, was quantitatively assessed on both the macro and nanoscale. α-actinin KO did not impair the ability of LAT to cluster, however the clustering characteristics of LAT differed upon α-actinin silencing. For example, it was found that more LAT clusters were present in α-actinin KO synapses. This could be ascribed to enhanced vesicular recruitment, which could become more rapid upon actin disruption. On the other hand, the lateral mobility of plasma membrane residing LAT could be altered upon α-actinin KO, resulting in differing clustering behaviour, although evidence presented in this Thesis alone is not sufficient to substantiate this theory. Interestingly, a lack of spatial co-localisation was observed for both the control and α-actinin KO synapses. LAT clusters were not found to reside on actin filaments, rather, LAT clusters appeared to be randomly arranged in relation to the actin meshwork for both the control (Peters et al., 2018b) and α-actinin KO synapses. As such, loss of α-actinin was suggested to not directly impair the spatial recruitment of LAT to the synapse.

6.1.1 Discussion in the context of the current literature

Fibrous SPPs were firstly presented over a decade ago, appearing in the ground breaking papers of the Zhuang and Betzig labs (Betzig et al., 2006, Rust et al., 2006). However, whist the field of SMLM cluster analysis has rapidly expanded, the analogous study of fibrous SPP has remained comparatively understudied. Only a handful of studies concerning fibre SPP analysis exist. (Nieuwenhuizen et al., 2015) provided a tool for the quantification of co-

orientation for example of two fibrous meshworks on a global scale, whereas (Zhang et al., 2017) developed a local tracing method for the study of microtubule networks. The method presented by Zhang et al. relies upon the pixelation of the SMLM data, rather than taking the SMLM co-ordinates as input. Directly analysing the pointillist, raw SMLM data is an important advance. Firstly, there are numerous methods of rendering a pixelated image from pointillist data with no clear consensus on the preferred approach. User defined variability is thus induced when performing pixelation, and the comparison of tracing techniques becomes intrinsically difficult, as methods could perform differently for pixelated images of varying statistical composition. Secondly, whilst the method of Zhang et al. is well suited to the study of microtubule structures, the authors state that it is not currently applicable for more complex networks such as those formed by actin. This could be due to the manual identification stage in the algorithm and the geometric constrains imposed during the tracing. Thirdly, by using the SMLM co-ordinates, rather than their intensities spread over a pixel grid, one can further extend the analysis to include numerous experimentally derived parameters, such as the localisation uncertainty. This will be particularly important for the more recent data sets SMLM is providing, for example marked SPPs. Marked SPP analysis generally applies to pointillist data (spatial information) containing specific marks (additional information) for each localisation. For example, marked SPP analysis could be useful for spectrally resolved SMLM (Bongiovanni et al., 2016, Yan et al., 2018), in which functional information is provided by a wavelength associated with each detected localisation. This reasoning holds true for more generic fibre analysis tools of pixelated data, such as those provided by IMARIS or ImageJ plug-ins.

In terms of the biological applications of this work, the macro and nanoscale distributions of actin at the T cell immunological synapse quantified by the developed analysis tools is consistent with previous results. For example, the preferential directionalities of fibrous networks at the pSMAC and cSMAC have been previously observed by numerous T cell biology groups (Kaizuka et al., 2007, Huppa and Davis, 2003, Burkhardt et al., 2008), whose formation is crucial for the structure and function of the T cell immunological synapse. It is becoming increasing clear that numerous actin networks, other than the extensively studied branched lamellipodium network, at the immunological synapse exist (Roy and Burkhardt, 2018). Whilst some studies pre-date the commercialisation of SMLM microscopes, more recent studies would benefit from a quantitative evaluation of actin networks in T cells, to work towards a more comprehensive structure-function relationship of actin (Kumari et al., 2014, Yu et al., 2013). Moreover, since defects in actin architecture have been implicated in numerous human health diseases, quantifying the nanoscale effect of actin disruption via pharmacological agents is highly important. The family of Cytochalasins for example, which act to promote global depolymerisation of actin filaments, are commonly used in cancer therapy research (Trendowski, 2015). Cytochalasins appear to preferentially damage cancerous cells, impair mitosis and induce apoptosis. As such, the use of actin disrupting agents (in unison with microtubule targeted drugs) could improve the efficacy of cancer treatment (Trendowski, 2015). The dose-response of these drug treatments is of the upmost importance, and by use of quantitative analysis methods, one could begin to address the local effects of actin disruption in cancerous cells for example.

The quantitative evidence presented in this Thesis for the organisation of actin arcs at the pSMAC of mature (Jurkat E6.1) immunological synapse has been also studied in the context of Arp 2/3 and formin nucleation (Murugesan et al., 2016). Using live cell SIM imaging, Murugesan et al. demonstrated that actin arcs originate at the plasma membrane in formin-rich zones, and their formation is largely Arp 2/3 independent. Upon addition of small-molecule inhibitor of formin homology 2 domain (SMIFH2), a formin inhibitor, actin arcs of the pSMAC rapidly disassemble. On the other hand, addition of CK666, an Arp 2/3 nucleation inhibitor, results in an increased number of actin arcs at the pSMAC. Since Arp 2/3 and formins are competitors for the limited actin monomer population, inhibiting one nucleator could provide the other with more available monomers, thus rendering its network more robust. In terms of the functional aspect of the actin arcs, the authors demonstrate that upon formin inhibition, TCR microclusters are less centralised and LFA-1 clusters are more disperse in the pSMAC. The authors employ SIM (3D and TIRF-SIM), which offers limited spatial resolution in comparison to SMLM. For actin arc analysis, maximum projections of the 3D data were used for analysis, which could induce error as SIM data relies on intensity-based measurements. Further, thresholds for F-actin intensity were used and the pixelated data was analysed using an ImageJ plug in (Boudaoud et al., 2014) to obtain arc morphologies. Nonetheless, for capturing the live cell dynamics of the formation and flow of these actin arcs, 3D SIM is highly appropriate.

α-actinin crosslinks actin fibres and binds various transmembrane proteins. Mutations in all four human genes encoding α-actinin have been implicated in human diseases and acquired traits. Previous studies have demonstrated the localisation of α-actinin to the dSMAC region of the mature immunological synapse, which is highly correlated with actin (Ashdown et

al., 2017). In agreement with these observations, a significant loss of actin intensity at the dSMAC of α-actinin KO synapses was observed. Further, upon silencing of α-actinin disruptions in the SMAC zone architecture of the mature immunological synapse have been reported, assessed by conventional fluorescence microscopy (Gordón-Alonso et al., 2012). This Thesis highlights this distribution of the canonical immunological synapse organisation on the nanoscale, providing local descriptions of the actin architecture perturbations.

An interesting avenue of research currently in the T cell biology community is the mechanical aspect of immunological synapse formation and sustentation. The mechanotransduction and mechanosensitive properties of the immune synapse has garnered increasing attention over the last few years, and the role of the actin cytoskeleton and its many accessory proteins, including α-actinin, in force generation is beginning to be explored (Das et al., 2015, Janoštiak et al., 2014, Liu et al., 2016). *In vitro* experiments indicate that networks of actin crosslinked by α-actinin disintegrate at stresses around 0.3 Pa, whereas filamin networks withstand up to 100 Pa shear stress (Ferrer et al., 2008). The force generated by the actin cytoskeleton via polymerisation for example is well studied across varied biological systems (Borisy and Svitkina, 2000), however the binding of ABPs and their individual contributions to this force remains to be further studied. As such, whist it is suggested in this Thesis that α-actinin KO results in a perturbation of the force generated upon T cell spreading, further study would be required to validate this model.

The transmembrane protein LAT was chosen for investigation for several reasons. First and foremost, LAT is indispensable for T cell signalling. The presence of plasma membrane associated and vesicular LAT, and their roles in T cell activation, is also a current subject of debate (Williamson et al., 2011,

Balagopalan et al., 2018). Of the many signalling molecules at the immunological synapse, LAT is an ideal candidate to test the membrane compartmentalisation per the actin fence of Kusumi owing to its large intracellular domain and its association with lipid rafts. In terms of the current literature however, LAT has no directly demonstrated interaction with actin. However, LAT clustering during T cell activation is part of a broader multivalent assembly of several other adapters and kinases, some of which are ultimately involved in the regulation of actin networks (Balagopalan et al., 2015, Sherman et al., 2011). For example, pLAT-associated Gads and SLP-76 recruit Nck, Vav1, and Itk which in turn activate the small GTPases Rac1 and Cdc42, which engage WASP-family proteins to promote Arp 2/3 driven actin polymerization (Zhang et al., 2000). Whilst LAT has no obvious interaction with α-actinin at the synapse, the clustering activity of LAT is likely to be altered upon perturbing the actin meshwork, consistent with previous reports. Recently it has been demonstrated that EWI-2, a member of the Ig superfamily, interacts with α-actinin in a PIP_2 dependent manner. Upon T cell activation, EWI-2 localises to CD3 (Gordón-Alonso et al., 2012), in the vicinity of the LAT signalosome. LAT interacts with PLCγ1, which acts to hydrolyse PIP_2 which in turn could permit the EWI-2-α-actinin interaction at the immunological synapse. Disrupting the SMAC zones of the immunological synapse via α-actinin KO has been also shown to disrupt the translocation of EWI-2 to the synapse, and its implications on LAT clustering has not yet been studied (Gordón-Alonso et al., 2012).

The analysis methods presented in this Thesis were universally applied to the study of filamentous actin at the T cell immunological synapse. Besides the T cell immunological synapse, the formation of acto-myosin rings has far reaching consequences in numerous biological systems. For example, acto-

myosin rings are crucial for the cytokinesis of both animal and fungi cells, participate in wound healing and stabilise cell-cell contacts (Schwayer et al., 2016). The methods presented in this Thesis are readily applicable to the study of such systems, provided that the data remains a SPP. Besides actin, there are several examples in which the characterisation of fibrous structures is important. For example, in unison with actin, microtubule networks facilitate cytokinesis, intracellular transport of cargo and cell movement to name but a few examples (Nogales, 2000). Similarly to actin, the execution of many cellular functions is partially ascribed to the macro and nanoscale architecture of microtubule networks and thus understanding their nanoscale distributions will complement structure-function studies. Septins are small GTPases that can organise into filamentous structures and are becoming increasingly recognised as the fourth component of the cytoskeleton. Compared to their cytoskeletal partners, septins are less studied and much of their structure-function relationships remain to be elucidated. An interesting study by (Ewers et al., 2014) demonstrated the role of septin filaments in constraining the diffusion of receptors within dendritic spine necks, suggesting that the septin cytoskeleton could contribute to the plasma membrane delimitation, as hypothesised for actin.

6.2 Future work

6.2.1 Extensions of the analysis methods

One of the main limitations of the analysis methods developed in the context of this Thesis is their use of user-definable parameters. For batch processing, this issue is exacerbated, as multiple ROIs are analysed using the same sub-optimal analysis parameters. Whilst the concept of tuning the

analysis parameters to suit a particular data set (for example microtubule structures) is fathomable, one must do so in a principled manner with statistical reasoning. For example, the radius and angle over which the tracing is performed could be optimised per data set, by scoring the results against a pre-defined model. Upon performing the analysis for a combination of radius-angle pairs, the results could be evaluated against a posterior probability, estimated via a fully characterised model (Rubin-Delanchy et al., 2015). In this way, the analysis parameters for the tracing routine could be adapted in a principled, statistical manner to suit diverse fibrous SPPs.

One of the drawbacks of this approach is the computational time required to perform the analysis. Further, the model must be indicative of experimental data. For fibrous SPPs this could involve estimating prior distributions for the fibre persistence lengths (which differs per structure), the number of branching fibres per ROI and their bundling properties, at the bare minimum. The diversity in fibre topology and diversity in fibre architecture within a single cell is nowhere better illustrated than at the mature T cell immunological synapse. The outer ring comprises a highly dense meshwork of actin, displaying fibre bundles, crosslinked and branched networks whereas the inner ring is sparsely populated with actin fibres. As such, defining a model that accounts for such a diversity, purely considering actin filaments at this stage, could be challenging. To then extend this framework to the study of other fibrous structures, such as microtubules, would add an additional layer of complexity. For example, microtubules do not undergo Arp 2/3 branching, and their networks are thus geometrically different to those formed by actin (Zhang et al., 2017). Further, their widths and maximum curvatures are intrinsically different to actin filaments. To account for this, one

could provide multiple models and estimate numerous prior distributions however this would require significantly increased computational time.

Another approach which could be implemented for the study of fibrous SPPs is machine learning. Machine learning is a widely used tool in diverse fields such as image recognition and security. One of the major advantages of machine learning is the minimal human intervention required for analysis, whether this be recognising patterns or making decisions. A second advantage is the ability of machine learning algorithms to cope with the growing volumes and varieties of data. Thirdly, analysis via machine learning is extremely rapid. Broadly, there are three genres of machine learning: supervised, unsupervised and reinforcement learning (Angra and Ahuja, 2017). In the simplest case, supervised learning provides target outcomes predicted from input variables by approximating a mapping function. The analysis method is trained until a desired accuracy is achieved, and examples of this learning include decision trees and random forest classifiers. In the case of unsupervised learning, the learning is data driven. There are no target outcomes to predict, and the algorithm approximates the underlying structure of the data without labelled inputs. Examples of unsupervised learning are clustering analysis and dimensionality reduction (Angra and Ahuja, 2017). Semi-supervised learning is a compromise between supervised and unsupervised methods, as the input data is not completely labelled. Reinforcement learning on the other hand, enables the system to learn via trial and error and is typically used for complex problems. By use of training data, the system could be taught to classify features in a fibrous SPP such as bundled or branched fibres. This approach could account for the shortcomings of a Bayesian approach for fibre analysis, as no *a priori* knowledge is required.

The analysis methods developed in this Thesis do not currently take into account the individual, estimated localisation uncertainties of each point within the SPP. Indeed, most SMLM analysis methods consider the effect of the localisation uncertainty as negligible. Numerous imaging techniques (in unison with dye performances) are in fact validated by their ability to localise individual molecules with a high precision. For the Angular K-function, the localisation uncertainties could be used as an additional input parameter. In the simplest scenario, this could involve computing a weighted Angular K value. By modelling the localisation uncertainty as a circle, whose centre position represents the co-ordinate (x, y) of the localisation and whose diameter is equal to the localisation uncertainty, one could estimate the degree at which the given localisation truly resides within each angular range of the K-function calculation. The uncertainty weight for example, could be calculated by performing a ratio of areas (area encompassed in the angular range: sum of area inside and area outside of range). In this way, the K-values are related to the uncertainty at which the molecules are localised, and the local density becomes related to the certainty in measurement (Figure 99a). For the tracing routine, incorporating the localisation uncertainties is simpler. When calculating the weighted density parameter (assessed by Voronoi tessellation and the fibre directionality vector), one could also include the localisation uncertainties of the candidate points (Figure 99b).

Throughout this Thesis, the distribution of the actin cytoskeleton was assessed by 2D microscopy methods. By visualising this 3D structure by 2D microscopy, information is lost, and the data is prone to misinterpretation (Figure 100). Specifically, the 2D image comprises a projection of the illuminated volume, ~ 100 nm for TIRF studies, thereby creating features in the 2D image that do not exist in the 3D volume (Figure 100). A prime example

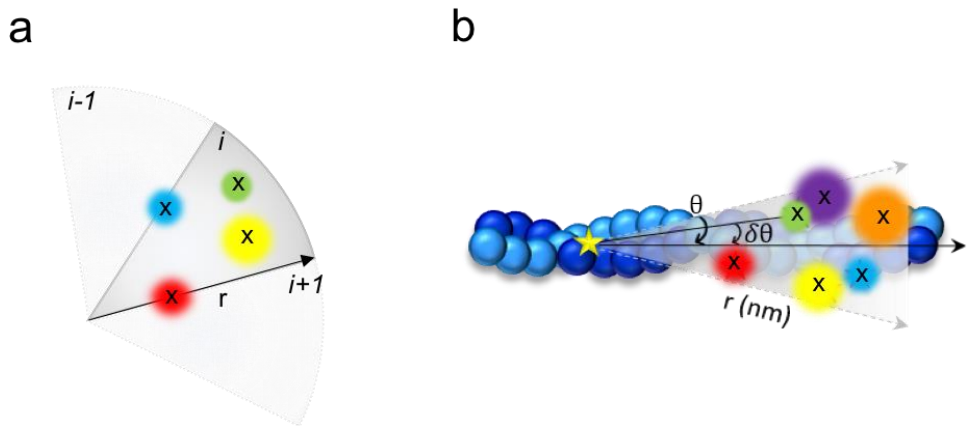

Figure 99: Schematic depicting the introduction of the localisation uncertainty as a parameter in the presented analysis methods. For the Angular K-function (a), this could entail estimating a weighted K value. For example, consider the K value calculation for the i^{th} section, where each localisation within this angular range (whose centre positions are represented by a x and whose localisation uncertainties are depicted as a circle) is presented. Localisations whose circles lie completely within the angular range (for example the green and yellow circles) will be assigned a weight of unity. For those extending to the neighbouring angular ranges (i-1, i+1 segments), their weights could be calculated by computing their enclosing areas divided by their entire areas. In the case of the tracing method (b), the localisation uncertainties could similarly be used as an additional weighting factor for the weighted density parameter calculation.

of this is the intersection of fibres, which in 3D would lie on top of one another. In terms of analysis method presented in Chapter 4, the most vulnerable descriptors to projection induced errors are the detected areas of enclosed regions and the branching angles. Indeed, throughout the experimental data the Arp 2/3 mediated nucleation was not quantified (70° branching angle) despite the methods capability in detecting this architecture (via simulated SPPs). Extending the presented analysis methods for the study of 3D fibrous SPPs is an obvious extension. The information gained by this is however reliant upon the method of acquiring the 3D information. As previously discussed, a trade-off between spatial resolution, sample depth and many

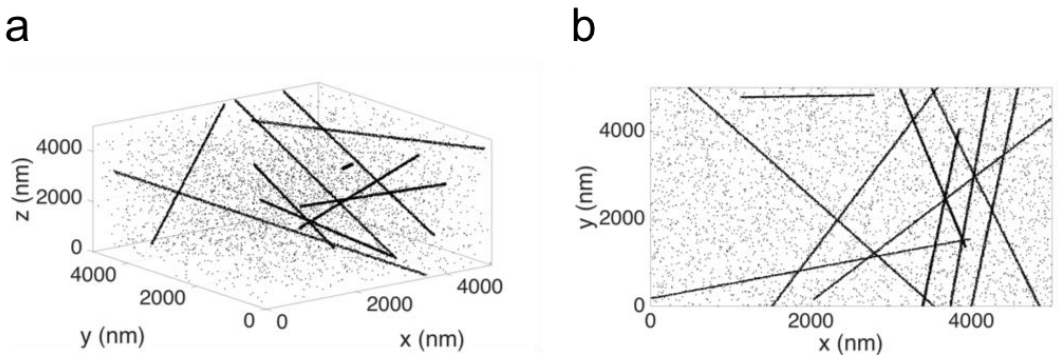

Figure 100: The impact of the 2D projection of 3D information in SMLM techniques. A simulated example of the distribution of randomly placed fibres spanning the ROI in 3D (a) and its 2D projection (b) is presented. The 2D projection of 3D structures can result in artificial compartments formed through false fibre intersections. Whilst the number of detected fibres for example, may remain accurate, descriptors such as the branching points and areas of enclosed regions are greatly impacted by this projection.

other factors must be considered. For example, 3D iPALM offers the best theoretical spatial resolution, which is isotropic in all three dimensions (Shtengel et al., 2009). This however is at the cost of sample depth, as information only ~ 600 nm (under ideal conditions) proximal to the surface is obtainable. Whole cell methods of achieving 3D via DHPSF for example can achieve 15 μm – thick cell volumes (Carr et al., 2017) however isotropic resolution is not currently possible. Typically, the localisation precision in the axial plane is up to three times poorer than that of the lateral plane (Schermelleh et al., 2010). Ideally, one would combine the isotropic resolution of the iPALM system with depth of field attainable via the DHPSF, although the compatibility of these different techniques is yet to be challenged.

In a preliminary experiment the 3D nature of the actin cytoskeleton at the T cell immunological synapse was assessed by the iPALM technique (Figure 101a). The global analysis method, presented in Chapter 3, was also extended to suit 3D, fibrous SPPs (Peters et al., 2018b). Briefly, this consisted of performing a 3D Angular H-function, counting localisations within a sphere of any given radius (r = 500 nm), elevation (θ, $0 < \theta \leq 360°$) and azimuthal (φ, $0 < \varphi \leq 180°$) angles. By performing a 3D Angular H-function, one can deduce that actin fibres are largely horizontal in the axial range, in agreement with the model of the cortical actin meshwork juxtaposed to the inner surface of the plasma membrane (Figure 101b, c). The 3D nature of the actin meshwork appears to be flattened, owing to the low sample depth achievable with the iPALM technique. In theory, it is possible to extend this study to derive quantitative descriptors of the underlying point pattern. One could for example, reconstruct fibres from their distinct angular features in the analysis. However, this type of analysis remains limited to the study of global properties of 3D fibrous distributions and as a result the location and interplay between fibres comprising the meshwork cannot be inferred. One could also extend the tracing method to the study of 3D structures. The information to be gained from this is however uncertain, as the method requires a relatively high localisation precision (~ 40 nm) and the current 3D modalities of SMLM either allow for isotropic high spatial resolution at the cost of sample depth, or these constraints imposed contrariwise.

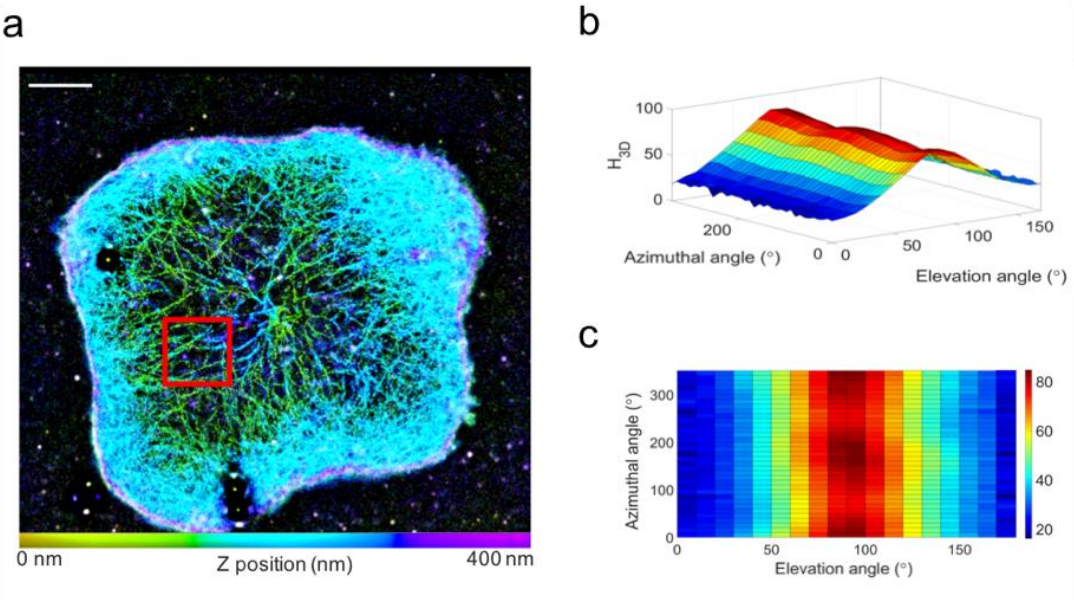

Figure 101: iPALM imaging of the actin cytoskeleton in artificial T cell synapses. A representative example iPALM image (Scale bar = 5 μm) pseudo-coloured by axial depth (a), from which the displayed region was analysed (b-c) using a 3D H (θ, ϕ)-function analysis.

6.2.2 Extensions of the experimental study

The biological study in this Thesis is focused on the impact of α-actinin KO on the 2D architecture of the actin cytoskeleton and LAT clustering at the T cell immunological synapse. Whilst α-actinin KO did not impede LATs ability to cluster, an interesting avenue for further study could be the dynamic behaviour of such protein clusters at the immunological synapse, upon SMAC disruption via α-actinin KO. The actin retrograde flow observed in mature immunological synapses guides the translocation of certain protein clusters across the synaptic zones as previously discussed, and upon α-actinin KO, it could prove interesting to track these dynamics. One would expect a less organised translocation, although the role of this impaired dynamic behaviour in T cell signalling remains to be elucidated. In addition to LAT, one could

examine the effect of α-actinin KO on the clustering ability of non-raft associated proteins such as CD2-associated protein (CD2AP). Previous studies have reported on the importance of CD2AP for TCR internalisation (Lee et al., 2003), which is now thought to occur at the cSMAC. One might expect for example, upon actin disruption by α-actinin KO internalisation may occur on a faster time scale. The impact of this accelerated internalisation and the resetting of T cell signalling on the disassociation phase of the synapse could be of interest.

As previously discussed, the effect of formin and Arp 2/3 inhibition on actin organisation at the T cell immunological synapse has been conducted by SIM, achieving ~ 120 nm spatial (lateral) resolution. In a preliminary experiment, the impact of Arp 2/3 and formin inhibition on the nanoscale organisation of the actin cytoskeleton in Jurkat T cell immunological synapses via fixed cell, 2D SMLM was visualised (Figure 102). Extending this study to the α-actinin KO synapses could be of great interest, as α-actinin crosslinked actin networks could exhibit differing mechanical properties to those of formin driven actin networks. Further, the clustering behaviour of LAT upon these drug treatments could be augmented, perhaps substantially so in the Arp 2/3 inhibited synapses owing to LATs interaction with Nck and Vav1, which activate RhoGTPases responsible for the recruitment of WASP to promote Arp 2/3 nucleated networks (Balagopalan et al., 2015).

Many other transmembrane proteins are proposed to link the actin cytoskeleton to plasma membrane components. The ERM family of proteins for example anchor transmembrane proteins such as CD43 to the actin cytoskeleton, either through direct or adaptor mediated interactions (Bretscher et al., 2002). CD43 localises to actin rich regions (d and pSMAC) of

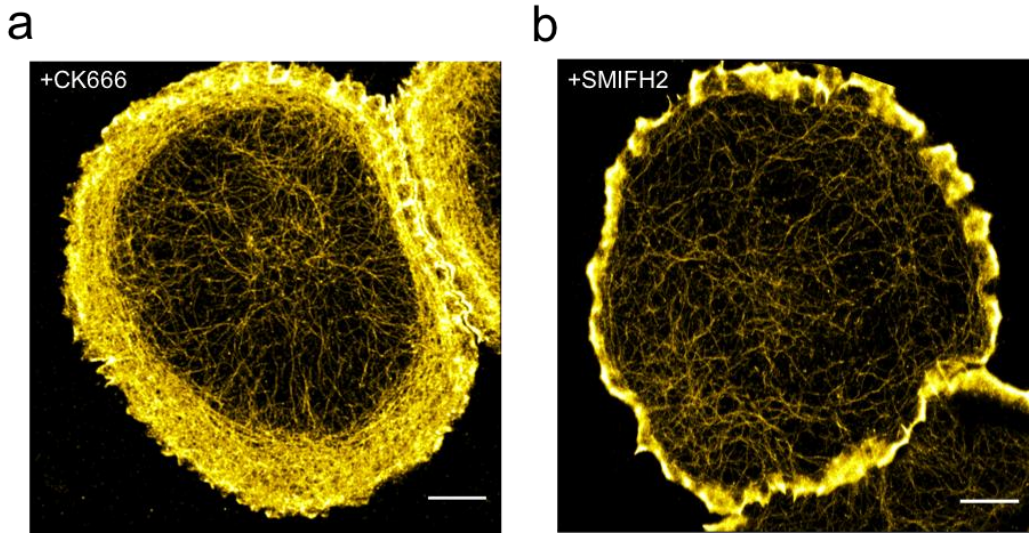

Figure 102: The impact of Arp 2/3 (a) and formin inhibition (b) on the architecture of actin at the T cell immunological synapse assessed by SMLM. Scale = 5 μm.

the immunological synapse, and is speculated to be transiently trapped in actin compartments per the Picket Fence model (Sperling et al., 1998, Kusumi et al., 2005b). Increasing experimental evidence to support this theory is emerging. One particular study demonstrates a reduction in the mobility of lipid anchored molecules in early axon initial segment (AIS) formation in hippocampal neurons (Albrecht et al., 2016). This confinement was induced by the regularly spaced actin cytoskeleton of the AIS, assessed by single particle tracking and dSTORM. This confinement has not yet been fully characterised at the T cell immunological synapse.

Mainly due to imaging and labelling constraints, much of our current knowledge regarding how T cells initiate, sustain and facilitate signalling is derived from fixed cell, *in vitro* studies of artificial synapse systems. This of course opens the door for questioning the validity of the reductionist approach, and whether *in vitro* observations are replicated *in vivo.* The SMAC

organisational structure of the immunological synapse for example remains an interesting source of debate. SMAC formation is not required for mounting an immune response (Davis and Dustin, 2004, Mitxitorena et al., 2014), however many *in vivo* studies to date have captured the formation of cSMAC and pSMAC structures in species as diverse as rodents (Barcia et al., 2006) and primates (Barcia et al., 2008). A promising approach is lattice light sheet microscopy, which can be integrated with super resolution techniques such as SIM and dSTORM. A recent study reported the clustering activity of the TCR complex expressed on the surface of lymph-node resident T cells *in vivo* pre and post activation, by use of light sheet dSTORM imaging (Hu et al., 2016). In transgenic mice injected with peptide, Hu et al. Demonstrate that TCRs were found to cluster in a similar fashion to *in vitro* studies. Broad adopting of this imaging modality is an important and necessary advance for the study of T cell biology in a physiological, nanometric context.

6.3 Current limitations of quantitative SMLM

Despite the remarkable growth of the SMLM field over the last decade, many issues remain to be addressed, the most prominent of which will be discussed.

6.3.1 Labelling requirements

The labelling density of an SMLM image, the distance between fluorophores in the sample, is an important factor for quantitative SMLM. For high resolution imaging, an inadequate labelling density of the target structure can manifest in inaccuracies in the reconstruction of structures. This effect is particularly noticeable for structures such as filaments, which appear

punctate when subject to sub-Nyquist sampling. When performing SMLM, it is the reporter of fluorescence that is imaged not the protein of interest itself, and as a result one must consider the physical size of the probe, typically ~ 15 nm for antibodies. Large probes can result in low labelling densities and increase their distance from target structures. As such, the need for smaller probes that bind closer to their target structures is highly desirable. Several approaches, such as the use of nanobodies and PAINT, are becoming increasingly popular although the number of bright, specific probes remains limited to date.

Another consideration when performing SMLM is achieving the correct labelling to ensure sparsity in fluorophore activation, per image frame. This condition must be met in order to temporally separate the PSFs of individual molecules that would otherwise overlap at the detector if activated collectively. Analysis approaches to identify artefacts induced by high-density labelling have gathered increasing attention over the past year. Super-resolution quantitative image rating and reporting of error locations (SQUIRREL) (Culley et al., 2018), Haar wavelet kernel (HAWK) (Marsh et al., 2018) and robust statistical estimation algorithm (RoSE) (Mazidi et al., 2018) report on image quality, albeit in different approaches. When integrated into super resolution systems to monitor image quality in real time, these techniques will undoubtedly improve the data acquisition stage and subsequent biological interpretation of the data. These methods are particularly interesting for fibrous SPPs, in which multiple intersections of fibres can induce errors in structural classifications.

6.3.2 Blinking requirements

In an attempt to improve quantitative SMLM by improving the labelling density of target structures, one may further induce error. For example, for absolute quantification studies, IRIS is unsuitable owing to its repetitive binding. For structural SMLM however, performed for much of this Thesis, multiple blinking can prove useful. Even when labelling density requirements are met, the photophysical properties of the fluorescent marker can impose constraints on the attainable resolution. An ideal fluorophore will exist in the inactive, dark state and transition to the bright, active state, emitting a high number of photons for precise detection. Upon detection, ideally the fluorescent marker would be irreversibly photobleached, and as such, detected only once per image. However, many fluorescent markers have been demonstrated to undergo multiple blinking, resulting in errors in molecule counting measurements. The reoccurrence of the fluorescent protein mEos has been shown to be close to 1, on average (Annibale et al., 2010). Further, if a single molecule blinks multiple times, the spatial scale over which this occurs does not change, and as a result false clustering can be reported. Attempts at correcting for this behaviour in the post-processed data have been adopted in the context of this Thesis, and have made good progress in determining stoichiometry (Rollins et al., 2015). Understanding the photophysical properties of fluorophores in greater detail represents the first step for their control and manipulation and will improve absolute quantification of SMLM techniques.

6.3.3 Detection efficiency

Owing to numerous factors such as incomplete photoactivation, premature photobleaching, masking or quenching by proximal fluorophores and focal

drift, not all fluorescent molecules within a sample will be imaged. This can influence molecule counting studies and co-localisation studies, in which two different fluorophores could present differing detection efficiencies, although the effect is relatively understudied (Shivanandan et al., 2014). Absolute fibrous quantification, for example counting the number of molecules assigned to a fibre, is not presented in this Thesis.

6.3.4 Fixation artefacts

Hardware developments, such as the scientific complementary metal-oxide-semiconductor (sCMOS) camera, have helped push the field of SMLM towards the fast imaging realm, however owing to the number of frames (of the order of tens of thousands) required to reconstruct a SMLM image, this technique is temporally limited. As such, SMLM is particularly suited to the study of chemically fixed samples. To date, much of the quantitative SMLM studies of protein or indeed fibrous SPPs have been performed using fixed cells. It is therefore of a critical importance that the distribution of proteins or fibres remains intact during and post-fixation. Numerous studies however have reported the perturbation of protein configuration upon the addition of a fixative (Annibale et al., 2012, Tanaka et al., 2010). This challenge is not particularly novel, plaguing the EM community for decades, however, this issue has not been fully addressed for quantitative SMLM studies and no universal strategy has been adopted. A recent study highlights the disruption of the actin cytoskeleton upon fixation with 4% paraformaldehyde (PFA), which further induces changes in transmembrane clustering (Pereira et al., 2018). By use of a pre-warmed specific buffer that acts to preserve the cytoskeleton however, these effects are minimal when compared to live cell data. For transmembrane proteins such as LAT, the authors state that upon

addition of 4% PFA in the cytoskeletal preservation buffer, transmembrane proteins immediately begin to immobilise and after 10 minutes at 37°C + 5% CO_2, 97% of the proteins are immobile. Whilst artefacts induced by fixation are an important concern in the context of this Thesis, reliable protocols and careful sample preparation were employed to preserve actin ultrastructure.

6.4 Outlook for the field

SMLM is arguably the most valuable fluorescence-based tool for structural studies, owing to its high spatial resolution. However, SMLM lacks much of the flexibility of conventional microscopes or indeed of other super resolution systems in the context of live cell imaging. Indeed, live SMLM encounters the same, fundamental challenges of target labelling as fixed cell acquisitions, in addition to requiring a high temporal resolution to avoid motion blur, and remaining cell friendly. Using PA-FPs, live cell labelling is however relatively routine. Underlying the success of these experiments are the developments in hardware (described in Section 1.3.4), enabling a temporal resolution capable of detecting dynamic behaviours in physiological conditions. However, SMLM remains currently limited to ~ 500 – 3200 Hz frame rates, and as such the detection of rapid processes by SMLM is unattainable. The most important challenge faced by live cell SMLM is phototoxicity. Whilst a higher power laser can produce a higher number of localisations per image frame, fluorophores can produce toxic substances upon illumination.

Structural studies of live cell SMLM data sets are currently in their infancy, partially due to the aforementioned imaging constraints. Whilst analysis methods such as super-resolution radial fluctuations (SRRF) (Gustafsson et al.,

2016) have been proposed for achieving high speed, live cell friendly images of up to 150 nm spatial resolution, this strategy is not particularly suited for fine nanometric structures such as actin. Further, the SRRF method does not embrace pointillist data requirements. Interestingly, from an analysis point of view, the exact quantity of information required for a robust quantification does not necessarily equate to thousands of raw image frames. A recent live cell cluster analysis method for SMLM data exemplifies this, by definition of a minimum point requirement (MPR) for accurate quantification (Griffié et al., 2018). A strategy based on a MPR for live cell fibre analysis could be promising, in which splines could be fit to data or machine learning could be implemented to predict filament growth or termination, for example.

Concurrent with the development of live cell friendly approaches to SMLM is the development of high throughput, large FOV, automated systems (Douglass et al., 2016, Beghin et al., 2017). The study of biological processes is intrinsically multi scale and turning SMLM into a high-throughput technique is an attractive prospect owing to its lengthy acquisition process and the large quantities of data garnered. For example, a typical IRIS image of the actin cytoskeleton within a single Jurkat T cell amounts to 12 GB and typically takes over an hour to produce. Moreover, variations in cell morphologies and actin ultrastructures for example are important to observe, to gather reliable and accurate statistics. In the case of T cells, the study of primary cells would particularly benefit from this approach due to their increased variability in comparison to Jurkat T cells, and their inability to be maintained in cell culture, without immortalisation. Integrating high content screening (HCS) with SMLM in an automated manner is thus attractive for high throughput drug screening and large-scale evaluation of protein dynamics on the nanoscale. A limiting factor of this approach is time. When performing SMLM

that requires buffers to induce blinking behaviours such as dSTORM for example, one must consider the lifetime of the buffer for estimating the number of sequential cells achievable. When performing IRIS this consideration is mitigated, however, the acquisition process is highly time-consuming owing to the increased integration times required.

Correlative approaches that combine super resolution microscopy with other modalities such as atomic force microscopy (AFM) or EM, exploit the strengths of each technique whilst offsetting their individual weaknesses. Correlative super resolution is a fast-growing field, with broad and varied biological applications. One can for example, exploit the sub nanometre resolution of EM whilst reporting on highly specific intracellular events through fluorescence or one could combine atomic force microscopy (AFM) with SMLM, to extract mechanical and structural information (Hauser et al., 2017, Sartori et al., 2007, Odermatt et al., 2015). When combining two imaging modalities however, one must carefully consider the compatibility of fixation methods, buffer and hydration requirements and the substrates used. The nanoscale structure-function relationships of various cellular entities can be probed by quantitative analysis of the complementary information garnered by correlative microscopy. Currently, this field remains in its infancy and exciting opportunities for method and multimodal analysis development exist.

In terms of T cell biology, T cell activation in response to the stiffness of the substrate has become a recent subject of interest. O'Connor et al. report up to four fold enhancement of IL-2 production in T cells activated on soft substrates (Young's modulus < 100 kPa) compared to stiffer counterparts (Young's modulus > 2 MPa) (O'Connor et al., 2012). The rigidity of the substrate is thus

begging to be considered as an additional regulator of activation. As previously discussed, the mechanosensitive nature of the T cell immunological synapse is currently not well understood. The crosstalk between the biophysical properties of T cells and the likely mechanosensing properties of immunological synapse related proteins could be analysed by correlative SMLM. This would improve our understanding of which actin networks at the immunological synapse are the major drivers of force production upon activation and could further highlight the mechanisms by which immunological synapse associated proteins sense environmental stimuli and initiate the appropriate response, dependent upon the substrate.

Concerted efforts to improve available fluorescent probes, compatibility with live cell imaging, advanced chemical approaches to modulate fluorescence signals and instrumentation could provide SMLM with the potential to become the dominant fluorescence microscopy technique across the life sciences. In unison with acquisition improvements, advances in localisation algorithms and SPP post-processing analytics could propel SMLM into an ideal imaging technique for quantitative biology.

Chapter 7 Methods

7.1 Cell culture

Jurkat E6.1 T cells (ATCC TIB-152) were cultured at 37°C + 5% CO_2 in supplemented Roswell Park Memorial Institute (RPMI-1640; Thermo Fisher, USA) medium (+10% fetal bovine serum (FBS) and 1% Penicillin; Thermo Fisher, USA). Cells were initially seeded to 200,000 cells/mL and reached up to 1.2 x 10^6 cells/mL before passage, every 3 days.

7.2 LAT transfection protocol

Jurkat T cells were transiently transfected via electroporation with 2 μg LAT-mEos2 (a kind gift from Dr. David Williamson) 24 hours prior to plating using an Amaxa system and the Amaxa Nucleofector Kit V (Lonza, USA). A dedicated program for Jurkat T cell viability (X-001) was used and an optimised protocol followed, per the manufacturers guide. To ensure a logarithmic growth phase, cells were seeded 48 hours prior to the transfections. Cells were counted using a haemocytometer and 1 x 10^6 cells were used per transfection, obtained via centrifugation at 90g for 10 minutes at room temperature. The supernatant was removed, and cell pellets were resuspended in 100 μL room-temperature Nucleofector® Solution V. 2 μg of the DNA vector was added to the cell solution and transferred to the provided

cuvettes, ensuring that no bubbles were present. The high viability program was then applied to each cuvette sample, which were allowed to recover for 10 minutes at room temperature post electroporation. Transfected cells were then transferred to 12 well plates containing equilibrated supplemented RPMI medium and maintained at 37°C + 5% CO_2. Expression typically occurred after 8+ hours.

7.3 Formation of immunological synapses

μ-Slide 8 well glass bottom coverslips (Ibidi, Germany) suitable for TIRFM (for 2D SMLM experiments) or a single glass #1.5 coverglass (22 mm diameter) with embedded gold fiducial markers (for 3D iPALM experiments), were coated with 2 μg/mL anti-CD3 (clone OKT3) and 5 μg/mL anti-CD28 (clone 28.2) antibodies (Cambridge Bioscience, UK) and left overnight at 4°C. This method acts to crosslink CD3 and CD28 molecules in the T cell membrane upon their encounter with the antibody coated surface. It is this artificial engagement and clustering of CD3 that prompts TCR associated signalling events, without the provision of the specific peptide. Whilst this method allows the formation of an artificial immunological synapse, one of its limitations is the immobilisation of stimulated CD3/CD28 molecules upon contact with the stimulus.

Prior to plating, coverslips were washed x3 with phosphate buffered saline (PBS) to remove surplus antibody and equilibrated at 37°C + 5% CO_2. For F-actin disrupting studies, cells were pre-incubated with 0.1 μM Cytochalasin D (Sigma-Aldrich, USA) for 15 minutes at 37°C. Cells were then placed on the stimulatory coverslips and allowed to form mature synapses for 8 minutes at

37°C + 5% CO_2 at a density of 80,000 cells per well. Surplus medium was removed, and cells were quickly fixed using a pre-warmed cytoskeletal/ fixation buffer (10 mM MES (6.1 pH), 5 mM EGTA, 5 mM fresh glucose, 150mM NaCl, 3mM MgCl pH.7.0 + 4% paraformaldehyde (PFA)) for 15 minutes at 37°C + 5% CO_2. Post-fixation, cells were washed x2 using the cytoskeletal buffer alone. For the LAT transfected (single colour, 2D fixed experiments) cells, at this stage the sample preparation was complete, as permeabilisation, staining, blocking and imaging buffers were not required for PALM experiments. For all other experiments, synapses were permeabilised post-fixation with 0.01% (w/v) L-α-Lysophosphatidylcholine (LPC; Sigma-Aldrich, Germany) in cytoskeletal buffer for 10 minutes at room temperature. Cells were then washed x2 in PBS to remove the detergent. Autofluorescence was then quenched using 0.1% (w/v) sodium borohydride (Sigma-Aldrich, Germany) for 7 minutes at room temperature. Cells were then washed x2, and coverslips blocked using 5% (w/v) bovine serum albumin (BSA; Sigma-Aldrich, Germany) for 1 hour at room temperature, to limit non-specific antibody binding. The blocking agent was then washed x2 prior to staining.

7.3.1 F-actin labelling procedure for IRIS experiments

For 2D, fixed cell IRIS imaging of the actin cytoskeleton, the IRIS probe (LifeAct-Atto655N, a kind gift from Prof. Helge Ewers) was added to the blocked sample at a concentration of 0.5 nM.

7.3.2 F-actin labelling procedure for TIRFM, 2D and 3D dSTORM experiments

Post blocking, cells were labelled with Alexa Fluor® 647 Phalloidin (Thermo Fisher, USA) at a concentration of 1U per well, and left at 4°C overnight per the method of (van de Linde et al., 2011). Prior to imaging, cells were washed gently in PBS (termination of protocol for TIRFM studies), and an oxygen scavenging buffer was added either to flood the chamber (for 2D, dSTORM imaging) or sealed between two glass coverslips (for iPALM 3D dSTORM imaging), to reduce the effects of oxidation. The oxygen scavenging buffer comprised a base solution maintained at 4°C and additional components that must be freshly made. The base buffer consisted of 50 mM Tris pH 8.5, 10 mM NaCl and 0.56 M Glucose. For the imaging buffer, 5 U/ml pyranose oxidase, 50 mM mercaptoethylamine (MEA), 40 μg/mL catalase and 2 mM cyclooctatetraene (COT) were freshly added to the base buffer, for each experiment.

7.3.3 F-actin and LAT (multicolour) labelling procedure

For the dual colour data presented in Chapter 5, the labelling strategy of Section 7.3.2 was followed, once the chamber had been chemically blocked, using transfected cells per Section 7.2. Multicolour SMLM was achieved by the photoconvertible fluorescent protein mEos2 labelling the LAT molecules, and Alexa Fluor® 647 Phalloidin labelling the actin filaments. All other experimental procedures, such as fixation and permeabilisation, were maintained as per the single colour experiments.

7.4 TIRFM imaging

TIRFM was performed using a Nikon Ti-E microscope (Nikon, Japan), with a 60 x 1.49 N_A Apo-TIRF oil immersion objective lens. Excitation of sample fluorophores was achieved though application of a 640 nm (for Alexa Fluor® 647 Phalloidin samples) or through a 488 nm laser (for LAT mEos2 samples) and fluorescence was collected onto a sCMOS camera (Andor Technology Ltd., UK).

7.5 2D IRIS, dSTORM and PALM imaging procedures

A commercial N-STORM system (Nikon, Japan), operated in TIRF mode, was used for all 2D SMLM imaging, with a 100 x 1.49 N_A oil immersion objective lens. Cells were imaged using the appropriate excitation laser and fluorescence was collected on an electron multiplying charged coupled device EMCCD camera (iXon3 DU-897E (Andor Technology Ltd., UK)). A quad bandpass emission filter set (Chroma 89902-ET-405/488/561/647 nm) was used to filter the fluorescence collected from the sample. After selecting an appropriate ROI (512 x 512 pixels), the acquisition can begin.

For IRIS imaging, the 647 nm laser was applied to the sample, and images were collected at 50 ms integration time, with 50,000 – 100,000 frames typically recorded. The sparsity in activation is achieved through the transient binding events of the probe to actin filaments and does not rely upon photoactivation or conversion. Whilst in theory, the probe can be photobleached, owing to the essentially unlimited number of freely diffusing probe that exists in the pool, photobleaching is not typically observed within an acquisition. A trade-off must however be made. The laser power was set to 50% of maximum power

for IRIS acquisitions to the limit background signal. Whilst the number of photons collected per fluorophore may be reduced by this, the uncertainty in localisations remained substantially lower than that of dSTORM images.

For 2D dSTORM imaging, cells were imaged using a 647 nm laser at full power, with 405 nm photoactivation. Camera integration time was set to 10 ms, and up to 50,000 frames were typically recorded. For PALM imaging, cells were imaged again under TIRF illumination with a 563 nm laser with photo-activation at 405 nm, and fluorescence was captured within 575 – 625 nm. The camera integration time was set to 30 ms, and up to 30,000 frames were typically collected.

7.6 Multicolour SMLM imaging

To perform dual colour SMLM, PALM was firstly performed of the LAT - associated population of fluorophores (as described in Section 2.5) followed by dSTORM imaging (as described in Section 2.5) of the fluorophores bound to F-actin. The axial drift perfect focus system (PFS) was used throughout.

7.7 3D iPALM imaging

The 3D iPALM data presented in the Discussion of this Thesis was collected at the Advanced Imaging Center at the Howard Hughes Medical Institute's Janelia Research Campus. A dual system of 60x oil immersion objective lenses (Nikon, Japan) were used with a 642 nm continuous excitation laser for imaging (with low 405 nm photoactivation) onto a system of 3

EMCCD cameras (iXon3-DU897E; Andor). Typically, 50,000 frames were recorded for reconstruction and camera integration time was set to 10 ms.

7.8 Image reconstruction of SMLM data sets

With the exception of the iPALM data presented in the Discussion of this Thesis, the ImageJ plug-in ThunderSTORM was used to reconstruct SMLM images (Ovesný et al., 2014). ThunderSTORM is an open source package, allows user definable parameters and offers computation strategies to overcome SMLM artefacts, such multiple fluorophore blinking per the merging tool. The ThunderSTORM workflow commences with image filtering. A wavelet filter (B-spline) of order 3 and scale 2 was used for image de-noising and feature enhancement. The approximate localisations of molecules were first estimated using a local maximum approach, with 8-neighbourhood connectivity. This method considers all pixels in the filtered image and calculates if firstly, the pixel intensity at the given pixel is higher than that of a user defined threshold (1.5 * std (Wave.F1); default) and secondly if the given pixel intensity is higher than or equal to all values within the 8-connected neighbourhood. If both conditions are met, the pixel is considered as an appropriate candidate for the approximate position of a molecule. For sub-pixel localisation of molecules, the integrated Gaussian method was used. The integrated form of a 2D symmetric Gaussian function is proposed to account for the discrete nature of the camera pixels, whereas a Gaussian function alone does not.

Post-processing included uncertainty filtering, drift correction by cross correlation and merging of molecules detected in more than 20 consecutive

frames (within a 20 nm radius) (Annibale et al., 2010). For IRIS data sets, owing to the high number of detected molecules per image (typically 12 million localisations per cell), one can afford to apply stringent filtering criteria to obtain high quality images. As such, for IRIS data sets, localisations with uncertainties greater than 16 nm (calculated per the method of Thompson et al., 2000) were removed. For 2D dSTORM data sets, localisations with uncertainties greater than 40 nm were removed, in line with the analysis requirements of the tracing method.

3D dSTORM iPALM data was reconstructed using Peak Selector software (IDL, courtesy of Harald Hess). Briefly, drift and tilt correction were applied to each data set by use of the gold embedded fiducial markers in the #1.5 coverglass. Localisations with uncertainties less than 40 nm were retained for analysis.

7.9 Statistical analysis

All statistical analysis was performed in GraphPad Prism software (GraphPad Software Inc, USA). P values were calculated using an unpaired, two-tailed, non-parametric, Mann-Whitney test, except when stated otherwise.

7.10 Code

All simulation and analysis code presented in this Thesis were written in Matlab 2015b, with exception of the Bayesian cluster analysis code (written in

R per the authors' preference. Software developed in this Thesis is freely available at GitHub: OwenlabKCL.

Publications

1. J. Griffié, R. Peters, D. M. Owen. *An agent-based model of molecular aggregation at the cell membrane (2018)*. PLoS ONE (In peer review).

2. R. Peters, J. Griffié, D. J. Williamson, D. M. Owen. *Development of 2-colour and 3D SMLM data analysis methods for fibrous spatial point patterns (2018).* Journal of Physics D: Applied Physics, 52 (1).

3. R. Peters, J. Griffié, G. L. Burn, D. J. Williamson, D. M. Owen. *Quantitative Fibre Analysis of Single Molecule Localization Microscopy Data (2018).* Scientific Reports 8 (1), 10418.

4. J. Griffié, G. L. Burn, D. J. Williamson, R. Peters, P. Rubin-Delanchy, D. M. Owen. *Dynamic Bayesian Cluster Analysis of Live-Cell Single Molecule Localisation Microscopy Datasets (2018).* Small Methods 2 (9), 1800008.

5. E. Kemal, R. Peters, L. Sandiford, D. M. Owen, L.A. Dailey, M. Green. *Magnetic Conjugated Polymer Nanoparticles Doped with a Europium Complex for Biomedical Imaging (2018)***.** Photochemical & Photobiological Sciences 17, 718-721.

6. J. Griffié, L. Shlomovich, D. J. Williamson, M. Shannon, J. Aaron, S. Khuon, G. L. Burn, L. Boelen, R. Peters, A. P. Cope, E. A. K. Cohen, P. Rubin-Delanchy, D. M. Owen. *3D Bayesian cluster analysis of super-resolution data reveals LAT recruitment to the T cell synapse (2017)***.** Scientific Reports 7 (1), 4077.

7. R. Peters, M. Muniz-Benthem, J. Griffié, D. J. Williamson, G. W. Ashdown, C. D. Lorenz, D. M. Owen. *Quantification of fibrous spatial point patterns from single-molecule localization microscopy (SMLM) data (2017).* Bioinformatics 33 (11), 1703-1711.

8. G. W. Ashdown, G. L. Burn, D. J. Williamson, E. Pandžić, R. Peters, M. Holden, H. Ewers, L. Shao, P. W. Wiseman, D. M. Owen. *Live-Cell Super-Resolution Reveals F-Actin and Plasma Membrane Dynamics at the T Cell Synapse (2017).* Biophysical Journal 112 (8), 1703-1713.

9. E. Kemal, T. Fedatto Abelha, L. Urbano, R. Peters, D. M. Owen, P. Howes, M. Green, L. A. Dailey. *Bright, near infrared emitting PLGA–PEG dye-doped CN-PPV nanoparticles for imaging applications (2017).* RSC Advances 7 (25), 15255-15264.

10. R. Peters, L. Sandiford, D. M. Owen, E. Kemal, S. Bourke, L. A. Dailey, M. Green. *Red-emitting protein-coated conjugated polymer nanoparticles (2016).* Photochemical & Photobiological Sciences 15 (11), 1448-1452.

Other publications

1. R. Peters, D. M. Owen, J. Griffié. *Analysis of Fibrous Spatial Point Patterns from Single-Molecule Super-Resolution Microscopy Data (2017).* Biophysical Journal 112 (3), 142a.

2. R. Peters, D. M. Owen. *On the use of Ripley's K-function to quantify fibrous spatial point patterns (2017).* Microscopy & Analysis, Life Sciences Supplement September/October 2017.

Conference presentations

1. D.J. Williamson, R. Peters, J. Griffié, and D.M. Owen. *Machine-learning based cluster analysis of SMLM data*. SMLMS2018, Berlin, Germany (2018). (Poster).

2. J. Griffié, R. Peters, G. Burn, P. Rubin-Delanchy & D.M. Owen. *Quantifying protein nanoscale aggregation*. 84th Harden Conference, Oxford, UK (2018). (Poster).

3. R. Peters, J. Griffié, & D.M. Owen. *Post-processing analytics and the information content of single-molecule localisation microscopy, SMLM*. Photonex, London, UK (2018). (Oral presentation).

4. J. Griffié, R. Peters, D.J. Williamson, G. Burn, M. Shannon, L. Shlomovich, E.A.K. Cohen, P. Rubin-Delanchy & D.M. Owen. *Beyond the pretty picture*. SMLMS2017, London, UK (2017). (Oral presentation).

5. R. Peters, J. Griffié, D.J. Williamson and D.M. Owen. *Quantitative analysis of cytoskeletal nanoarchitecture at the T cell immunological synapse*. SMLMS2017, London, UK (2017) (Poster).

6. R. Peters, D.M. Owen, J. Griffié. *Analysis of Fibrous Spatial Point Patterns from Single-Molecule Super-Resolution Microscopy Data*. Microscopy and Microscience Congress, Manchester, UK (2017). ***Best poster award**

7. J. Griffié, G. Burn, D.J. Williamson**,** R. Peters, P. Rubin-Delanchy & D.M. Owen. *On the need of cluster analysis for super resolution pointillist data.* MMC, Manchester, UK (2017). (Oral presentation).

8. R. Peters, J. Griffié, D.M. Owen. *Analysis of Fibrous Spatial Point Patterns from Single-Molecule Super-Resolution Microscopy Data.* BPS, New Orleans, USA (2017). (Poster).

9. G.W. Ashdown, G.L. Burn, E. Pandžić, R. Peters, M. Holden, H. Ewers, L. Shao, P.W. Wiseman and D.M. Owen. *Live-cell super-resolution reveals the architecture, dynamics and coupling of F-actin and the plasma membrane at the T cell immunological synapse*. EMBL Symposium: Actin in Action: From Molecules to Cellular Functions, Heidelberg, Germany (2016). (Poster)

References

AHUJA, R., PINYOL, R., REICHENBACH, N., CUSTER, L., KLINGENSMITH, J., KESSELS, M. M. & QUALMANN, B. 2007. Cordon-bleu is an actin nucleation factor and controls neuronal morphology. *Cell,* 131**,** 337-350.

AIRY, G. 1834. On the Diffraction of an Object-glass with Circular Aperture. *Transactions of the Cambridge Philosophical Society,* 5**,** 283.

AIVAZIAN, D. & STERN, L. J. 2000. Phosphorylation of T cell receptor ζ is regulated by a lipid dependent folding transition. *Nature Structural Biology,* 7**,** 1023.

AL-ALWAN, M. M., LIWSKI, R. S., HAERYFAR, S. M. M., BALDRIDGE, W. H., HOSKIN, D. W., ROWDEN, G. & WEST, K. A. 2003. Cutting Edge: Dendritic Cell Actin Cytoskeletal Polarization during Immunological Synapse Formation Is Highly Antigen-Dependent. *The Journal of Immunology,* 171**,** 4479.

AL-ALWAN, M. M., ROWDEN, G., LEE, T. D. G. & WEST, K. A. 2001. Cutting Edge: The Dendritic Cell Cytoskeleton Is Critical for the Formation of the Immunological Synapse. *The Journal of Immunology,* 166**,** 1452.

ALARCÓN, B., MESTRE, D. & MARTÍNEZ-MARTÍN, N. 2011. The immunological synapse: a cause or consequence of T-cell receptor triggering? *Immunology,* 133**,** 420-425.

ALBRECHT, D., WINTERFLOOD, C. M., SADEGHI, M., TSCHAGER, T., NOÉ, F. & EWERS, H. 2016. Nanoscopic compartmentalization of membrane protein motion at the axon initial segment. *The Journal of Cell Biology*.

ALIOSCHA-PEREZ, M., BENADIBA, C., GOOSSENS, K., KASAS, S., DIETLER, G., WILLAERT, R. & SAHLI, H. 2016. A Robust Actin Filaments Image Analysis Framework. *PLOS Computational Biology,* 12**,** e1005063.

ANDREW, S. M. & TITUS, J. A. 2003. Fragmentation of Immunoglobulin G. *Current Protocols in Cell Biology,* 17**,** 16.4.1-16.4.10.

ANDREWS, C., SWAIN, S. L. & MURALIDHAR, G. 1997. CD4 T cell anergy in murine AIDS: costimulation via CD28 and the addition of IL-12 are not sufficient to rescue anergic CD4 T cells. *The Journal of Immunology,* 159**,** 2132.

ANDRONOV, L., ORLOV, I., LUTZ, Y., VONESCH, J.-L. & KLAHOLZ, B. P. 2016. ClusterViSu, a method for clustering of protein complexes by Voronoi tessellation in super-resolution microscopy. *Scientific Reports,* 6**,** 24084.

ANGRA, S. & AHUJA, S. Machine learning and its applications: A review. 2017 International Conference on Big Data Analytics and Computational Intelligence (ICBDAC), 23-25 March 2017 2017. 57-60.

ANNIBALE, P., SCARSELLI, M., GRECO, M. & RADENOVIC, A. 2012. Identification of the factors affecting co-localization precision for quantitative multicolor localization microscopy. *Optical Nanoscopy,* 1**,** 1-13.

ANNIBALE, P., SCARSELLI, M., KODIYAN, A. & RADENOVIC, A. 2010. Photoactivatable Fluorescent Protein mEos2 Displays Repeated Photoactivation after a Long-Lived Dark State in the Red Photoconverted Form. *Journal of Physical Chemistry Letters,* 1**,** 1506-1510.

ANNIBALE, P., VANNI, S., SCARSELLI, M., ROTHLISBERGER, U. & RADENOVIC, A. 2011a. Identification of clustering artifacts in photoactivated localization microscopy. *Nature Methods,* 8**,** 527-528.

ANNIBALE, P., VANNI, S., SCARSELLI, M., ROTHLISBERGER, U. & RADENOVIC, A. 2011b. Quantitative Photo Activated Localization Microscopy: Unraveling the Effects of Photoblinking. *PLoS ONE,* 6**,** e22678.

ASHDOWN, G. W., BURN, G. L., WILLIAMSON, D. J., PANDŽIĆ, E., PETERS, R., HOLDEN, M., EWERS, H., SHAO, L., WISEMAN, P. W. & OWEN, D. M. 2017. Live-Cell Super-resolution Reveals F-Actin and Plasma Membrane Dynamics at the T Cell Synapse. *Biophysical Journal,* 112**,** 1703-1713.

AXELROD, D. 1981. Cell surface contacts illuminated by total internal reflection fluorescence. *Journal of Cell Biology,* 89**,** 141-145.

BABICH, A., LI, S., O'CONNOR, R. S., MILONE, M. C., FREEDMAN, B. D. & BURKHARDT, J. K. 2012. F-actin polymerization and retrograde flow drive sustained PLCγ1 signaling during T cell activation. *The Journal of Cell Biology,* 197**,** 775-787.

BACHIR, A. I., HORWITZ, A. R., NELSON, W. J. & BIANCHINI, J. M. 2017. Actin-Based Adhesion Modules Mediate Cell Interactions with the Extracellular Matrix and Neighboring Cells. *Cold Spring Harbor perspectives in biology,* 9**,** a023234.

BADDELEY, D., CANNELL, M. B. & SOELLER, C. 2010. Visualization of Localization Microscopy Data. *Microscopy and Microanalysis,* 16**,** 64-72.

BADOUR, K., ZHANG, J., SHI, F., MCGAVIN, M. K. H., RAMPERSAD, V., HARDY, L. A., FIELD, D. & SIMINOVITCH, K. A. 2003. The Wiskott-Aldrich Syndrome Protein Acts Downstream of CD2 and the CD2AP and PSTPIP1 Adaptors to Promote Formation of the Immunological Synapse. *Immunity,* 18**,** 141-154.

BALAGOPALAN, L., KORTUM, R. L., COUSSENS, N. P., BARR, V. A. & SAMELSON, L. E. 2015. The Linker for Activation of T Cells (LAT)

Signaling Hub: From Signaling Complexes to Microclusters. *Journal of Biological Chemistry,* 290**,** 26422-26429.

BALAGOPALAN, L., YI, J., NGUYEN, T., MCINTIRE, K. M., HARNED, A. S., NARAYAN, K. & SAMELSON, L. E. 2018. Plasma membrane LAT activation precedes vesicular recruitment defining two phases of early T-cell activation. *Nature Communications,* 9**,** 2013.

BAMBURG, J. R. & BERNSTEIN, B. W. 2016. Actin dynamics and cofilin-actin rods in alzheimer disease. *Cytoskeleton,* 73**,** 477-497.

BARCELLONA, M. L. & GRATTON, E. 1990. The Fluorescence Properties of a DNA Probe - 4'-6-Diamidino-2- Phenylindole (Dapi). *European Biophysics Journal,* 17**,** 315-323.

BARCIA, C., GOMEZ, A., DE PABLOS, V., FERNÁNDEZ-VILLALBA, E., LIU, C., KROEGER, K. M., MARTÍN, J., BARREIRO, A. F., CASTRO, M. G., LOWENSTEIN, P. R. & HERRERO, M.-T. 2008. CD20, CD3, and CD40 ligand microclusters segregate three-dimensionally in vivo at B-cell-T-cell immunological synapses after viral immunity in primate brain. *Journal of virology,* 82**,** 9978-9993.

BARCIA, C., THOMAS, C. E., CURTIN, J. F., KING, G. D., WAWROWSKY, K., CANDOLFI, M., XIONG, W.-D., LIU, C., KROEGER, K., BOYER, O., KUPIEC-WEGLINSKI, J., KLATZMANN, D., CASTRO, M. G. & LOWENSTEIN, P. R. 2006. In vivo mature immunological synapses forming SMACs mediate clearance of virally infected astrocytes from the brain. *The Journal of experimental medicine,* 203**,** 2095-2107.

BARDA-SAAD, M., BRAIMAN, A., TITERENCE, R., BUNNELL, S. C., BARR, V. A. & SAMELSON, L. E. 2004. Dynamic molecular interactions linking the T cell antigen receptor to the actin cytoskeleton. *Nature Immunology,* 6**,** 80.

BASU, R. & HUSE, M. 2017. Mechanical Communication at the Immunological Synapse. *Trends in Cell Biology,* 27**,** 241-254.

BECKER, W. 2012. Fluorescence lifetime imaging – techniques and applications. *Journal of Microscopy,* 247**,** 119-136.

BEEMILLER, P. & KRUMMEL, M. F. 2010. Mediation of T-Cell Activation by Actin Meshworks. *Cold Spring Harbor Perspectives in Biology,* 2.

BEGHIN, A., KECHKAR, A., BUTLER, C., LEVET, F., CABILLIC, M., ROSSIER, O., GIANNONE, G., GALLAND, R., CHOQUET, D. & SIBARITA, J.-B. 2017. Localization-based super-resolution imaging meets high-content screening. *Nature Methods,* 14**,** 1184.

BENNETT, V. & BAINES, A. J. 2001. Spectrin and Ankyrin-Based Pathways: Metazoan Inventions for Integrating Cells Into Tissues. *Physiological Reviews,* 81**,** 1353-1392.

BETZIG, E., PATTERSON, G. H., SOUGRAT, R., LINDWASSER, O. W., OLENYCH, S., BONIFACINO, J. S., DAVIDSON, M. W., LIPPINCOTT-

SCHWARTZ, J. & HESS, H. F. 2006. Imaging Intracellular Fluorescent Proteins at Nanometer Resolution. *Science,* 313**,** 1642-1645.

BEYERSDORF, N., KERKAU, T. & HÜNIG, T. 2015. CD28 co-stimulation in T-cell homeostasis: a recent perspective. *ImmunoTargets and therapy,* 4**,** 111-122.

BIANCO, B. & DIASPRO, A. 1989. Analysis of three-dimensional cell imaging obtained with optical microscopy techniques based on defocusing. *Cell Biophysics,* 15**,** 189-199.

BLANCHOIN, L., BOUJEMAA-PATERSKI, R., SYKES, C. & PLASTINO, J. 2014. Actin Dynamics, Architecture, and Mechanics in Cell Motility. *Physiological Reviews,* 94**,** 235-263.

BLYTHE, K. L., TITUS, E. J. & WILLETS, K. A. 2013. Triplet-State-Mediated Super-Resolution Imaging of Fluorophore-Labeled Gold Nanorods. *ChemPhysChem,* 15**,** 784-793.

BOBROFF, N. 1986. Position measurement with a resolution and noise-limited instrument. *Review of Scientific Instruments,* 57**,** 1152-1157.

BONGIOVANNI, M. N., GODET, J., HORROCKS, M. H., TOSATTO, L., CARR, A. R., WIRTHENSOHN, D. C., RANASINGHE, R. T., LEE, J.-E., PONJAVIC, A., FRITZ, J. V., DOBSON, C. M., KLENERMAN, D. & LEE, S. F. 2016. Multi-dimensional super-resolution imaging enables surface hydrophobicity mapping. *Nature Communications,* 7**,** 13544.

BOOMER, J. S. & GREEN, J. M. 2010. An enigmatic tail of CD28 signaling. *Cold Spring Harbor perspectives in biology,* 2**,** a002436-a002436.

BORISY, G. G. & SVITKINA, T. M. 2000. Actin machinery: pushing the envelope. *Current Opinion in Cell Biology,* 12**,** 104-112.

BOROVAC, J., BOSCH, M. & OKAMOTO, K. 2018. Regulation of actin dynamics during structural plasticity of dendritic spines: Signaling messengers and actin-binding proteins. *Molecular and Cellular Neuroscience,* 91**,** 122-130.

BOUDAOUD, A., BURIAN, A., BOROWSKA-WYKRĘT, D., UYTTEWAAL, M., WRZALIK, R., KWIATKOWSKA, D. & HAMANT, O. 2014. FibrilTool, an ImageJ plug-in to quantify fibrillar structures in raw microscopy images. *Nature Protocols,* 9**,** 457.

BOVELLAN, M., ROMEO, Y., BIRO, M., BODEN, A., CHUGH, P., YONIS, A., VAGHELA, M., FRITZSCHE, M., MOULDING, D., THOROGATE, R., JÉGOU, A., THRASHER, ADRIAN J., ROMET-LEMONNE, G., ROUX, PHILIPPE P., PALUCH, EWA K. & CHARRAS, G. 2014. Cellular Control of Cortical Actin Nucleation. *Current Biology,* 24**,** 1628-1635.

BRAY, D. 2001. *Cell Movements: From Molecules to Motility*, Garland Pub.

BRENNER, M. B., TROWBRIDGE, I. S. & STROMINGER, J. L. 1985. Cross-linking of human T cell receptor proteins: association between the T cell idiotype β subunit and the T3 glycoprotein heavy subunit. *Cell,* 40**,** 183-190.

BRETSCHER, A., EDWARDS, K. & FEHON, R. G. 2002. ERM proteins and merlin: integrators at the cell cortex. *Nature Reviews Molecular Cell Biology,* 3**,** 586.

BROMLEY, S. K., BURACK, W. R., JOHNSON, K. G., SOMERSALO, K., SIMS, T. N., SUMEN, C., DAVIS, M. M., SHAW, A. S., ALLEN, P. M. & DUSTIN, M. L. 2001. The Immunological Synapse. *Annual Review of Immunology,* 19**,** 375-396.

BROSSARD, C., FEUILLET, V., SCHMITT, A., RANDRIAMAMPITA, C., ROMAO, M., RAPOSO, G. & TRAUTMANN, A. 2005. Multifocal structure of the T cell – dendritic cell synapse. *European Journal of Immunology,* 35**,** 1741-1753.

BROWN, D. A. & ROSE, J. K. 1992. Sorting of GPI-anchored proteins to glycolipid-enriched membrane subdomains during transport to the apical cell surface. *Cell,* 68**,** 533-544.

BROWN, M. J., NIJHARA, R., HALLAM, J. A., GIGNAC, M., YAMADA, K. M., ERLANDSEN, S. L., DELON, J., KRUHLAK, M. & SHAW, S. 2003. Chemokine stimulation of human peripheral blood T lymphocytes induces rapid dephosphorylation of ERM proteins, which facilitates loss of microvilli and polarization. *Blood,* 102**,** 3890.

BRUEHL, R. E., SPRINGER TA FAU - BAINTON, D. F. & BAINTON, D. F. 1996. Quantitation of L-selectin distribution on human leukocyte microvilli by immunogold labeling and electron microscopy. *Journal of Histochemistry & Cytochemistry* 8**,** 835-844.

BUNNELL, S. C., HONG, D. I., KARDON, J. R., YAMAZAKI, T., MCGLADE, C. J., BARR, V. A. & SAMELSON, L. E. 2002. T cell receptor ligation induces the formation of dynamically regulated signaling assemblies. *The Journal of Cell Biology,* 158**,** 1263.

BURKE, THOMAS A., CHRISTENSEN, JENNA R., BARONE, E., SUAREZ, C., SIROTKIN, V. & KOVAR, DAVID R. 2014. Homeostatic Actin Cytoskeleton Networks Are Regulated by Assembly Factor Competition for Monomers. *Current Biology,* 24**,** 579-585.

BURKHARDT, J. K., CARRIZOSA, E. & SHAFFER, M. H. 2008. The Actin Cytoskeleton in T Cell Activation. *Annual Review of Immunology,* 26.

BUSTELO, X. R., SAUZEAU, V. & BERENJENO, I. M. 2007. GTP-binding proteins of the Rho/Rac family: regulation, effectors and functions in vivo. *BioEssays : news and reviews in molecular, cellular and developmental biology,* 29**,** 356-370.

CAMPI, G., VARMA, R. & DUSTIN, M. L. 2005. Actin and agonist MHC-peptide complex-dependent T cell receptor microclusters as scaffolds for signaling. *Journal of Experimental Medicine,* 202**,** 1031-1036.

CARLIN, L. M., ELEME, K., MCCANN, F. E. & DAVIS, D. M. 2001. Intercellular Transfer and Supramolecular Organization of Human

Leukocyte Antigen C at Inhibitory Natural Killer Cell Immune Synapses. *Journal of Experimental Medicine,* 194**,** 1507-1517.

CARPÉN, O., PALLAI, P., STAUNTON, D. E. & SPRINGER, T. A. 1992. Association of intercellular adhesion molecule-1 (ICAM-1) with actin-containing cytoskeleton and alpha-actinin. *The Journal of Cell Biology,* 118**,** 1223.

CARR, A. R., PONJAVIC, A., BASU, S., MCCOLL, J., SANTOS, A. M., DAVIS, S., LAUE, E. D., KLENERMAN, D. & LEE, S. F. 2017. Three-Dimensional Super-Resolution in Eukaryotic Cells Using the Double-Helix Point Spread Function. *Biophysical Journal,* 112**,** 1444-1454.

CHALFIE, M., TU, Y., EUSKIRCHEN, G., WARD, W. W. & PRASHER, D. C. 1994. Green fluorescent protein as a marker for gene expression. *Science,* 263**,** 802-805.

CHAN, A. C., IWASHIMA, M., TURCK, C. W. & WEISS, A. 1992. ZAP-70: A 70 kd protein-tyrosine kinase that associates with the TCR ζ chain. *Cell,* 71**,** 649-662.

CHHABRA, E. S. & HIGGS, H. N. 2007. The many faces of actin: matching assembly factors with cellular structures. *Nature Cell Biology,* 9**,** 1110.

CHUGH, P. & PALUCH, E. K. 2018. The actin cortex at a glance. *Journal of Cell Science,* 131.

COHEN, I. B. 1958. A History of Luminescence From the Earliest Times Until 1900. By E. Newton Harvey. [Memoirs of the American Philosophical Society, Volume 44]. (Philadelphia: the Society. 1957. Pp. xxiv, 692. $6.00.). *The American Historical Review,* 63**,** 937-939.

COLLINS, A., WARRINGTON, A., TAYLOR, KENNETH A. & SVITKINA, T. 2011. Structural Organization of the Actin Cytoskeleton at Sites of Clathrin-Mediated Endocytosis. *Current Biology,* 21**,** 1167-1175.

COLÓN-FRANCO, J. M., GOMEZ, T. S. & BILLADEAU, D. D. 2011. Dynamic remodeling of the actin cytoskeleton by FMNL1γ is required for structural maintenance of the Golgi complex. *Journal of Cell Science,* 124**,** 3118.

COMRIE, W. A., LI, S., BOYLE, S. & BURKHARDT, J. K. 2015. The dendritic cell cytoskeleton promotes T cell adhesion and activation by constraining ICAM-1 mobility. *The Journal of cell biology,* 208**,** 457-473.

COOPER, G. M. 2009. The Cell: A Molecular Approach. *The Cell: A Molecular Approach.* Washington, D.C: ASM Press.

COOPER, J. A. 1987. Effects of cytochalasin and phalloidin on actin. *The Journal of Cell Biology,* 105**,** 1473.

CORMACK, B. P., VALDIVIA, R. H. & FALKOW, S. 1996. FACS-optimized mutants of the green fluorescent protein (GFP). *Gene,* 173**,** 33-38.

COTTE, Y., TOY, M. F., PAVILLON, N. & DEPEURSINGE, C. 2010. Microscopy image resolution improvement by deconvolution of complex fields. *Optics Express,* 18**,** 19462-19478.

CRITES, T. J., PADHAN, K., MULLER, J., KROGSGAARD, M., GUDLA, P. R., LOCKETT, S. J. & VARMA, R. 2014. TCR Microclusters pre-exist and contain molecules necessary for TCR signal transduction. *Journal of immunology (Baltimore, Md. : 1950),* 193**,** 56-67.

CULLEY, S., ALBRECHT, D., JACOBS, C., PEREIRA, P. M., LETERRIER, C., MERCER, J. & HENRIQUES, R. 2018. Quantitative mapping and minimization of super-resolution optical imaging artifacts. *Nature Methods,* 15**,** 263.

DAS, D. K., FENG, Y., MALLIS, R. J., LI, X., KESKIN, D. B., HUSSEY, R. E., BRADY, S. K., WANG, J.-H., WAGNER, G., REINHERZ, E. L. & LANG, M. J. 2015. Force-dependent transition in the T-cell receptor β-subunit allosterically regulates peptide discrimination and pMHC bond lifetime. *Proceedings of the National Academy of Sciences,* 112**,** 1517.

DAS, V., NAL, B., DUJEANCOURT, A., THOULOUZE, M.-I., GALLI, T., ROUX, P., DAUTRY-VARSAT, A. & ALCOVER, A. 2004. Activation-Induced Polarized Recycling Targets T Cell Antigen Receptors to the Immunological Synapse: Involvement of SNARE Complexes. *Immunity,* 20**,** 577-588.

DAVIS, D. M., CHIU, I., FASSETT, M., COHEN, G. B., MANDELBOIM, O. & STROMINGER, J. L. 1999. The human natural killer cell immune synapse. *Proceedings of the National Academy of Sciences,* 96**,** 15062-15067.

DAVIS, D. M. & DUSTIN, M. L. 2004. What is the importance of the immunological synapse? *Trends in Immunology,* 25**,** 323-327.

DAVIS, S. J. & VAN DER MERWE, P. A. 2006. The kinetic-segregation model: TCR triggering and beyond. *Nature Immunology,* 7**,** 803.

DAVIS, S. J. & VAN DER MERWE, P. A. 2011. Lck and the nature of the T cell receptor trigger. *Trends in immunology,* 32**,** 1-5.

DAY, R. N. & DAVIDSON, M. W. 2009. The fluorescent protein palette: tools for cellular imaging. *Chemical Society reviews,* 38**,** 2887-2921.

DE LA CRUZ, E. M. & POLLARD, T. D. 1996. Kinetics and Thermodynamics of Phalloidin Binding to Actin Filaments from Three Divergent Species. *Biochemistry,* 35**,** 14054-14061.

DELON, J., BERCOVICI, N., LIBLAU, R. & TRAUTMANN, A. 2006. Imaging antigen recognition by naive CD4+ T cells: compulsory cytoskeletal alterations for the triggering of an intracellular calcium response. *European Journal of Immunology,* 28**,** 716-729.

DEMCHENKO, A. P., MÉLY, Y., DUPORTAIL, G. & KLYMCHENKO, A. S. 2009. Monitoring Biophysical Properties of Lipid Membranes by Environment-Sensitive Fluorescent Probes. *Biophysical Journal,* 96**,** 3461-3470.

DEMOND, A. L., MOSSMAN, K. D., STARR, T., DUSTIN, M. L. & GROVES, J. T. 2008. T Cell Receptor Microcluster Transport through Molecular

Mazes Reveals Mechanism of Translocation. *Biophysical Journal,* 94**,** 3286-3292.

DEMPSEY, G. T., VAUGHAN, J. C., CHEN, K. H., BATES, M. & ZHUANG, X. 2011. Evaluation of fluorophores for optimal performance in localization-based super-resolution imaging. *Nature Methods,* 8**,** 1027-1036.

DESCHOUT, H., ZANACCHI, F. C., MLODZIANOSKI, M., DIASPRO, A., BEWERSDORF, J., HESS, S. T. & BRAECKMANS, K. 2014. Precisely and accurately localizing single emitters in fluorescence microscopy. *Nature Methods,* 11**,** 253-266.

DESTAINVILLE, N., DUMAS, F. & SALOMÉ, L. 2008. What do diffusion measurements tell us about membrane compartmentalisation? Emergence of the role of interprotein interactions. *Journal of chemical biology,* 1**,** 37-48.

DICKSON, R. M., CUBITT, A. B., TSIEN, R. Y. & MOERNER, W. E. 1997. On/off blinking and switching behaviour of single molecules of green fluorescent protein. *Nature,* 388**,** 355.

DOCTOR, R. B. & FOUASSIER, L. 2002. Emerging Roles of the Actin Cytoskeleton in Cholangiocyte Function and Disease. *Semin Liver Dis,* 22**,** 263-276.

DOMINGUEZ, R. 2004. Actin-binding proteins – a unifying hypothesis. *Trends in Biochemical Sciences,* 29**,** 572-578.

DONG, J., RADAU, B., OTTO, A., MÜLLER, E.-C., LINDSCHAU, C. & WESTERMANN, P. 2000. Profilin I attached to the Golgi is required for the formation of constitutive transport vesicles at the trans-Golgi network. *Biochimica et Biophysica Acta (BBA) - Molecular Cell Research,* 1497**,** 253-260.

DOUGLASS, K. M., SIEBEN, C., ARCHETTI, A., LAMBERT, A. & MANLEY, S. 2016. Super-resolution imaging of multiple cells by optimised flat-field epi-illumination. *Nature photonics,* 10**,** 705-708.

DRENCKHAHN, D. & POLLARD, T. D. 1986. Elongation of actin filaments is a diffusion-limited reaction at the barbed end and is accelerated by inert macromolecules. *Journal of Biological Chemistry,* 261**,** 12754-12758.

DURISIC, N., LAPARRA-CUERVO, L., SANDOVAL-ÁLVAREZ, Á., BORBELY, J. S. & LAKADAMYALI, M. 2014. Single-molecule evaluation of fluorescent protein photoactivation efficiency using an in vivo nanotemplate. *Nature Methods,* 11**,** 156.

DUSHEK, O., MUELLER, S., SOUBIES, S., DEPOIL, D., CARAMALHO, I., COOMBS, D. & VALITUTTI, S. 2008. Effects of Intracellular Calcium and Actin Cytoskeleton on TCR Mobility Measured by Fluorescence Recovery. *PLOS ONE,* 3**,** e3913.

DUSTIN, M. L. 2014. The immunological synapse. *Cancer immunology research,* 2**,** 1023-33.

DUSTIN, M. L. & COOPER, J. A. 2000. The immunological synapse and the actin cytoskeleton: molecular hardware for T cell signaling. *Nature Immunology,* 1**,** 23-29.

EGHIAIAN, F., RIGATO, A. & SCHEURING, S. 2015. Structural, mechanical, and dynamical variability of the actin cortex in living cells. *Biophysical journal,* 108**,** 1330-1340.

EHRLICH, L. I. R., EBERT, P. J. R., KRUMMEL, M. F., WEISS, A. & DAVIS, M. M. 2002. Dynamics of p56lck Translocation to the T Cell Immunological Synapse following Agonist and Antagonist Stimulation. *Immunity,* 17**,** 809-822.

ELOSEGUI-ARTOLA, A., JORGE-PEÑAS, A., MORENO-AROTZENA, O., OREGI, A., LASA, M., GARCÍA-AZNAR, J. M., DE JUAN-PARDO, E. M. & ALDABE, R. 2014. Image Analysis for the Quantitative Comparison of Stress Fibers and Focal Adhesions. *PLOS ONE,* 9**,** e107393.

ELTZNER, B., WOLLNIK, C., GOTTSCHLICH, C., HUCKEMANN, S. & REHFELDT, F. 2015. The Filament Sensor for Near Real-Time Detection of Cytoskeletal Fiber Structures. *PLOS ONE,* 10**,** e0126346.

ENDERLEIN, J., TOPRAK, E. & SELVIN, P. R. 2006. Polarization effect on position accuracy of fluorophore localization. *Optics Express,* 14**,** 8111-8120.

EWERS, H., TADA, T., PETERSEN, J. D., RACZ, B., SHENG, M. & CHOQUET, D. 2014. A Septin-Dependent Diffusion Barrier at Dendritic Spine Necks. *PLOS ONE,* 9**,** e113916.

FENG, Y. & WALSH, C. A. 2004. The many faces of filamin: A versatile molecular scaffold for cell motility and signalling. *Nature Cell Biology,* 6**,** 1034.

FENG, Z., NING CHEN, W., VEE SIN LEE, P., LIAO, K. & CHAN, V. 2005. The influence of GFP-actin expression on the adhesion dynamics of HepG2 cells on a model extracellular matrix. *Biomaterials,* 26**,** 5348-5358.

FERRER, J. M., LEE, H., CHEN, J., PELZ, B., NAKAMURA, F., KAMM, R. D. & LANG, M. J. 2008. Measuring molecular rupture forces between single actin filaments and actin-binding proteins. *Proceedings of the National Academy of Sciences of the United States of America,* 105**,** 9221-9226.

FINCO, T. S., KADLECEK, T., ZHANG, W., SAMELSON, L. E. & WEISS, A. 1998. LAT Is Required for TCR-Mediated Activation of PLCγ1 and the Ras Pathway. *Immunity,* 9**,** 617-626.

FISCHER, M. B., HAUBER, I., EGGENBAUER, H., THON, V., VOGEL, E., SCHAFFER, E., LOKAJ, J., LITZMAN, J., WOLF, H. M. & MANNHALTER, J. W. 1994. A defect in the early phase of T-cell receptor-mediated T-cell activation in patients with common variable immunodeficiency. *Blood,* 84**,** 4234.

FOOKSMAN, D. R., VARDHANA, S., VASILIVER-SHAMIS, G., LIESE, J., BLAIR, D. A., WAITE, J., SACRISTÁN, C., VICTORA, G. D., ZANIN-ZHOROV, A. & DUSTIN, M. L. 2010. Functional Anatomy of T Cell Activation and Synapse Formation. *Annual Review of Immunology,* 28**,** 79-105.

FORNBERG, B. & ZUEV, J. 2007. The Runge phenomenon and spatially variable shape parameters in RBF interpolation. *Computers & Mathematics with Applications,* 54**,** 379-398.

FUJIWARA, I., VAVYLONIS, D. & POLLARD, T. D. 2007. Polymerization kinetics of ADP- and ADP-Pi-actin determined by fluorescence microscopy. *Proceedings of the National Academy of Sciences of the United States of America,* 104**,** 8827-8832.

FULLER, C. L., BRACIALE, V. L. & SAMELSON, L. E. 2003. All roads lead to actin: the intimate relationship between TCR signaling and the cytoskeleton. *Immunological Reviews,* 191**,** 220-236.

GALLWITZ, D. & SURES, I. 1980. Structure of a split yeast gene: complete nucleotide sequence of the actin gene in Saccharomyces cerevisiae. *Proceedings of the National Academy of Sciences of the United States of America,* 77**,** 2546-2550.

GEIGER, B. & SINGER, S. J. 1979. The participation of α-actinin in the capping of cell membrane components. *Cell,* 16**,** 213-222.

GEISLER, C., HOTZ, T., SCHÖNLE, A., HELL, S. W., MUNK, A. & EGNER, A. 2012. Drift estimation for single marker switching based imaging schemes. *Optics Express,* 20**,** 7274-7289.

GHOSH, M., SONG, X., MOUNEIMNE, G., SIDANI, M., LAWRENCE, D. S. & CONDEELIS, J. S. 2004. Cofilin Promotes Actin Polymerization and Defines the Direction of Cell Motility. *Science,* 304**,** 743.

GIANNONE, G., HOSY, E., LEVET, F., CONSTALS, A., SCHULZE, K., SOBOLEVSKY, ALEXANDER I., ROSCONI, M. P., GOUAUX, E., TAMPÉ, R., CHOQUET, D. & COGNET, L. 2010. Dynamic Superresolution Imaging of Endogenous Proteins on Living Cells at Ultra-High Density. *Biophysical Journal,* 99**,** 1303-1310.

GIEPMANS, B. N. G., ADAMS, S. R., ELLISMAN, M. H. & TSIEN, R. Y. 2006. The Fluorescent Toolbox for Assessing Protein Location and Function. *Science,* 312**,** 217-224.

GOLDSCHMIDT-CLERMONT, P. J., MACHESKY, L. M., BALDASSARE, J. J. & POLLARD, T. D. 1990. The actin-binding protein profilin binds to PIP2 and inhibits its hydrolysis by phospholipase C. *Science,* 247**,** 1575.

GOLEY, E. D. & WELCH, M. D. 2006. The ARP2/3 complex: an actin nucleator comes of age. *Nature Reviews Molecular Cell Biology,* 7**,** 713.

GOMEZ, T. S., KUMAR, K., MEDEIROS, R. B., SHIMIZU, Y., LEIBSON, P. J. & BILLADEAU, D. D. 2007. Formins regulate the actin-related protein

2/3 complex-independent polarization of the centrosome to the immunological synapse. *Immunity,* 26**,** 177-190.

GOMEZ, T. S., MCCARNEY, S. D., CARRIZOSA, E., LABNO, C. M., COMISKEY, E. O., NOLZ, J. C., ZHU, P., FREEDMAN, B. D., CLARK, M. R., RAWLINGS, D. J., BILLADEAU, D. D. & BURKHARDT, J. K. 2006. HS1 Functions as an Essential Actin-Regulatory Adaptor Protein at the Immune Synapse. *Immunity,* 24**,** 741-752.

GOODE, B. L. & ECK, M. J. 2007. Mechanism and Function of Formins in the Control of Actin Assembly. *Annual Review of Biochemistry,* 76**,** 593-627.

GORDÓN-ALONSO, M., SALA-VALDÉS, M., ROCHA-PERUGINI, V., PÉREZ-HERNÁNDEZ, D., LÓPEZ-MARTÍN, S., URSA, A., ÁLVAREZ, S., KOLESNIKOVA, T. V., VÁZQUEZ, J., SÁNCHEZ-MADRID, F. & YÁÑEZ-MÓ, M. 2012. EWI-2 Association with α-Actinin Regulates T Cell Immune Synapses and HIV Viral Infection. *The Journal of Immunology,* 189**,** 689.

GOWRISHANKAR, K., GHOSH, S., SAHA, S., C, R., MAYOR, S. & RAO, M. 2012. Active Remodeling of Cortical Actin Regulates Spatiotemporal Organization of Cell Surface Molecules. *Cell,* 149**,** 1353-1367.

GRAKOUI, A., BROMLEY, S. K., SUMEN, C., DAVIS, M. M., SHAW, A. S., ALLEN, P. M. & DUSTIN, M. L. 1999. The Immunological Synapse: A Molecular Machine Controlling T Cell Activation. *Science,* 285**,** 221-227.

GRANADA-RAMÍREZ, D. A., ARIAS-CERÓN, J. S., RODRIGUEZ-FRAGOSO, P., VÁZQUEZ-HERNÁNDEZ, F., LUNA-ARIAS, J. P., HERRERA-PEREZ, J. L. & MENDOZA-ÁLVAREZ, J. G. 2018. 16 - Quantum dots for biomedical applications. *In:* NARAYAN, R. (ed.) *Nanobiomaterials*. Woodhead Publishing.

GRIFFIÉ, J., BURN, G. L., WILLIAMSON, D. J., PETERS, R., RUBIN-DELANCHY, P. & OWEN, D. M. 2018. Dynamic Bayesian Cluster Analysis of Live-Cell Single Molecule Localization Microscopy Datasets. *Small Methods,* 2**,** 1800008.

GUNNING, P. W., GHOSHDASTIDER, U., WHITAKER, S., POPP, D. & ROBINSON, R. C. 2015. The evolution of compositionally and functionally distinct actin filaments. *Journal of Cell Science,* 128**,** 2009.

GUSTAFSSON, M. G. L. 2000. Surpassing the lateral resolution limit by a factor of two using structured illumination microscopy. *Journal of Microscopy,* 198**,** 82-87.

GUSTAFSSON, N., CULLEY, S., ASHDOWN, G., OWEN, D. M., PEREIRA, P. M. & HENRIQUES, R. 2016. Fast live-cell conventional fluorophore nanoscopy with ImageJ through super-resolution radial fluctuations. *Nature Communications,* 7.

GUSTAVSSON, A.-K., PETROV, P. N. & MOERNER, W. E. 2018. Light sheet approaches for improved precision in 3D localization-based super-

resolution imaging in mammalian cells [Invited]. *Optics Express,* 26**,** 13122-13147.

HAASE, P. 1995. Spatial Pattern Analysis in Ecology Based on Ripley's K-Function: Introduction and Methods of Edge Correction. *Journal of Vegetation Science,* 6**,** 575-582.

HAILMAN, E., BURACK, W. R., SHAW, A. S., DUSTIN, M. L. & ALLEN, P. M. 2002. Immature CD4+CD8+ Thymocytes Form a Multifocal Immunological Synapse with Sustained Tyrosine Phosphorylation. *Immunity,* 16**,** 839-848.

HALL, A. 1994. Small GTP-Binding Proteins and the Regulation of the Actin Cytoskeleton. *Annual Review of Cell Biology,* 10**,** 31-54.

HASHIMOTO-TANE, A. & SAITO, T. 2016. Dynamic Regulation of TCR-Microclusters and the Microsynapse for T Cell Activation. *Frontiers in immunology,* 7**,** 255-255.

HATANO, S. & OOSAWA, F. 1966. Isolation and characterization of plasmodium actin. *Biochimica et Biophysica Acta (BBA) - General Subjects,* 127**,** 488-498.

HAUSER, M., WOJCIK, M., KIM, D., MAHMOUDI, M., LI, W. & XU, K. 2017. Correlative Super-Resolution Microscopy: New Dimensions and New Opportunities. *Chemical Reviews,* 117**,** 7428-7456.

HEILEMANN, M., VAN DE LINDE, S., MUKHERJEE, A. & SAUER, M. 2009. Super-Resolution Imaging with Small Organic Fluorophores. *Angewandte Chemie International Edition,* 48**,** 6903-6908.

HEILEMANN, M., VAN DE LINDE, S., SCHÜTTPELZ, M., KASPER, R., SEEFELDT, B., MUKHERJEE, A., TINNEFELD, P. & SAUER, M. 2008. Subdiffraction-Resolution Fluorescence Imaging with Conventional Fluorescent Probes. *Angewandte Chemie International Edition,* 47**,** 6172-6176.

HEINE, J., WURM, C. A., KELLER-FINDEISEN, J., SCHÖNLE, A., HARKE, B., REUSS, M., WINTER, F. R. & DONNERT, G. 2018. Three dimensional live-cell STED microscopy at increased depth using a water immersion objective. *Review of Scientific Instruments,* 89**,** 053701.

HELL, S. W., STELZER, E. H. K., LINDEK, S. & CREMER, C. 1994. Confocal microscopy with an increased detection aperture: type-B 4Pi confocal microscopy. *Optics Letters,* 19**,** 222-224.

HELL, S. W. & WICHMANN, J. 1994. Breaking the diffraction resolution limit by stimulated emission: Stimulated-emission-depletion fluorescence microscopy. *Optics Letters,* 19**,** 780-782.

HENG, Y.-W. & KOH, C.-G. 2010. Actin cytoskeleton dynamics and the cell division cycle. *The International Journal of Biochemistry & Cell Biology,* 42**,** 1622-1633.

HENNEY, C. S. & BUBBERS, J. E. 1973. Antigen-T Lymphocyte Interactions: Inhibition by Cytochalasin B. *The Journal of Immunology,* 111**,** 85.

HERBERICH, G., WÜRFLINGER, T., SECHI, A., WINDOFFER, R., LEUBE, R. & AACH, T. Fluorescence microscopic imaging and image analysis of the cytoskeleton. 2010 Conference Record of the Forty Fourth Asilomar Conference on Signals, Systems and Computers, 7-10 Nov. 2010 2010. 1359-1363.

HERMAN, I. M. 1993. Actin isoforms. *Current Opinion in Cell Biology,* 5**,** 48-55.

HERNANDEZ, J. B., NEWTON, R. H. & WALSH, C. M. 2010. Life and death in the thymus--cell death signaling during T cell development. *Current opinion in cell biology,* 22**,** 865-871.

HERSCHEL, J. F. W. 1845. Case of superficial colour presented by a homogeneous liquid internally colourless. *Philosophical Transactions of the Royal Society of London,* 135**,** 143-145.

HESS, S. T., GIRIRAJAN, T. P. K. & MASON, M. D. 2006. Ultra-High Resolution Imaging by Fluorescence Photoactivation Localization Microscopy. *Biophysical Journal,* 91**,** 4258-4272.

HESS, S. T., KUMAR, M., VERMA, A., FARRINGTON, J., KENWORTHY, A. & ZIMMERBERG, J. 2005. Quantitative electron microscopy and fluorescence spectroscopy of the membrane distribution of influenza hemagglutinin. *The Journal of Cell Biology,* 169**,** 965.

HOESSLI, D., RUNGGER-BRÄNDLE, E., JOCKUSCH, B. M. & GABBIANI, G. 1980. Lymphocyte alpha-actinin. Relationship to cell membrane and co-capping with surface receptors. *The Journal of Cell Biology,* 84**,** 305.

HOLDEN, S. J., UPHOFF, S. & KAPANIDIS, A. N. 2011. DAOSTORM: an algorithm for high- density super-resolution microscopy. *Nature Methods,* 8**,** 279-280.

HOLMES, K. C., POPP, D., GEBHARD, W. & KABSCH, W. 1990. Atomic model of the actin filament. *Nature,* 347**,** 44.

HOTULAINEN, P. & LAPPALAINEN, P. 2006. Stress fibers are generated by two distinct actin assembly mechanisms in motile cells. *The Journal of Cell Biology,* 173**,** 383.

HOUTMEYERS, E., GOSSELINK, R., GAYAN-RAMIREZ, G. & DECRAMER, M. 1999. Regulation of mucociliary clearance in health and disease. *European Respiratory Journal,* 13**,** 1177.

HU, Y. S., CANG, H. & LILLEMEIER, B. F. 2016. Superresolution imaging reveals nanometer- and micrometer-scale spatial distributions of T-cell receptors in lymph nodes. *Proceedings of the National Academy of Sciences,* 113**,** 7201-7206.

HUANG, F., SCHWARTZ, S. L., BYARS, J. M. & LIDKE, K. A. 2011. Simultaneous multiple-emitter fitting for single molecule super-resolution imaging. *Biomedical Optics Express,* 2**,** 1377-1393.

HUANG, K.-Y., LAI, M.-W., LEE, W.-I. & HUANG, Y.-C. 2008. Fatal Cytomegalovirus Gastrointestinal Disease in an Infant with Wiskott-

Aldrich Syndrome. *Journal of the Formosan Medical Association,* 107**,** 64-67.

HUISKEN, J., SWOGER, J., DEL BENE, F., WITTBRODT, J. & STELZER, E. H. K. 2004. Optical Sectioning Deep Inside Live Embryos by Selective Plane Illumination Microscopy. *Science,* 305**,** 1007-1009.

HUPPA, J. B. & DAVIS, M. M. 2003. T-cell-antigen recognition and the immunological synapse. *Nature Reviews Immunology,* 3**,** 973.

ISAKOV, N. 1997. Immunoreceptor tyrosine-based activation motif (ITAM), a unique module linking antigen and Fc receptors to their signaling cascades. *Journal of Leukocyte Biology,* 61**,** 6-16.

JACOBSON, K., MOURITSEN, O. G. & ANDERSON, R. G. W. 2007. Lipid rafts: at a crossroad between cell biology and physics. *Nature Cell Biology,* 9**,** 7-14.

JAIN, A. & PASARE, C. 2017. Innate Control of Adaptive Immunity: Beyond the Three-Signal Paradigm. *The Journal of Immunology,* 198**,** 3791.

JANEWAY , C. A. J., TRAVERS, P., WALPORT, M. & SHLOMCHIK, M. 2005. *Immunobiology: The Immune System in Health and Disease,* New York, Garland Science Publishing.

JANOŠTIAK, R., PATAKI, A. C., BRÁBEK, J. & RÖSEL, D. 2014. Mechanosensors in integrin signaling: The emerging role of p130Cas. *European Journal of Cell Biology,* 93**,** 445-454.

JOHANNES, L., PEZESHKIAN, W., IPSEN, J. H. & SHILLCOCK, J. C. 2018. Clustering on Membranes: Fluctuations and More. *Trends in Cell Biology,* 28**,** 405-415.

JOHNSON, M., EAST, DANIEL A. & MULVIHILL, DANIEL P. 2014. Formins Determine the Functional Properties of Actin Filaments in Yeast. *Current Biology,* 24**,** 1525-1530.

JONES, L. J. F., CARBALLIDO-LÓPEZ, R. & ERRINGTON, J. 2001. Control of Cell Shape in Bacteria: Helical, Actin-like Filaments in Bacillus subtilis. *Cell,* 104**,** 913-922.

JUNG, Y., RIVEN, I., FEIGELSON, S. W., KARTVELISHVILY, E., TOHYA, K., MIYASAKA, M., ALON, R. & HARAN, G. 2016. Three-dimensional localization of T-cell receptors in relation to microvilli using a combination of superresolution microscopies. *Proceedings of the National Academy of Sciences,* 113**,** E5916.

JUNGMANN, R., AVENDANO, M. S., WOEHRSTEIN, J. B., DAI, M., SHIH, W. M. & YIN, P. 2014. Multiplexed 3D cellular super-resolution imaging with DNA-PAINT and Exchange-PAINT. *Nature Methods,* 11**,** 313-318.

JUNGMANN, R., STEINHAUER, C., SCHEIBLE, M., KUZYK, A., TINNEFELD, P. & SIMMEL, F. C. 2010. Single-Molecule Kinetics and Super-Resolution Microscopy by Fluorescence Imaging of Transient Binding on DNA Origami. *Nano Letters,* 10**,** 4756-4761.

KABOURIDIS, P. S. 2006. Lipid rafts in T cell receptor signalling. *Molecular membrane biology,* 23**,** 49-57.

KABSCH, W., MANNHERZ, H. G., SUCK, D., PAI, E. F. & HOLMES, K. C. 1990. Atomic structure of the actin: DNase I complex. *Nature,* 347**,** 37.

KAIZUKA, Y., DOUGLASS, A. D., VARMA, R., DUSTIN, M. L. & VALE, R. D. 2007. Mechanisms for segregating T cell receptor and adhesion molecules during immunological synapse formation in Jurkat T cells. *Proceedings of the National Academy of Sciences,* 104**,** 20296-20301.

KANG, F., PURICH, D. L. & SOUTHWICK, F. S. 1999. Profilin Promotes Barbed-end Actin Filament Assembly without Lowering the Critical Concentration. *Journal of Biological Chemistry,* 274**,** 36963-36972.

KHAN, A. O., SIMMS, V. A., PIKE, J. A., THOMAS, S. G. & MORGAN, N. V. 2017. CRISPR-Cas9 Mediated Labelling Allows for Single Molecule Imaging and Resolution. *Scientific Reports,* 7**,** 8450.

KIM, A. S., KAKALIS, L. T., ABDUL-MANAN, N., LIU, G. A. & ROSEN, M. K. 2000. Autoinhibition and activation mechanisms of the Wiskott–Aldrich syndrome protein. *Nature,* 404**,** 151.

KIUCHI, T., HIGUCHI, M., TAKAMURA, A., MARUOKA, M. & WATANABE, N. 2015. Multitarget super-resolution microscopy with high-density labeling by exchangeable probes. *Nature Methods,* 12**,** 743-746.

KLEIN, T., LOSCHBERGER, A., PROPPERT, S., WOLTER, S., VAN DE LINDE, S. & SAUER, M. 2011. Live-cell dSTORM with SNAP-tag fusion proteins. *Nature Methods,* 8**,** 7-9.

KLOC, M., KUBIAK, J. Z., LI, X. C. & GHOBRIAL, R. M. 2013. The newly found functions of MTOC in immunological response. *Journal of Leukocyte Biology,* 95**,** 417-430.

KOLDSØ, H., REDDY, T., FOWLER, P. W., DUNCAN, A. L. & SANSOM, M. S. P. 2016. Membrane Compartmentalization Reducing the Mobility of Lipids and Proteins within a Model Plasma Membrane. *The journal of physical chemistry. B,* 120**,** 8873-8881.

KORENBAUM, E., NORDBERG, P., BJÖRKEGREN-SJÖGREN, C., SCHUTT, C. E., LINDBERG, U. & KARLSSON, R. 1998. The Role of Profilin in Actin Polymerization and Nucleotide Exchange. *Biochemistry,* 37**,** 9274-9283.

KÖSTER, D. V., HUSAIN, K., ILJAZI, E., BHAT, A., BIELING, P., MULLINS, R. D., RAO, M. & MAYOR, S. 2016. Actomyosin dynamics drive local membrane component organization in an in vitro active composite layer. *Proceedings of the National Academy of Sciences*.

KOZMA, R., AHMED, S., BEST, A. & LIM, L. 1995. The Ras-related protein Cdc42Hs and bradykinin promote formation of peripheral actin microspikes and filopodia in Swiss 3T3 fibroblasts. *Molecular and Cellular Biology,* 15**,** 1942.

KRONLAGE, C., SCHÄFER-HERTE, M., BÖNING, D., OBERLEITHNER, H. & FELS, J. 2015. Feeling for Filaments: Quantification of the Cortical Actin Web in Live Vascular Endothelium. *Biophysical Journal,* 109**,** 687-698.

KRUMMEL, M. F. & DAVIS, M. M. 2002. Dynamics of the immunological synapse: finding, establishing and solidifying a connection. *Current Opinion in Immunology,* 14**,** 66-74.

KRUMMEL, M. F., SJAASTAD, M. D., WÜLFING, C. & DAVIS, M. M. 2000. Differential Clustering of CD4 and CD3ζ During T Cell Recognition. *Science,* 289**,** 1349.

KUHNÉ, M. R., LIN, J., YABLONSKI, D., MOLLENAUER, M. N., EHRLICH, L. I. R., HUPPA, J., DAVIS, M. M. & WEISS, A. 2003. Linker for Activation of T Cells, ζ-Associated Protein-70, and Src Homology 2 Domain-Containing Leukocyte Protein-76 are Required for TCR-Induced Microtubule-Organizing Center Polarization. *The Journal of Immunology,* 171**,** 860.

KUMAR, B. V., CONNORS, T. J. & FARBER, D. L. 2018. Human T Cell Development, Localization, and Function throughout Life. *Immunity,* 48**,** 202-213.

KUMARI, S., CURADO, S., MAYYA, V. & DUSTIN, M. L. 2014. T cell antigen receptor activation and actin cytoskeleton remodeling. *Biochimica et Biophysica Acta (BBA) - Biomembranes,* 1838**,** 546-556.

KUMARI, S., VARDHANA, S., CAMMER, M., CURADO, S., SANTOS, L., SHEETZ, M. & DUSTIN, M. 2012. T Lymphocyte Myosin IIA is Required for Maturation of the Immunological Synapse. *Frontiers in Immunology,* 3.

KUPFER, A., MOSMANN, T. R. & KUPFER, H. 1991. Polarized expression of cytokines in cell conjugates of helper T cells and splenic B cells. *Proceedings of the National Academy of Sciences,* 88**,** 775.

KUPFER, A., SWAIN, S. L. & SINGER, S. J. 1987. The specific direct interaction of helper T cells and antigen-presenting B cells. II. Reorientation of the microtubule organizing center and reorganization of the membrane-associated cytoskeleton inside the bound helper T cells. *The Journal of experimental medicine,* 165**,** 1565-1580.

KUSUMI, A., IKE, H., NAKADA, C., MURASE, K. & FUJIWARA, T. 2005a. Single-molecule tracking of membrane molecules: plasma membrane compartmentalization and dynamic assembly of raft-philic signaling molecules. *Seminars in Immunology,* 17**,** 3-21.

KUSUMI, A., NAKADA, C., RITCHIE, K., MURASE, K., SUZUKI, K., MURAKOSHI, H., KASAI, R. S., KONDO, J. & FUJIWARA, T. 2005b. Paradigm shift of the plasma membrane concept from the two-dimensional continuum fluid to the partitioned fluid: High-speed

single-molecule tracking of membrane molecules. *Annual Review of Biophysics and Biomolecular Structure,* 34**,** 351-378.

KUSUMI, A., SHIRAI, Y. M., KOYAMA-HONDA, I., SUZUKI, K. G. N. & FUJIWARA, T. K. 2010. Hierarchical organization of the plasma membrane: Investigations by single-molecule tracking vs. fluorescence correlation spectroscopy. *FEBS Letters,* 584**,** 1814-1823.

LAI, F. P. L., SZCZODRAK, M., BLOCK, J., FAIX, J., BREITSPRECHER, D., MANNHERZ, H. G., STRADAL, T. E. B., DUNN, G. A., SMALL, J. V. & ROTTNER, K. 2008. Arp2/3 complex interactions and actin network turnover in lamellipodia. *The EMBO Journal,* 27**,** 982.

LAKOWICZ, J. R. 2006. *Principles of fluorescence spectroscopy,* New York, Springer Science + Business Media, LLC.

LANZETTI, L. 2007. Actin in membrane trafficking. *Current Opinion in Cell Biology,* 19**,** 453-458.

LAPPALAINEN, P. & DRUBIN, D. G. 1997. Cofilin promotes rapid actin filament turnover in vivo. *Nature,* 388**,** 78.

LEE, K.-H., DINNER, A. R., TU, C., CAMPI, G., RAYCHAUDHURI, S., VARMA, R., SIMS, T. N., BURACK, W. R., WU, H., WANG, J., KANAGAWA, O., MARKIEWICZ, M., ALLEN, P. M., DUSTIN, M. L., CHAKRABORTY, A. K. & SHAW, A. S. 2003. The Immunological Synapse Balances T Cell Receptor Signaling and Degradation. *Science,* 302**,** 1218-1222.

LEE, S. H. & DOMINGUEZ, R. 2010. Regulation of actin cytoskeleton dynamics in cells. *Molecules and cells,* 29**,** 311-325.

LEVET, F., HOSY, E., KECHKAR, A., BUTLER, C., BEGHIN, A., CHOQUET, D. & SIBARITA, J.-B. 2015. SR-Tesseler: a method to segment and quantify localization-based super-resolution microscopy data. *Nature Methods,* 12**,** 1065-1071.

LIDKE, K. A., RIEGER, B., JOVIN, T. M. & HEINTZMANN, R. 2005. Superresolution by localization of quantum dots using blinking statistics. *Optics Express,* 13**,** 7052-7062.

LILLEMEIER, B. F., MORTELMAIER, M. A., FORSTNER, M. B., HUPPA, J. B., GROVES, J. T. & DAVIS, M. M. 2010. TCR and Lat are expressed on separate protein islands on T cell membranes and concatenate during activation. *Nature Immunology,* 11**,** 90-96.

LILLEMEIER, B. F., PFEIFFER, J. R., SURVILADZE, Z., WILSON, B. S. & DAVIS, M. M. 2006. Plasma membrane-associated proteins are clustered into islands attached to the cytoskeleton. *Proceedings of the National Academy of Sciences,* 103**,** 18992-18997.

LIU, H.-S., JAN, M.-S., CHOU, C.-K., CHEN, P.-H. & KE, N.-J. 1999a. Is Green Fluorescent Protein Toxic to the Living Cells? *Biochemical and Biophysical Research Communications,* 260**,** 712-717.

LIU, R., ABREU-BLANCO, M. T., BARRY, K. C., LINARDOPOULOU, E. V., OSBORN, G. E. & PARKHURST, S. M. 2009. Wash functions downstream of Rho and links linear and branched actin nucleation factors. *Development (Cambridge, England),* 136**,** 2849-2860.

LIU, S. K., FANG, N., KORETZKY, G. A. & JANE MCGLADE, C. 1999b. The hematopoietic-specific adaptor protein Gads functions in T-cell signaling via interactions with the SLP-76 and LAT adaptors. *Current Biology,* 9**,** 67-75.

LIU, Y., BLANCHFIELD, L., MA, V. P.-Y., ANDARGACHEW, R., GALIOR, K., LIU, Z., EVAVOLD, B. & SALAITA, K. 2016. DNA-based nanoparticle tension sensors reveal that T-cell receptors transmit defined pN forces to their antigens for enhanced fidelity. *Proceedings of the National Academy of Sciences,* 113**,** 5610.

MABUCHI, I., HAMAGUCHI Y FAU - FUJIMOTO, H., FUJIMOTO H FAU - MORII, N., MORII N FAU - MISHIMA, M., MISHIMA M FAU - NARUMIYA, S. & NARUMIYA, S. 1993. A rho-like protein is involved in the organisation of the contractile ring in dividing sand dollar eggs.

MACHESKY, L. M. & INSALL, R. H. 1998. Scar1 and the related Wiskott–Aldrich syndrome protein, WASP, regulate the actin cytoskeleton through the Arp2/3 complex. *Current Biology,* 8**,** 1347-1356.

MACHESKY, L. M., MULLINS, R. D., HIGGS, H. N., KAISER, D. A., BLANCHOIN, L., MAY, R. C., HALL, M. E. & POLLARD, T. D. 1999. Scar, a WASp-related protein, activates nucleation of actin filaments by the Arp2/3 complex. *Proceedings of the National Academy of Sciences,* 96**,** 3739.

MACHICOANE, M., DE FRUTOS, C. A., FINK, J., ROCANCOURT, M., LOMBARDI, Y., GAREL, S., PIEL, M. & ECHARD, A. 2014. SLK-dependent activation of ERMs controls LGN–NuMA localization and spindle orientation. *The Journal of Cell Biology,* 205**,** 791.

MAGENAU, A., OWEN, D. M., YAMAMOTO, Y., TRAN, J., KWIATEK, J. M., PARTON, R. G. & GAUS, K. 2015. Discreet and distinct clustering of five model membrane proteins revealed by single molecule localization microscopy. *Molecular Membrane Biology,* 32**,** 11-18.

MAJSTORAVICH, S., ZHANG, J., NICHOLSON-DYKSTRA, S., LINDER, S., FRIEDRICH, W., SIMINOVITCH, K. A. & HIGGS, H. N. 2004. Lymphocyte microvilli are dynamic, actin-dependent structures that do not require Wiskott-Aldrich syndrome protein (WASp) for their morphology. *Blood,* 104**,** 1396.

MANLEY, S., GILLETTE, J. M., PATTERSON, G. H., SHROFF, H., HESS, H. F., BETZIG, E. & LIPPINCOTT-SCHWARTZ, J. 2008. High-density mapping of single-molecule trajectories with photoactivated localization microscopy. *Nature Methods,* 5**,** 155-157.

MARSH, R. J., PFISTERER, K., BENNETT, P., HIRVONEN, L. M., GAUTEL, M., JONES, G. E. & COX, S. 2018. Artifact-free high-density localization microscopy analysis. *Nature Methods,* 15**,** 689-692.

MARTÍN-CÓFRECES, N. B., ROBLES-VALERO, J., CABRERO, J. R., MITTELBRUNN, M., GORDÓN-ALONSO, M., SUNG, C.-H., ALARCÓN, B., VÁZQUEZ, J. & SÁNCHEZ-MADRID, F. 2008. MTOC translocation modulates IS formation and controls sustained T cell signaling. *The Journal of Cell Biology,* 182**,** 951.

MAZIDI, H., LU, J., NEHORAI, A. & LEW, M. D. 2018. Minimizing Structural Bias in Single-Molecule Super-Resolution Microscopy. *Scientific Reports,* 8**,** 13133.

METZLER, W. J., BELL, A. J., ERNST, E., LAVOIE, T. B. & MUELLER, L. 1994. Identification of the poly-L-proline-binding site on human profilin. *Journal of Biological Chemistry,* 269**,** 4620-4625.

MIKHAYLOVA, M., CLOIN, B. M. C., FINAN, K., VAN DEN BERG, R., TEEUW, J., KIJANKA, M. M., SOKOLOWSKI, M., KATRUKHA, E. A., MAIDORN, M., OPAZO, F., MOUTEL, S., VANTARD, M., PEREZ, F., VAN BERGEN EN HENEGOUWEN, P. M. P., HOOGENRAAD, C. C., EWERS, H. & KAPITEIN, L. C. 2015. Resolving bundled microtubules using anti-tubulin nanobodies. *Nature Communications,* 6**,** 7933.

MINGUENEAU, M., RONCAGALLI, R., GRÉGOIRE, C., KISSENPFENNIG, A., MIAZEK, A., ARCHAMBAUD, C., WANG, Y., PERRIN, P., BERTOSIO, E., SANSONI, A., RICHELME, S., LOCKSLEY, R. M., AGUADO, E., MALISSEN, M. & MALISSEN, B. 2009. Loss of the LAT Adaptor Converts Antigen-Responsive T Cells into Pathogenic Effectors that Function Independently of the T Cell Receptor. *Immunity,* 31**,** 197-208.

MINSKY, M. 1961. *Microscopy Apparatus*. USA patent application.

MITXITORENA, I., SAAVEDRA, E. & BARCIA, C. 2014. Kupfer-type immunological synapses in vivo: Raison D'être of SMAC. *Immunology & Cell Biology,* 93**,** 51-56.

MLODZIANOSKI, M. J., SCHREINER, J. M., CALLAHAN, S. P., SMOLKOVÁ, K., DLASKOVÁ, A., ŠANTOROVÁ, J., JEŽEK, P. & BEWERSDORF, J. 2011. Sample drift correction in 3D fluorescence photoactivation localization microscopy. *Optics Express,* 19**,** 15009-15019.

MOERNER, W. E. & KADOR, L. 1989. Optical detection and spectroscopy of single molecules in a solid. *Physical Review Letters,* 62**,** 2535-2538.

MONKS, C. R. F., FREIBERG, B. A., KUPFER, H., SCIAKY, N. & KUPFER, A. 1998. Three-dimensional segregation of supramolecular activation clusters in T cells. *Nature,* 395**,** 82-86.

MULLINS, R. D., HEUSER, J. A. & POLLARD, T. D. 1998. The interaction of Arp2/3 complex with actin: Nucleation, high affinity pointed end

capping, and formation of branching networks of filaments. *Proceedings of the National Academy of Sciences,* 95**,** 6181.

MURPHY, A. C. H. & YOUNG, P. W. 2015. The actinin family of actin cross-linking proteins - a genetic perspective. *Cell & bioscience,* 5**,** 49-49.

MURUGESAN, S., HONG, J., YI, J., LI, D., BEACH, J. R., SHAO, L., MEINHARDT, J., MADISON, G., WU, X., BETZIG, E. & HAMMER, J. A. 2016. Formin-generated actomyosin arcs propel T cell receptor microcluster movement at the immune synapse. *The Journal of Cell Biology,* 215**,** 383.

MYERS, D. R., ZIKHERMAN, J. & ROOSE, J. P. 2017. Tonic Signals: Why Do Lymphocytes Bother? *Trends in Immunology,* 38**,** 844-857.

NEISCH, A. L. & FEHON, R. G. 2011. Ezrin, Radixin and Moesin: key regulators of membrane–cortex interactions and signaling. *Current Opinion in Cell Biology,* 23**,** 377-382.

NIEUWENHUIZEN, R. P. J., LIDKE, K. A., BATES, M., PUIG, D. L., GRUNWALD, D., STALLINGA, S. & RIEGER, B. 2013. Measuring image resolution in optical nanoscopy. *Nature Methods,* 10**,** 557-562.

NIEUWENHUIZEN, R. P. J., NAHIDIAZAR, L., MANDERS, E. M. M., JALINK, K., STALLINGA, S. & RIEGER, B. 2015. Co-Orientation: Quantifying Simultaneous Co-Localization and Orientational Alignment of Filaments in Light Microscopy. *PLOS ONE,* 10**,** e0131756.

NOBES, C. D. & HALL, A. 1999. Rho GTPases Control Polarity, Protrusion, and Adhesion during Cell Movement. *The Journal of Cell Biology,* 144**,** 1235.

NOGALES, E. 2000. Structural Insights into Microtubule Function. *Annual Review of Biochemistry,* 69**,** 277-302.

NOLZ, J. C., GOMEZ, T. S., ZHU, P., LI, S., MEDEIROS, R. B., SHIMIZU, Y., BURKHARDT, J. K., FREEDMAN, B. D. & BILLADEAU, D. D. 2006. The WAVE2 complex regulates actin cytoskeletal reorganization and CRAC-mediated calcium entry during T cell activation. *Current biology : CB,* 16**,** 24-34.

NUÑEZ-CRUZ, S., AGUADO, E., RICHELME, S., CHETAILLE, B., MURA, A.-M., RICHELME, M., POUYET, L., JOUVIN-MARCHE, E., XERRI, L., MALISSEN, B. & MALISSEN, M. 2003. LAT regulates γδ T cell homeostasis and differentiation. *Nature Immunology,* 4**,** 999.

NYQUIST, H. 1928. Certain Topics in Telegraph Transmission Theory. *Transactions of the American Institute of Electrical Engineers,* 47**,** 617-644.

O'CONNOR, R. S., HAO, X., SHEN, K., BASHOUR, K., AKIMOVA, T., HANCOCK, W. W., KAM, L. C. & MILONE, M. C. 2012. Substrate Rigidity Regulates Human T Cell Activation and Proliferation. *The Journal of Immunology,* 189**,** 1330.

ODERMATT, P. D., SHIVANANDAN, A., DESCHOUT, H., JANKELE, R., NIEVERGELT, A. P., FELETTI, L., DAVIDSON, M. W., RADENOVIC,

A. & FANTNER, G. E. 2015. High-Resolution Correlative Microscopy: Bridging the Gap between Single Molecule Localization Microscopy and Atomic Force Microscopy. *Nano Letters,* 15**,** 4896-4904.

OKABE, A., BOOTS, B., SUGIHARA, K. & CHIU, S. 2000. *Spatial Tessellations: Concepts and Applications of Voronoi Diagrams*.

OLAVE, I. A., RECK-PETERSON, S. L. & CRABTREE, G. R. 2002. Nuclear Actin and Actin-Related Proteins in Chromatin Remodeling. *Annual Review of Biochemistry,* 71**,** 755-781.

OLIVIER, N., KELLER, D., GÖNCZY, P. & MANLEY, S. 2013a. Resolution Doubling in 3D-STORM Imaging through Improved Buffers. *PLoS ONE,* 8**,** e69004.

OLIVIER, N., KELLER, D., RAJAN, V. S., GÖNCZY, P. & MANLEY, S. 2013b. Simple buffers for 3D STORM microscopy. *Biomedical Optics Express,* 4**,** 885-899.

OTEY, C. A. & CARPEN, O. 2004. α-actinin revisited: A fresh look at an old player. *Cell Motility,* 58**,** 104-111.

OTEY, C. A., PAVALKO, F. M. & BURRIDGE, K. 1990. An interaction between alpha-actinin and the beta 1 integrin subunit in vitro. *The Journal of cell biology,* 111**,** 721-729.

OTOMO, T., TOMCHICK, D. R., OTOMO, C., PANCHAL, S. C., MACHIUS, M. & ROSEN, M. K. 2005. Structural basis of actin filament nucleation and processive capping by a formin homology 2 domain. *Nature,* 433**,** 488.

OVESNÝ, M., KŘÍŽEK, P., BORKOVEC, J., ŠVINDRYCH, Z. & HAGEN, G. M. 2014. ThunderSTORM: a comprehensive ImageJ plug-in for PALM and STORM data analysis and super-resolution imaging. *Bioinformatics,* 30**,** 2389-2390.

OWEN, D. M., RENTERO, C., ROSSY, J., MAGENAU, A., WILLIAMSON, D., RODRIGUEZ, M. & GAUS, K. 2010. PALM imaging and cluster analysis of protein heterogeneity at the cell surface. *Journal of Biophotonics,* 3**,** 446-454.

PALUCH, E. K. & RAZ, E. 2013. The role and regulation of blebs in cell migration. *Current opinion in cell biology,* 25**,** 582-590.

PANCHUK-VOLOSHINA, N., HAUGLAND, R. P., BISHOP-STEWART, J., BHALGAT, M. K., MILLARD, P. J., MAO, F., LEUNG, W.-Y. & HAUGLAND, R. P. 1999. Alexa Dyes, a Series of New Fluorescent Dyes that Yield Exceptionally Bright, Photostable Conjugates. *Journal of Histochemistry & Cytochemistry,* 47**,** 1179-1188.

PANTALONI, D. & CARLIER, M.-F. 1993. How profilin promotes actin filament assembly in the presence of thymosin β4. *Cell,* 75**,** 1007-1014.

PAVANI, S. R. P., THOMPSON, M. A., BITEEN, J. S., LORD, S. J., LIU, N., TWIEG, R. J., PIESTUN, R. & MOERNER, W. E. 2009. Three-dimensional, single-molecule fluorescence imaging beyond the

diffraction limit by using a double-helix point spread function. *Proceedings of the National Academy of Sciences,* 106**,** 2995-2999.

PAZ, H., PATHAK, N. & YANG, J. 2014. Invading one step at a time: the role of invadopodia in tumor metastasis. *Oncogene,* 33**,** 4193-4202.

PERCIPALLE, P. & VISA, N. 2006. Molecular functions of nuclear actin in transcription. *The Journal of cell biology,* 172**,** 967-971.

PEREIRA, P. M., ALBRECHT, D., JACOBS, C., MARSH, M., MERCER, J. & HENRIQUES, R. 2018. Fix your membrane receptor imaging: Actin cytoskeleton and CD4 membrane organization disruption by chemical fixation. *bioRxiv*.

PETERS, R., BENTHEM MUÑIZ, M., GRIFFIÉ, J., WILLIAMSON, D. J., ASHDOWN, G. W., LORENZ, C. D. & OWEN, D. M. 2017. Quantification of fibrous spatial point patterns from single-molecule localization microscopy (SMLM) data. *Bioinformatics,* 33**,** 1703-1711.

PETERS, R. & CHERRY, R. J. 1982. Lateral and rotational diffusion of bacteriorhodopsin in lipid bilayers: experimental test of the Saffman-Delbrück equations. *Proceedings of the National Academy of Sciences,* 79**,** 4317.

PETERS, R., GRIFFIÉ, J., BURN, G. L., WILLIAMSON, D. J. & OWEN, D. M. 2018a. Quantitative fibre analysis of single-molecule localization microscopy data. *Scientific Reports,* 8**,** 10418.

PETERS, R., GRIFFIE, J., WILLIAMSON, D., AARON, J., KHUON, S. & OWEN, D. 2018b. *Development of 2-colour and 3D SMLM data analysis methods for fibrous spatial point patterns*. Journal of Physics D: Applied Physics, 52, 1.

PFAENDTNER, J., BRANDUARDI, D., PARRINELLO, M., POLLARD, T. D. & VOTH, G. A. 2009. Nucleotide-dependent conformational states of actin. *Proceedings of the National Academy of Sciences,* 106**,** 12723.

PIRAGYTE, I. & JUN, C.-D. 2012. Actin engine in immunological synapse. *Immune network,* 12**,** 71-83.

POLLARD, T. D. & BORISY, G. G. 2003. Cellular Motility Driven by Assembly and Disassembly of Actin Filaments. *Cell,* 112**,** 453-465.

POLLARD, T. D. & COOPER, J. A. 2009. Actin, a Central Player in Cell Shape and Movement. *Science,* 326**,** 1208-1212.

PONTI, A., MACHACEK, M., GUPTON, S. L., WATERMAN-STORER, C. M. & DANUSER, G. 2004. Two Distinct Actin Networks Drive the Protrusion of Migrating Cells. *Science,* 305**,** 1782.

PRING, M., EVANGELISTA, M., BOONE, C., YANG, C. & ZIGMOND, S. H. 2003. Mechanism of Formin-Induced Nucleation of Actin Filaments. *Biochemistry,* 42**,** 486-496.

PRIOR, I. A., MUNCKE, C., PARTON, R. G. & HANCOCK, J. F. 2003. Direct visualization of Ras proteins in spatially distinct cell surface microdomains. *The Journal of cell biology,* 160**,** 165-170.

PRUYNE, D., EVANGELISTA, M., YANG, C., BI, E., ZIGMOND, S., BRETSCHER, A. & BOONE, C. 2002. Role of Formins in Actin Assembly: Nucleation and Barbed-End Association. *Science,* 297**,** 612.

QU, X., JIANG, Y., CHANG, M., LIU, X., ZHANG, R. & HUANG, S. 2015. Organization and regulation of the actin cytoskeleton in the pollen tube. *Frontiers in Plant Science,* 5**,** 786.

QUALMANN, B. & KESSELS, M. M. 2009. New players in actin polymerization – WH2-domain-containing actin nucleators. *Trends in Cell Biology,* 19**,** 276-285.

RAAB, M., DA SILVA, A. J., FINDELL, P. R. & RUDD, C. E. 1997. Regulation of Vav-SLP-76 binding by ZAP-70 and its relevance to TCR zeta/CD3 induction of interleukin-2. *Immunity,* 6**,** 155-164.

RAM, S., WARD, E. S. & OBER, R. J. 2006. Beyond Rayleigh's criterion: A resolution measure with application to single-molecule microscopy. *Proceedings of the National Academy of Sciences of the United States of America,* 103**,** 4457.

RAYLEIGH 1879. XXXI. Investigations in optics, with special reference to the spectroscope. *The London, Edinburgh, and Dublin Philosophical Magazine and Journal of Science,* 8**,** 261-274.

RETH, M. 1989. Antigen receptor tail clue. *Nature,* 338**,** 383-384.

RIDLEY, A. J. & HALL, A. 1992. The small GTP-binding protein rho regulates the assembly of focal adhesions and actin stress fibers in response to growth factors. *Cell,* 70**,** 389-399.

RIDLEY, A. J., PATERSON, H. F., JOHNSTON, C. L., DIEKMANN, D. & HALL, A. 1992. The small GTP-binding protein rac regulates growth factor-induced membrane ruffling. *Cell,* 70**,** 401-410.

RIES, J., KAPLAN, C., PLATONOVA, E., EGHLIDI, H. & EWERS, H. 2012. A simple, versatile method for GFP-based super-resolution microscopy via nanobodies. *Nature Methods,* 9**,** 582-584.

RIPLEY, B. D. 1977. Modelling spatial patterns. *Journal of the Royal Statistical Society B,* 39**,** 172-192.

RIPLEY, B. D. 1979. Tests of 'Randomness' for Spatial Point Patterns. *Journal of the Royal Statistical Society B,* 41**,** 368-374.

RISUEÑO, R. M., VAN SANTEN, H. M. & ALARCÓN, B. 2006. A conformational change senses the strength of T cell receptor–ligand interaction during thymic selection. *Proceedings of the National Academy of Sciences,* 103**,** 9625.

RITTER, ALEX T., ASANO, Y., STINCHCOMBE, JANE C., DIECKMANN, N. M. G., CHEN, B.-C., GAWDEN-BONE, C., VAN ENGELENBURG, S., LEGANT, W., GAO, L., DAVIDSON, MICHAEL W., BETZIG, E., LIPPINCOTT-SCHWARTZ, J. & GRIFFITHS, GILLIAN M. 2015. Actin Depletion Initiates Events Leading to Granule Secretion at the Immunological Synapse. *Immunity,* 42**,** 864-876.

RIVAS, F. V., KEEFE, J. P., ALEGRE, M.-L. & GAJEWSKI, T. F. 2004. Actin Cytoskeleton Regulates Calcium Dynamics and NFAT Nuclear Duration. *Molecular and Cellular Biology,* 24**,** 1628.

RODIONOV, V. I. & BORISY, G. G. 1997. Microtubule Treadmilling in Vivo. *Science,* 275**,** 215.

ROLLINS, G. C., SHIN, J. Y., BUSTAMANTE, C. & PRESSÉ, S. 2015. Stochastic approach to the molecular counting problem in superresolution microscopy. *Proceedings of the National Academy of Sciences,* 112**,** E110.

ROSSBOTH, B., ARNOLD, A. M., TA, H., PLATZER, R., KELLNER, F., HUPPA, J. B., BRAMESHUBER, M., BAUMGART, F. & SCHÜTZ, G. J. 2018. TCRs are randomly distributed on the plasma membrane of resting antigen-experienced T cells. *Nature Immunology,* 19**,** 821-827.

ROY, N. H. & BURKHARDT, J. K. 2018. The Actin Cytoskeleton: A Mechanical Intermediate for Signal Integration at the Immunological Synapse. *Frontiers in cell and developmental biology,* 6**,** 116-116.

RUBIN-DELANCHY, P., BURN, G. L., GRIFFIE, J., WILLIAMSON, D. J., HEARD, N. A., COPE, A. P. & OWEN, D. M. 2015. Bayesian cluster identification in single-molecule localization microscopy data. *Nature Methods,* 12**,** 1072-1076.

RUST, M. J., BATES, M. & ZHUANG, X. 2006. Sub-diffraction-limit imaging by stochastic optical reconstruction microscopy (STORM). *Nature Methods,* 3**,** 793-796.

SAGE, D., KIRSHNER, H., PENGO, T., STUURMAN, N., MIN, J., MANLEY, S. & UNSER, M. 2015. Quantitative evaluation of software packages for single-molecule localization microscopy. *Nature Methods,* 12**,** 717-724.

SALAZAR-FONTANA, L. I., BARR, V., SAMELSON, L. E. & BIERER, B. E. 2003. CD28 Engagement Promotes Actin Polymerization Through the Activation of the Small Rho GTPase Cdc42 in Human T Cells. *The Journal of Immunology,* 171**,** 2225.

SALOJIN, K. V., ZHANG, J. & DELOVITCH, T. L. 1999. TCR and CD28 Are Coupled Via ZAP-70 to the Activation of the Vav/Rac-1-/PAK-1/p38 MAPK Signaling Pathway. *The Journal of Immunology,* 163**,** 844.

SAMELSON, L. E., HARFORD, J. B. & KLAUSNER, R. D. 1985. Identification of the components of the murine T cell antigen receptor complex. *Cell,* 43**,** 223-231.

SANTOS, A. M., PONJAVIC, A., FRITZSCHE, M., FERNANDES, R. A., DE LA SERNA, J. B., WILCOCK, M. J., SCHNEIDER, F., URBANČIČ, I., MCCOLL, J., ANZILOTTI, C., GANZINGER, K. A., AßMANN, M., DEPOIL, D., CORNALL, R. J., DUSTIN, M. L., KLENERMAN, D., DAVIS, S. J., EGGELING, C. & LEE, S. F. 2018. Capturing resting T cells: the perils of PLL. *Nature Immunology,* 19**,** 203-205.

SARTORI, A., GATZ, R., BECK, F., RIGORT, A., BAUMEISTER, W. & PLITZKO, J. M. 2007. Correlative microscopy: Bridging the gap

between fluorescence light microscopy and cryo-electron tomography. *Journal of Structural Biology,* 160**,** 135-145.

SCHAEFER, L. H., SCHUSTER, D. & SCHAFFER, J. 2004. Structured illumination microscopy: artefact analysis and reduction utilizing a parameter optimization approach. *Journal of Microscopy,* 216**,** 165-74.

SCHÄTZLE, P., ESTEVES DA SILVA, M., TAS, R. P., KATRUKHA, E. A., HU, H. Y., WIERENGA, C. J., KAPITEIN, L. C. & HOOGENRAAD, C. C. 2018. Activity-Dependent Actin Remodeling at the Base of Dendritic Spines Promotes Microtubule Entry. *Current Biology,* 28**,** 2081-2093.e6.

SCHERMELLEH, L., HEINTZMANN, R. & LEONHARDT, H. 2010. A guide to super-resolution fluorescence microscopy. *Journal of Cell Biology,* 190**,** 165-175.

SCHNELL, U., DIJK, F., SJOLLEMA, K. A. & GIEPMANS, B. N. G. 2012. Immunolabeling artifacts and the need for live-cell imaging. *Nature Methods,* 9**,** 152.

SCHWAYER, C., SIKORA, M., SLOVÁKOVÁ, J., KARDOS, R. & HEISENBERG, C.-P. 2016. Actin Rings of Power. *Developmental Cell,* 37**,** 493-506.

SEELAND, I., XIONG, Y., ORLIK, C., DEIBEL, D., PROKOSCH, S., KÜBLBECK, G., JAHRAUS, B., DE STEFANO, D., MOOS, S., KURSCHUS, F. C., ARNOLD, B. & SAMSTAG, Y. 2018. The actin remodeling protein cofilin is crucial for thymic αβ but not γδ T-cell development. *PLoS biology,* 16**,** e2005380-e2005380.

SEMINARIO, M.-C. & BUNNELL, S. C. 2008. Signal initiation in T-cell receptor microclusters. *Immunological Reviews,* 221**,** 90-106.

SENGUPTA, P., JOVANOVIC-TALISMAN, T. & LIPPINCOTT-SCHWARTZ, J. 2013. Quantifying spatial organization in point-localization superresolution images using pair correlation analysis. *Nature Protocols,* 8**,** 345-354.

SEPT, D. & MCCAMMON, J. A. 2001. Thermodynamics and Kinetics of Actin Filament Nucleation. *Biophysical Journal,* 81**,** 667-674.

SHAN, X. & WANGE, R. L. 1999. Itk/Emt/Tsk Activation in Response to CD3 Cross-linking in Jurkat T Cells Requires ZAP-70 and Lat and Is Independent of Membrane Recruitment. *Journal of Biological Chemistry,* 274**,** 29323-29330.

SHANNON, C. E. 1949. Communication in the Presence of Noise. *Proceedings of the IRE,* 37**,** 10-21.

SHARONOV, A. & HOCHSTRASSER, R. M. 2006. Wide-field subdiffraction imaging by accumulated binding of diffusing probes. *Proceedings of the National Academy of Sciences,* 103**,** 18911-18916.

SHERMAN, E., BARR, V., MANLEY, S., PATTERSON, G., BALAGOPALAN, L., AKPAN, I., REGAN, CAROLE K., MERRILL, ROBERT K., SOMMERS, CONNIE L., LIPPINCOTT-SCHWARTZ, J. &

SAMELSON, LAWRENCE E. 2011. Functional Nanoscale Organization of Signaling Molecules Downstream of the T Cell Antigen Receptor. *Immunity,* 35**,** 705-720.

SHIMOMURA, O. 1979. Structure of the chromophore of Aequorea green fluorescrent protein. *FEBS Letters,* 104**,** 220–222.

SHIMOMURA, O., JOHNSON, F. H. & SAIGA, Y. 1962. Extraction, purification and properties of aequorin, a bioluminescent protein from the luminous hydromedusan, Aequorea. *Journal of Cell Computational Physiology,* 59**,** 223–239.

SHIVANANDAN, A., DESCHOUT, H., SCARSELLI, M. & RADENOVIC, A. 2014. Challenges in quantitative single molecule localization microscopy. *FEBS Letters,* 588**,** 3595-3602.

SHIVANANDAN, A., UNNIKRISHNAN, J. & RADENOVIC, A. 2016. On characterizing protein spatial clusters with correlation approaches. *Scientific Reports,* 6**,** 31164.

SHROFF, H., GALBRAITH, C. G., GALBRAITH, J. A. & BETZIG, E. 2008. Live-cell photoactivated localization microscopy of nanoscale adhesion dynamics. *Nature Methods,* 5**,** 417-423.

SHTENGEL, G., GALBRAITH, J. A., GALBRAITH, C. G., LIPPINCOTT-SCHWARTZ, J., GILLETTE, J. M., MANLEY, S., SOUGRAT, R., WATERMAN, C. M., KANCHANAWONG, P., DAVIDSON, M. W., FETTER, R. D. & HESS, H. F. 2009. Interferometric fluorescent super-resolution microscopy resolves 3D cellular ultrastructure. *Proceedings of the National Academy of Sciences,* 106**,** 3125-3130.

SIMONS, K. & VAN MEER, G. 1988. Lipid sorting in epithelial cells. *Biochemistry,* 27**,** 6197-6202.

SINGER, S. J. & NICOLSON, G. L. 1972. The fluid mosaic model of the structure of cell membranes. *Science,* 175**,** 720-731.

SIT, S.-T. & MANSER, E. 2011. Rho GTPases and their role in organizing the actin cytoskeleton. *Journal of Cell Science,* 124**,** 679.

SJÖBLOM, B., SALMAZO, A. & DJINOVIĆ-CARUGO, K. 2008. α-Actinin structure and regulation. *Cellular and Molecular Life Sciences,* 65**,** 2688.

SKAU, C. T. & WATERMAN, C. M. 2015. Specification of Architecture and Function of Actin Structures by Actin Nucleation Factors. *Annual Review of Biophysics,* 44**,** 285-310.

SMALL, J. V. 1995. Getting the actin filaments straight: nucleation-release or treadmilling? *Trends in Cell Biology,* 5**,** 52-55.

SOARES, H., HENRIQUES, R., SACHSE, M., VENTIMIGLIA, L., ALONSO, M. A., ZIMMER, C., THOULOUZE, M.-I. & ALCOVER, A. 2013. Regulated vesicle fusion generates signaling nanoterritories that control T cell activation at the immunological synapse. *The Journal of Experimental Medicine,* 210**,** 2415.

SOMMERS, C. L., MENON, R. K., GRINBERG, A., ZHANG, W., SAMELSON, L. E. & LOVE, P. E. 2001. Knock-in Mutation of the Distal Four Tyrosines of Linker for Activation of T Cells Blocks Murine T Cell Development. *The Journal of Experimental Medicine,* 194**,** 135.

SPERLING, A. I., SEDY, J. R., MANJUNATH, N., KUPFER, A., ARDMAN, B. & BURKHARDT, J. K. 1998. Cutting Edge: TCR Signaling Induces Selective Exclusion of CD43 from the T Cell-Antigen-Presenting Cell Contact Site. *Journal of Immunology,* 161**,** 6459-6462.

SQUIRE, J. M. 1997. Architecture and function in the muscle sarcomere. *Current Opinion in Structural Biology,* 7**,** 247-257.

STOKES, G. G. 1852. On the change of refrangibility of light. *Philosophical Transactions of the Royal Society of London,* 142**,** 463--562.

STOLP, B. & FACKLER, O. T. 2011. How HIV takes advantage of the cytoskeleton in entry and replication. *Viruses,* 3**,** 293-311.

STRINGARI, C., CINQUIN, A., CINQUIN, O., DIGMAN, M. A., DONOVAN, P. J. & GRATTON, E. 2011. Phasor approach to fluorescence lifetime microscopy distinguishes different metabolic states of germ cells in a live tissue. *Proceedings of the National Academy of Sciences,* 108**,** 13582-13587.

SURANENI, P., RUBINSTEIN, B., UNRUH, J. R., DURNIN, M., HANEIN, D. & LI, R. 2012. The Arp2/3 complex is required for lamellipodia extension and directional fibroblast cell migration. *The Journal of cell biology,* 197**,** 239-251.

SWEDLOW, J. R. 2013. Chapter 17 - Quantitative Fluorescence Microscopy and Image Deconvolution. *In:* SLUDER, G. & WOLF, D. E. (eds.) *Methods in Cell Biology*. Academic Press.

TANAKA, K. A. K., SUZUKI, K. G. N., SHIRAI, Y. M., SHIBUTANI, S. T., MIYAHARA, M. S. H., TSUBOI, H., YAHARA, M., YOSHIMURA, A., MAYOR, S., FUJIWARA, T. K. & KUSUMI, A. 2010. Membrane molecules mobile even after chemical fixation. *Nature Methods,* 7**,** 865-866.

TANIMURA, N., SAITOH, S.-I., KAWANO, S., KOSUGI, A. & MIYAKE, K. 2006. Palmitoylation of LAT contributes to its subcellular localization and stability. *Biochemical and Biophysical Research Communications,* 341**,** 1177-1183.

TAS, R. P., BOS, T. G. A. A. & KAPITEIN, L. C. 2018. Purification and Application of a Small Actin Probe for Single-Molecule Localization Microscopy. *In:* PETERMAN, E. J. G. (ed.) *Single Molecule Analysis: Methods and Protocols.* New York, NY: Springer New York.

TAVANO, R., CONTENTO, R. L., BARANDA, S. J., SOLIGO, M., TUOSTO, L., MANES, S. & VIOLA, A. 2006. CD28 interaction with filamin-A controls lipid raft accumulation at the T-cell immunological synapse. *Nature Cell Biology,* 8**,** 1270-1276.

THOMPSON, R. E., LARSON, D. R. & WEBB, W. W. 2002. Precise Nanometer Localization Analysis for Individual Fluorescent Probes. *Biophysical Journal,* 82**,** 2775–2783.

TRENDOWSKI, M. 2015. Using cytochalasins to improve current chemotherapeutic approaches. *Anti-cancer agents in medicinal chemistry,* 15**,** 327-335.

TRULSSON, M., YU, H., GISSELSSON, L., CHAO, Y., URBANO, A., AITS, S., MOSSBERG, A.-K. & SVANBORG, C. 2011. HAMLET Binding to α-Actinin Facilitates Tumor Cell Detachment. *PLOS ONE,* 6**,** e17179.

TSIEN, R. Y. 1998. The green fluorescent protein. *Annual Review of Biochemistry,* 67**,** 509-544.

TSKVITARIA-FULLER, I., SETH, A., MISTRY, N., GU, H., ROSEN, M. K. & WÜLFING, C. 2006. Specific patterns of Cdc42 activity are related to distinct elements of T cell polarization. *Journal of immunology (Baltimore, Md. : 1950),* 177**,** 1708-1720.

TSOUKAS, C. D., LANDGRAF, B., BENTIN, J., VALENTINE, M., LOTZ, M., VAUGHAN, J. H. & CARSON, D. A. 1985. Activation of resting T lymphocytes by anti-CD3 (T3) antibodies in the absence of monocytes. *Journal of Immunology,* 135**,** 1719.

TYBULEWICZ, V. L. J. & HENDERSON, R. B. 2009. Rho family GTPases and their regulators in lymphocytes. *Nature Reviews Immunology,* 9**,** 630.

URUNO, T., ZHANG, P., LIU, J., HAO, J.-J. & ZHAN, X. 2003. Haematopoietic lineage cell-specific protein 1 (HS1) promotes actin-related protein (Arp) 2/3 complex-mediated actin polymerization. *Biochemical Journal,* 371**,** 485.

VALADES CRUZ, C. A., SHABAN, H. A., KRESS, A., BERTAUX, N., MONNERET, S., MAVRAKIS, M., SAVATIER, J. & BRASSELET, S. 2016. Quantitative nanoscale imaging of orientational order in biological filaments by polarized superresolution microscopy. *Proceedings of the National Academy of Sciences,* 113**,** E820-E828.

VALITUTTI, S., DESSING, M., AKTORIES, K., GALLATI, H. & LANZAVECCHIA, A. 1995a. Sustained signaling leading to T cell activation results from prolonged T cell receptor occupancy. Role of T cell actin cytoskeleton. *The Journal of experimental medicine,* 181**,** 577-584.

VALITUTTI, S., MÜLLER, S., CELLA, M., PADOVAN, E. & LANZAVECCHIA, A. 1995b. Serial triggering of many T-cell receptors by a few peptide–MHC complexes. *Nature,* 375**,** 148.

VAN DE LINDE, S., LOSCHBERGER, A., KLEIN, T., HEIDBREDER, M., WOLTER, S., HEILEMANN, M. & SAUER, M. 2011. Direct stochastic optical reconstruction microscopy with standard fluorescent probes. *Nature Protocols,* 6**,** 991-1009.

VAN DEN ENT, F., AMOS, L. A. & LÖWE, J. 2001. Prokaryotic origin of the actin cytoskeleton. *Nature,* 413**,** 39.

VAN OERS, N., KILLEEN, N. & WEISS, A. 1996. Lck regulates the tyrosine phosphorylation of the T cell receptor subunits and ZAP-70 in murine thymocytes. *Journal of Experimental Medicine,* 183**,** 1053-1062.

VARMA, R., CAMPI, G., YOKOSUKA, T., SAITO, T. & DUSTIN, M. L. 2006. T Cell Receptor-Proximal Signals Are Sustained in Peripheral Microclusters and Terminated in the Central Supramolecular Activation Cluster. *Immunity,* 25**,** 117-127.

VEILLETTE, A., BOOKMAN, M. A., HORAK, E. M. & BOLEN, J. B. 1988. The CD4 and CD8 T cell surface antigens are associated with the internal membrane tyrosine-protein kinase p56lck. *Cell,* 55**,** 301-308.

WANG, Y., LI, D., NURIEVA, R., YANG, J., SEN, M., CARREÑO, R., LU, S., MCINTYRE, B. W., MOLLDREM, J. J., LEGGE, G. B. & MA, Q. 2009. LFA-1 affinity regulation is necessary for the activation and proliferation of naive T cells. *The Journal of biological chemistry,* 284**,** 12645-12653.

WANGE, R. L. 2000. LAT, the Linker for Activation of T Cells: A Bridge Between T Cell-Specific and General Signaling Pathways. *Science STKE,* 63**,** re1.

WARDENBURG, J. B., FU, C., JACKMAN, J. K., FLOTOW, H., WILKINSON, S. E., WILLIAMS, D. H., JOHNSON, R., KONG, G., CHAN, A. C. & FINDELL, P. R. 1996. Phosphorylation of SLP-76 by the ZAP-70 Protein-tyrosine Kinase Is Required for T-cell Receptor Function. *Journal of Biological Chemistry,* 271**,** 19641-19644.

WATSON, C. L., FURLONG, S. J. & HOSKIN, D. W. 2008. Impaired Interleukin-2 Synthesis and T Cell Proliferation Following Antibody-mediated CD3 and CD2 or CD28 Cross-linking in Trans: Evidence that T Cell Activation Requires the Engagement of Costimulatory Molecules Within the Immunological Synapse. *Immunological Investigations,* 37**,** 63-78.

WEBER, A., PENNISE, C. R., BABCOCK, G. G. & FOWLER, V. M. 1994. Tropomodulin caps the pointed ends of actin filaments. *The Journal of Cell Biology,* 127**,** 1627.

WEGNER, A. 1976. Head to tail polymerization of actin. *Journal of Molecular Biology,* 108**,** 139-150.

WEGNER, A. & ENGEL, J. 1975. Kinetics of the cooperative association of actin to actin filament. *Biophysical Chemistry,* 3**,** 215-225.

WEGNER, W., ILGEN, P., GREGOR, C., VAN DORT, J., MOTT, A. C., STEFFENS, H. & WILLIG, K. I. 2017. In vivo mouse and live cell STED microscopy of neuronal actin plasticity using far-red emitting fluorescent proteins. *Scientific Reports,* 7**,** 11781.

WEINBERG, J. & DRUBIN, D. G. 2012. Clathrin-mediated endocytosis in budding yeast. *Trends in Cell Biology,* 22**,** 1-13.

WESTON, L., COUTTS, A. S. & LA THANGUE, N. B. 2012. Actin nucleators in the nucleus: an emerging theme. *Journal of cell science,* 125**,** 3519-3527.

WILLIAMS, B. L., SCHREIBER, K. L., ZHANG, W., WANGE, R. L., SAMELSON, L. E., LEIBSON, P. J. & ABRAHAM, R. T. 1998. Genetic evidence for differential coupling of Syk family kinases to the T-cell receptor: reconstitution studies in a ZAP-70-deficient Jurkat T-cell line. *Molecular and cellular biology,* 18**,** 1388-1399.

WILLIAMSON, D. J., OWEN, D. M., ROSSY, J., MAGENAU, A., WEHRMANN, M., GOODING, J. J. & GAUS, K. 2011. Pre-existing clusters of the adaptor Lat do not participate in early T cell signaling events. *Nature Immunology,* 12**,** 655-662.

WU, J., WANG, H., GUO, X. & CHEN, J. 2016. Cofilin-mediated actin dynamics promotes actin bundle formation during Drosophila bristle development. *Molecular biology of the cell,* 27**,** 2554-2564.

WU, J., ZHAO, Q., KUROSAKI, T. & WEISS, A. 1997. The Vav Binding Site (Y315) in ZAP-70 Is Critical for Antigen Receptor–mediated Signal Transduction. *The Journal of Experimental Medicine,* 185**,** 1877.

YAMAGUCHI, H. & CONDEELIS, J. 2007. Regulation of the actin cytoskeleton in cancer cell migration and invasion. *Biochimica et Biophysica Acta (BBA) - Molecular Cell Research,* 1773**,** 642-652.

YAMASHITA, A., MAEDA, K. & MAÉDA, Y. 2003. Crystal structure of CapZ: structural basis for actin filament barbed end capping. *The EMBO journal,* 22**,** 1529-1538.

YAN, R., MOON, S., KENNY, S. J. & XU, K. 2018. Spectrally Resolved and Functional Super-resolution Microscopy via Ultrahigh-Throughput Single-Molecule Spectroscopy. *Accounts of Chemical Research,* 51**,** 697-705.

YARAR, D., TO, W., ABO, A. & WELCH, M. D. 1999. The Wiskott–Aldrich syndrome protein directs actin-based motility by stimulating actin nucleation with the Arp2/3 complex. *Current Biology,* 9**,** 555-S1.

YI, J., WU, X. S., CRITES, T., HAMMER, J. A. & POLLARD, T. D. 2012. Actin retrograde flow and actomyosin II arc contraction drive receptor cluster dynamics at the immunological synapse in Jurkat T cells. *Molecular Biology of the Cell,* 23**,** 834-852.

YU, Y., SMOLIGOVETS, A. A. & GROVES, J. T. 2013. Modulation of T cell signaling by the actin cytoskeleton. *Journal of Cell Science,* 126**,** 1049-1058.

ZAMIR, E. & GEIGER, B. 2001. Molecular complexity and dynamics of cell-matrix adhesions. *Journal of Cell Science,* 114**,** 3583.

ZEISSIG, S., PETERSEN, B.-S., TOMCZAK, M., MELUM, E., HUC-CLAUSTRE, E., DOUGAN, S. K., LAERDAHL, J. K., STADE, B., FORSTER, M., SCHREIBER, S., WEIR, D., LEICHTNER, A. M., FRANKE, A. & BLUMBERG, R. S. 2015. Early-onset Crohn's disease

and autoimmunity associated with a variant in CTLA-4. *Gut,* 64**,** 1889-1897.

ZENG, R., CANNON, J. L., ABRAHAM, R. T., WAY, M., BILLADEAU, D. D., BUBECK-WARDENBERG, J. & BURKHARDT, J. K. 2003. SLP-76 Coordinates Nck-Dependent Wiskott-Aldrich Syndrome Protein Recruitment with Vav-1/Cdc42-Dependent Wiskott-Aldrich Syndrome Protein Activation at the T Cell-APC Contact Site. *The Journal of Immunology,* 171**,** 1360.

ZHANG, J., BÁRDOS, T., LI, D., GÁL, I., VERMES, C., XU, J., MIKECZ, K., FINNEGAN, A., LIPKOWITZ, S. & GLANT, T. T. 2002. Cutting Edge: Regulation of T Cell Activation Threshold by CD28 Costimulation Through Targeting Cbl-b for Ubiquitination. *The Journal of Immunology,* 169**,** 2236.

ZHANG, W., SLOAN-LANCASTER, J., KITCHEN, J., TRIBLE, R. P. & SAMELSON, L. E. 1998. LAT: The ZAP-70 Tyrosine Kinase Substrate that Links T Cell Receptor to Cellular Activation. *Cell,* 92**,** 83-92.

ZHANG, W., TRIBLE, R. P., ZHU, M., LIU, S. K., MCGLADE, C. J. & SAMELSON, L. E. 2000. Association of Grb2, Gads, and Phospholipase C-γ1 with Phosphorylated LAT Tyrosine Residues: Effect of LAT tyrosine mutations on T cell angigen receptor-mediated signaling. *Journal of Biological Chemistry,* 275**,** 23355-23361.

ZHANG, Z., NISHIMURA, Y. & KANCHANAWONG, P. 2017. Extracting microtubule networks from superresolution single-molecule localization microscopy data. *Molecular Biology of the Cell,* 28**,** 333-345.